MICROFLUIDICS-BASED STRATEGIES FOR PROTEIN CRYSTALLOGRAPHY

Thesis by

Megan J. Anderson

In Partial Fulfillment of the Requirements

For the Degree of

Doctor of Philosophy

CALIFORNIA INSTITUTE OF TECHNOLOGY

Pasadena, California

2009

(Defended September 18, 2008)

ACKNOWLEDGEMENTS

I would first like to thank my advisor, Stephen Quake, for his mentorship and guidance over the past five years. Working for Steve was an invaluable experience and I thoroughly enjoyed my time in his laboratory.

I would also like to thank our collaborators Axel Brunger and James Berger for their interest in this work. In particular, I would like to thank Byron DeLaBarre in Axel Brunger's lab for sharing his knowledge of crystallography and assisting me with my first crystal structure. I also appreciate all of the protein samples that Scott Gradia in James Berger's lab has continually provided me with over the past years.

I am grateful for all of the colleagues I have had an opportunity to work with over the past five years in the Quake lab. Carl Hansen was an excellent mentor when I joined the lab and shared with me his enthusiasm for science and this project. Rafael Gomez was a tremendous resource when I was starting out and has always been willing to lend a hand around the lab whenever anyone needs help. I would also like to thank Sebastian Maerkl, Doron Gerber, YinThai Chan, Steve Bates, Jenny Ning, Frank Lee, Jerrod Schwartz, Thomas Schneider, Stavros Stavrakis and Josh Weinstein for their company in lab and for the many trips to the Thai café and coffee breaks we have shared. Additionally, I have really enjoyed working with Aaron Streets for the past few years and I wish him the best of luck in the continuation of this project.

I would also like to thank all of the microfluidic foundry technicians who provided me with an unending supply of chips for my work over the past five years, especially Christina Morrales, Alejandra Torres, Canh Nguyen, Jesse Emberton, and Anastasia Potanina.

Finally, I would like to thank my family who has always been there for me. I appreciate the continual support and encouragement from my parents, John and Sally, and my brothers John, Scott, and Kyle. Above all, I thank my husband Matthew Dicken for his unending love, patience, and support as we have journeyed down this road together.

ABSTRACT

Protein crystallography is an invaluable tool for the study of biological processes at the molecular level. While several crystallization techniques are actively pursued in both academic and industrial laboratories to produce high-quality protein crystals, the use of microfluidic technology for structural biology was previously shown to improve protein crystallization over more traditional methods. This thesis describes a microfluidics-based crystallization strategy that was developed to increase the success rate of crystallizing challenging proteins. The crystallization strategy involves using multiple microfluidic devices to characterize the solubility trends of the crystallization target, to perform nanoliter volume free interface diffusion crystallization experiments designed around the solubility trends, and to enable in situ diffraction analysis of crystals grown in microfluidic devices. The crystallization strategy was applied to the crystallization of a dozen challenging proteins and increased the overall crystallization and diffraction success rates compared with conventional automation. The crystallization strategy was also utilized to crystallize four metabolic proteins and provides the first demonstration of in situ structure determination for novel crystallization targets using a microfluidic crystallization platform. Additional technological advances were accomplished by the development of a novel microfluidic device designed to address the specific challenges of membrane protein crystallography. To date, this microfluidic crystallization strategy has produced four novel protein structures and holds great promise for future work in the field of protein crystallography.

TABLE OF CONTENTS

LIST OF FIGURES

LIST OF TABLES

ABBREVIATIONS

MSL, multilayer soft lithography; PSI, Protein Structure Initiative; AlaRS, alanyl-tRNA synthetase; AMG, amelogenin; bR, bacteriorhodopsin; bR D85S, bacteriorhodopsin mutant D85S; Cbb3, cytochrome cbb3; 19S Lid, proteasome 19S Lid particle; P450 1-12G, cytochrome P450 mutant 1-12G; Tf/TfR, transferrin/transferrin receptor mutant complex; VCP/Vimp, VCP-97/Vimp complex; PEG, polyethylene glycol; MME, monomethyl ether; pI, theoretical isoelectric point; Hepes, 4-(2-hydroxyethyl)-1-piperazineethanesulfonic acid; GK, glycerol kinase; PTS, phosphotransferase system; FBP, fructose 1,6-bisphosphate; βME, β-mercaptoethanol; SEC-MALLS, Size Exclusion Chromatography - Multi-Angle Laser Light Scattering Studies; asu, asymmetric unit; NCS, non-crystallographic symmetry; rmsd, root-mean-square deviation; TAPS, N-Tris(hydroxymethyl)methyl-3-aminopropanesulfonic acid; ATF, phosphodifluoromethylphosphonic acid-adenylate ester; Mg-ATP, magnesium adenosine 5'-triphosphate; FMS, Poly(3,3,3-trifluoropropylmethylsiloxan); DM, n-decyl-β-D-maltoside; DMPC, 1,2-dimyristoyl-*sn*-glycero-3-phosphocholine; CHAPS, 3-[(Cholamidopropyl)dimethylammonio]-1-propane-sulfonate; PDMS, polydimethylsiloxane; I/O, input/output; HMDS, hexamethyldisilazane; TMCS, trimethylchlorosilane; CAPS, 3-(cyclohexylamino)-1-propanesulfonic acid; MES, 2-(N-morpholino)ethanesulfonic acid; AMP, ampicillin; IPTG, isopropyl β-D-1-thiogalactopyranoside; Ni-NTA, nickel-nitrilotriacetic acid; FPLC, Fast Protein Liquid Chromatography; cv, column volume; PAGE, polyacrylamide gel electrophoresis; TEV, Tobacco Etch Virus; DTT, dithiothreitol

Chapter 1

OVERVIEW

Introduction

The underlying goal of structural biology is to enable biological systems to be understood at the molecular level. In particular, macromolecular structures are used to study the function of proteins, macromolecule complex formation, the multiple conformations of proteins, and signaling pathways within cells. Macromolecular structures have also proven to be an invaluable tool for rational drug design (*1*). While over 40,000 protein structures have been determined using X-ray crystallography since the first crystal structure was solved almost 50 years ago (*2*), this represents only a small fraction of the proteins involved in living processes. As the list of known proteins continually expands due to advances in genome sequencing technology, parallel advances in X-ray crystallography techniques are required to keep pace.

The success of large-scale protein crystallography efforts are currently limited by the production of protein crystals of sufficient size and quality for X-ray diffraction analysis. Crystal production is limited by bottlenecks in the expression, purification, and identification of successful crystallization conditions for crystallization targets (*3*). Additional difficulties are encountered as more challenging crystallization targets, including membrane proteins and large macromolecule complexes, are attempted. For crystallization targets that are difficult to express in large quantities, the number of crystallization trials that can be performed is

restricted. Therefore, crystallization techniques for the high-throughput production of diffraction-quality crystals using limited amounts of protein are needed to advance structural biology efforts.

Recently, microfluidic technology has been utilized to develop crystallization devices that are ideal for high-throughput crystallization experiments (*4–6*). Microfluidic technology allows for the parallel implementation and automation of biological assays on a nanoliter scale, increasing speed and throughput compared to conventional laboratory techniques. Additionally, microfluidic devices provide economy of scale in protein and reagent consumption, reduce experimental costs, and increase the sensitivity of biological assays. Multilayer soft lithography (MSL) technology is used to fabricate microfluidic devices out of elastomeric materials with integrated valves (*7*). Active valves can be used to create microfluidic devices with individually addressable chambers, peristaltic pumps, and mixers for complex fluid-handling capabilities (*8–10*).

In particular, a suite of microfluidic devices was developed to address all stages of protein crystallography, from the identification of crystallization reagents to the production of larger format crystal for in situ diffraction analysis (*4, 6, 10*). The microfluidic devices perform free interface diffusion crystallization experiments, which is enabled by the unique diffusion-driven mixing of fluids in the microscale environment (*11*). The work presented in this thesis utilizes the microfluidic crystallization platform for the structure determination of novel crystallization targets (*12, 13*).

Context

This work builds on the microfluidic crystallization platform previously developed in our lab by Carl Hansen (*4, 6, 10*). When the author began this work, three devices for protein crystallization had been developed using MSL technology. The utility of each of the devices was validated with model proteins and it remained to be seen if the devices could be used to produce crystal structures of novel proteins. As a starting point, the author began using the microfluidic crystallization platform to crystallize challenging proteins. Since the microfluidic crystallization platform was essential for all aspects of this work, a brief description of the crystallization devices is provided. Additionally, modified fabrication protocols for each of the devices are presented in Appendix A.

The first component in the microfluidic crystallization platform is the formulator device (Figure 1.1). The formulator systematically characterizes the solubility behavior of crystallization targets in the presence of thousands of chemical conditions to identify crystallization reagents. Additionally, the formulator generates complete phase diagrams with each of the crystallization reagents that are used to design customized crystallization experiments. Crystallization reagents are identified by their ability to manipulate protein solubility by causing protein aggregation. The chemical conditions used in the solubility characterization are created within the device using a multiplexer with 40 input lines for different salt solutions, buffering agents, and precipitating agents. All solubility measurements are performed in a rotary mixer in the center of the device and require only nanoliter volumes of the crystallization target. The formulator setup is fully automated and solubility experiments can be carried out for days without any user input.

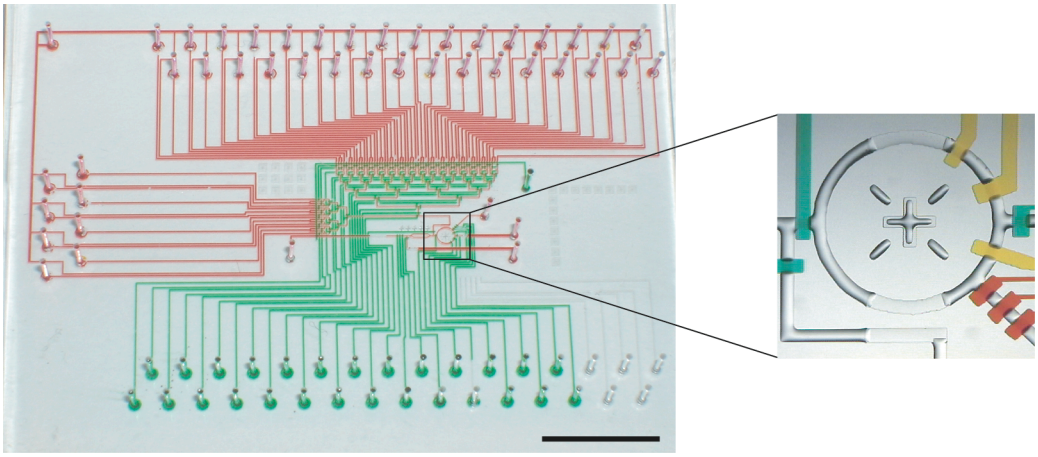

Figure 1.1: Microfluidic formulator device. The reagent input ports for the multiplexer are located at the top and the right side of the device and are filled with red dye. The control lines are filled with green dye and are pressurized through the input ports located at the bottom of the device. The rotary mixer is located in the center of the device and a close up of the mixer is shown on the right. The flow layer is filled with air, the peristaltic pump on the rotary mixer that creates different chemical conditions from the multiplexer is filled with yellow dye, the peristaltic pump controlling protein inlet into the mixer is filled with red dye, and the input and output control valves on the mixer are filled with green dye. Protein aggregation is measured in the flat section at the bottom of the rotary mixer. This figure was adapted from Figure 2 in (*10*). The scale bar represents 1 cm.

The second component in the microfluidic crystallization platform is the free interface diffusion screening device (Figure 1.2). The screening device performs nanoliter volume free interface diffusion experiments to screen the crystallization reagents identified with the formulator device. Each screening device tests 48 different crystallization reagents at five different protein:reagent mixing ratios for a total of 240 free interface diffusion experiments.

The screening device can be set up in a matter of minutes using only 3 μl of protein and crystallization experiments can proceed for weeks within the device.

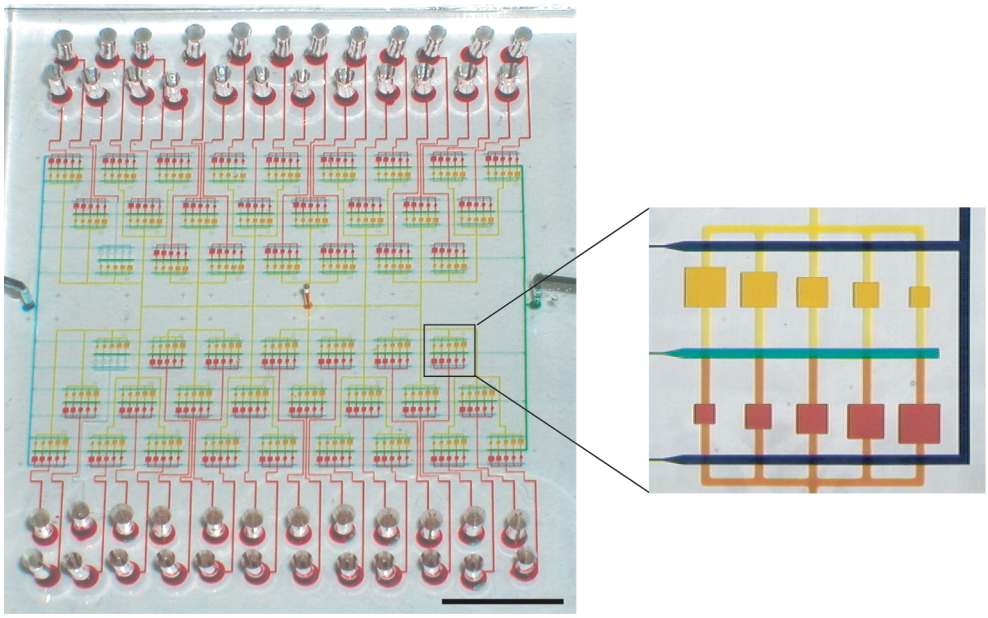

Figure 1.2: Microfluidic free interface diffusion screening device. The crystallization reagents are loaded through large input ports at the top and the bottom of the device and the reagent chambers are filled with red dye. Protein is loaded in the center of the device using a gel loading tip and the protein chambers are filled with yellow dye. The interface line separates the protein chambers from the reagent chambers during loading and is filled with green dye. The containment lines isolate each of the free interface diffusion experiments from the rest of the device and are filled with blue dye. A close up of the five free interface diffusion experiments for one reagent is shown on the right. See (*4*) for details. The scale bar represents 1 cm.

The final component in the microfluidic crystallization platform is the scale-up diffraction device (Figure 1.3). The scale-up diffraction device performs larger format free interface diffusion experiments to produce crystals of sufficient dimensions for in situ diffraction analysis. Each scale-up diffraction device performs 100 free interface diffusion experiments with one reagent and utilizes multiple free interface diffusion path lengths to manipulate crystal growth. The crystallization experiments are encapsulated in a thin layer of elastomer, and sections of the device surrounding the crystals can be removed using a punching tool and placed directly into the X-ray beam for in situ diffraction analysis. Osmotic solutions are placed on top of the thin elastomer layer during crystallization to prevent dehydration.

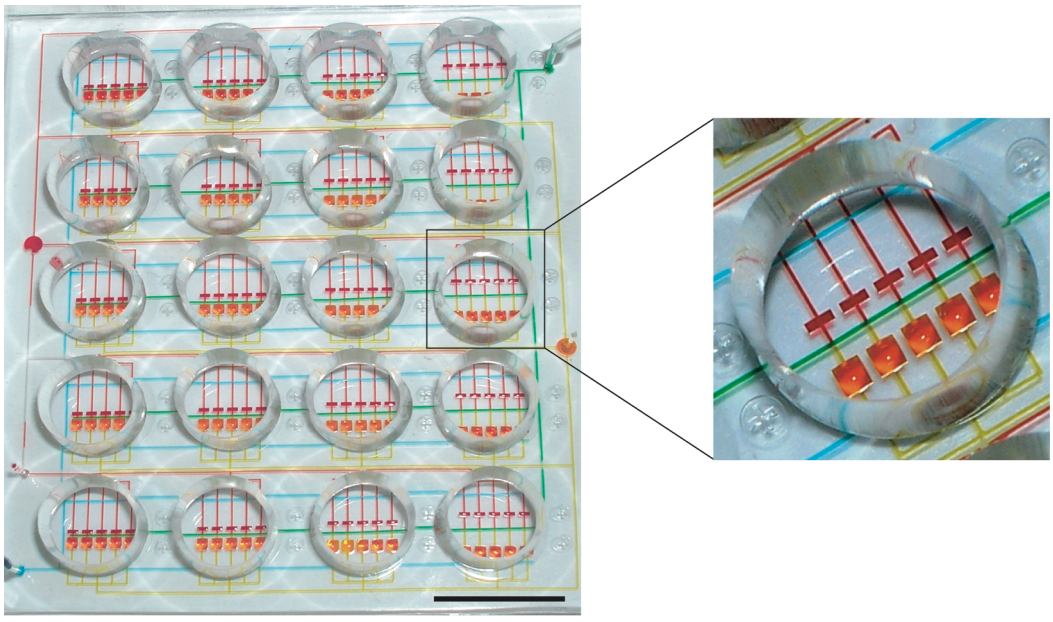

Figure 1.3: Microfluidic scale-up diffraction device. The crystallization reagent is loaded on one side of the device using a gel loading tip and the reagent chambers are filled with red dye. Protein is loaded on the opposite side of the device using a gel loading tip and the protein chambers are filled with yellow dye. The interface line is filled with green dye and

the containment lines are filled with blue dye. A close up of the thin section of the device with one set of free interface diffusion chambers is shown on the right. A circular disk is created when one section of the device is punched out and a small alligator clip is used to position the disk in the X-ray beam for diffraction analysis. See (*6*) for details. The scale bar represents 1 cm.

Organization and Collaborations

Chapter 2 describes a crystallization strategy based on the knowledge of the phase behavior of a protein that allows one to create rational crystallization screens to increase the success rate of crystallizing challenging proteins (*12*). The strategy is based on using the microfluidic formulator device to perform large numbers of protein solubility experiments across a broad range of chemical conditions to identify reagents for crystallization experiments. Phase diagrams were subsequently generated for the identified reagents and used to design customized crystallization screens for every protein. This strategy was applied with a 75% success rate to the crystallization of twelve challenging proteins. The overall diffraction success rate was 33%, about double what was achieved with conventional automation in large-scale protein structure consortia.

Protein samples were provided by the following collaborators: Manal Swairjo, Scripps Research Institute; Stefan Habelitz, University of California, San Francisco; Marc Facciotti, Lee Hood Laboratory, Institute for Systems Biology; Michael Merckel, University of Helsinki; Takumi Koshiba, David Chan Laboratory, California Institute of Technology; Xavier Ambroggio, Douglas Rees and Raymond Deshaies Laboratories, California Institute of Technology; Pavel Strop, Axel Brunger Laboratory, Stanford University; Matthew Peters

and Peter Meinhold, Frances Arnold Laboratory, California Institute of Technology; Scott Gradia, James Berger Laboratory, University of California, Berkeley; Anthony Giannetti, Pamela Bjorkman Laboratory, California Institute of Technology; and Byron DeLaBarre, Axel Brunger Laboratory, Stanford University. Carl Hansen, currently at the University of British Columbia, assisted with the early formulator experiments and data analysis.

In Chapter 3 the crystal structure of an *Escherichia coli* glycerol kinase mutant Gly230→Asp is presented (*13*). The structure was determined to 2.0 Å and is the first demonstration of in situ structure determination for a novel crystallization target using a microfluidics-based crystallization platform. Parallel vapor diffusion experiments were performed and revealed the diffraction limit of crystals grown in the scale-up diffraction device was higher than the 3.0 Å diffraction limit of crystals grown in the vapor diffusion format.

The *Escherichia coli* genomic DNA for the glycerol kinase mutant was provided by Anu Raghunathan, Bernhard Palsson Laboratory, University of California, San Diego. The structure was solved in collaboration with Byron DeLaBarre, Axel Brunger Laboratory, Stanford University.

In Chapter 4 crystal structures of *Escherichia coli* glycerol kinase mutants Asp72 → Ala, 235Lys-Gly-Gly insert, and Met271 → Ile were determined to 2.3 Å, 2.8 Å, and 2.9 Å, respectively. Each of the structures was obtained using the microfluidics-based crystallization platform, including in situ diffraction collection from the scale-up diffraction devices.

The *Escherichia coli* genomic DNA for the glycerol kinase mutants was provided by M. Kenyon Applebee, Bernhard Palsson Laboratory, University of California, San Diego. The structures were solved in collaboration with Pete Dunten, Stanford Synchrotron Radiation Laboratory.

In Chapter 5 a novel microfluidic device was developed for membrane protein crystallization in the presence of lipids. The dialysis device for membrane protein crystallization was designed to perform multiple crystallization experiments in a lipid environment using detergent-solubilized membrane protein samples. The microfluidic device incorporates a dialysis platform for the removal of detergent monomers from purified protein-detergent micelles with a free interface diffusion crystallization platform. A detergent-solubilized KcsA potassium channel was used to validate the utility of the microfluidic dialysis device for membrane protein crystallization.

The KcsA channel protein was provided by Joel Butterwick, Roderick MacKinnon Laboratory, Rockefeller University.

Chapter 2

PHASE KNOWLEDGE ENABLES RATIONAL SCREENS FOR PROTEIN CRYSTALLIZATION

Introduction

One of the main bottlenecks in the application of protein crystallography to large-scale structural biology efforts is the production of diffraction-quality crystals. Protein crystallization relies on the identification of reagents that promote crystal formation and an understanding of protein solubility in the presence of these reagents to achieve optimal crystal growth. Traditional techniques to identify reagents for crystallization include incomplete factorial searches across chemical space and sparse-matrix screening around reagents previously shown to crystallize proteins (*14, 15*). While these techniques provide a starting point for crystallization experiments, they are not designed around the biophysical properties of individual proteins and have met with limited success for more challenging crystallization targets. For example, the NIH Protein Structure Initiative (PSI) was able to generate diffraction-quality crystals from less than one in five of the 10,000 purified protein targets it has attempted to date (http://targetdb.pdb.org/statistics/TargetStatistics.html).

Knowledge of protein solubility in the presence of a crystallizing reagent enables one to effectively utilize the reagent in a way that will promote crystallization. The traditional method to study protein solubility in response to reagents is to construct a phase diagram that measures the solubility at different protein and reagent concentrations. The protein solubility

curve outlined in each phase diagram depicts the most favorable protein and reagent concentrations to use in a crystallization experiment for optimal crystal growth. Currently, phase diagrams are only generated for readily available model proteins and for proteins with known crystallization conditions to improve crystal morphology (*16–25*). The infrequent use of phase diagrams for crystallization experiments is due to the large sample volumes and time required to construct the diagrams. The general utilization of phase diagrams to analyze protein solubility before starting crystallization experiments would lead to a more physical and rational approach to protein crystallization.

In this study, the utilization of a crystallization strategy based on a detailed understanding of protein solubility is shown to increase the crystallization success rate for challenging proteins. A microfluidic formulator device is used to systematically screen hundreds of reagents against protein targets at several points on the phase diagrams to identify reagents that affect the solubility of the protein. Next, each of the identified reagents is explored by constructing a complete phase diagram outlining the solubility limits of the protein in the presence of the reagent. The phase diagrams are then used to design individualized crystallization screens tailored to the solubility properties of the target protein. This device was previously demonstrated to greatly enrich crystallization conditions for xylanase, UMP kinase, and the integral membrane protein SERCA (*10, 26*), although no novel crystal structures have been obtained using this device. The customized crystallization screens are tested using a redesigned free interface diffusion screening device. Successful crystallization conditions are transported to a larger scale crystal growth format for diffraction analysis.

This rational screening strategy was applied to the crystallization of twelve biologically diverse and challenging proteins, eight of which failed to crystallize using traditional techniques. The crystallization targets range in size from 16 kDa to 360 kDa complexes and include membrane proteins, large multiprotein complexes, a protein/RNA complex, a metalloprotein complex, metabolic proteins, and an extracellular matrix protein. Identification of reagents and phase diagram generation for each target was completed using only microliters of sample, and the crystallization and diffraction success rates were roughly double that obtained by the PSI using conventional automation. The increased success rates are noteworthy given the target diversity and that 67% of the targets are from eukaryotic sources while the PSI crystallization targets to date are biased towards prokaryotic sources with only 30% of the targets from eukaryotic sources (http://targetdb.pdb.org/statistics/TargetStatistics.html).

Experimental Procedures

Protein Preparation. Protein samples were provided by the following collaborators: 98 kDa *Aquifex aeolicus* alanyl-tRNA synthetase (AlaRS) at 15 mg/ml from Manal Swairjo, The Scripps Research Institute; 22 kDa human amelogenin (AMG) at 2 mg/ml from Stefan Habelitz, University of California, San Francisco; 27 kDa *Halobacteria* bacteriorhodopsin (bR) and bacteriorhodopsin mutant D85S (bR D85S) at 18 mg/ml from Marc Facciotti, Institute for Systems Biology; 126 kDa *Rhodobacter sphaeroides* cytochrome cbb3 (Cbb3) at 10 mg/ml from Michael Merckel, University of Helsinki; 16 kDa *Saccharomyces cerevisiae* Fis1 at 60 mg/ml from Takumi Koshiba, California Institute of Technology; 360 kDa *Saccharomyces cerevisiae* proteasome 19S Lid particle (19S Lid) at 25 mg/ml from Xavier

Ambroggio, California Institute of Technology; 45 kDa *Mus musculus* P2X at 6 mg/ml from Pavel Strop, Stanford University; the 54 kDa heme domain of *Bacillus subtilis* cytochrome P450 mutant 1-12G (P450 1-12G) at 30 mg/ml from Matthew Peters and Peter Meinhold, California Institute of Technology; 123 kDa *Aquifex aeolicus* SMC/ScpA complex at 22 mg/ml from Scott Gradia, University of California, Berkeley; 72 kDa human tranferrin/transferrin receptor mutant complex (Tf/TfR) at 27 mg/ml from Anthony Giannetti, California Institute of Technology; and 254 kDa *Rattus norvegicus* VCP-97/Vimp complex (VCP/Vimp) at 10 mg/ml from Byron DeLaBarre, Stanford University.

Solubility Screening and Phase Diagram Generation. Solubility experiments were performed using a microfluidic formulator device developed by Hansen et al. (2004). Device fabrication, automation, experimental setup, and data acquisition were previously described (*10*) (Appendix A). The formulator device was used to create 448 unique reagents for solubility screening by systematically combining fourteen salt solutions, four buffering agents, and eight precipitating agents (see Appendix B for a complete list of the reagents). Salt solutions and precipitating agents were used near the maximal solubility and viscosity levels of each species. Each of the reagents was tested against the protein targets at six different protein and precipitant concentrations across the boundary of the phase diagram while holding the salt solution and buffering agent at a fixed level for a total of 2,688 solubility experiments for each protein target. Protein aggregation was quantified by imaging the protein in solution with each reagent using a charge coupled device camera, calculating the pixel intensity standard deviation, and subtracting the background pixel intensity standard deviation of the reagent in the absence of protein. Reagents that caused the

protein to aggregate above 3 pixel intensity standard deviation units for at least one of the six points tested were classified as potential crystallization reagents. For 3.3% of the images, the pixel intensity standard deviation value was negative due to errors in the formulator device, and for these measurements the pixel intensity standard deviation was set to zero.

Complete phase diagrams were generated for a subset of the crystallizing reagents identified with the solubility screening. For each phase diagram, the reagent was combined with the protein at 72 different precipitant and protein concentrations. The protein concentration was tested between 5–80% and the precipitant concentration was tested between 2.5–77.5%. Again, buffering agent and salt solution concentrations were held constant throughout the phase diagram at the concentrations used for the solubility screening. Protein aggregation was measured at each point as described above. Positions on the phase diagram that caused the protein to aggregate above 3 pixel intensity standard deviation units were classified as insoluble and positions below 3 were classified as soluble.

Crystallization Experiments and Device Fabrication. Initial crystallization experiments were performed using a modified version of the microfluidic free interface diffusion screening device (*4*). The screening device design was modified to perform five free interface diffusion experiments per reagent instead of three. The protein:reagent mixing ratios used are 1:4, 1:2, 1:1, 2:1, and 4:1, with a total reaction volume of 25 nl per free interface diffusion experiment. One screening device is used to test 48 reagents for a total of 240 parallel free interface diffusion experiments. The previous design utilized a hybrid glass/elastomer device and was modified to consist solely of elastomer to facilitate faster

fabrication. The devices were fabricated using multilayer soft lithography (*7*) and the fabrication protocol is outlined in Appendix A.

The crystallization experimental setup was previously described (*4*). Crystal hits were verified using IZIT protein stain, the crush test, or diffraction analysis. Crystal hits were transported to microfluidic scale-up diffraction devices, vapor diffusion format, or microbatch format for diffraction experiments. Device fabrication and experimental setup using the scale-up diffraction device was previously described (*6*) (Appendix A). Scale-up diffraction devices were incubated at room temperature up to two weeks and cryoprotectant was introduced by diffusion 24 hours before flash-freezing the crystals in the devices. For vapor diffusion experiments, 1 μl of protein was combined with 1 μl of reagent and suspended over 500 μl of reagent and incubated at room temperature up to two weeks. For microbatch experiments, a layer of paraffin oil was place over the microbatch wells and 1 μl of protein was combined with 1 μl of reagent under the oil and incubated at room temperature up to two weeks. For vapor diffusion and microbatch experiments the crystals were looped from the drops and through cryoprotectant before flash-freezing in liquid nitrogen.

Diffraction Studies. Diffraction data for Cbb3 was collected at station 11.1 of the Stanford Linear Accelerator Center (Stanford University), at an incident wavelength of 1.0 Å with a 15 second exposure and 1º oscillation. Diffraction data for bR and bR D85S was collected at station 8.3.1 of the Advanced Light Source (Lawrence Berkeley National Laboratory), at an incident wavelength of 1.0 Å with a 20 second exposure and 1º oscillation. Diffraction data

for P450 1-12G was collected on an R-axis IV (California Institute of Technology) at an incident wavelength of 1.54 Å with a 30 minute exposure and 1º oscillation.

Results and Discussion

Solubility Characterization. The phase-diagram-based approach to protein crystallography was used to design and implement customized crystallization strategies for twelve challenging protein targets. To begin, protein solubility was screened against an extensive set of chemical conditions to identify suitable reagents for crystallization trials (Figure 2.1). The solubility screening included a full factorial search of 448 reagents composed of unique precipitant, buffer, and salt combinations. For each reagent, protein phase behavior was explored by sampling protein solubility at six different protein and precipitant concentrations across the phase diagram for a total of 2,688 solubility experiments per target. The ability of each reagent to manipulate protein solubility was quantified by the amount of protein aggregation observed when the protein was introduced to the reagent. Reagents that caused protein aggregation above a threshold level were considered to be potential crystallizing reagents for that target. The solubility screening across chemical and phase space identified between 51 and 246 potential crystallizing reagents for each of the targets.

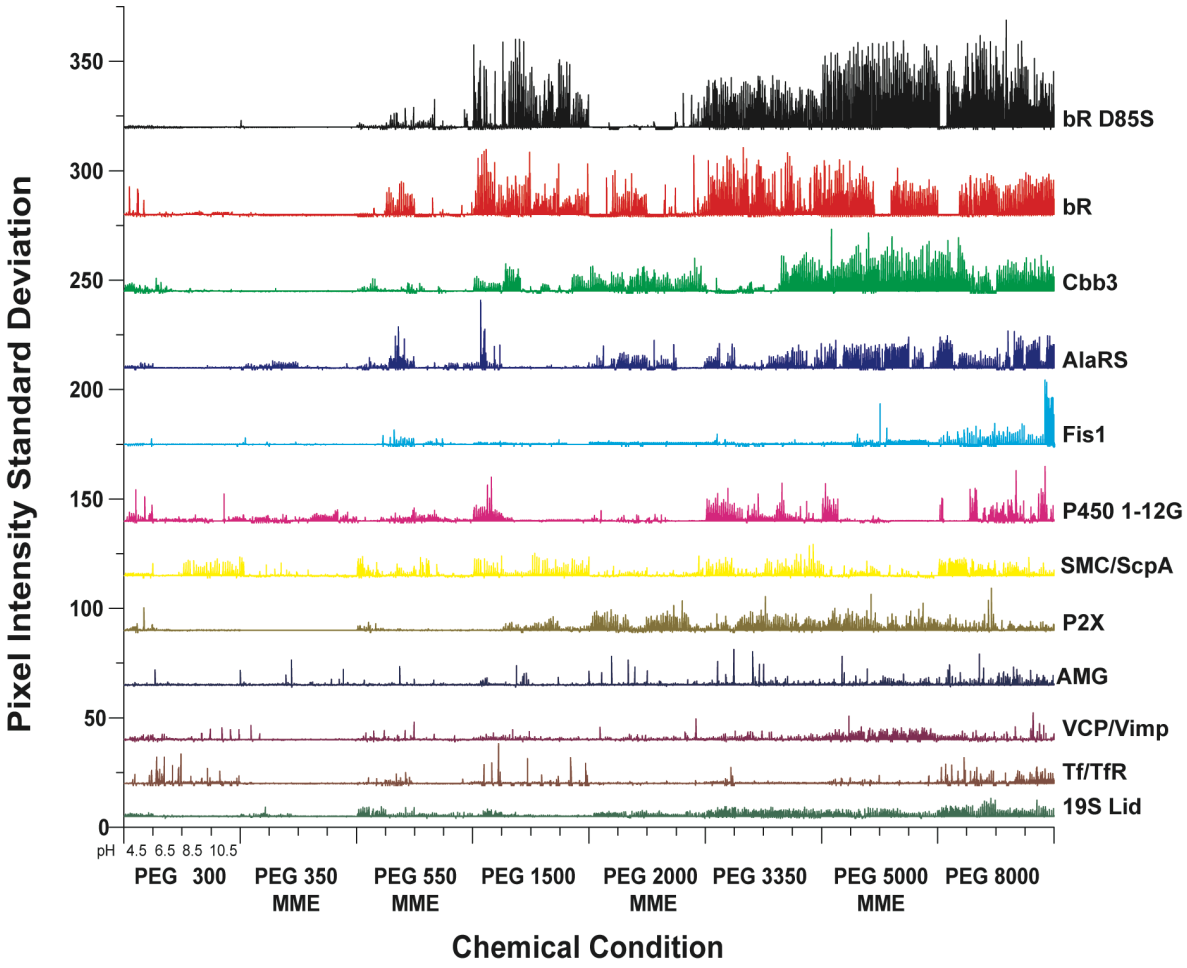

Figure 2.1: Solubility screening results for twelve protein targets. Pixel intensity standard deviation represents the amount of protein aggregation seen in response to each reagent. The proteins are displayed from top to bottom in the order of decreasing protein aggregation: bR D85S, bR, Cbb3, AlaRS, Fis1, P450 1-12G, SMC/ScpA, P2X, AMG, VCP/Vimp, Tf/TfR, and 19S Lid. The solubility screening results are grouped by precipitating agent and are further subdivided by buffering agent. See Appendix B for a complete list of the reagents screened.

Trends in the solubility screening results indicate protein phase behavior was predominately controlled by the precipitating component of the reagent (Figure 2.2A). The effectiveness of each of the reagent components on protein aggregation was determined by comparing the solubility results of reagents with two of the three components held constant. The precipitants utilized in the solubility experiments are polyethylene glycol (PEG) polymers with different chain lengths and end groups, giving each PEG polymer unique volume exclusion properties. Since the volume exclusion effect is more significant in longer polymers due to their larger radius of gyration, the longer polymers were used at a lower concentration than the shorter polymers. Polymers of four different chain lengths were examined and for every target the number of potential reagents identified with longer polymers surpassed the number of reagents identified with shorter polymers. Additionally, a second PEG polymer with a modified monomethyl ether (MME) end group was screened at each polymer length; the MME polymers produced fewer identified reagents at each polymer length. Therefore, increasing the polymer chain length of the precipitating agent increases the protein aggregation response, and the polymer chemical composition also influences protein aggregation.

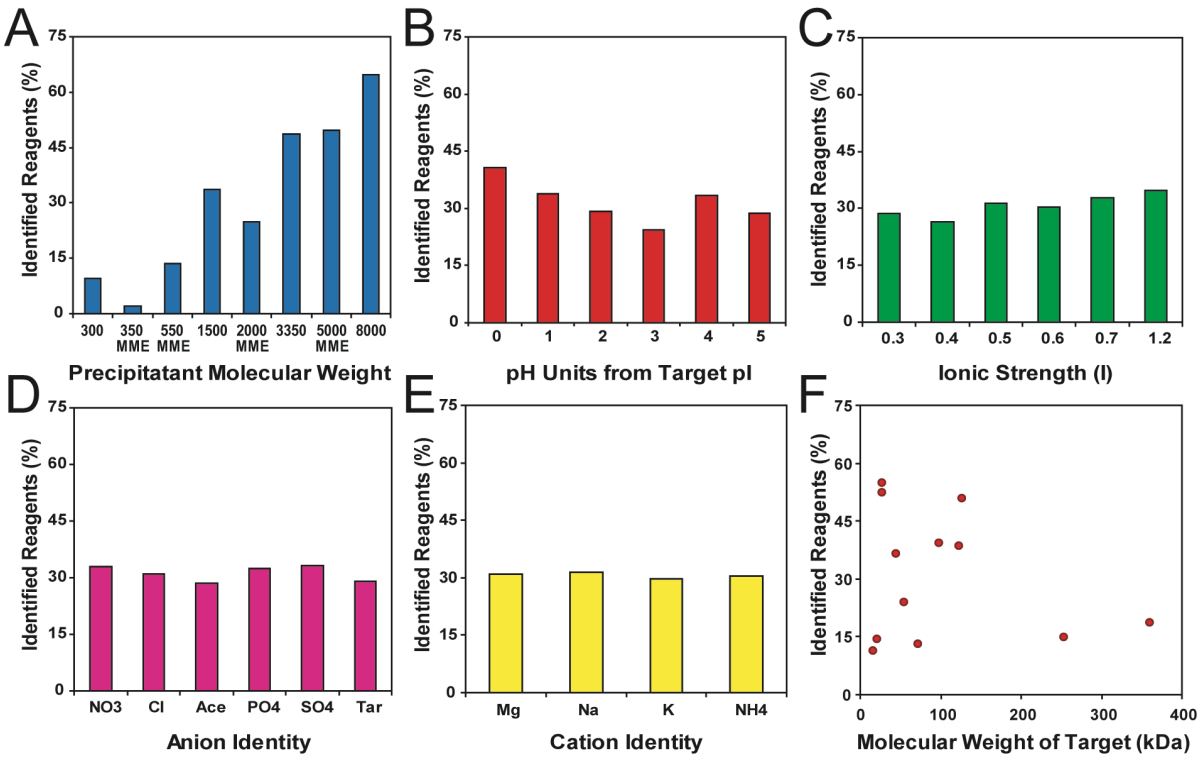

Figure 2.2: Solubility trends for crystallization targets. (A) Classification of identified reagents by the molecular weight of the precipitating agent. (B) Classification of identified reagents by the deviation from the pI of the protein targets. (C) Classification of identified reagents by the ionic strength of the solution. (D) Classification of the identified reagents by the anion component of the reagent. The anions acetate and tartrate are abbreviated as Ace and Tar, respectively. (E) Classification of the identified reagents by the cation component of the reagent. (F) Comparison of the target molecular weight and the identified reagents for each target. For (A–F), the percentage of identified reagents is normalized by the number of reagents screened in each category.

The solubility screening results also show that reagents with a pH value in the vicinity of the theoretical isoelectric point (pI) of the targets were identified as potential reagents with a

higher frequency than reagents that deviated from the target pI values (Figure 2.2B). This increased identification of reagents is consistent with the reduced intermolecular electrostatic repulsion of proteins near their pI. The variation in the identified reagents at different pH values was moderate in comparison to the variations seen for precipitant composition. The ionic strength of the salt solutions used in the solubility screening exhibited the expected trend of increased identified reagents at higher ionic strengths (Figure 2.2C). While ionic strength had a slight influence on the identified reagents, no trends were observable for the ionic composition of the reagents (Figure 2.2D–E). The ions are displayed by increasing protein aggregation strength based on the Hofmeister series, and little variation in the identified reagents is seen for the cation or anion components of the reagent (*27*). A trend is also evident between the decreasing molecular weight of the target and an increasing number of identified reagents (Figure 2.2F).

Protein phase behavior was further characterized by the generation of complete phase diagrams for a subset of the reagents identified during the solubility screening. Empirically determined solubility boundaries allow for the selection of precipitant and protein concentrations that maximize the chance of successful crystallization by excluding areas of phase space that lie far into the precipitation or soluble regions. The complete phase diagrams were produced by combining protein and reagent at 72 different protein and precipitating agent concentrations across the phase diagram and measuring protein aggregation at each position (Figure 2.3). Positions where the protein aggregated above a threshold level were classified as insoluble and positions where the protein did not aggregate above a threshold value were classified as soluble. The phase diagrams were used to design

free interface diffusion experiments that target the solubility boundary of the protein with each reagent. For example, the phase diagram shown in Figure 2.3A suggests that targeting the position corresponding to 6 mg/ml bR D85S and 20% PEG 1500 would promote crystallization. A free interface diffusion experiment targeting this position requires combining 12 mg/ml bR D85S with 40% PEG 1500 at a one-to-one protein-to-reagent ratio. As the free interface diffusion experiment proceeds, the trajectories for each solution will evolve to reach the desired position and promote protein crystallization (see Figure 3 in (*4*) for details). Customized crystallization conditions were designed using this technique for the specific reagents identified for each of the targets.

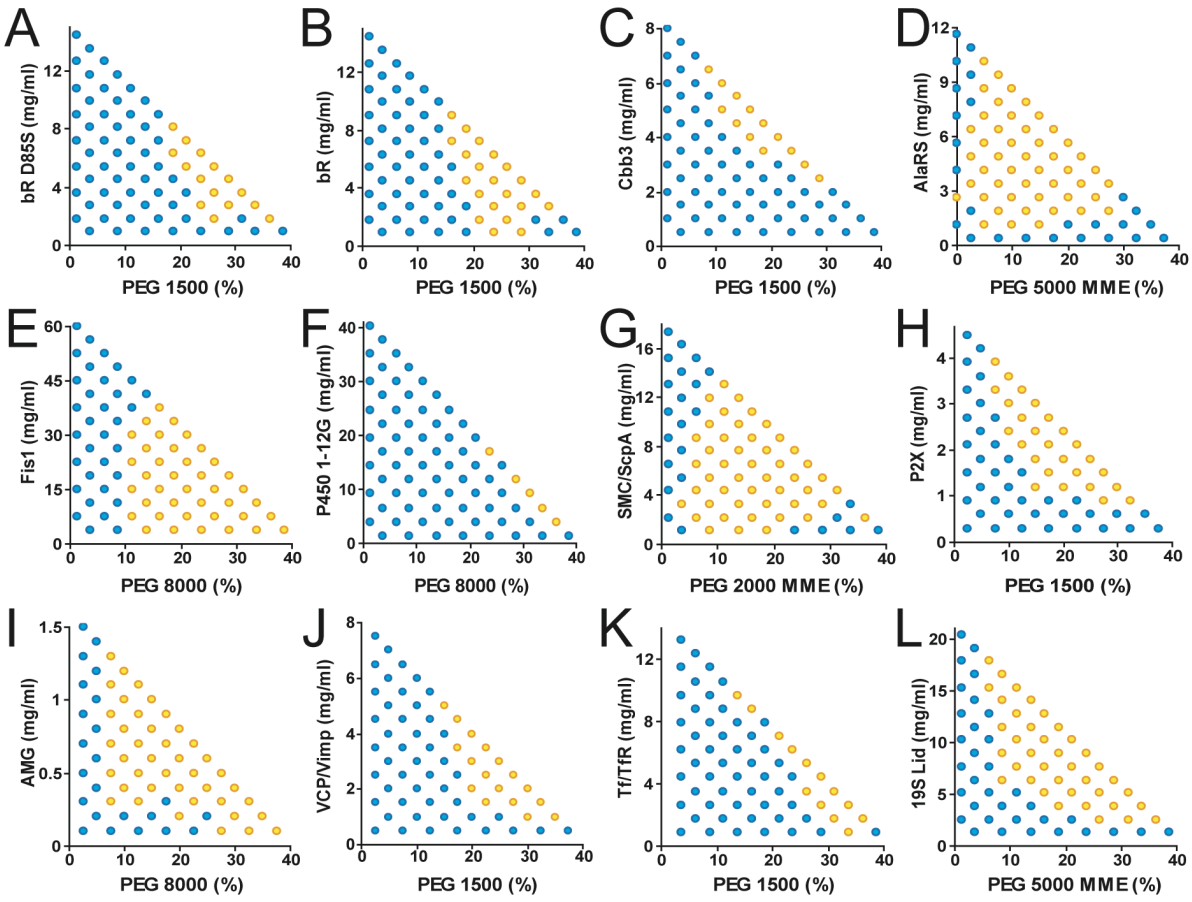

Figure 2.3: Phase behavior characterization. One complete phase diagram is shown for each target. (A) bR D85S with 0.125 M potassium acetate, 0.1 M sodium citrate (pH 6.5), and PEG 1500. (B) bR with 0.125 M ammonium chloride, 0.1 M sodium acetate (pH 4.5), and PEG 1500. (C) Cbb3 with 0.075 M sodium acetate, 0.1 M sodium citrate (pH 6.5), and PEG 1500. (D) AlaRS with 0.1 M magnesium sulfate, 0.1 M sodium citrate (pH 5.5), and PEG 5000 MME. (E) Fis1 with 0.1 M ammonium acetate, 0.1 M Tris·HCl (pH 8.5), and PEG 8000. (F) P450 1-12G with 0.2 M ammonium sulfate, 0.1 M Imidazole pH 7.5, and PEG 8000. (G) SMC/ScpA with 0.05 M magnesium sulfate, 0.1 M sodium citrate (pH 5.5), and PEG 2000 MME. (H) P2X with 0.3 M sodium acetate, 0.1 M 4-(2-hydroxyethyl)-1-piperazineethanesulfonic acid (Hepes) (pH 7.5), and PEG 1500. (I) AMG with 0.5 M sodium chloride, 0.1 M Tris·HCl (pH 8.5), and PEG 8000. (J) VCP/Vimp with 0.4 M ammonium acetate, 0.1 M sodium citrate (pH 6.5), and PEG 1500. (K) Tf/TfR with 0.2 M ammonium sulfate, 0.1 M Hepes (pH 7.5), and PEG 1500. (L) 19S Lid with 0.1 M ammonium chloride, 0.1 M sodium citrate (pH 5.5), and PEG 5000 MME. Each phase diagram screened protein solubility at 72 different precipitant and protein concentrations. The blue points represent concentrations where the protein is soluble and the yellow points represent concentrations where the protein is insoluble. Refer to Appendix C to see all of the phase diagrams generated for each target.

Crystallization Results. Crystallization experiments were carried out with the individualized rational screens using a redesigned free interface diffusion screening device (*4*). Each of the crystallization conditions was tested against the protein at five different mixing ratios to completely sample the solubility boundary of the associated phase diagram (see

Experimental Procedures for details). Free interface diffusion experiments with the rational screens resulted in a 75% crystallization success rate for the proteins, while previous crystallization attempts in the labs of collaborators failed to identify crystallization conditions for the majority of the samples (Figure 2.4). For the successfully crystallized proteins, between 12% to 79% of the reagents screened produced crystals. The targets were bimodal in their crystallization success rates; the majority of the targets crystallized for a small subset of the reagents screened while the remaining targets crystallized for the majority of the reagents.

The crystallization results show that the crystal hits fall within a well-defined region of precipitant and pH (Figure 2.5). Among the precipitants used for crystallization experiments, more crystal hits occurred with larger precipitants and no crystal hits were identified for the smallest precipitants. In contrast to the observed protein aggregation trends, more crystal hits were identified with the chemically modified MME precipitants for the larger precipitants. Although the variation in pH was larger, more crystal hits were identified from reagents near the pI value of the targets. No trend is observed in the number of crystal hits and the ionic strength of the reagent. As was observed for the protein aggregation results, the variation in crystal hits based on the ion identity of the reagent is small with no apparent trends.

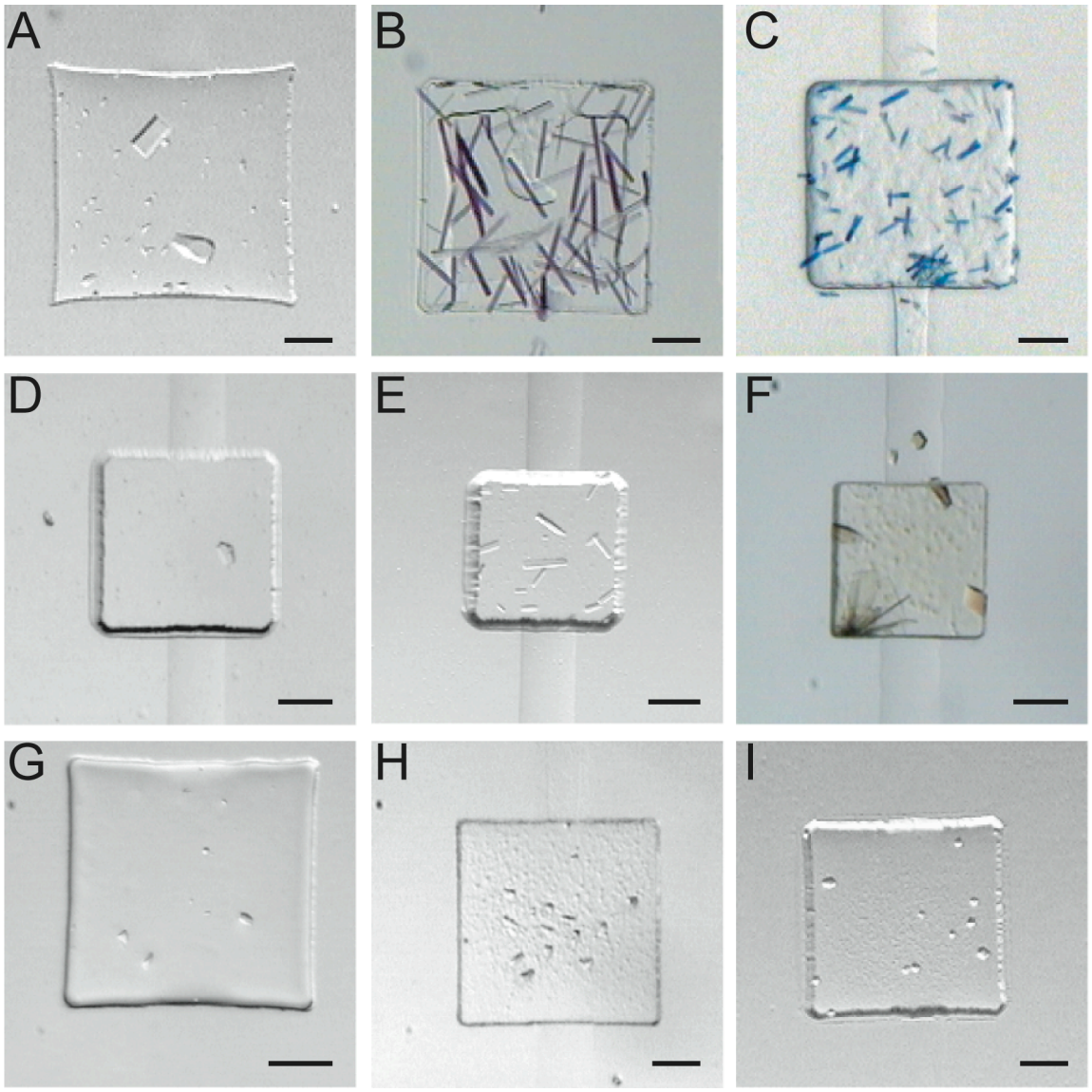

Figure 2.4: Crystallization using phase behavior information. Nine of the twelve targets were crystallized in free interface diffusion screening devices. (A) VCP/Vimp rhombohedral crystals were grown in 0.44 M sodium chloride, 0.1 M sodium citrate (pH 6.0), and 6% PEG 1500. (B) bR rod crystals were grown in 0.25 M ammonium chloride, 0.1 M sodium acetate (pH 4.5), and 35% PEG 1500. (C) bR D85S rod crystals were grown in 0.125 M potassium acetate, 0.1 M sodium citrate (pH 6.5), and 35% PEG 1500. (D) Fis1 crystals were grown in

0.1 M ammonium acetate, 0.1 M Tris·HCl (pH 8.5), and 20% PEG 8000. (E) 19S Lid rectangular prism crystals were grown in 0.15 M sodium acetate, 0.1 M sodium citrate (pH 5.5), and 15% PEG 8000. (F) P450 1-12G plate crystals were grown in 0.28 M ammonium sulfate, 15% 1,3-propanediol, 0.1 M imidazole (pH 7.5), and 30% PEG 8000. (G) AlaRS crystals were grown in 0.15 M magnesium sulfate, 0.1 M sodium citrate (pH 5.5), and 15% PEG 5000 MME. (H) SMC/ScpA crystals were grown in 0.05 M magnesium acetate, 0.1 M sodium citrate (pH 5.5), and 60% PEG 550 MME. (I) Cbb3 hexagonal crystals were grown in 0.125 M sodium chloride, 0.1 M sodium citrate (pH 6.5), and 15% PEG 1500. The scale bars represent 100 μm.

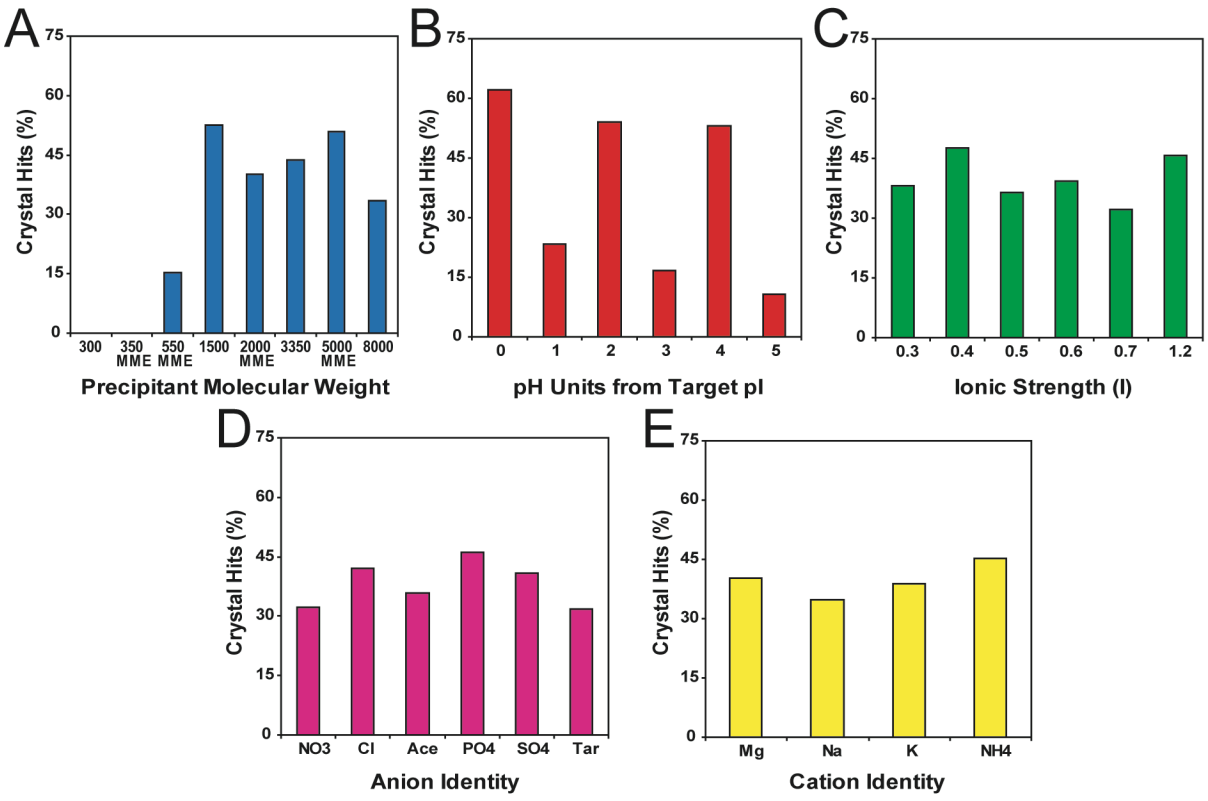

Figure 2.5: Trends in the crystal hits of targets. (A) Classification of crystal hits by the molecular weight of the precipitating agent. (B) Classification of crystal hits by the deviation from the pI of the protein targets. (C) Classification of the crystal hits by the ionic component of the reagent. (D) Classification of crystal hits by the ionic strength of the reagent. The percentage of identified reagents is normalized by the number of reagents screened in each category.

Various crystal morphologies appeared in response to different reagents, including rectangular prism crystals, rhombohedral crystals, hexagonal crystals, rod crystals, plates, needles, dendrites, and spherulites. Optimization of the initial crystallization results with additional free interface diffusion experiments improved crystal size and morphology. The

best crystallization conditions for each target were transported to larger experimental formats to generate crystals large enough for diffraction analysis (Figure 2.6). The crystallization conditions were translated to scale-up diffraction devices (*6*), vapor diffusion format, or microbatch format with a 67% success rate. Successful translation to larger formats was also clearly correlated with the crystal quality attainable in the smaller format crystallization experiments.

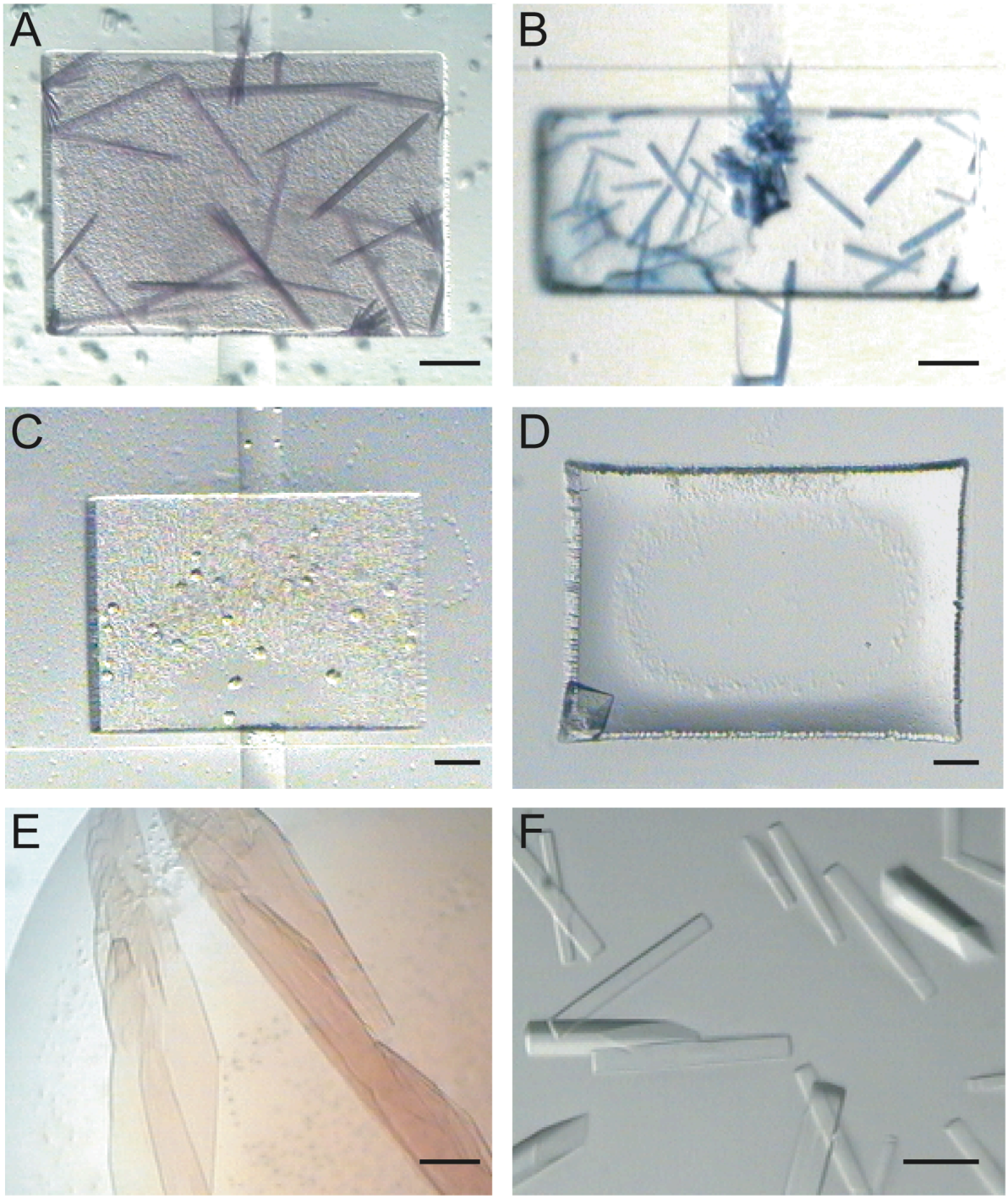
A
B
C
D
E
F

Figure 2.6: Larger format crystals for diffraction analysis. Initial hits for six of the nine targets were transported to a larger scale growth format. (A) bR rod crystals were grown in scale-up diffraction devices with 0.1 M potassium sodium tartrate, 0.1 M sodium acetate (pH 4.5), and 35% PEG 1500. (B) bR D85S rod crystals were grown in scale-up diffraction devices with 0.1 M sodium nitrate, 0.1 M sodium citrate (pH 6.5), and 25% PEG 1500. (C) Cbb3 hexagonal crystals were grown in scale-up diffraction devices with 0.15 M ammonium acetate, 0.1 M sodium citrate (pH 5.5), and 30% PEG 1500. (D) VCP/Vimp rhombohedral crystals were grown in scale-up diffraction devices with 0.4 M sodium chloride, 0.1 M sodium citrate (pH 6.5), and 10% PEG 1500. (E) P450 1-12G plate crystals were grown using vapor diffusion with 0.3 M ammonium sulfate, 0.1 M imidazole (pH 7.8), and 28% PEG 8000. (F) 19S Lid rectangular prism crystals were grown in microbatch with 0.175 M sodium acetate, 0.1 M sodium citrate (pH 5.5), and 14% PEG 8000. The scale bars represent 100 μm.

Diffraction Analysis. Diffraction experiments were performed on the crystals grown in larger formats to evaluate the quality of the crystals. Of the 6 crystals successfully transported to larger formats for diffraction studies, 67% of these crystals produced diffraction data (Figure 2.7). This corresponds to a 33% overall success rate of starting with purified protein and finishing with diffraction-quality crystals. The membrane proteins diffracted to between 6.6 Å and 16 Å, and the metabolic protein diffracted to 3.7 Å with a centered monoclinic unit cell of dimensions a = 220.0 Å, b = 62.2 Å, c = 188.7 Å, $\alpha = 90°$, $\beta = 118.91°$, and $\gamma = 90°$.

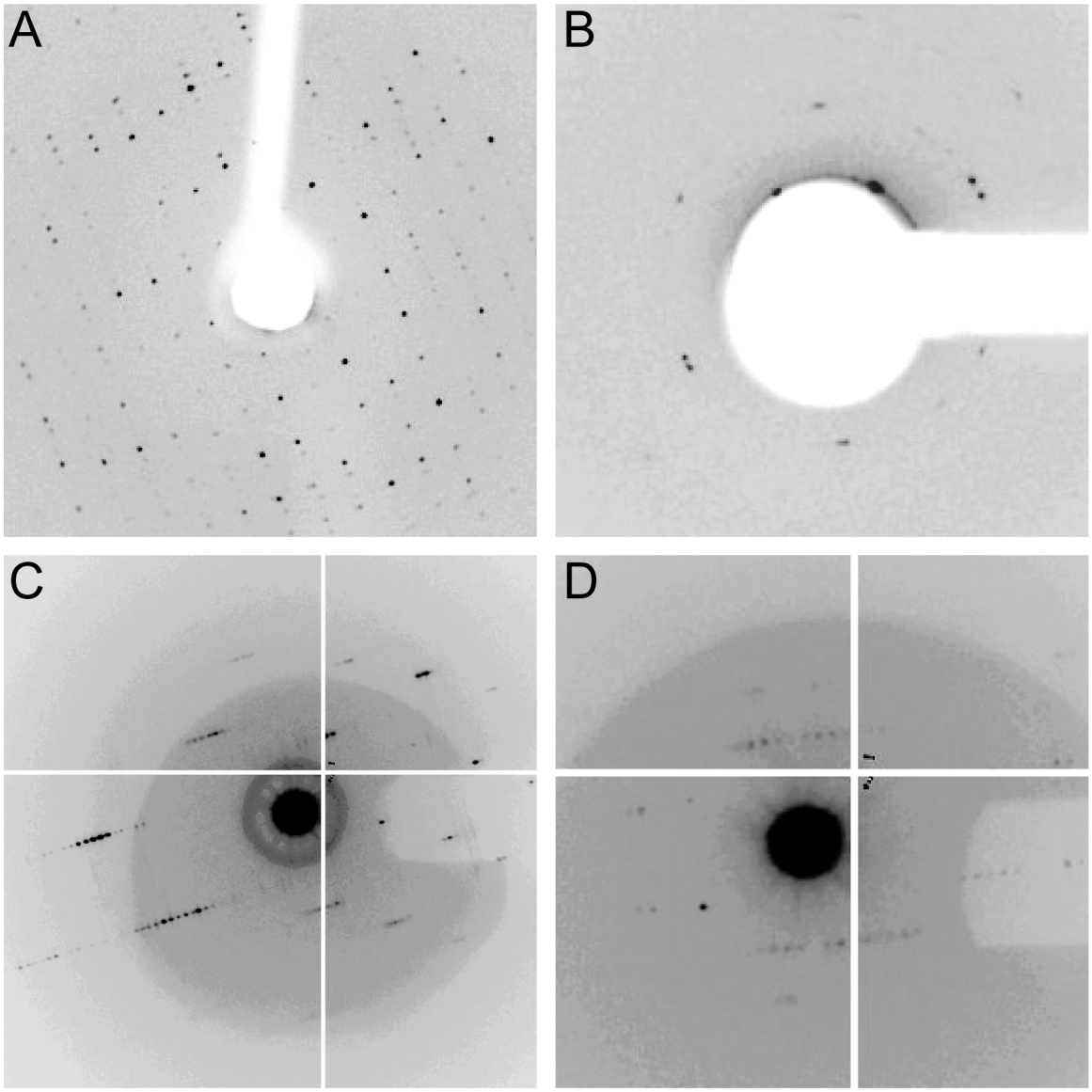

Figure 2.7: Diffraction analysis of larger format crystals. (*A*) P450 1-12G crystals were harvested using 25% ethylene glycol as a cryoprotectant and diffracted to 3.7 Å. The unit cell is centered monoclinic with dimensions a = 219.9 Å, b = 62.2 Å, c = 188.7 Å, α = 90°, β = 118.91°, and γ = 90°. (*B*) Diffraction data for Cbb3 crystals was collected at room temperature using scale-up diffraction devices and the crystals diffracted to 14.5 Å. (*C*) Diffraction data for bR D85S crystals was collected through scale-up diffraction devices

using 20% Glycerol as a cryoprotectant and diffracted to 6.7 Å. (*D*) bR crystals grown in scale-up diffraction devices were harvested using 15% PEG 1500 as a cryoprotectant and diffracted to 16 Å.

A point of concern is that although this method is highly successful at generating diffraction-quality crystals, the diffraction resolution has not been high enough to solve the structures. In contrast, the PSI has been quite successful in transitioning from diffraction-quality crystals to solved structures. Reasons for this discrepancy could include the inherent crystallization difficulty of the targets that were attempted, quality control on the protein production side, and a lack of target optimization by the systematic truncation of floppy subunits. Additionally, further optimization of the crystal growth conditions using tools such as small molecule additive screening or temperature control could improve the diffraction resolution of the crystals. The crystal optimization efforts were directly proportional to the limited amount of material provided for each of the targets.

Our success rates of 75% for crystallization and 33% overall rate of producing diffraction-quality crystals from purified protein are roughly double those of the PSI, which are 38% and 18%, respectively (http://targetdb.pdb.org/statistics/TargetStatistics.html). One must, however, also take into account the relatively small sample size in the present survey (N = 12) compared to the large number (N ~ 10,000) tested by the PSI, which leads to a lower statistical significance in our observed rates. To mitigate this effect protein targets were selected that are well above average in their crystallization difficulty; the vast majority of our targets failed conventional crystallization attempts. The size of the present data set

notwithstanding, the evidence presented is strong enough to suggest that microfluidic crystallization tools should become incorporated in large-scale structural genomics efforts.

In conclusion, the rational phase-diagram-based crystallization strategy presented in this paper was successfully used to crystallize diverse and challenging proteins. The use of solubility information to design customized crystallization screens doubled the crystallization success rate over traditional screening techniques and increased the production of diffraction-quality crystals. Microfluidic devices such as these consume small amounts of protein, are inexpensive, and are amenable to use in high throughput crystallization efforts.

Chapter 3

CRYSTAL STRUCTURE OF A HYPERACTIVE *ESCHERICHIA COLI* GLYCEROL KINASE MUTANT GLY230 → ASP OBTAINED USING MICROFLUIDIC CRYSTALLIZATION DEVICES

Introduction

In depth analysis of *Escherichia coli* metabolism over the past decades has revealed complex, tightly regulated metabolic networks that facilitate optimal growth under diverse environmental conditions. A constraints-based in silico model of *E. coli* metabolism was recently developed and used to predict the optimal growth rates of *E. coli* on various substrates (*28*). The experimental growth rate for each substrate was determined and *E. coli* grew at the predicted optimal growth rate on all of the substrates with the exception of glycerol. An adaptive evolution study of *E. coli* growth on glycerol revealed that after 700 generations *E. coli* strains evolved to reach the predicted optimal growth rate for glycerol. Sequence analysis of the evolved *E. coli* strains identified ten distinct species, eight of which contain mutations in the glycerol kinase gene (*29, 30*).

Glycerol kinase (GK) is the enzyme responsible for the transfer of the γ-phosphoryl group from ATP to glycerol to produce glycerol-3-phosphate and is the rate-limiting step in glycerol metabolism (*31, 32*). Under physiological conditions GK exists in a dimer-tetramer equilibrium where the dimer is active and the tetramer is inactive, although a series of kinetic studies suggest an active tetramer may also exist (*33–35*). GK dimers exhibit 'half-of-the-

sites binding' for glycerol and ATP substrates, in which one monomer has a high-affinity active site and the other has a low-affinity active site (*36*). GK is a member of the ATPase superfamily and shares a common βββαβαβα tertiary fold and catalytic mechanism with actin, hexokinase, and the heat shock protein 70 (*37*). GK undergoes a large conformational change from an open to a closed form during enzymatic activity similar to actin and hexokinase, although the conformational change occurs at a different stage in GK activity (*38–41*).

Allosteric regulation of GK activity is necessary to prevent the accumulation of toxic levels of glycolytic intermediates and to promote the preferential use of glucose over glycerol (Figure 3.1). GK activity is regulated by two distinct allosteric effectors; the sugar phosphotransferase system (PTS) phosphocarrier protein IIA^{Glc} (*42, 43*) and the glycolytic pathway intermediate fructose 1,6-bisphosphate (FBP) (*44*). The PTS protein IIA^{Glc} inhibits GK activity in the presence of glucose by binding to a coil and an α-helix on the surface of GK and transforming the region into a 3_{10} helix (*45, 46*). One IIA^{Glc} molecule is bound per GK monomer at a position near the dimer interface and opposite the tetramer interface.

Feedback inhibition by FBP involves the formation and stabilization of an inactive tetrameric form of GK. Two FBP molecules are bound per GK tetramer with one half of the FBP binding site contributed by an FBP binding loop in each monomer at the tetramer interface (*47*). The sequence of the FBP binding loop is similar to a Walker-type nucleotide phosphate binding loop (residues 229–236 IGGKGGTR (*48*); Walker-type motif GxxGxGKT/S). Although Walker-type loops in ATP binding proteins are traditionally involved in nucleotide

binding, the FBP binding loops bind to the 1- and 6-phosphate moieties of FBP (*47*). FBP regulation of GK is dependent on tetramer formation and disruption of the GK tetramer interface eliminates FBP inhibition (*38, 47, 49, 50*).

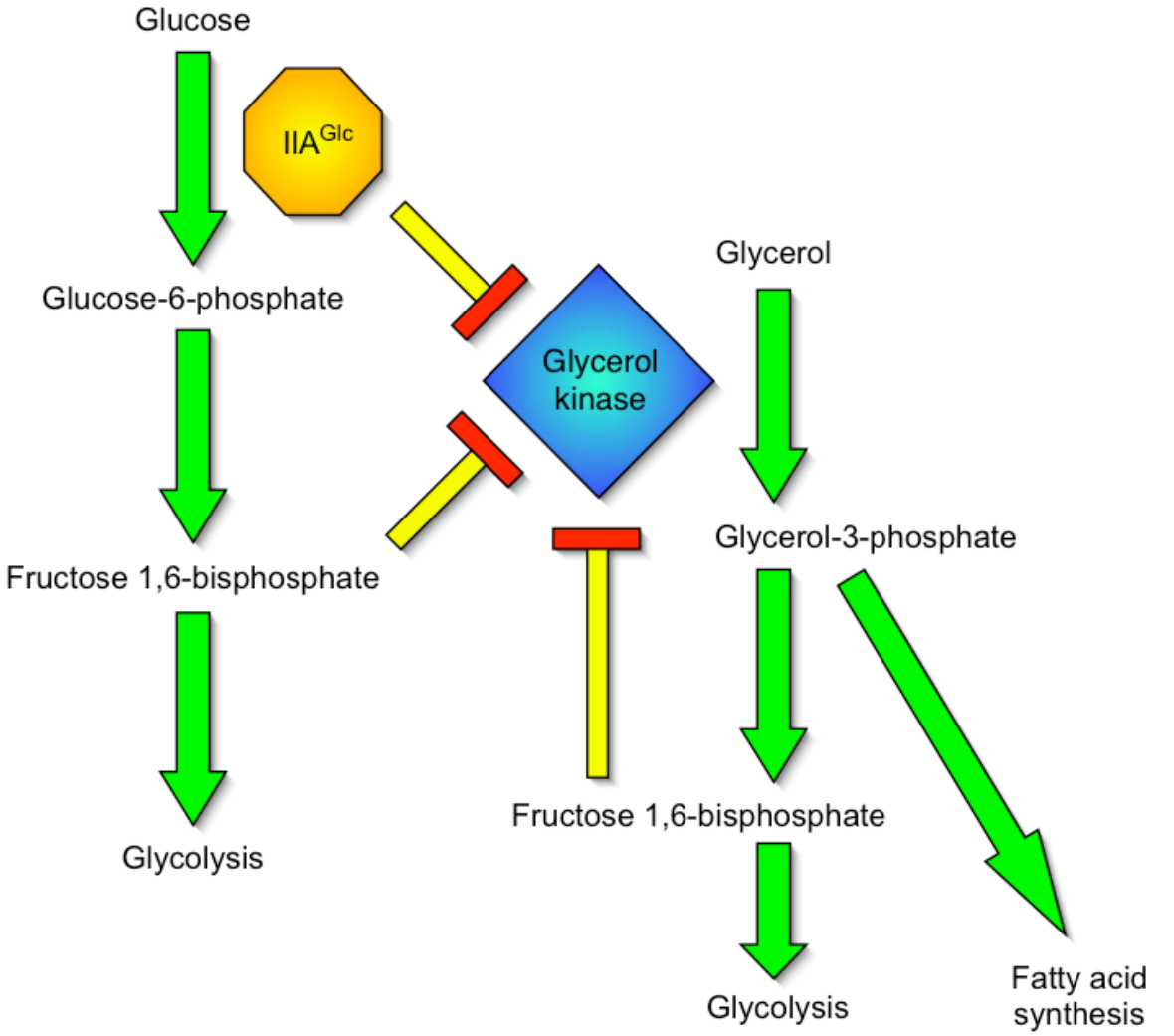

Figure 3.1: Overview of *E. coli* metabolism. GK is involved in glycolysis and fatty acid synthesis. Glucose is the preferred carbon source for the glycolytic pathway, and in the presence of glucose GK is repressed by IIA^{Glc} binding and FBP binding. In the absence of glucose, glycerol is utilized and GK is subject to feedback regulation by FBP.

Notably, six of the seven GK mutations identified during the above-mentioned adaptive evolution experiments occurred at the FBP binding site and the tetramer interface in regions associated with FBP regulation. The mutation that appeared with the greatest frequency was located in the FBP binding loop at Gly230→Asp (GK^{G230D}). Kinetic investigation of GK^{G230D} revealed a 12-fold increase in enzyme activity and a 33% decrease in FBP inhibition compared to wild-type GK (GK^{WT}) (*29*). The crystal structure of GK^{G230D} is presented to investigate the increased activity and altered allosteric regulation of this hyperactive glycerol kinase mutant. The crystal structure of GK^{G230D} was obtained using a microfluidic crystallization platform and is the first demonstration of in situ structure determination for a novel crystallization target.

Experimental Procedures

Protein Preparation. The *Escherichia coli* GK^{G230D} protein expression and purification were performed as previously described with minor modifications (*51, 52*) and the protocols are outlined in Appendix D. The purified protein was stored in standard buffer at -80 °C (20 mM Tris·HCl (pH 7.5), 10 mM glycerol, 1 mM β-mercaptoethanol (βME)). The activity of GK^{G230D} was measured using an ADP-coupled assay (*36*) and compared to the activity of GK^{WT} using commercially available lyophilized *E. coli* GK^{WT} (Fluka). GK^{G230D} and GK^{WT} activity was on the order of the previously published values (*36, 53*). All enzyme standards and chemicals for the assay were purchased from Sigma-Aldrich.

Size Exclusion Chromatography—Multi-Angle Laser Light Scattering (SEC-MALLS) Studies. A DAWN EOS (Wyatt Technology) equipped with a K5 flow cell and a 30 mW linearly

polarized GaAs laser of wavelength 690 nm was used in all experiments. The construction, principles and operation of this apparatus were previously described (*54, 55*). All measurements were made in the in-line flow mode. Elution buffer (standard buffer ± 1 mM FBP) was pumped at 0.5 ml/min through a Shimadzu DGU-14A degasser (Shimadzu Corp.) onto a Shodex KW-804 gel filtration column (Shoko America) and 100 ml of 2 mg/ml protein was injected into the system for each analysis. GK^{G230D} was purified as described above and GK^{WT} was purchased from Fluka. Protein concentration was determined with an Optilab Rex refractive index detector, using a value of 0.185 ml/g for the dn/dc. Light scattering data was measured by 12 detectors ranging from 34.8° to 142.5°. The detector responses were normalized by measuring the signal from monomeric bovine serum albumin. The temperature of the light scattering unit and the refractometer were maintained at 25 °C and the column and all external connections were at ambient temperature.

Solubility Characterization and Crystallization. A microfluidic formulator device was used to characterize the solubility of GK^{G230D} and to generate phase diagrams for crystallization experiments. The solubility screening was performed as previously described with minor modifications in the experimental setup (*4, 12*). GK^{G230D} was screened with 680 unique reagents produced using 17 salt solutions, 5 buffering agents, and 8 precipitating agents (see Appendix B for a complete list of the reagents). GK^{G230D} was used at a stock concentration of 30 mg/ml for all solubility and crystallization experiments. Each reagent was screened at six different protein and precipitant concentrations while holding the salt solution and buffering agent at a fixed level. Protein aggregation was quantified as previously described and reagents that caused protein aggregation above 2 pixel intensity standard deviation units

were classified as crystallization reagents. Phase diagrams were generated for a subset of the identified crystallization reagents as previously described (*4, 12*). Each phase diagram screened GK^{G230D} solubility at 64 different protein and precipitating agent combinations (between 5–75% of the stock concentrations) while the salt solution and buffering agent were held at a constant concentration. Positions with protein aggregation above 2 pixel intensity standard deviation units were categorized as insoluble and positions with protein aggregation below 2 were categorized as soluble.

Initial crystallization experiments were performed using a modified microfluidic free interface diffusion screening device as described in Anderson et al. (*12*). Crystals formed after one week at ambient temperature and the best crystallization condition (0.3 M magnesium chloride, 0.1 M Tris·HCl (pH 8.5), and 20% PEG 1500) was transported to microfluidic scale-up diffraction devices. Device fabrication and experimental setup for the scale-up diffraction devices were previously described (*6*). Crystals appeared in the scale-up diffraction devices after one week at ambient temperature. Sections of the scale-up diffraction device surrounding the crystals were removed from the rest of the device and flash-frozen for in situ diffraction analysis. Cryoprotectant (30% ethylene glycol) was introduced into the diffraction devices by diffusion one hour before flash-freezing the crystals within the diffraction devices. Vapor diffusion crystallization experiments were performed in parallel and crystals appeared after one week at ambient temperature using the crystallization condition 0.1 M magnesium chloride, 0.1 M Tris·HCl (pH 8.5), and 10% PEG 1500. The crystals were flash-frozen using 30% ethylene glycol as a cryoprotectant.

Data Collection and Processing. Data sets for GK^{G230D} crystals were collected at station 11.3 of the Stanford Linear Accelerator Center (Stanford University) at an incident wavelength of 1.0 Å with a 1° oscillation. Data sets were collected to 2.0 Å from a crystal grown in a scale-up diffraction device and to 3.0 Å from a vapor diffusion crystal for comparison. The data sets were indexed and scaled using DENZO and SCALEPACK and the data set from the scale-up diffraction device was used for structure determination (*56*).

Structural Determination and Refinement. The phases for the diffraction data were determined by molecular replacement using a monomer from the PDB structure 1GLF as a search model. The 'fastdirect' method as implemented in CNS (*57*) was used to search with one monomer at a time until eight monomers were placed within the asymmetric unit (asu). The asu contained two complete tetrameric species. Non-crystallographic symmetry (NCS) restraints were applied such that corresponding protomers between the two tetramers were restrained. The initial round of minimization and group B factor refinement resulted in a starting R/R_{free} value of 38.7/42.3. Simulated annealing did not improve the structure, so iterative rounds of manual rebuilding with O (*58*) and minimization/B factor refinement in CNS were used to further the structure refinement. Rebuilding was focused on addressing the hinge motion that created a variety of positions for the second lobe (~ residues 250–500) of the different protomers. Eight glycerol molecules were placed into well-defined electron density in each of the active sites. NCS restraints were removed completely at this point. The combined effect of these changes enabled a reduction in the R/R_{free} to 26.6/30.5 through alternating minimization and grouped B factor refinement. The addition of 638 water molecules further reduced the R/R_{free} values to 23.5/27.3. Several regions of the protein did

not have clear electron density and were set to 0 occupancy at this point. These regions are: segment X_I, residues 229–234 and 501–509; segment O_I residues 229–235; segment Z_I residues 498–511; segment X_{II} residues 229–235 and 324–327; segment Y_{II} residues 229–235 and 324–327; segment O_{II} residues 229–234 and residue 463; segment Z_{II} residues 229–235. The correct orientation of several side chains were established by analyzing likely hydrogen bonding patterns (*59*). TLS refinement, as implemented in REFMAC (*60*), was used in the final stages. B factors were reset to 20 before attempting TLS and refined immediately following TLS as restrained individual B factors. The X-ray/geometry weight was optimized to 1.0 to yield the final R/R_{free} values of 21.0/25.9. The data collection and refinement statistics are presented in Table 3.1.

Domain Motion Analysis. The analysis was performed with the Hingefind algorithm, as implemented in VMD (*61*). A partition value of 1.8 Å was used for all measurements. The rotation axis defining the two domains in the GK^{G230D} monomers was essentially identical to that found by Bystrom et al. (*38*). Root-mean-square deviation (rmsd) values were calculated by superpositioning the C_α atoms of residues 2–499 from one monomer onto the second monomer.

Results

Microfluidic Crystallization Strategy for GK^{G230D}. The microfluidics-based crystallization platform for GK^{G230D} involved a suite of microfluidic devices that characterized the solubility trends of GK^{G230D} to create a rational crystallization screen, performed hundreds of parallel free interface diffusion crystallization experiments, transported initial crystal hits into larger

scale free interface diffusion experiments, and allowed for in situ data collection from diffraction-quality crystals. The microfluidic crystallization platform enabled nanoliter volume solubility characterization and crystallization experiments and eliminated the necessity of crystal harvesting before data collection.

The crystallization scheme began with a comprehensive characterization of GK^{G230D} solubility using a microfluidic formulator device (*10*). GK^{G230D} was systematically screened against 680 reagents with distinct salt, buffer, and precipitant components and reagents that caused protein aggregation were classified as potential crystallization reagents (Figure 3.2). Protein phase behavior was broadly screened in response to each reagent by measuring GK^{G230D} solubility at six positions on the phase diagrams. The solubility characterization of GK^{G230D} included a total of 4080 solubility experiments and 28% of the reagents were identified as potential crystallization reagents. GK^{G230D} aggregation occurred with the highest frequency for reagents that contained one of the following components: magnesium sulfate salt, sodium phosphate salt, citric acid (pH 3.5) buffer, and PEG 20000 precipitant. Following the broad solubility characterization, complete phase diagrams were generated for GK^{G230D} with a subset of the identified crystallization reagents (Figure 3.3). Phase diagrams outline the solubility regimes of a protein in combination with a reagent and are used to design crystallization conditions that target the solubility boundary of a protein. Each complete phase diagram measured GK^{G230D} solubility at 64 different positions and protein aggregation was used to map the insoluble region of the phase diagram. The identified crystallization reagents and the phase behavior information were incorporated into a customized crystallization screen for GK^{G230D}.

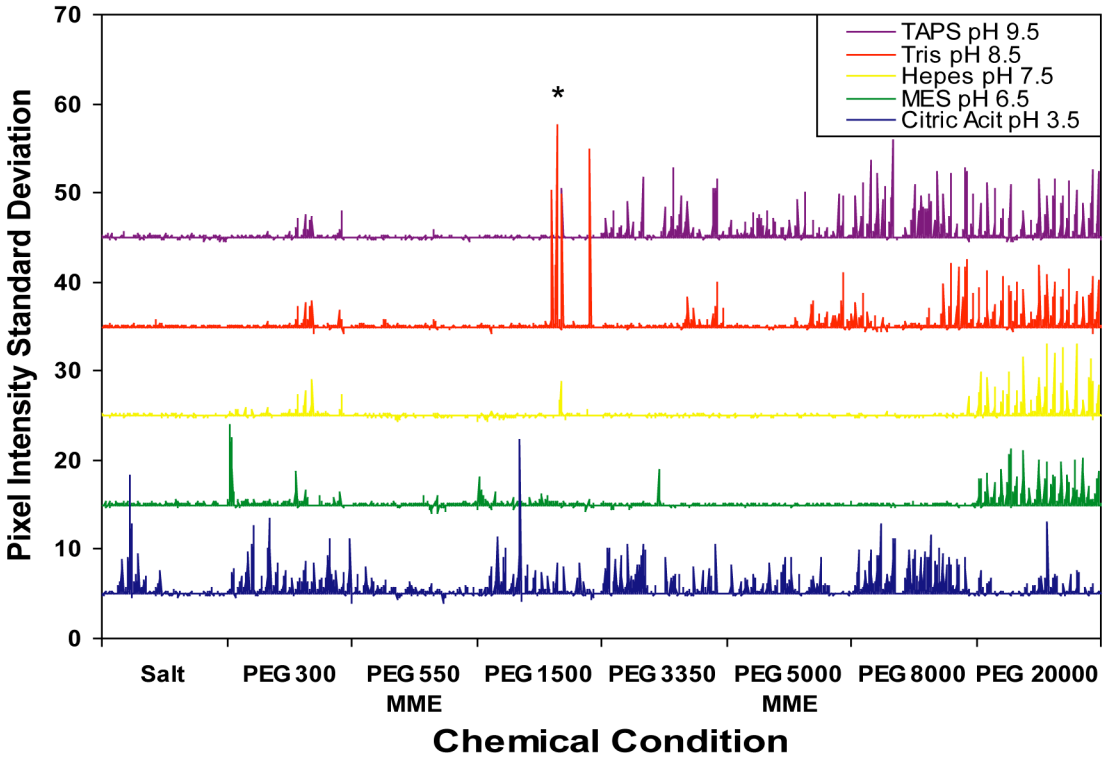

Figure 3.2: Solubility screening results for GK^{G230D}. The reagents are displayed on separate lines according to buffer composition, and each line is divided by precipitant composition and subdivided by salt composition. The crystallization reagent used for structure determination is highlighted with an asterisk.

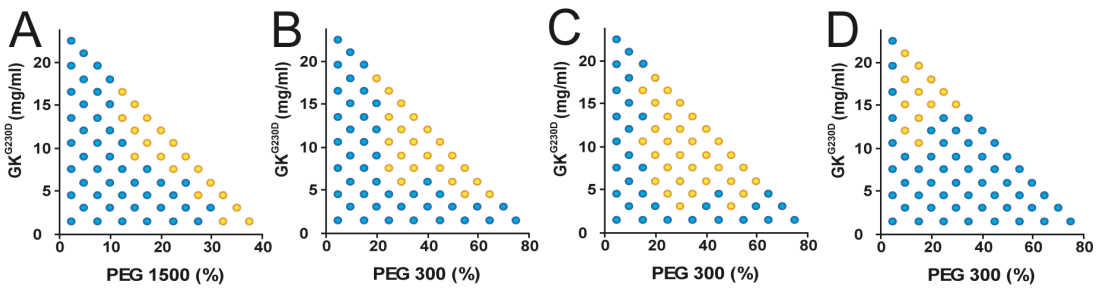

Figure 3.3: Complete phase diagrams for GK^{G230D}. (A) Reagent 0.2 M magnesium chloride, 0.1 M Tris·HCl (pH 8.5), and PEG 1500. (B) Reagent 0.2 M magnesium sulfate, 0.1 M Hepes pH 7.5. (C) Reagent 0.2 M magnesium acetate, 0.1 M Tris·HCl (pH 8.5), and PEG 300. (D) Reagent 0.2 M magnesium acetate, 0.1 M citric acid (pH 4.5), and PEG 300. Blue circles represent soluble positions and yellow circles represent insoluble positions.

The crystallization screen for GK^{G230D} was implemented using microfluidic free interface diffusion screening devices and 16% of the reagents produced crystals (*4, 12*). Crystal hits were observed most frequently for crystallization conditions with one of the following components: potassium acetate salt, N-Tris(hydroxymethyl)methyl-3-aminopropanesulfonic acid (TAPS) (pH 9.5) buffer, and PEG 1500 precipitant. Optimization of the best initial crystallization condition improved crystal size and morphology and produced rhombohedral crystals of dimensions 200 x 150 x 50 μm (Figure 3.4A). The crystallization condition was transported to a microfluidic scale-up diffraction device (*6*) to produce rhombohedral crystals of dimensions 500 x 200 x 100 μm (Figure 3.4B). The scale-up diffraction device was designed to produce large crystals encapsulated within a thin layer of elastomeric material to allow for diffraction analysis of the crystals directly through the device. Once crystals appeared in the scale-up diffraction device, a small section of the device surrounding the

crystal was cut out and extracted from the rest of the device. The extracted section of the device formed a thin disk that was mounted onto a customized crystal cap, placed directly onto the goniometer head, and data was collected from the crystal through the device. The crystal in Figure 3.4B was used for in situ data collection through the scale-up diffraction device and diffracted to 2.0 Å (Figure 3.5). The structure of GK^{G230D} was solved using molecular replacement and the statistics for the refined model are reported in Table 3.1. The entire process from the solubility characterization to the production of diffraction-quality crystals required only 31 μl of sample, corresponding to less than 1 mg of GK^{G230D}.

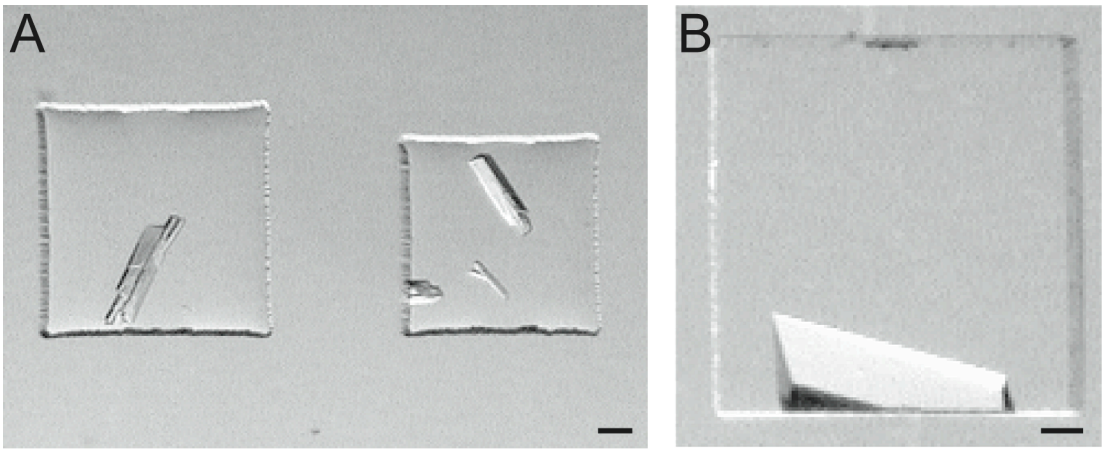

Figure 3.4: Crystallization results for GK^{G230D}. (A) Crystal plates in a free interface diffusion device. (B) Rhombohedral crystal in a scale-up diffraction device. The crystal was grown with the reagent 0.3 M magnesium chloride, 0.1 M Tris·HCl (pH 8.5), and 20% PEG 1500. The scale bars represent 100 μm.

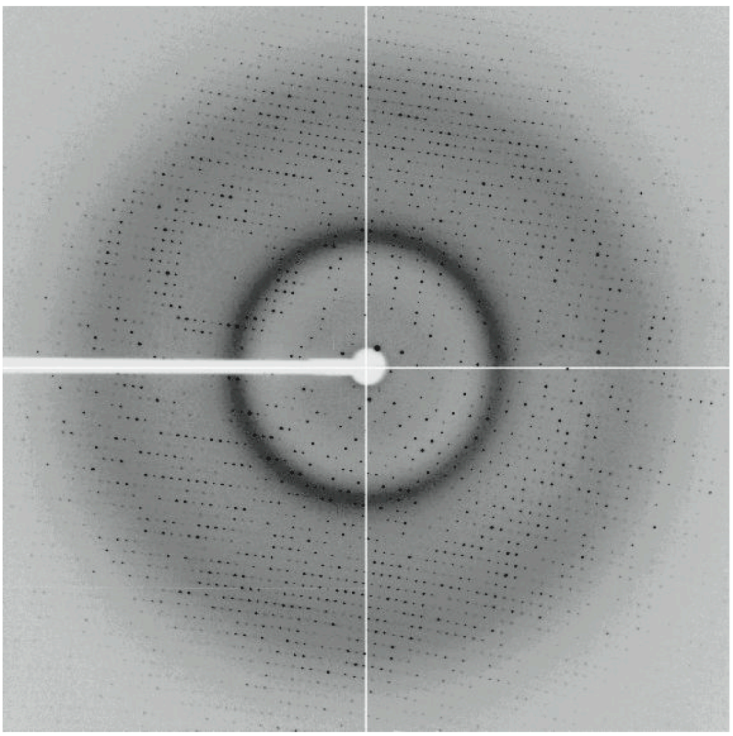

Figure 3.5: In situ diffraction analysis of crystals. GK^{G230D} crystallized in space group $P2_1$ with a unit cell of a = 91.1 Å, b = 114.3 Å, c = 212.6 Å, and β = 91.1º, and a mosaicity of 0.265. The faint powder ring around 7 Å is due to X-ray scattering off of the elastomeric material of the scale-up diffraction device.

Table 3.1: Data collection and refinement statistics for GK^{G230D}

Data collection	
Wavelength (Å)	1.0
Space group	$P2_1$
Cell dimensions	
a (Å)	91.1
b (Å)	114.3
c (Å)	212.6
β (°)	91.1
Resolution[a] (Å)	50-2.0 (2.1-2.0)
Unique observations[a]	250186 (21731)
Redundancy[a]	5.9 (3.4)
Completeness[a]	84.0 (73.2)
Mosiacity	0.265
$I/\sigma(I)$ [a]	36.8 (6.6)
R_{sym} [b]	5.9 (22.5)
Refinement	
Resolution (Å)	20-2.0
No. of reflections	221751
No. of refined protein atoms	31752
No. of refined solvent atoms	638
No. of glycerol molecules	8
R_{cryst} [c]	21.0
R_{free} [d]	25.9
Average B-factor ($Å^2$)	21.2
Bond length rmsd (Å)	0.018
Angle rmsd (°)	1.74
Ramachandran plot (% in most favored/ allowed/generous/disallowed regions[e])	90.7/8.8/0.3/0.2

[a] Numbers in parenthesis refer to the highest resolution shell. [b] $R_{sym} = \Sigma_{ijj}|I_i(j) - \langle I(j)\rangle| / \Sigma_{ij}I_i(j)$, where $I_i(j)$ is the intensity of the i-th observation of reflection j, I(j) is the weighted mean of all measurements of j. [c] $R_{cryst} = \Sigma_j|F_o(j) - F_c(j)|/\Sigma_j|F_o(j)|$, where F_o and F_c are the observed and calculated structure factors. [d] $R_{free} = R_{cryst}$ calculated by using 10% of the reflection data chosen randomly and omitted from the start of refinement (*62*). [e] The residues in the disallowed regions were found in the active site interacting with glycerol.

Structural Overview. GK^{G230D} crystallized in space group $P2_1$ with two tetramers of 222 point symmetry in the asu. The monomers of tetramers I and II are designated O_I, X_I, Y_I, Z_I, and O_{II}, X_{II}, Y_{II}, Z_{II}, respectively, following the previously established GK notation (Figure

3.6). The tertiary structure of tetramers I and II mimics the tetramer geometry seen in an earlier structure of GK that is postulated to be the physiologically relevant tetrameric form of the protein (*46*). The O-Y and X-Z monomer interfaces are identical to the functional dimer interface seen in GK^{WT} and indicate the O-Y and X-Z monomers also form the functional dimer in GK^{G230D}. Each dimer has one monomer in the closed conformation and one monomer in the open conformation, similar to the putative active conformation of GK seen in the presence of glycerol and ATP analogs (*38*). The FBP binding loops, located at the O-X and Y-Z tetramer interfaces, are ordered at the Y_I-Z_I tetramer interface in GK^{G230D} and differ significantly from the GK^{WT} FBP binding loops. Monomer domain organization is identical to GK^{WT} and has previously been described (*45*). All monomers in the asu have a glycerol molecule bound at the cleft of the active site.

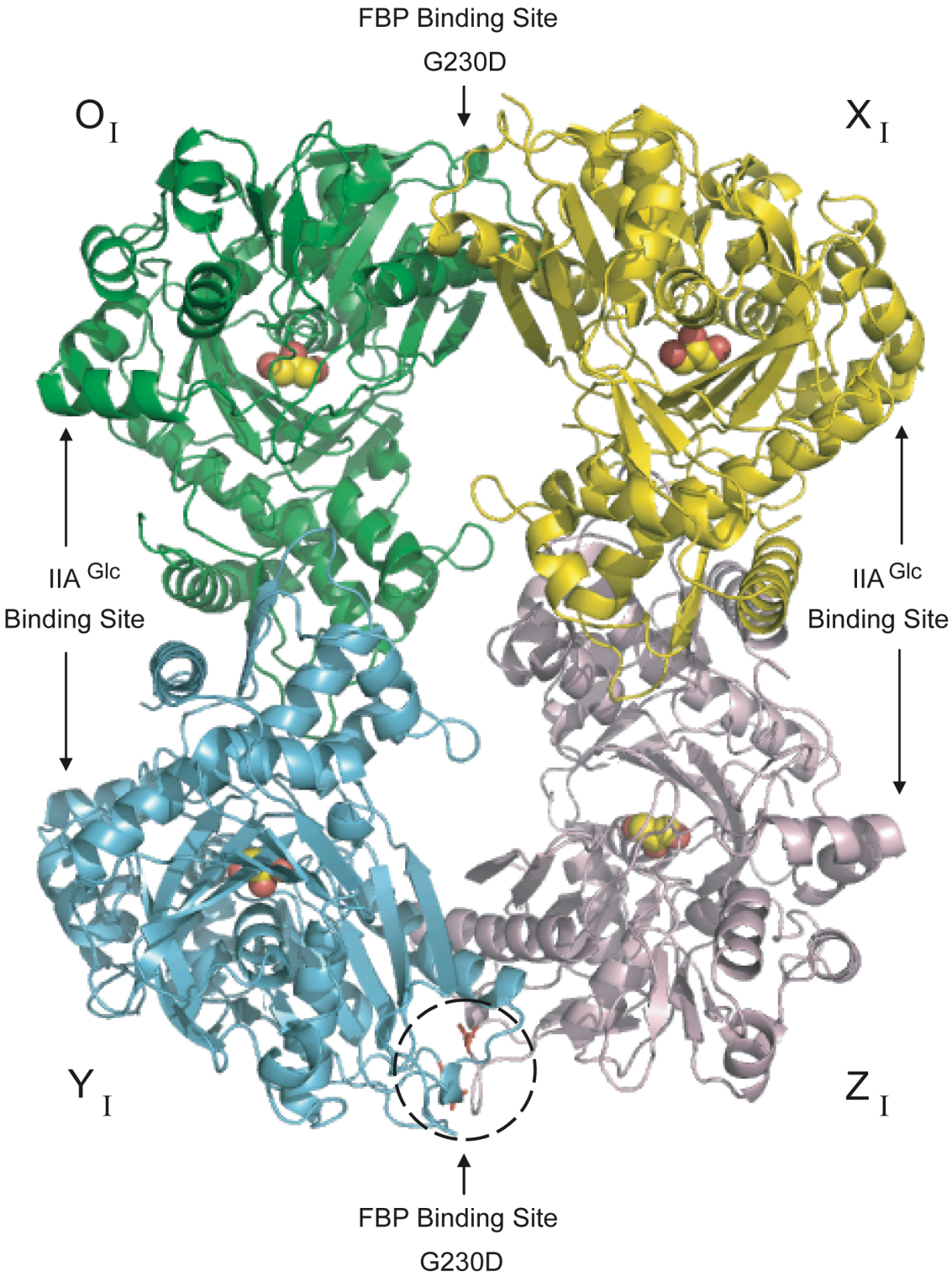
FBP Binding Site
G230D
O I
X I
IIA Glc
Binding Site
IIA Glc
Binding Site
Y I
Z I
FBP Binding Site
G230D

Figure 3.6: Tetramer structure of GK^{G230D}. GK^{G230D} tetramer I is shown with the O_I, X_I, Y_I, and Z_I monomers colored green, yellow, blue, and pink, respectively. The X_I and Y_I monomers are in the closed conformation, the O_I monomer is in the open conformation, and the Z_I monomer is in the 'very open' conformation. The FBP binding sites are located at the top and the bottom of the tetramer in the O_I-X_I and Y_I-Z_I interface loops. The mutation GK^{G230D} is circled and shown in orange using stick representation at the Y_I-Z_I tetramer interface. The IIA^{Glc} binding sites are located at a 3_{10} helix on each monomer near the dimer interface. Glycerol is shown in a space-filling representation and indicates the location of the active site and the base of the hinge region in each monomer. All structural images were prepared with PyMOL (*63*).

The FBP Binding Loops. The G230D mutation in the FBP binding loops (residues 229–236) is ordered at the Y_I-Z_I tetramer interface in the GK^{G230D} structure. The average B factor for the Y_I-Z_I FBP binding loops is 21.1 $Å^2$, comparable to the average B factor of 21.2 $Å^2$ for the overall structure. Large conformational changes are evident between the GK^{G230D} and GK^{WT} FBP binding loops; the Y-Z loops of GK^{WT} superposition onto the Y_I-Z_I loops of GK^{G230D} (residues 225–240) with a C_α rmsd of 2.6 Å (Figure 3.7). In GK^{WT}, the main chain loop conformations and the side chain positions are identical in monomers Y and Z, creating a symmetrical FBP binding site at the tetramer interface. In GK^{G230D}, the Y_I and Z_I FBP binding loops have unique main chain conformations in each monomer and disrupt FBP binding by eliminating the symmetrical binding pocket for FBP at the tetramer interface.

The wild-type FBP binding loop conformation in GK^{WT} is stabilized through intramolecular and intermolecular loop interactions. The intramolecular loop interactions include hydrogen bond interactions between $O_{\delta 1}$ of Asn228 and the backbone amide of Gly230, and between the backbone oxygen of Thr235 and N_{ε} of Arg236 (*46*). Intermolecular loop hydrogen bond interactions also occur across the tetramer interface between $N_{\delta 2}$ of Asn228 and the backbone oxygen of Gly231, and between the backbone oxygen of Asn228 and the backbone amide of Gly231 in both monomers (*46*).

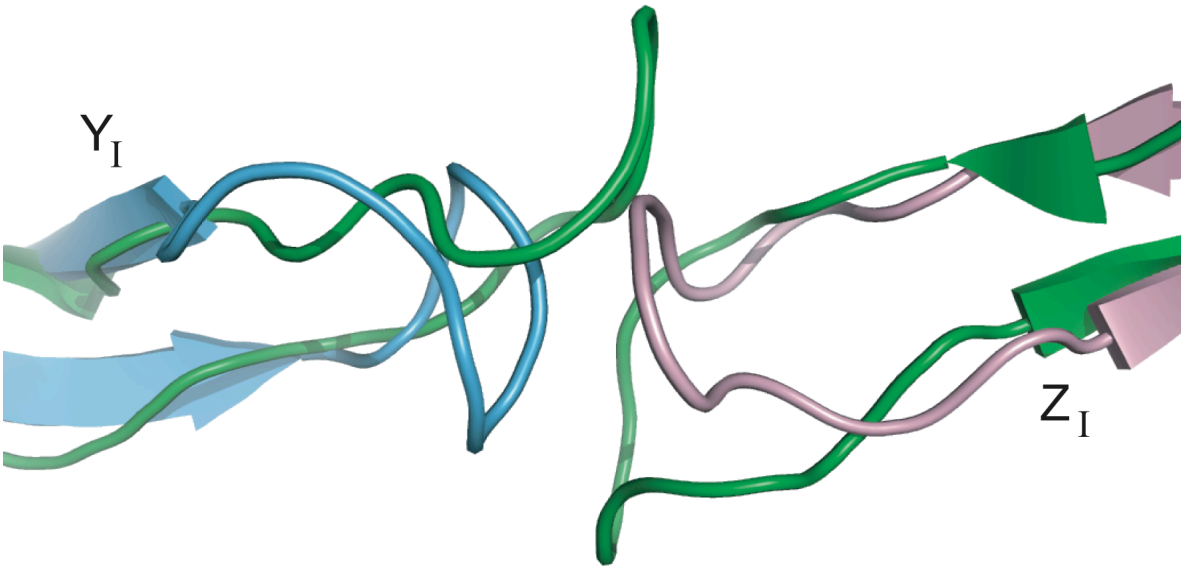

Figure 3.7: Comparison of the FBP binding loop conformations in GK^{G230D} and GK^{WT}. Residues 225 to 240 of the Y-Z FBP binding site in GK^{WT} (PDB entry 1GLF) are superpositioned onto the Y_I-Z_I FBP binding site in GK^{G230D}.

Intramolecular hydrogen bonding networks in the GK^{G230D} FBP binding loops replace the wild-type loop interactions and hold the Y_I and Z_I loops in two main chain conformations that are significantly different than in GK^{WT} (Figure 3.8A). In the Y_I monomer there are two hydrogen bond interactions between $O_{\delta 2}$ of Asp230 and the backbone amide of Thr235, and between the backbone oxygen of Gly231 and the backbone amide of Gly234. In the Z_I monomer there are two hydrogen bond interactions between $O_{\delta 1}$ of Asn228 and the backbone amide of Asp230, and between the backbone oxygen of Gly231 and the backbone amide of Gly234. A simplified view of the GK^{WT} FBP binding loops is presented for comparison with the GK^{G230D} intramolecular loop interactions (Figure 3.8B). Notably, the backbone oxygen atoms of Gly231 in GK^{WT} are involved in intermolecular loop interactions, whereas the backbone oxygen atoms of Gly231 in GK^{G230D} are utilized in intramolecular loop interactions.

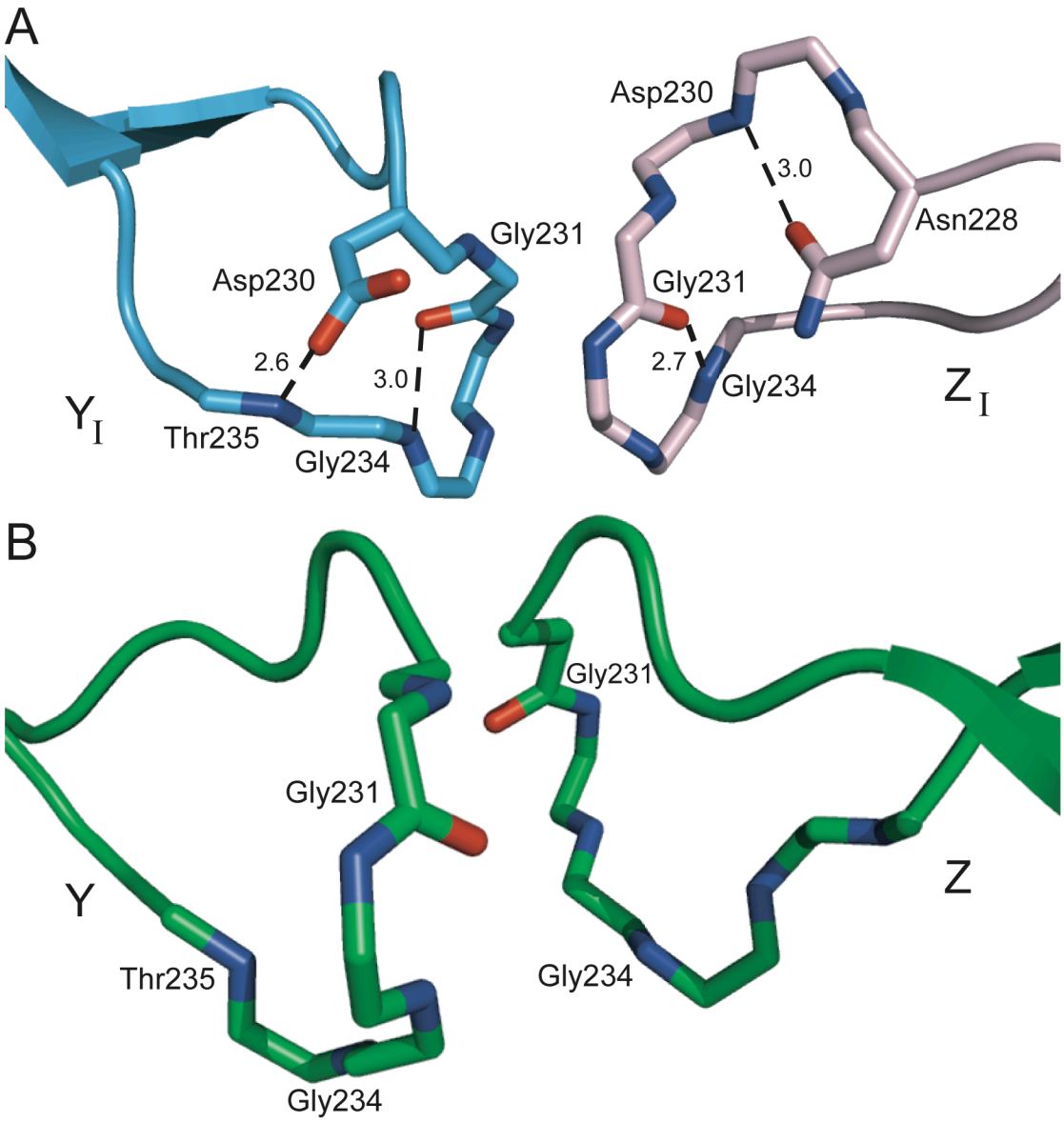

Figure 3.8: Altered FBP binding loop conformations in GK^{G230D}. (A) Intramolecular hydrogen bonding networks in the GK^{G230D} FBP binding loops. The Y_I monomer has two hydrogen bond interactions between Asp230 and Thr235, and between Gly231 and Gly234. The Z_I monomer has two hydrogen bond interactions between Asn228 and Asp230, and between Gly231 and Gly234. The Y_I and Z_I monomers of GK^{G230D} are blue and pink, respectively. (B) FBP binding loop conformation in GK^{WT} at the Y-Z tetramer interface.

Note that GK^{WT} is shown as it appears when aligned to the GK^{G230D} FBP binding loops as displayed in (A).

The FBP Binding Site. In GK^{WT}, residues Gly234 and Arg236 from each monomer are located at the tetramer interface and are required for FBP binding. Five interactions between GK^{WT} residues Gly234 and Arg236 and the phosphate moieties of FBP occur in the wild-type regulatory binding site (*47*). The majority of the interactions position the 6-phosphate of FBP at a central location between the two FBP binding loops (Figure 3.9A). Specifically, $N_{\eta 1}$ of Arg236 in monomer Y interacts with the 6-phosphate of FBP in monomer Y, and $N_{\eta 2}$ of Arg236 in monomer Z interacts with the 6-phosphate of FBP. The 6-phosphate of FBP is also bound by interactions with the backbone amide of Gly234 in monomers Y and Z. Furthermore, $N_{\eta 2}$ of Arg236 in monomer Y interacts with the 1-phosphate of FBP and serves to bridge both phosphate groups of FBP.

The appearance of Asp230 in the FBP binding site of GK^{G230D} repositions the surrounding residues and eliminates the wild-type FBP binding site (Figure 3.9B). The C_α of Asp230 is shifted from the wild-type C_α of Gly230 by 4.3 Å in the Y_I monomer of GK^{G230D}. In addition, the C_α of Lys232 in the Z_I monomer is shifted by 10.3 Å from the wild-type position and appears at the tetramer interface in GK^{G230D}. To accommodate Asp230 and Lys232 in the FBP binding site, the FBP binding residues Gly234 and Arg236 are shifted away from their wild-type FBP binding positions in each of the monomers. The C_α of Gly234 is shifted by 3.3 Å in the Z_I monomer and the N_ε of Arg236 is shifted by 9.7 Å in the Y_I monomer of GK^{G230D}. The repositioning of the FBP binding residues Gly234 and Arg236

to the outside of the FBP binding site could explain why a decrease in FBP inhibition is observed for GK^{G230D}.

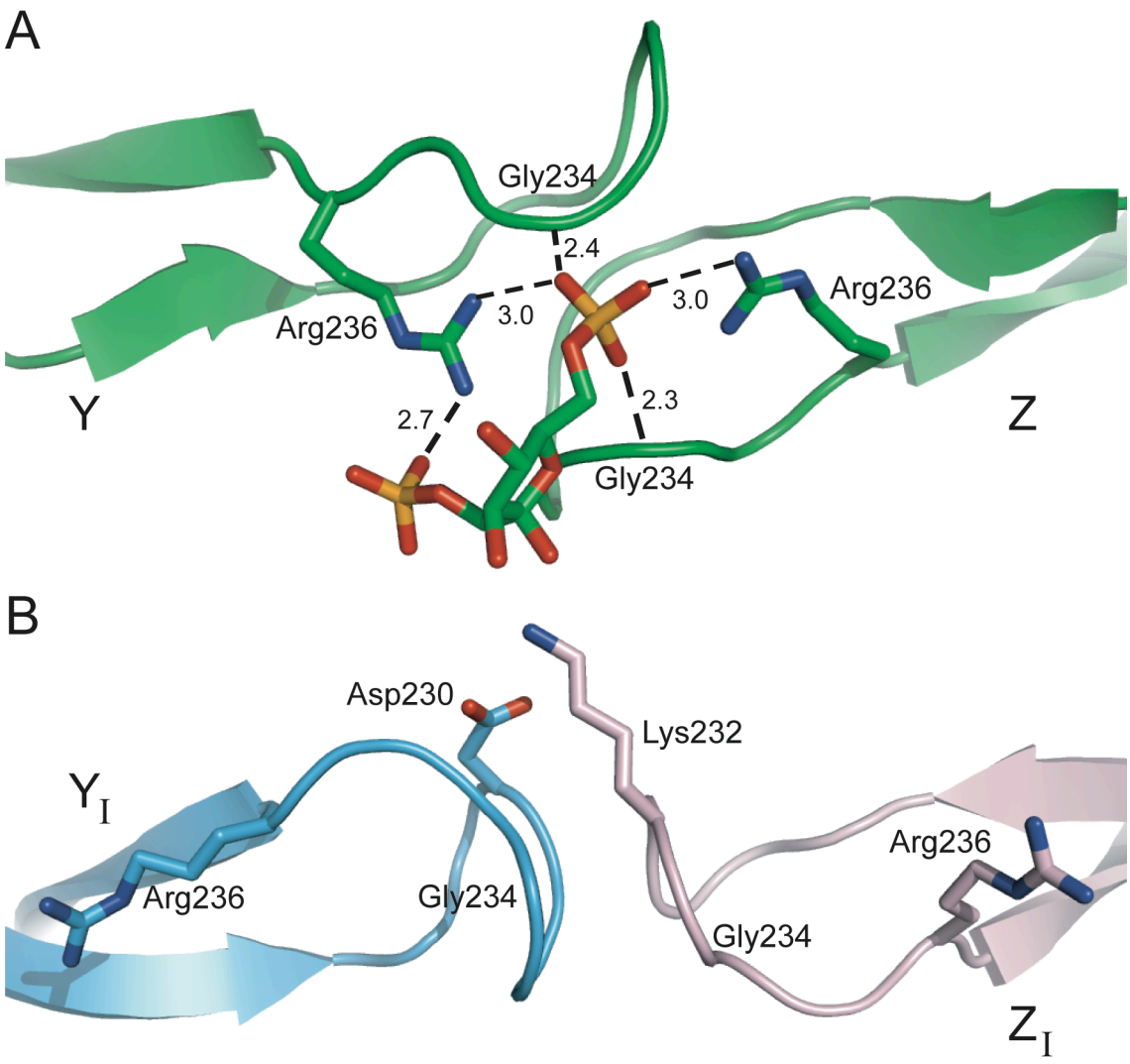

Figure 3.9: Altered FBP binding site in GK^{G230D}. (A) FBP binding mechanism in GK^{WT} at the Y-Z tetramer interface (PDB entry 1BO5). FBP is positioned between the Y and Z monomers by a network of interactions involving Gly234 and Arg236. FBP is shown in stick representation with the 1-phosphate at the bottom and the 6-phosphate at the top of the

image. (B) The Y_I-Z_I tetramer interface of GK^{G230D}. The residues Asp230 of the Y_I monomer and Lys232 of the Z_I monomer are positioned at the tetramer interface in GK^{G230D} and disrupt the wild-type FBP binding site. Note that the Arg236 side chains are shifted away from the FBP binding site in both monomers.

The Oligomeric State of GK^{G230D}. To further explore the decreased FBP inhibition and increased activity of GK^{G230D}, light scattering was used to compare the oligomeric states of GK^{G230D} and GK^{WT} in the presence and the absence of FBP. In the absence of FBP, the GK^{G230D} sample contained a principal dimer peak with a molecular weight of 113 ± 1 kDa and a secondary tetramer peak of 227 ± 16 kDa that was ~ 2% (estimated mass) of the principal peak (Figure 3.10). Under the same conditions, the GK^{WT} sample had a principal dimer peak with a molecular weight of 177 ± 1 kDa and a secondary peak of 391 ± 4 kDa that comprised ~ 9% (estimated mass) of the total sample. The GK^{WT} dimer peak eluted ~ 0.3 ml later than the GK^{G230D} dimer peak and the GK^{WT} secondary peak was more predominant than in GK^{G230D}. The secondary peak of GK^{WT} likely represents a tetramer species mixed in with some higher molecular weight species, as indicated by the sharp rise in the molecular weight versus volume plot. The later elution time for the GK^{WT} dimer peak is indicative of a dynamic dimer-tetramer species, in contrast to the predominantly dimeric species in the GK^{G230D} sample.

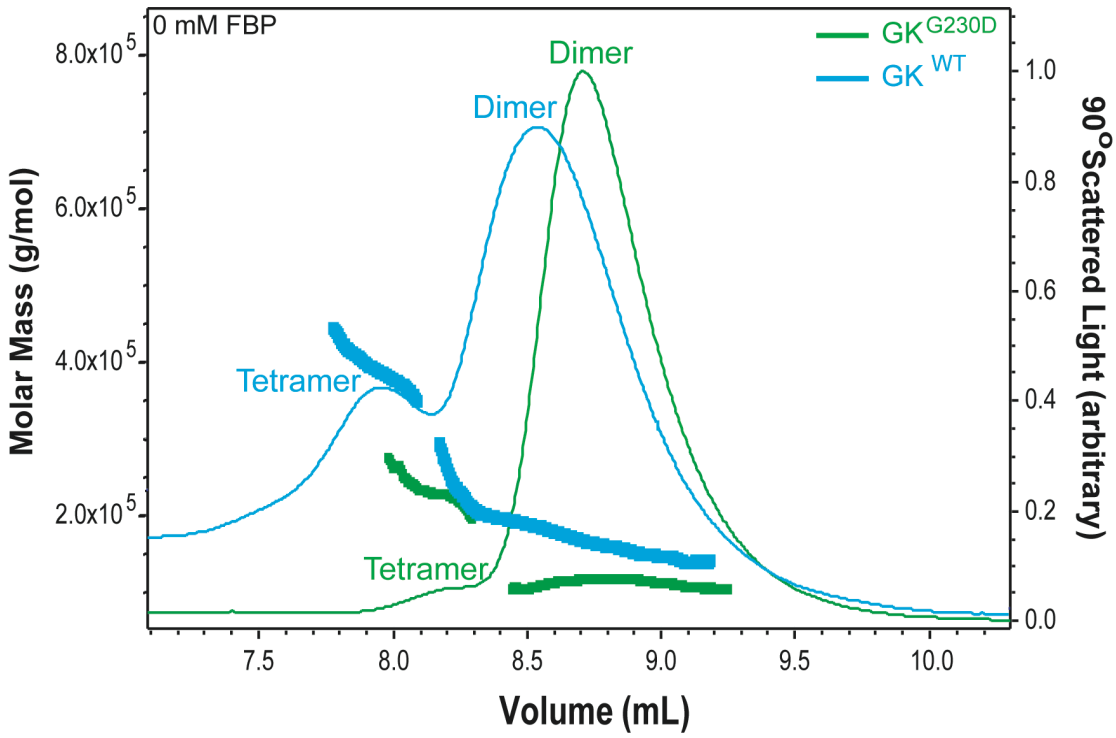

Figure 3.10: Light scattering results in the absence of FBP. GK^{G230D} is shown in green and exists primarily as dimers with a very slight amount of tetramers in a ~ 140:1 molar ratio. GK^{WT} is shown in blue and exists as a mixture of dimers and tetramers in a ~ 10:1 molar ratio. The molecular weight of each species was determined on a gel filtration column using a light scattering setup as described in the Experimental Procedures section. The thin continuous line represents the signal from the right angle scattered light and is similar to the UV trace usually presented for protein chromatography. It should be noted that the scattered light is proportional to the square of the molecular weight, so heavier species are disproportionately represented on the plot. The heavier discontinuous lines plot the molecular weight determinations of the protein eluting from the column at that particular time.

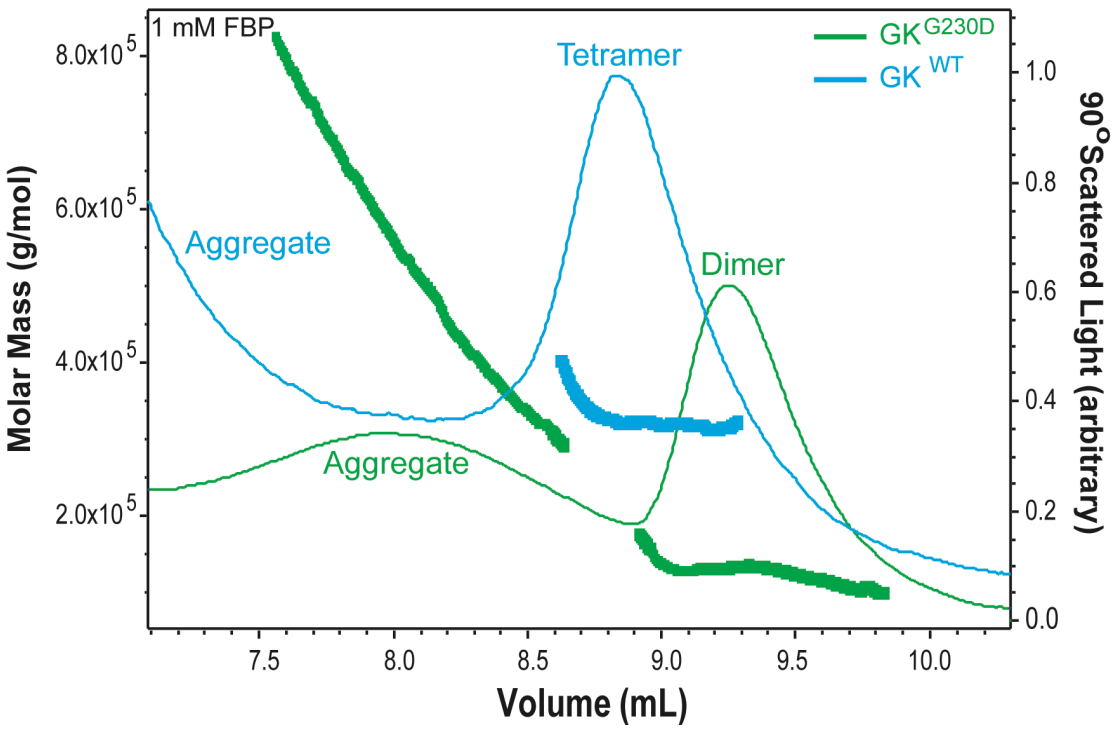

Figure 3.11: Light scattering results in the presence of FBP. GK^{G230D} remained a primarily dimeric species while GK^{WT} was primarily tetrameric and contained no dimeric species. The addition of FBP to the elution buffer also caused a certain degree of nonhomogenous aggregation for both GK^{G230D} and GK^{WT}, forming species with molecular weights ranging from ~ 400 to greater than 1000 kDa. Note that the GK^{G230D} dimer peak of was eluted ~ 0.7 ml later and the GK^{WT} tetramer peak was eluted ~ 1 ml later than the corresponding peaks observed in the absence of FBP.

In the presence of FBP, the GK^{G230D} sample had a principal dimer peak with a molecular weight of 127 ± 3 kDa and an aggregate peak with ~ $1/4^{th}$ the mass that contained species ranging from 200–800 kDa (Figure 3.11). The GK^{WT} sample eluted as two peaks in the

presence of FBP: one large aggregate peak just after the dead volume and a second peak that did not completely resolve from the aggregation peak. The aggregate peak contained species in excess of 1 Mda. The second peak had a molecular weight of 328 ± 10 kDa and is similar to the tetramer + aggregate peak observed in the absence of FBP. The addition of FBP to the elution buffer appeared to create a certain degree of nonhomogenous aggregation for both of the samples. Despite the aggregation, the GK^{G230D} sample was primarily dimeric, whereas the GK^{WT} dimeric species was completely eliminated in the presence of FBP.

The IIA^{Glc} Binding Site. The IIA^{Glc} binding site adopts the IIA^{Glc}-free conformation seen in GK^{WT} in all of the GK^{G230D} monomers with the exception of the O_I monomer. In the absence of IIA^{Glc}, residues 473 to 475 have a random coil conformation and residues 476 to 501 form the C-terminal a-helix. In the presence of IIA^{Glc}, residues 473 to 478 are shifted into a 3_{10} helix and the C-terminal a-helix begins at residue 479 (*46*). A crystal contact at Arg402 in the O_I monomer, supplied by an X_I symmetry operator, alters the conformation of O_I at the IIA^{Glc} binding site to form the 3_{10} helix seen when IIA^{Glc} is present. The crystal contact at Arg402 appears to be inducing the structural rearrangements that occur upon IIA^{Glc} binding.

Changes in Quaternary Structure. The quaternary structure of GK^{G230D} is similar to that seen in GK^{WT}. The functional dimer interfaces of O_I-Y_I, X_I-Z_I, O_{II}-Y_{II}, and X_{II}-Z_{II} are identical to the O-Y and X-Z interfaces of GK^{WT}. GK^{G230D} tetramers I and II have an almost identical quaternary structure, verified by the low 2.0 Å C_α rmsd between the tetramers. The GK^{WT} tetramer superpositions onto GK^{G230D} tetramers I and II with a C_a rmsd of 3.6 and 3.3 Å, respectively. The primary deviations in the quaternary structure of GK^{G230D} and GK^{WT} arise

from changes at the tetramer interface as a result of the G230D mutation at the FBP binding site. It should be noted that while GK^{G230D} crystallized as a tetramer, the light scattering analysis demonstrated that GK^{G230D} exists primarily as a dimer (Figure 3.10). The GK^{G230D} structure is not the first example of a GK mutant crystallizing as a tetramer when it was shown to exist as a dimer in solution (*38, 46*).

Domain Motion. The eight monomers in the glycerol-bound GK^{G230D} structure (GK^{G230D}·glyc) exhibit a range of open and closed conformations. The X_I and Y_I monomers in GK^{G230D}·glyc have a main chain conformation identical to the closed conformation of GK^{WT} and the O_I and O_{II} monomers have a main chain conformation identical to the open conformation previously seen in the structure of a GK mutant with both glycerol and the non-hydrolyzable ATP analog phosphodifluoromethylphosphonic acid-adenylate ester bound (GK^{S58W}·glyc·ATF) (*38*). The X_{II} and Y_{II} monomers exist in an intermediate conformation between the closed and open conformation and the Z_I and Z_{II} monomers adopt a more open ('very open') conformation than is seen in the previously reported open conformation.

Domain motion analysis of the GK^{S58W}·glyc·ATF structure revealed a difference of ~ 6° between the open and closed form of the GK monomers. The GK^{G230D}·glyc structure exhibited a larger difference between the open and closed forms, with rotations between monomer domains I and II in the range of 10 to 18°. The larger difference observed for the GK^{G230D}·glyc open versus closed state is more in line with the ~ 12° rotation observed for the yeast hexokinase structure (*40*). The motion in the yeast hexokinase structure was, however,

attributable to the binding of glucose. The motion in the GK^{G230D}·glyc structure cannot be attributed to the binding of glycerol since the large domain motion occurred with glycerol-bound to all of the individual protomers. Thus it appears that unlike hexokinase, the binding of glycerol alone to glycerol kinase does not influence the open versus closed state of the molecule.

In contrast to the wide range of conformations observed for the binary complex GK^{G230D}·glyc, the structure representing the ternary complex GK^{S58W}·glyc·ATF was observed to exist within a rather narrow range of domain orientations. Apparently, glycerol kinase does not adopt a catalytically competent conformation until both glycerol and nucleotide are bound within the active site. A comparison between the closed form, as represented by the Y protomer from GK^{S58W}·glyc·ATF, and the open form as represented by the either the O_{II} or Z_{II} protomers from GK^{G230D}·glyc, indicates that there is a ~ 14° rigid body rotation that occurs upon nucleotide binding (Table 3.2). This is comparable to the value observed between the open and closed state of yeast hexokinase structure, suggesting that nucleotide triphosphate binding is the determining factor in creating the 'closed' state of the molecule.

Table 3.2: Domain rotation for GK^{G230D}

Pair	Rotation Angle	RMSD (Å)
Y_I-O_I	15.5	1.6
X_I-Z_I	18.0	1.8
Y_{II}-O_{II}	11.3	1.0
X_{II}-Z_{II}	10.0	1.5
BWF[a] - Y_I[b]	n.d.	0.5
BWF - X_{II}[c]	7.2	0.9
BWF - O_{II}	14.7	1.5
BWF - Z_{II}	14.3	1.5

Used Hingefind algorithm to determine effective motion of domains. Used a partition value of 1.8 Å with the VMD implementation. Automatically determined domains were essentially identical to previous analysis (*38*). [a] BWF monomer Y was used for all calculations. [b] BWF – Y_I: no difference (n.d.) between BWF and Y_I protomer. [c] Rotation axis for X_{II} is not the same as the rotation axis for O_{II} and Z_{II}.

Discussion

Use of the microfluidic crystallization platform allowed us to determine the high-resolution structure of GK^{G230D} using less than 1 mg of protein, significantly less than is required using traditional crystallization techniques. The solubility screening and phase diagram measurements consumed ~ 200 μg of protein, the crystal screening and optimization consumed ~ 250 μg, and the crystal scale-up consumed ~ 450 μg. Vapor diffusion crystallization experiments with the same crystallization reagent were performed in parallel to compare the diffraction limits of crystals grown in the scale-up diffraction devices to crystals grown in traditional formats. The vapor diffusion crystallization experiments produced rhombohedral crystals of dimensions 1000 x 500 x 500 μm that diffracted to 3.0 Å (with unit cell a = 91.3 Å, b = 102.9 Å, c = 222.6 Å, β = 90.6° and a mosaicity of 0.636) in the same space group as the diffraction device crystals. The vapor diffusion crystals were not used for structure determination due to the higher quality of the crystals grown in the scale-

up diffraction devices. The higher diffraction resolution (2.0 Å) and lower mosaicity (0.265) of the crystals grown in the microfluidic devices can be attributed two factors: the crystal growth kinetics of the free interface diffusion crystallization experiments and the avoidance of crystal damage, a corollary of crystal harvesting, by in situ data collection from the diffraction devices.

GK^{G230D} provides the first structural overview of a GK variant with a mutation in the FBP binding site and is the first glycerol kinase structure where the FBP binding loops are ordered in the absence of a bound FBP or buffer molecule. GK^{G230D} contains an altered interaction network at the tetramer interface that replaces the wild-type FBP binding site. Most notably, the FBP binding loops in GK^{G230D} adopt a conformation different from what is observed in the wild-type enzyme. The GK^{G230D} FBP binding loop conformations are supported through a series of intramolecular hydrogen bond interactions in each of the FBP binding loops. Additionally, residues Asp230 and Lys232 are found at the tetramer interface in GK^{G230D} whereas the wild-type FBP binding residues Gly234 and Arg236 are directed away from the FBP binding site. The structural changes at the FBP binding site eliminate the wild-type FBP binding pocket at the tetramer interface and as a result decrease FBP inhibition in GK^{G230D}.

The existence of an active dimer form and an inactive tetramer form of GK^{WT} shows an inherent link between the oligomeric state of the protein and its activity. Since the crystal structure did not elucidate a reasonable explanation for the enhanced enzymatic activity observed for GK^{G230D}, light scattering studies were used to probe the oligomeric state of the protein. The light scattering results showed that in the absence of FBP, GK^{G230D} exists

primarily as a dimer with only a trace amount of tetramer species while GK^{WT} exists as a dynamic mixture of dimers and tetramers. The dimers observed for GK^{WT} disappeared upon the addition of FBP whereas the GK^{G230D} dimer population was essentially unaffected. Since GK^{WT} FBP inhibition is dependent upon tetramer formation, the absence of a GK^{G230D} tetramer species in the presence of FBP is consistent with the decreased FBP inhibition of GK^{G230D}. Furthermore, the higher proportion of GK^{G230D} dimer species in the absence of FBP and the resistance of GK^{G230D} dimers to tetramer formation in the presence of FBP suggest the primarily dimeric state of the enzyme is responsible for the increased activity of GK^{G230D}. Given the light scattering results, the GK^{G230D} tetramer in the crystal structure is probably the result of crystal packing energetics and most likely reflects one of potentially multiple dimer-dimer interactions that occur.

It should be noted that the functional implications of the mutation can not be completely established based on the ordered Y_I-Z_I FBP binding site given the appearance of disordered binding sites in the structure. The light scattering results confirmed GK^{G230D} is primarily dimeric in solution and suggest GK^{G230D} dimers form fleeting dimer-dimer interactions in solution that are unlikely to persist on a long timescale. Given the transient nature of the dimer-dimer interactions in solution, the ordered tetramer interface most likely depicts only one of many dimer-dimer interactions that occur at the FBP binding site of GK^{G230D} in solution. The general structural rearrangements in the GK^{G230D} Y_I-Z_I FBP binding loops reveal two ways in which the FBP binding site is altered: novel main chain loop conformations that disrupt the wild-type FBP binding pocket, and the repositioning of residues responsible for FBP binding away from the FBP binding site. Both types of

structural rearrangements seen in the Y_I-Z_I FBP binding loops provide a plausible explanation for the altered FBP regulation in GK^{G230D}, and other loop interactions based on one or both of these structural alterations could account for other fleeting dimer-dimer interactions that occur between GK^{G230D} dimers in solution.

GK^{G230D} also provides the first structural evidence of multiple GK monomer conformations in the presence of glycerol and the absence of a nucleotide substrate. Previous monomer domain motion analysis of a GK^{S58W}·glyc·ATF variant identified an open and closed conformation for GK monomers in the presence of glycerol and ATF. The open and closed monomer conformations were observed in the GK^{G230D}·glyc structure, and in addition a new 'very open' conformation of the enzyme hypothesized to exist in the absence of a bound nucleotide was evident in monomers Z_I and Z_{II}. The multiple GK^{G230D}·glyc monomer conformations conclusively demonstrate glycerol binding does not restrict the domain motion of GK monomers and confirms nucleotide binding is the determining factor in locking GK into the closed form required for enzyme activity.

In conclusion, the crystal structure of GK^{G230D} is the first demonstration of in situ structure determination for a novel crystallization target using a microfluidic crystallization platform. The GK^{G230D} structure revealed an altered interaction network at the tetramer interface that is responsible for disrupting the FBP binding site and decreasing the allosteric regulation of GK^{G230D} by FBP. The oligomeric state of GK^{G230D} was investigated with light scattering and showed the increased enzymatic activity is a result of the stable dimeric quaternary state of GK^{G230D}. Lastly, domain motion analysis revealed a wide range of GK^{G230D} monomer

conformations in the presence of glycerol and verified glycerol binding is not responsible for inducing the conformational change and locking GK into a catalytically active conformation.

Chapter 4

SOLUBILITY CHARACTERIZATION AND CRYSTAL STRUCTURES OF *ESCHERICHIA COLI* GLYCEROL KINASE MUTANTS ASP72 → ALA, 235LYS-GLY-GLY INSERT, AND MET271 → ILE

Introduction

The glycerol kinase crystallization experiments were continued using three additional GK mutants identified during the adaptive evolution experiments (*28–30*). The first GK mutant is Asp72 → Ala (GK^{D72A}), and the mutation occurs at the tetramer interface in close proximity to the FBP binding site. The second GK mutant, 235Lys-Gly-Gly (GK^{235KGG}), has an insertion of three residues in the FBP binding loops. The third GK mutant is Met271 → Ile (GK^{M271I}), and the mutation is buried within the GK monomer. Notably, GK^{M271I} is the only one of the seven GK mutants from the adaptive evolution experiments with a mutation that does not occur near the tetramer interface or the FBP binding site. The microfluidic crystallization platform was used to characterize the solubility properties of each GK mutant, to perform free interface diffusion crystallization experiments, and to produce larger format crystals for in situ diffraction analysis. The microfluidic crystallization strategy was successfully applied to each of the GK mutants and the structures were determined to 2.3 Å for GK^{D72A}, 2.8 Å for GK^{235KGG}, and 2.9 Å for GK^{M271I}.

Experimental Procedure

Protein Preparation. The *Escherichia coli* GK^{D72A}, GK^{235KGG}, and GK^{M271I} protein expression and purification were performed as previously described with minor modifications (*51, 52*) and the protocols are presented in Appendix D. The GK^{D72A} and GK^{235KGG} purified protein was concentrated to 10 mg/ml and the GK^{M271I} purified protein was concentrated to 15 mg/ml for crystallization experiments. The purified protein was stored in standard buffer at -80 °C (20 mM Tris·HCl (pH 7.5), 10 mM glycerol, 1 mM β-mercaptoethanol). The activity of GK^{D72A}, GK^{235KGG}, and GK^{M271I} were previously determined using an ADP-coupled assay (*30*).

Size Exclusion Chromatography—Multi-Angle Laser Light Scattering Studies. The oligomeric state of GK^{D72A}, GK^{235KGG}, and GK^{M271} was determined as described previously (*13*) (see Chapter 3 Experimental Procedures for details). Each measurement was made using 100 μl of 2 mg/ml protein with elution buffer composed of standard buffer ± 1 mM FBP.

Solubility Characterization and Crystallization. A microfluidic formulator device was used to characterize the solubility of GK^{D72A}, GK^{235KGG}, and GK^{M271I} for crystallization experiments. The device fabrication, experimental setup, and solubility screening was performed as previously described (*10, 13*). Each protein was screened with 765 unique reagents produced using 17 salt solutions, 5 buffering agents, and 9 precipitating agents (see Appendix B for a complete list of reagents). Each reagent was screened at six different

protein and precipitating agent concentrations to generate broad phase diagrams. Protein samples were used at a stock concentration of 30 mg/ml for all solubility experiments.

Crystallization screening experiments were performed with the identified crystallization reagents using microfluidic free interface diffusion screening devices (*4, 12*). The successful crystallization conditions were transported to microfluidic scale-up diffraction devices (*6*). Cryoprotectant (25–30% ethylene glycol) was introduced into the diffraction devices and crystals were frozen within the devices for diffraction analysis as previously described (*6, 12*).

Data Collection and Structure Determination. Data sets for GK^{D72A}, GK^{235KGG}, and GK^{M271I} crystals were collected at station 9.1 of the Stanford Linear Accelerator Center (Stanford University) at an incident wavelength of 1.0 Å with a 1° oscillation. The data sets were collected to 2.3 Å, 2.8 Å, and 2.9 Å, respectively, from crystals grown in scale-up diffraction devices. The data sets were indexed and scaled using DENZO and SCALEPACK (*56*). The GK^{D72A} data was further processed with ellipsoidal truncation and anisotropic scaling (*64*) using a $F/\sigma(F)$ cutoff of 3, resulting in resolution cutoffs of a* = 2.3 Å, b* = 2.8 Å, and c* = 2.3 Å.

The structures for GK^{D72A} and GK^{235KGG} were determined by molecular replacement using GK^{G230D} tetramer I (PDB entry 2P3R) as a search model. The rigid body refinement method as implemented in CCP4 (*65*) was used to search with eight rigid bodies defined by dividing each monomer in the tetramer into two domains (residues 2–249 and residues 250–500). The

starting models each had one tetramer in the asu. The structures were refined using alternate cycles of manual rebuilding with COOT (*66*) and refinement with REFMAC5 (*67*). Four glycerol molecules were placed into well-defined electron density in each of the active sites, and water molecules were automatically picked using COOT. Residues 229–235, which were missing in the O and X monomers in the 2P3R search model, were built into GK^{D72A} using real-space protein model completion software (*68*). Three alternate side chain conformations were placed into well-defined electron density for GK^{D72A}: monomer O residue 271, monomer X residue 147, and monomer Y residue 21. Regions of the models without clear electron density were set to zero occupancy. The regions set to zero occupancy for GK^{D72A} were monomer Y residues 230–233 and monomer Z residues 230–234. The regions set to zero occupancy for GK^{235KGG} were monomer O residues 231–237, monomer X residues 230–236, monomer Y residues 232–235, and monomer Z residues 232–236 and 503.

The structure for GK^{M271I} was determined by molecular replacement using GK^{D72A} as a search model. The rigid body refinement as implemented in PHENIX (*69*) was used to search with eight rigid bodies as described above. The starting model contained one tetramer in the asu. The structure was refined using alternate cycles of manual rebuilding with COOT (*66*) and refinement with REFMAC5 (*67*). Four glycerol molecules were placed into well-defined electron density in each of the active sites. The following regions of the model did not have clear electron density and were set to zero occupancy: monomer O residues 230–233, 322–327, 346–351, 358–361, 462–464, and 492–500; monomer X residues 231–233, 324–326, and 500; monomer Y residues 230–233, 323–327, and 493–500; and monomer Z

residues 158–159, 230–234, and 498–500. GK^{D72A}, GK^{235KGG}, and GK^{M271I} data collection and refinement statistics are summarized in Table 4.1.

Domain Motion Analysis. Effective domain motion analysis was determined using the VMD implementation of the Hingefind algorithm (*61*). A partition value of 1.8 Å was used for all measurements. The rotation axis defining the two domains in the monomers was identical to the previously reported rotation axis (*38*). The domain rotation angles for GK^{D72A}, GK^{235KGG}, and GK^{M271I} were computed between the monomers in each dimer and between each monomer and the previously reported closed conformation of GK (PDB entry 1BWF, monomer Y) (*38*).

Results

Solubility Characterization and Crystallization. The crystallization strategy for GK^{D72A}, GK^{235KGG} and GK^{M271I} began with a complete solubility characterization using 765 unique reagents composed of diverse salt solutions, buffering agents, and precipitating agents. A microfluidic formulator device (*10*) systematically combined nanoliter volumes of GK^{D72A}, GK^{235KGG} and GK^{M271I} with each reagent and broadly screened protein solubility across the associated phase diagram for a total of 13,770 solubility experiments (Figure 4.1). Reagents that caused protein aggregation at any point on the phase diagrams were identified as potential crystallization reagents and the broad phase diagrams were used to create individual crystallization screens for GK^{D72A}, GK^{235KGG} and GK^{M271I}. The GK^{235KGG} sample aggregated the most frequently of the three samples; 30% of the reagents screened were identified as potential crystallization reagents for GK^{235KGG}. On the other hand, only 17% of the reagents

screened for GK^{D72A} were identified as crystallization reagents. GK^{M271I} was in between the two samples and aggregated in response to 22% of the reagents screened. For comparison, the GK^{G230D} sample described in Chapter 3 aggregated in response to 34% of the 765 reagents screened for GK^{D72A}, GK^{235KGG}, and GK^{M271I}.

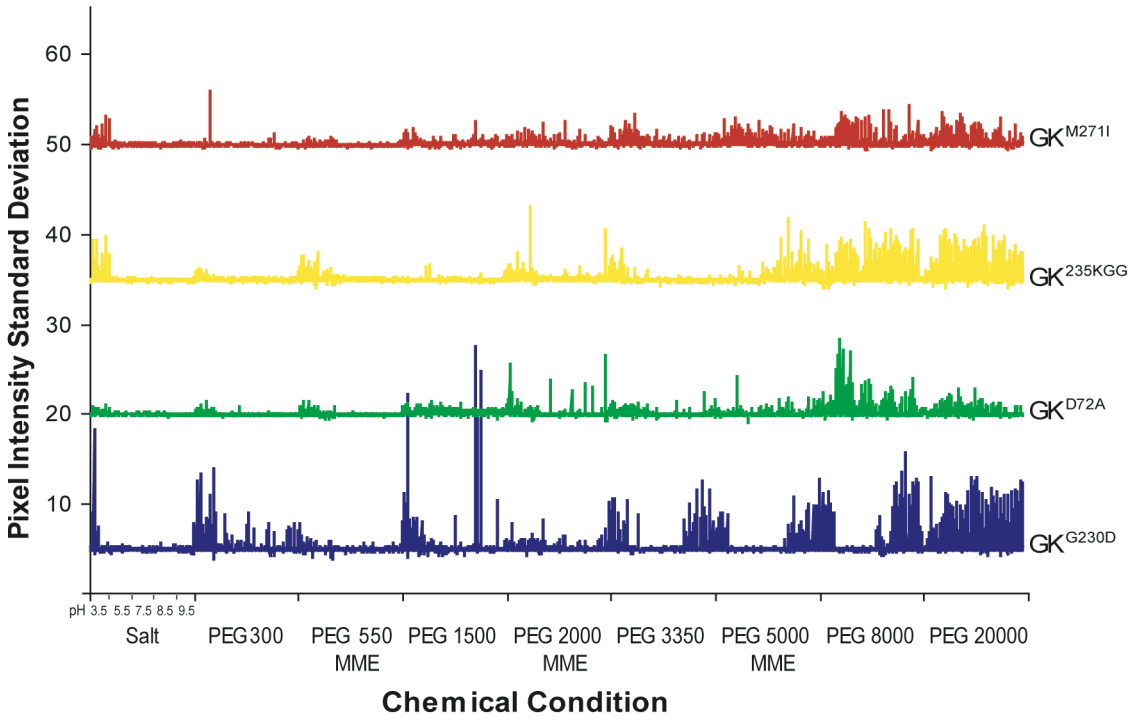

Figure 4.1: Solubility characterization of GK^{D72A}, GK^{235KGG}, and GK^{M271I}. The solubility screening results are grouped by precipitant composition and subdivided by buffer and salt composition, respectively. A total of 4590 solubility experiments were performed for each protein. The solubility characterization of GK^{G230D} described in Chapter 3 is also included for reference. Pixel intensity standard deviation represents the amount of protein aggregation observed in combination with each reagent; reagents that caused protein aggregation above 1 pixel intensity standard deviation unit were classified as crystallization reagents.

Although the GK mutants are identical except for single point mutations, the solubility characterization revealed unique solubility trends for each of the four GK mutants. The effect of each of the reagent components on protein solubility for the GK mutants was examined (Figure 4.2). Overall, the precipitating agent had the greatest effect on protein solubility and larger precipitating agents with longer PEG polymer chain lengths caused higher rates of aggregation (Figure 4.2A). For GK^{G230D} and GK^{M271I}, aggregation occurred most frequently for reagents containing the largest precipitating agent PEG 20000. For GK^{D72A} and GK^{235KGG}, aggregation occurred at the highest rate for reagents containing the precipitating agent PEG 8000. Additionally, the GK^{G230D} sample aggregated at a significantly higher rate for the smaller precipitating agents PEG 300, PEG 1500, and PEG 3350 than the other samples. One common trend for all of the GK mutants was a low rate of aggregation in response to the ionic precipitating agents.

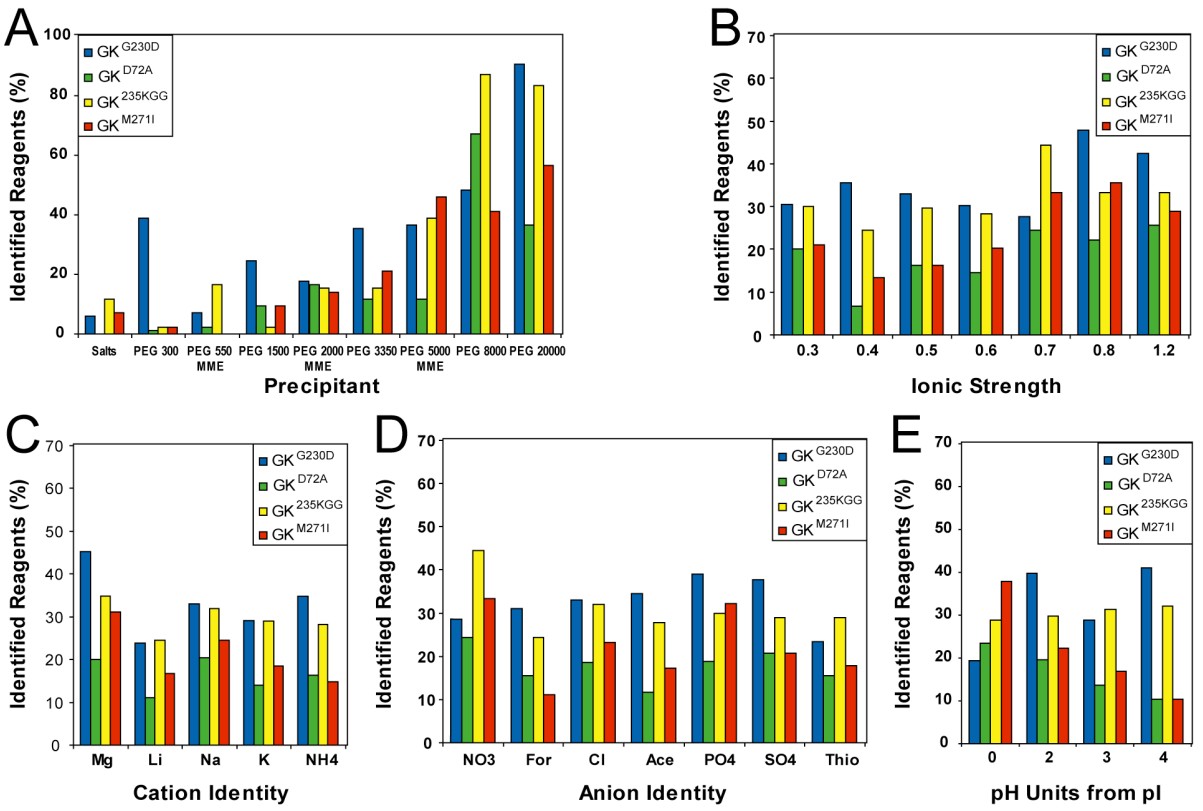

Figure 4.2: Solubility trends for GK mutants. (A) Classification of identified reagents for each mutant by the molecular weight of the precipitating agent. (B) Classification of identified reagents by the ionic strength of the reagent. (C) Classification of the identified reagents by the cation component of the salt solution. (D) Classification of the identified reagents by the anion component of the salt solution. The anions formate, acetate, and thiosulfate are abbreviated as For, Ace, and Thio, respectively. (E) Classification of identified reagents by the deviation from the 5.36 pI of glycerol kinase. For (A–E), the percentage of identified reagents is normalized by the number of reagents screened in each category.

Variations were also seen in the ionic strength and composition of the reagents identified for each of the GK mutants. The GK^{G230D} and GK^{M271I} samples aggregated most frequently for reagents with an ionic strength of 0.8, the GK^{235KGG} sample aggregated most often for reagents with an ionic strength of 0.7, and the GK^{D72A} sample aggregated most frequently for reagents with an ionic strength of 1.2 (Figure 4.2B). Notably, the GK^{M271I} and GK^{G230D} samples aggregated most often for reagents with the same precipitating agent composition and for reagents with the same ionic strength. The cation that occurred most frequently in the identified reagents for GK^{G230D}, GK^{235KGG}, and GK^{M271I} was magnesium (Figure 4.2C). For GK^{D72A}, the aggregation occurred most often for reagents containing sodium or magnesium cations. The anion that occurred most frequently in the reagents identified for GK^{D72A}, GK^{235KGG}, and GK^{M271I} was nitrate (Figure 4.2D). On the other hand, the GK^{G230D} sample aggregated most often for reagents containing phosphate or sulfate anions.

Lastly, the buffering agent composition had contrasting effects on the solubility responses of different GK mutants (Figure 4.2E). The GK^{D72A} and GK^{M271I} samples aggregated most often for reagents at the isoelectric point of GK. Alternatively, the GK^{G230D} and GK^{235KGG} samples aggregated most frequently for reagents far away from the pI of GK. The unique solubility properties exhibited within a series of four closely related point mutants highlights the potential limitations of using a generalized set of crystallization conditions for multiple proteins.

Following the solubility characterization, microfluidic free interface diffusion screening devices (*4, 12*) were used to screen the unique crystallization reagents identified for GK^{D72A},

GK^{235KGG}, and GK^{M271I}. The best crystal hits were optimized using additional free interface diffusion screening devices until the crystals were of sufficient quality for larger format crystallization experiments (Figure 4.3). The GK^{M271I} sample had the highest crystallization rate and crystallized with 47% of the reagents screened. The other two GK mutants also had high crystallization success rates; GK^{235KGG} produced crystals with 38% of the reagents screened, and GK^{D72A} crystallized with 37% of the reagents screened. These crystallization success rates are much higher than the 16% crystallization success rate observed for the GK^{G230D} sample.

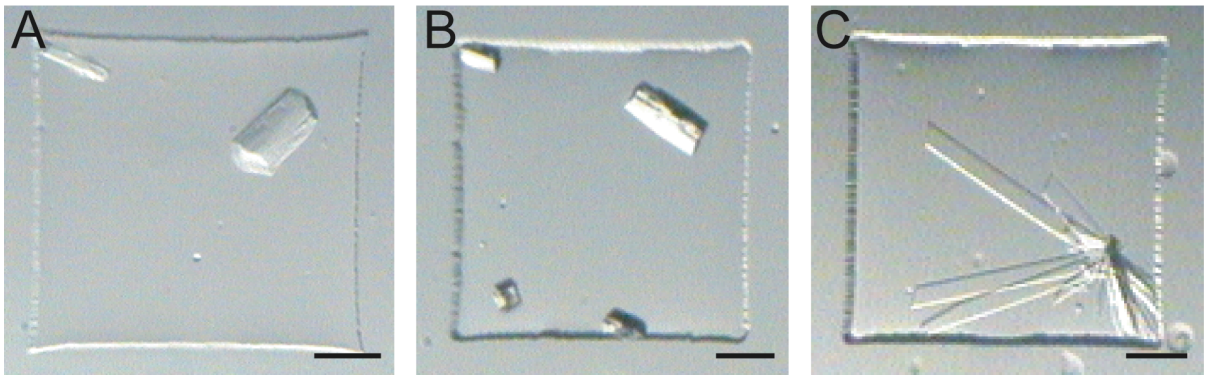

Figure 4.3: Crystallization of GK^{D72A}, GK^{235KGG}, and GK^{M271I}. (A) GK^{D72A} was crystallized with the reagent 0.2 M magnesium acetate, 0.1 M Hepes (pH 7.5), and 60% PEG 300. (B) GK^{235KGG} was crystallized with 0.75 M sodium chloride, 0.1 M TAPS (pH 9.5), and 24% PEG 3350. (C) GK^{M271I} was crystallized with 0.2 M magnesium chloride, 0.1 M Tris·HCl (pH 8.5), and 30% PEG 5000 MME. The scale bars represent 100 μm.

Similar to the unique solubility properties of the GK mutants, a distinct set of crystallization reagents produced crystals for each of the GK mutants. The crystallization reagents for each

of the GK mutants were compared and the effect of each of the reagent components on crystallization was examined (Figure 4.4). A different precipitating agent produced the highest percentage of crystal hits for each of the GK mutants (Figure 4.4A). For GK^{M271I} the smallest polymer precipitating agent, PEG 300, had the highest crystallization rate. For GK^{D72A} and GK^{235KGG}, chemically modified PEG MME precipitating agents had the highest crystallization rates. For GK^{G230D}, the largest percentage of crystal hits was observed with the precipitating agent PEG 1500. Notably, the larger precipitating agents that caused protein aggregation most frequently were not the reagents that produced the highest percentage of crystal hits.

The ionic strength of the reagents that produced the highest percentage of crystal hits was different for each of the GK mutants (Figure 4.4B). The highest percentage of crystal hits appeared for reagents with ionic strengths of 0.4, 0.7, 0.8, and 1.2 for samples GK^{M271I}, GK^{D72A}, GK^{G230D}, and GK^{235KGG}, respectively. Notably, the crystallization trends for GK^{M271I} favor reagents with a low ionic strength whereas the solubility trends showed protein aggregation occurred most frequently for reagents with a high ionic strength. Two cations were implicated in the highest percentage of crystal hits for the GK samples. Magnesium was the most frequent cation for GK^{D72A} and GK^{235KGG} crystallization and potassium appeared most often in the GK^{G230D} and GK^{M271I} crystallization reagents (Figure 4.4C). The anion that caused the most crystal hits for GK^{D72A} and GK^{235KGG} was formate (Figure 4.4D). For the GK^{D72A} sample, thiosulfate caused the highest percentage of crystal hits. For the GK^{235KGG} sample, nitrate and phosphate caused the highest percentage of crystal hits. Notice

that the same ionic components were identified for the GK^{D72A} and GK^{235KGG} reagents with the highest percentage of crystal hits.

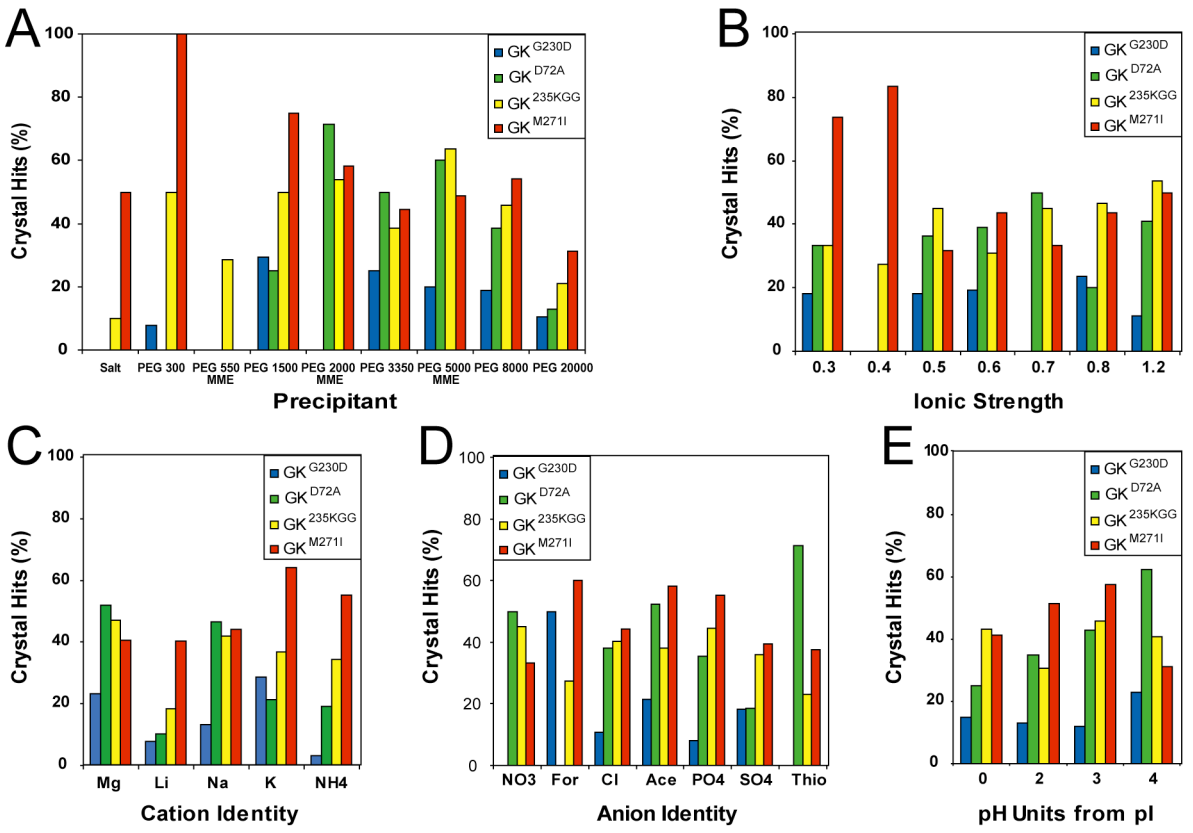

Figure 4.4: Crystallization trends for GK mutants. (A) Classification of crystal hits by the molecular weight of the precipitating agent. (B) Classification of crystal hits by the ionic strength of the reagent. (C) Classification of crystal hits by the cation component of the salt solution. (D) Classification of crystal hits by the anion component of the salt solution. (E) Classification of crystal hits by the deviation from the 5.36 pI of glycerol kinase. For (A–E), the percentage of crystal hits is normalized by the number of crystallization conditions screened in each category.

The buffering agent component of the crystallization reagents revealed that reagents with buffering agents far away from the pI of GK produce more crystals than reagents near the pI (Figure 4.4E). For GK^{235KGG} and GK^{M271I}, the most crystals were produced using reagents with buffering agents three units away from the pI of GK. For GK^{D72A} and GK^{G230D}, the most crystals were produced using reagents with buffering agents four units away from the pI of GK. Notice that the crystallization trends for GK^{D72A} and GK^{M271I} favor reagents far from the pI whereas the solubility trends showed protein aggregation occurs most frequently for reagents near the pI.

The best crystallization condition for each protein was transported to microfluidic scale-up diffraction devices (*6*). GK^{235KGG} and GK^{M271I} formed rhombohedral crystals, and GK^{D72A} formed rectangular prism crystals in the scale-up diffraction devices (Figure 4.5). The crystals were flash-frozen within the scale-up diffraction device for in situ diffraction analysis. The GK^{D72A}, GK^{235KGG}, and GK^{M271I} crystals diffracted to 2.3 Å, 2.8 Å, and 2.9 Å resolution, respectively, and the structures were solved using molecular replacement. Data collection and refinement statistics for each model are presented in Table 4.1.

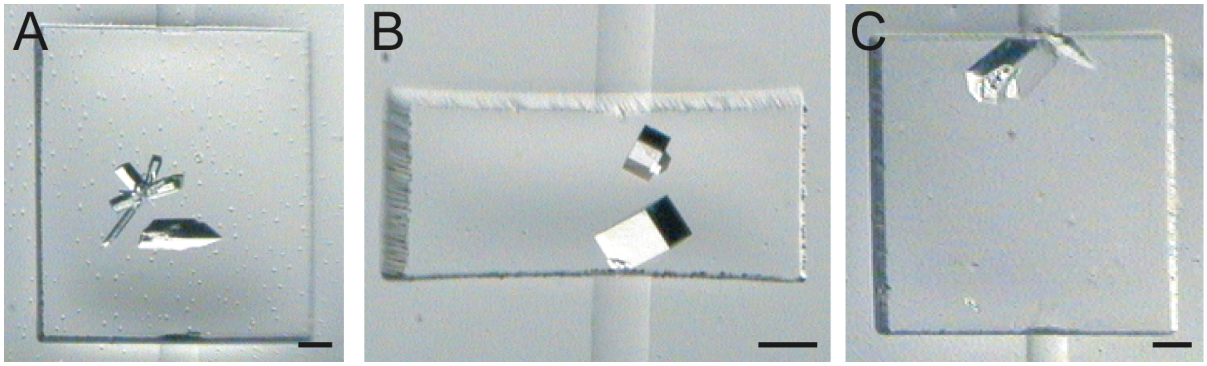

Figure 4.5: Larger format crystals in diffraction devices. (A) GK^{D72A} rectangular prism crystals, (B) GK^{235KGG} rhombohedral crystals, and (C) GK^{M271I} rhombohedral crystals were grown in scale-up diffraction devices for in situ data collection. The scale bars represent 100 μm.

Table 4.1: Data collection and refinement statistics

	GK^{D72A}	GK^{235KGG}	GK^{M271I}
Data collection			
wavelength (Å)	1.0	1.0	1.0
space group	$P2_12_12_1$	$P2_1$	$P2_1$
cell dimensions			
a (Å)	91.3	90.5	95.2
b (Å)	119.6	110.5	97.6
c (Å)	211.5	116.7	118.1
β (°)	90	92.8	113.0
resolution[a] (Å)	50-2.3 (2.4-2.3)	50-2.8 (2.9-2.8)	50-2.9 (3.0-2.9)
unique observations[a]	97883 (9076)	56144(5620)	42813 (4333)
redundancy[a]	16.7 (9.9)	12.1 (6.4)	8.6 (5.5)
completeness[a]	85.6 (27.4)[f]	99.8 (99.7)	97.4 (94.8)
$I/\sigma(I)$ [a]	13.7 (1.6)	17.7 (2.5)	23.1 (1.9)
R_{sym} [b]	19.1 (96.7)[f]	14.4 (70.8)	11.0 (76.2)
Refinement			
resolution (Å)	20-2.3	20-2.8	20-2.9
no. of reflections	80355	53010	40468
no. of refined protein atoms	15698	15652	15169
no. of refined solvent atoms	470	334	0
no. of glycerol molecules	4	4	4
R_{cryst} [c]	21.1	18.2	22.9
R_{free} [d]	29.1	26.5	32.2
average B-factor (Å^2)	37.0	45.2	62.6
bond length rmsd (Å)	0.017	0.015	0.013
angle rmsd (°)	1.61	1.55	1.45
Ramachandran plot (% in most favored/allowed/generous/ disallowed regions[e])	89.7/9.8/0.3/0.2	86.4/13.2/0.2/0.2	83.8 /15.5/0.5/0.2

[a] Numbers in parenthesis refer to the highest resolution shell. [b] $R_{sym} = \Sigma_{ij}|I_i(j) - \langle I(j)\rangle| / \Sigma_{ij}I_i(j)$, where $I_i(j)$ is the intensity of the *i*th observation of reflection j, I(j) is the weighted mean of all measurements of *j*. [c] $R_{cryst} = \Sigma_j|F_o(j) - F_c(j)|/\Sigma_j|F_o(j)|$, where F_o and F_c are the observed and calculated structure factors. [d] R_{free} = R_{cryst} calculated by using 5% of the reflection data chosen randomly and omitted from the start of refinement (*62*). [e] The residues in the disallowed regions were found in the active site interacting with glycerol. [f] The limited completeness and high R_{sym} values are due to the anisotropic processing of the data.

Structure Overviews. GK^{D72A}, GK^{235KGG}, and GK^{M271I} crystallized as tetramers in space groups $P2_12_12_1$, $P2_1$, and $P2_1$, respectively, with a glycerol molecule bound in the active site of each monomer (Figure 4.6). Each tetramer is composed of monomers O, X, Y, and Z, with the O-Y and X-Z monomers forming the functional dimers. The domain organization of each monomer and the O-Y and X-Z dimer interfaces are equivalent to that seen in GK^{WT} (*45, 46*). The tetramer interface is formed at the O-X and the Y-Z monomer interfaces. The quaternary structures of GK^{D72A} and GK^{235KGG} are similar to the physiologically relevant tetramer geometry of GK where the tetramer is composed of two identical dimers with one monomer in the closed conformation and one monomer in the open conformation (*46*). The GK^{D72A} and GK^{235KGG} X and Y monomers are in the closed conformation and the O and Z monomers are in the open conformation. Alternatively, the GK^{M271I} tetramer has a novel quaternary structure where every monomer in the tetramer exists in an open conformation. The IIA^{Glc} binding site, located at the C-terminal end of each monomer, retains the IIA^{Glc}-free conformation (*46*) in all of the structures with the exception of monomer X in GK^{M271I}. In GK^{M271I}, the IIA^{Glc}-bound conformation (*45*) occurs in monomer X as a result of a crystal contact between Glu475 and a monomer X symmetry operator. The FBP binding loops are located at the O-X and Y-Z tetramer interfaces and are ordered at the GK^{D72A} O-X tetramer interface.

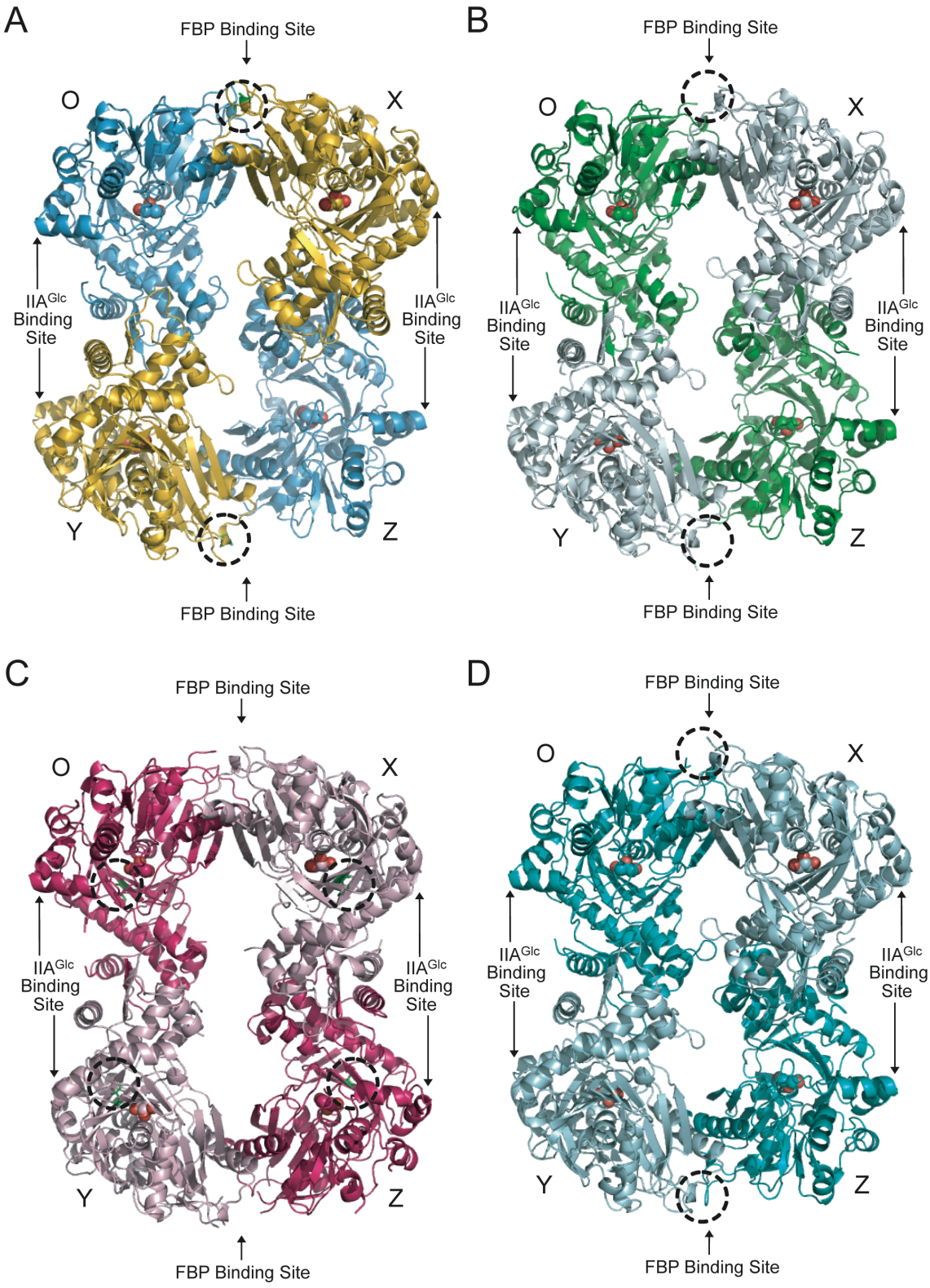
A
FBP Binding Site
O
X
IIA^Glc Binding Site
IIA^Glc Binding Site
Y
Z
FBP Binding Site
B
FBP Binding Site
O
X
IIA^Glc Binding Site
IIA^Glc Binding Site
Y
Z
FBP Binding Site
C
FBP Binding Site
O
X
IIA^Glc Binding Site
IIA^Glc Binding Site
Y
Z
FBP Binding Site
D
FBP Binding Site
O
X
IIA^Glc Binding Site
IIA^Glc Binding Site
Y
Z
FBP Binding Site

Figure 4.6: Tetramer structures of four GK mutants. (A) The GK^{D72A} tetramer structure. The gold X and Y monomers are in the wild-type closed conformation, and the blue O and Z monomers are in a more open conformation than in GK^{WT}. Ala72 is circled at the tetramer interfaces. (B) The GK^{235KGG} tetramer structure. The silver X and Y monomers are in the closed conformation, and the green O and Z monomers mimic the GK^{D72A} open conformation. The disordered location of the 235Lys-Gly-Gly insert in the FBP binding loops is circled at the tetramer interfaces. (C) The GK^{M271I} tetramer structure. The pink X and Y monomers and the magenta O and Z monomers all display a novel open conformation. Met271 is circled in each monomer. (D) The GK^{G230D} tetramer structure (PDB entry 2P3R) described in Chapter 3. The light blue X_I and Y_I monomers are in the wild-type closed conformation, the teal O_I monomer is in the wild-type open conformation, and the teal Z_I monomer is in a more open conformation than in GK^{WT}. The FBP binding sites and the IIA^{Glc} binding sites are highlighted and glycerol is shown in the hinge region of each monomer.

GK^{D72A} Tetramer Interface. The tetramer interface is comprised of an α-helix (residues 49–67) that packs in an antiparallel manner between the O-X and the Y-Z monomers and the FBP binding loops (residues 229–236) that associate to form the FBP binding sites (Figure 4.7). Within each monomer, the interface helix and the FBP binding loop are bridged by a short α-helix (residues 70–73) that includes the Asp72 → Ala mutation in GK^{D72A}. The helical interface is similar in GK^{WT} and GK^{D72A}, with the C_α backbone of the GK^{WT} O-X interface helices superpositioning on the GK^{D72A} helices with a rmsd of 0.4 Å. Conversely, the absence of Asp72 in the bridging helix of GK^{D72A} creates an open region between the

helix and the FBP binding loops and allows for a higher degree of conformational flexibility in the FBP binding loops. The C_α backbone of the O-X FBP binding loops of GK^{WT} are superpositioned on the GK^{D72A} FBP binding loops with an rmsd of 4.0 Å.

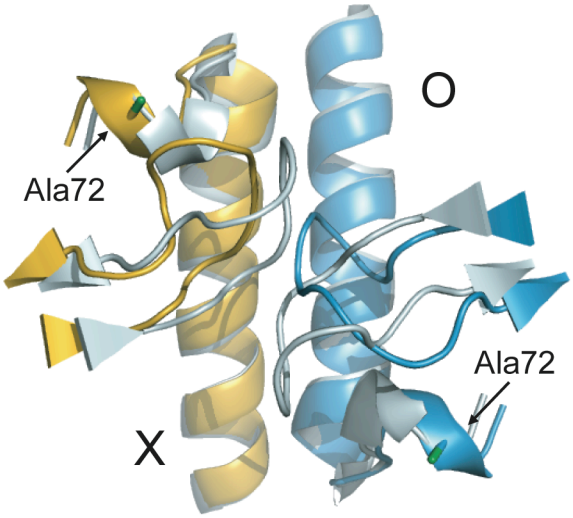

Figure 4.7: Overview of the GK^{D72A} tetramer interfaces. Residues 48 to 78 and 229 to 236 of the O-X tetramer interface of GK^{WT} (PDB entry 1GLF) are superpositioned on the O-X tetramer interface of GK^{D72A}. The FBP binding loops are located above the antiparallel α-helices. The O and X monomers of GK^{D72A} are blue and gold, respectively, Ala72 is green, and the O and X monomers of GK^{WT} are silver.

The GK^{WT} interaction network around Asp72 supports the main chain conformation of the bridging helix and positions Asp72 in the direction of the FBP binding loop (Figure 4.8A). Two hydrogen-bond interactions occur in GK^{WT} monomer X between the backbone oxygen of Ser70 and the backbone amide of Gln73 and between O_γ of Ser70 and $N_{\varepsilon 2}$ of Gln73. The

interaction networks in the O and X monomers are equivalent in GK^{WT}. The presence of the Asp72 side chain above the bridging helix prevents residues 232 to 235 of the FBP binding loop from coming within close proximity of the bridging helix.

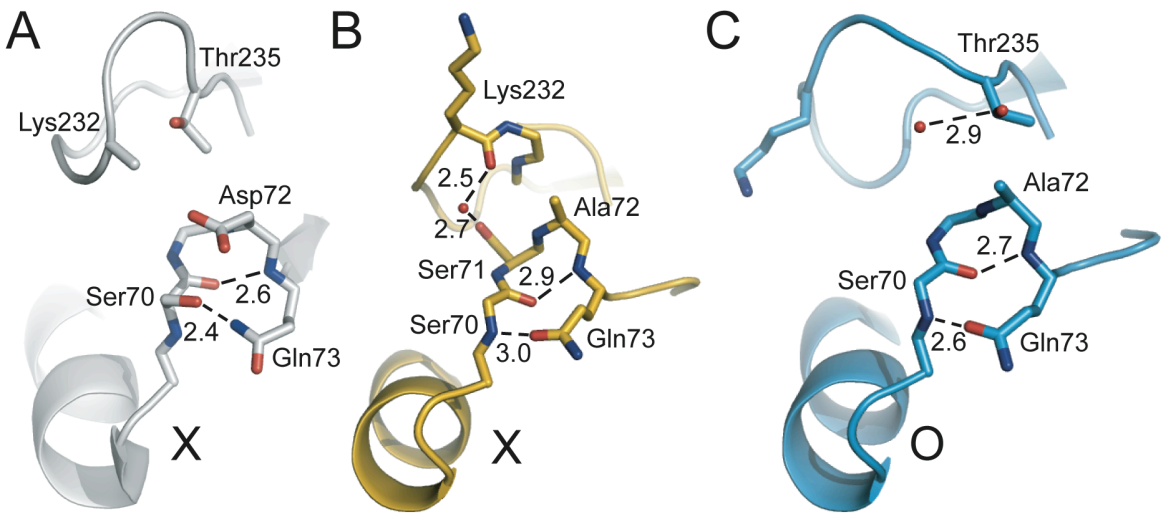

Figure 4.8: Comparison of the GK^{D72A} and GK^{WT} tetramer interfaces. (A) GK^{WT} hydrogen-bonding networks near Asp72 at the tetramer interface of monomer X. There are two hydrogen-bond interactions between Ser70 and Gln73. (B) Hydrogen-bonding networks in GK^{D72A} monomer X at the Ala72 mutation site. The X monomer has two hydrogen-bond interactions between Ser70 and Gln73 and one water-mediated interaction between Ser71 and Lys232. (C) Hydrogen-bonding networks in the GK^{D72A} monomer O at the Ala72 mutation site. The O monomer has two hydrogen-bond interactions between Ser70 and Gln73 and one hydrogen-bond interaction between Thr235 and a water molecule.

The GK^{D72A} interaction network around Ala72 deviates from the wild-type interaction network and also varies between monomers. The monomer X interaction network involves water-mediated contacts between the bridging helix and the FBP binding loop in addition to the hydrogen-bond interactions within the bridging helix (Figure 4.8B). The monomer X bridging helix main chain conformation is supported by two hydrogen bond interactions between the backbone amide of Ser70 and $O_{\varepsilon 1}$ of Gln73 and between the backbone oxygen of Ser70 and the backbone amide of Gln73. The Gln73 side chain is flipped 180° in GK^{D72A} and results in a main chain interaction with Ser70 instead of the side chain interaction with Ser70 in GK^{WT}. A water-mediated interaction also occurs in monomer X between O_{γ} of Ser71 and the backbone oxygen of Lys232. The GK^{D72A} monomer X water-mediated interaction is the only interaction observed between the bridging helix and the FBP binding loop in either GK^{D72A} or GK^{WT}. The closest residue in the FBP binding loop in monomer X to Ala72 is Lys232, whereas Thr235 is the closest residue to Asp72 in GK^{WT} and to Ala72 in monomer O of GK^{D72A}.

In monomer O of GK^{D72A} there are two hydrogen-bond interactions near Ala72 between the backbone oxygen of Ser70 and the backbone amide of Gln73 and between the backbone oxygen of Ser70 and $O_{\varepsilon 1}$ of Gln73 (Figure 4.8C). A third interaction occurs between $O_{\gamma 1}$ of Thr235 in the FBP binding loop and a water molecule. The Gln73 side chain is also flipped 180° in monomer O of GK^{D72A} compared to GK^{WT}. The other notable difference in the monomer O tetramer interface is the repositioning of Lys232 in the FBP binding loop away from the bridging helix; the C_{β} of Ala72 and the C_{β} of Lys232 are 11.0 Å apart in monomer O, compared to 6.4 Å in monomer X and 6.0 Å in GK^{WT}. Overall, the absence of Asp72 in

the bridging helix of GK^{D72A} enables large conformational changes at the tetramer interface FBP binding loops.

GK^{D72A} FBP Binding Site. The FBP binding site in GK^{D72A} consists of two unique FBP binding loops with main chain loop conformations unlike the wild-type loop conformations (Figure 4.7). The ordered FBP binding site at the O-X tetramer interface in GK^{D72A} has an average B factor of 32.9 $Å^2$. The wild-type FBP binding site is formed by two identical FBP binding loops that come together at the tetramer interface to create a symmetrical binding pocket for the phosphate groups of FBP. Alternatively, the GK^{D72A} FBP binding loops are dissimilar in each monomer and are not symmetrically positioned at the tetramer interface to create the FBP binding site.

FBP molecules bind to the GK^{WT} tetramer interface through a series of interactions with Gly234 and Arg236 on each monomer (Figure 4.9A). Arg236 was previously shown to be required for FBP binding and is involved in most of the interactions with FBP (*47*). The 6-phosphate of FBP is centered in the FBP binding site through four interactions with $N_{\eta 2}$ of Arg236 on monomer O, $N_{\eta 1}$ of Arg236 on monomer X, and the backbone amides of Gly234 on monomers O and X. The 1-phosphate of FBP has one interaction with $N_{\eta 2}$ of Arg236 on monomer X. In addition to the direct interactions with FBP, several intramolecular and intermolecular interactions support the symmetrical FBP binding loop conformations in GK^{WT} (*46*). Specifically, intermolecular loop hydrogen-bond interactions occur between the backbone oxygen of Asn228 and the backbone amide of Gly231, and between $N_{\delta 2}$ of Asn228 and the backbone oxygen of Gly231. Intramolecular hydrogen-bond interactions occur

between $O_{\delta 1}$ of Asn228 and the backbone amide of Gly230, and between the backbone oxygen of Thr235 and N_{ε} of Arg236.

The intermolecular loop interactions positioning the GK^{WT} FBP binding loops symmetrically across the tetramer interface are missing in GK^{D72A}. Instead, the GK^{D72A} FBP binding loops are held in unique conformations at the tetramer interface through different intramolecular interaction networks in each monomer (Figure 4.9B). One hydrogen-bond interaction exists in monomer X between $O_{\delta 1}$ of Asn228 and the backbone amide of Gly230. In contrast, the main chain conformation of monomer O is supported through four hydrogen-bond interactions between the backbone oxygen of Asn228 and the backbone amide of Gly230, $N_{\delta 2}$ of Asn228 and the backbone oxygen of Lys232, $O_{\delta 1}$ of Asn228 and N_{ε} of Arg236, and the backbone oxygen of Gly230 and the backbone amide Lys232. The asymmetry in the number of intramolecular loop interactions between the O and X monomers of GK^{D72A} is consistent with the diverging main chain loop conformations in each monomer.

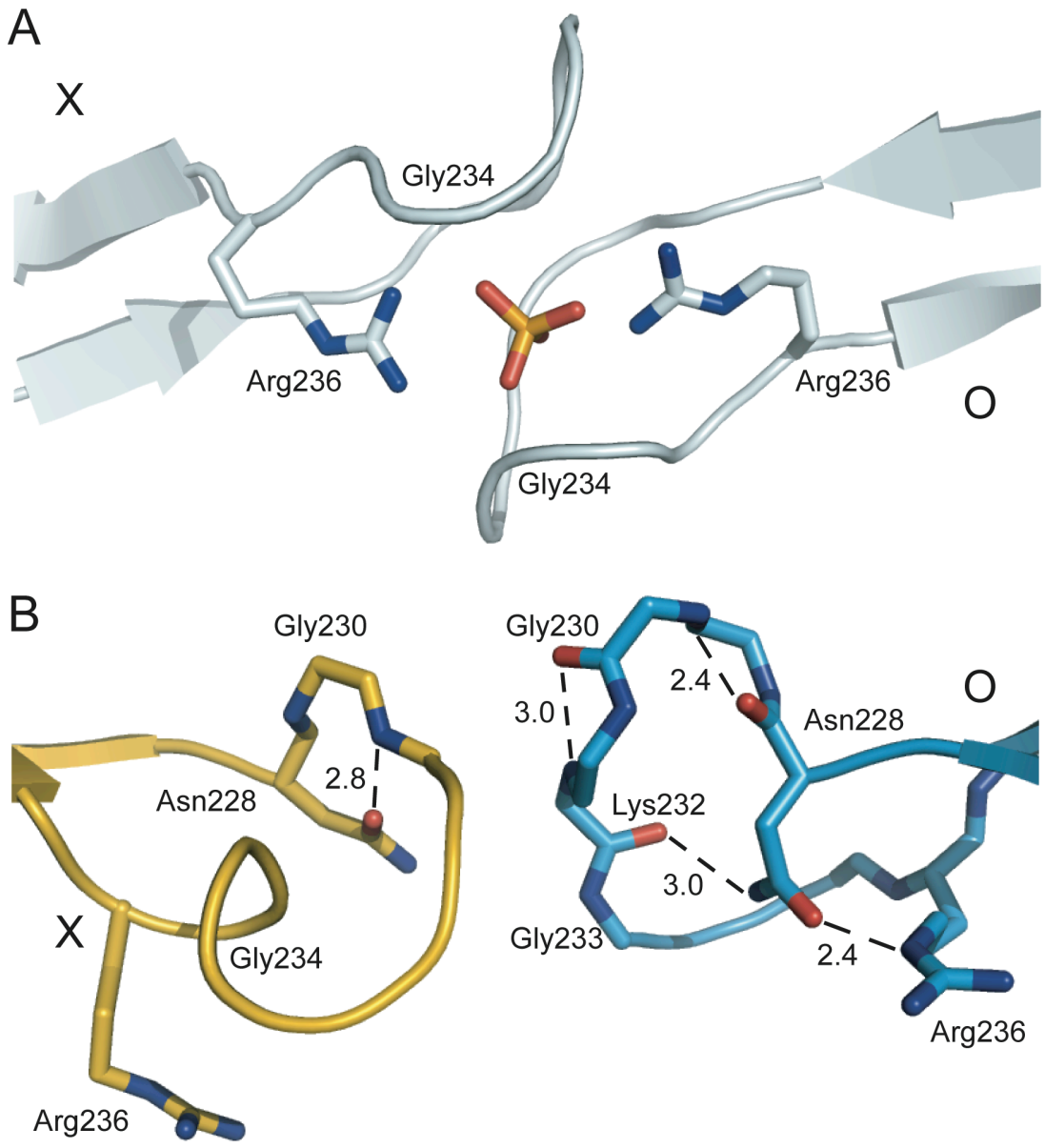

Figure 4.9: GK^{D72A} and GK^{WT} FBP binding sites. (A) GK^{WT} FBP binding site with bound phosphate molecule. Gly234 and Arg236 are centered in the symmetrical FBP binding loops and position the FBP molecule between the two monomers. The orange phosphate molecule binds in the location of the 6-phosphate group of FBP. (B) Intramolecular hydrogen-bonding networks in the GK^{D72A} FBP binding loops. The O monomer has four hydrogen-bond

interactions between Asn228 and Gly230, Asn228 and Lys232, Asn228 and Arg236, and between Gly230 and Lys232. The X monomer has one hydrogen-bond interaction between Asn228 and Gly230.

In GK^{D72A}, residues Gly234 and Arg236 are significantly altered from their wild-type positions and are no longer at the center of the tetramer interface. Arg236 in monomer O is involved in an intramolecular loop interaction that shifts N_{ε} of the side chain 4.4 Å away from the wild-type position in the FBP binding site and towards the outside of the FBP binding loop. The side chain of Arg236 in monomer X is also directed away from the tetramer interface, although this appears to be due in part to a crystal contact with a monomer Z symmetry operator. Furthermore, the C_{α} of Gly234 in monomer X is 6.4 Å from the GK^{WT} position at the tetramer interface. One other disparity in the main chain loop conformations of GK^{D72A} and GK^{WT} monomer O is the position of Gly233; the C_{α} of Gly233 is 4.2 Å from the GK^{WT} position and appears directly in between the 6-phosphate binding site in GK^{WT} and $N_{\eta 2}$ of Arg236 that is responsible for FBP binding. The C_{α} of Gly233 is 1.7 Å from O_1 of the 6-phosphate molecule and 1.2 Å from $N_{\eta 2}$ of Arg236 in GK^{WT}. The appearance of Gly233 in close proximity of the wild-type 6-phosphate binding site is likely to disrupt FBP binding. The combination of conformational changes in the GK^{D72A} FBP binding loops that disrupt the FBP binding site and the intramolecular loop interaction networks sustaining the unique loop conformations correlates well with the decreased FBP inhibition in GK^{D72A}.

Domain Motion of GK Mutants. The physiologically active form of GK^{WT} is a dimer with one monomer in a closed conformation and one monomer in an open conformation. The

GK^{WT} active form was identified using a Ser58 → Trp dimer mutant with glycerol and ATF bound (GK^{S58W}·glyc·ATF) in the active site of each monomer (*38*). The GK^{S58W}·glyc·ATF structure revealed the catalytically competent form of GK^{WT} has a ~ 6° rotation between domains I and II in the closed and open conformations. A second form of GK appeared in the GK^{G230D} structure: the GK^{G230D}·glyc dimers contain a closed conformation and an open conformation monomer with domain rotations of 10 to 18° (*13*). The increased domain motion in the GK^{G230D}·glyc open conformation monomer verified nucleotide triphosphate binding is required to achieve the catalytically competent dimeric form of GK.

Another form of GK is evident in the glycerol-bound GK^{235KGG} and GK^{D72A} (GK^{235KGG}·glyc and GK^{D72A}·glyc) structures. The X and Y monomers of GK^{235KGG}·glyc have a main chain conformation identical to the closed conformation of GK^{WT} and the O and Z monomers have a more open conformation than the GK^{G230D}·glyc open conformation. The GK^{D72A}·glyc monomer conformations are equivalent to the GK^{235KGG}·glyc monomer conformations. As expected, none of the monomers exhibit the wild-type catalytically competent open structure of GK^{S58W}·glyc·ATF, since nucleotide triphosphate is not present in the active sites of GK^{235KGG} and GK^{D72A}. The domain II rotation between the closed and open monomers is 18 to 20° in GK^{235KGG}·glyc and 18 to 19° in GK^{D72A}·glyc (Table 4.2). The increased domain motion in GK^{235KGG}·glyc and GK^{D72A}·glyc reveals a greater degree of conformational flexibility in GK monomers in the absence of bound nucleotide triphosphate than was previously reported (*13*).

Table 4.2: Domain rotation statistics

Mutant	Pair	Rotation Angle	RMSD (Å)
GK^{D72A}	Y - O	19.3	0.7
	X - Z	17.8	0.6
	1BWF[a] - Y	n.d.[b]	
	1BWF - X	n.d.	
	1BWF - O	18.6	0.7
	1BWF - Z	16.8	0.7
GK^{235KGG}	Y - O	17.6	0.8
	X - Z	19.5	0.8
	1BWF - Y	n.d.	
	1BWF - X	n.d.	
	1BWF - O	17.8	0.7
	1BWF - Z	18.4	0.7
GK^{M271I}	Y - O	n.d.	
	X - Z	n.d.	
	1BWF - Y	15.1	0.9
	1BWF - X	15.2	0.8
	1BWF - O	16.9	1.1
	1BWF - Z	13.7	1.1

Domain rotation was determined using the Hingefind algorithm. The automatically determined domains for each mutant agreed with the previously determined domains (*38*). [a] 1BWF monomer Y was used for all calculations. [b] No difference (n.d) in the rotation angles of the pair.

In contrast to both the limited domain motion in GK^{WT} monomers and the considerable domain motion in GK^{235KGG}·glyc monomers, every monomer in the glycerol-bound GK^{M271I} (GK^{M271I}·glyc) structure has an equivalent conformation with no perceptible domain motion. Each GK^{M271I}·glyc monomer exists in an open conformation greater than the GK^{WT} open conformation and similar to the GK^{G230D}·glyc open conformation. A comparison between the GK^{M271I}·glyc monomers and the GK^{WT} closed monomer conformation revealed a domain rotation of 14 to 17° (Table 4.2). The GK^{M271I}·glyc structure is the first demonstration of GK dimers that do not contain at least one monomer in the closed conformation. The Met271 → Ile mutation in the domain II hinge region of GK^{M271I} appears to prevent the wild-type

domain motion in GK^{M271I}·glyc and to obstruct the formation of the GK^{WT} closed conformation.

GK^{M271I} Quaternary Structure. A novel quaternary structure is evident in GK^{M271I} as a result of the exclusively open monomer conformation in GK^{M271I} dimers rather than the open and closed monomer conformations in GK^{WT} dimers. GK^{M271I} is the first structure where the mutation is buried within the monomer and not on the surface of the monomer at either the tetramer interface or the IIA^{Glc} binding site. The Met271 → Ile mutation is located at the beginning of GK^{M271I} domain II on a β-strand (residues 269–276) in the middle of a β-sheet in the domain II hinge region (Figure 4.10). Residue 271 is buried at the base of the domain II region and a large α-helix (residues 373–399) forms the closest contact with the β-sheet containing Ile271.

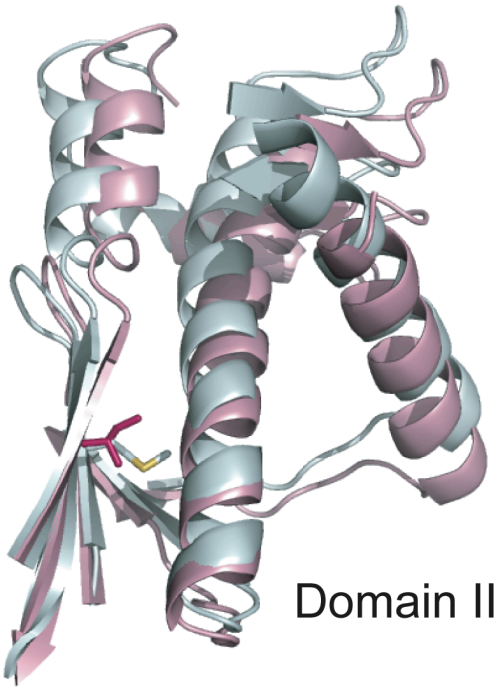

Figure 4.10: Overview of the GK^{M271I} domain II region. Residues 250 to 290 surrounding Met271 in monomer O of GK^{WT} (PDB entry 1GLF) are superpositioned on the corresponding residues in monomer Y of GK^{M271I}. Ile271 is magenta at the base of the domain II hinge region, domain II of GK^{M271I} is pink, and domain II of GK^{WT} is silver.

GK^{WT} contains a cluster of Methionine residues at the base of the domain II region with Met271 on one end of the cluster (Figure 4.11A). Met271 and Met273 are situated on the β-sheet with side chains directed towards the adjacent α-helix, and Met395 is located on the α-helix between Met271 and Met273 with the side chain pointed towards the β-sheet. The sulfur atoms in the Methionine side chains are loosely centered between the β-sheet and the α-helix, forming a line approximately parallel to the secondary structural elements.

Additionally, Leu392 on the α-helix in GK^{WT} is positioned away from the β-sheet owing to the close proximity of the Met271 side chain.

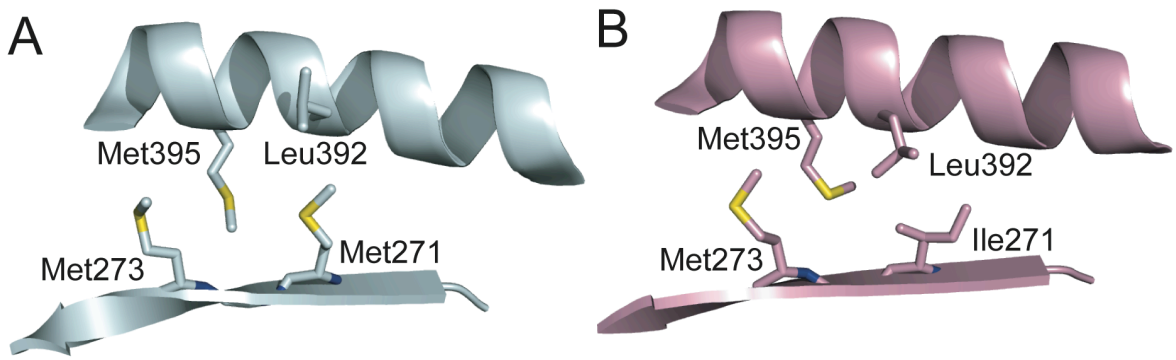

Figure 4.11: Comparison of GK^{M271I} and GK^{WT} Methionine network. (A) GK^{WT} monomer O Methionine network near Met271. Met 271, Met395, and Met273 are aligned between an α-helix and β-strand interface and position Leu392 away from Met271. (B) GK^{M271I} monomer Y altered Methionine network near Ile271. Ile271 is positioned away from Met273 and Met395, allowing Leu392 to reposition in between Ile271 and Met395. Note that the region surrounding Ile271 is similar in all GK^{M271I} monomers.

In GK^{M271I}, the removal of Met271 from the Methionine cluster enables side chain rearrangements and secondary structure shifts at the α-helix and β-sheet interface (Figure 4.11B). The primary alteration in GK^{M271I} is the repositioning of Leu392 into the region previously occupied by Met271. The C_γ of Leu392 is shifted 2.8 Å towards the β-sheet in GK^{M271I} and is only 2.1 Å from the wild-type position of S_δ in Met271. A 1.6 Å rotation in the α-helix at Leu392 is also responsible for directing Leu392 closer to the β-sheet. The repositioning of Leu392 is supported by the relocation of Ile271 away from the center of the

α-helix and β-sheet interface; the $C_{\delta 1}$ of Ile271 in GK^{M271I} is shifted 3.2 Å from S_{δ} in Met271 of GK^{WT}. In contrast to Leu392, Met273 and Met395 are similarly positioned in GK^{WT} and GK^{M271I} with the sulfur atoms still loosely centered between the β-sheet and the α-helix. Overall, the shift in the α-helix to position Leu392 closer to the β-sheet appears to support the GK^{M271I} open monomer conformation, as no other significant structural rearrangements occur in GK^{M271I}.

The Oligomeric State of GK^{D72A}, GK^{235KGG}, and GK^{M271I}. The oligomeric states of GK^{D72A}, GK^{235KGG}, and GK^{M271I} in the presence and absence of FBP were established using light scattering experiments. In the absence of FBP, GK^{D72A}, GK^{235KGG}, and GK^{M271I} exist as dimers in solution. In the presence of FBP, GK^{235KGG} and GK^{M271I} exist as dimers in solution while GK^{D72A} exists as tetramers in solution. For comparison, in the absence of FBP, GK^{WT} exists primarily as a dimer in solution with a small amount of tetramers detectable, and in the presence of FBP, GK^{WT} is transformed completely into tetramers (*13*).

Discussion

High-quality crystals were obtained for GK^{D72A}, GK^{235KGG}, and GK^{M271I} using a microfluidics-based crystallization strategy. An initial solubility characterization for the GK mutants revealed that each of the GK mutants had unique solubility behavior. Given the single point mutations that differentiate the GK samples from each other, it is interesting that the aggregation responses to the same chemicals were so varied for the four samples. In particular, only three residues separate the GK^{G230D} and GK^{235KGG} mutations and both occur within the FBP binding loops, and still the solubility trends varied considerably between the

samples. The most surprising result of the solubility characterization was the bimodal effect of pH on protein solubility: two of the mutants aggregated most frequently at the GK pI and the other two mutants aggregated most often far away from the pI. This result emphasizes the importance of a complete exploration of reagent pH levels for all crystallization samples to find the optimal pH level to drive protein aggregation. The solubility characterization also revealed that the ionic composition of the reagent has a relatively minor effect on protein solubility and might be left as a secondary parameter in the identification of potential crystallization reagents. The diverse results obtained from a complete solubility characterization of closely related protein samples demonstrates the significant effect minor changes can make on protein solubility behavior. Furthermore, these results suggest solubility characterization might be a useful precursor to crystallization in order to design crystallization experiments guaranteed to target the solubility boundary of the crystallization sample.

Crystallization experiments using the unique set of identified reagents for each of the GK mutants produced crystal hits for a large percentage of the reagents screened. The high crystallization success rates for each of the GK mutants allowed for multiple crystal morphologies to be pursued simultaneously in order to identify the crystal form with the highest diffraction limit. The crystallization experiments also revealed slight deviations between the reagents that frequently caused protein aggregation and the reagents that promoted crystal formation. The crystallization results emphasize the importance of exploring all potential crystallization reagents for a target in order to ensure the optimal crystallization condition is discovered. Overall, the customized crystallization strategy for

each GK mutant resulted in high crystallization rates and also allowed for in situ diffraction analysis of the crystals.

GK^{D72A} is the first glycerol kinase structure with a mutation in the short helix bridging the tetramer interface and the FBP binding site and establishes the inherent link between the bridging helix and the FBP binding loop conformation. The removal of the bulky side chain group of Asp72 that is directed towards the FBP binding site in GK^{WT} creates an open pocket of space below the FBP binding loops and enables a greater degree of conformational flexibility in the GK^{D72A} FBP binding loops. As a result, two unique main chain conformations appear in the FBP binding loops that are supported through altered intramolecular interaction networks that replace the wild-type intramolecular and intermolecular FBP loop interaction networks. The altered intramolecular interactions are responsible for repositioning the residues involved in FBP binding away from the tetramer interface and holding the FBP binding loops in conformations that directly interfere with the wild-type FBP binding pocket in order to decrease the FBP inhibition in GK^{D72A}. Therefore, the appearance of novel FBP binding loop conformations in the GK^{D72A} structure reveals the necessity of Asp72 in maintaining the wild-type FBP binding loop conformations and the integrity of the FBP binding site.

Notably, light scattering experiments investigating the oligomeric state of GK^{D72A} showed GK^{D72A} exists as a dimer in solution in contrast to the tetramer form of the enzyme in the crystal structure. This is not the first example of a tetramer structure resulting from a GK dimer solution and is most likely due to the high concentrations of GK required for

crystallization. Thus, the FBP binding loop conformations in the GK^{D72A} structure probably represent one of the multiple interactions that occur between dimers in solution. A second round of light scattering experiments confirmed the GK^{D72A} dimers are converted into tetramers in the presence of FBP, mimicking the wild-type response to FBP. The ability of GK^{D72A} dimers to form tetramers in the presence of FBP was unexpected due to the decreased FBP inhibition of GK^{D72A} compared to GK^{WT}. Additional structural studies of GK^{D72A} in the presence of FBP are needed to reconcile the existence of an inactive FBP-bound tetramer form of GK^{D72A} given the structural rearrangements in the FBP binding loops that disrupt the FBP binding site in the current GK^{D72A} structure.

The decreased FBP inhibition in GK^{235KGG} and GK^{M271I} is more apparent based on the resistance of both mutants to tetramer formation in the presence and absence of FBP. The inability of FBP to convert the GK^{235KGG} dimers into tetramers is in agreement with the primarily dimeric form of another GK FBP binding site mutant GK^{G230D} in the presence of FBP. The increased length of the FBP binding loops in GK^{235KGG} could enhance the flexibility of the FBP binding loops and prevent the formation of an ordered FBP binding site, thereby decreasing the FBP inhibition. The GK^{235KGG} dimers also exhibit a larger degree of domain motion in the presence of bound glycerol and in the absence of bound nucleotide than has been previously observed for any GK variant. The increased domain motion in the GK^{235KGG} monomers in the absence of bound nucleotide corresponds with the earlier hypothesis of nucleotide binding being the rate-limiting step in creating the catalytically competent form of GK.

A novel quaternary form of glycerol kinase was identified in the GK^{M271I} structure where every monomer exists in an open conformation. The inherent asymmetry of the wild-type GK dimers with one closed conformation monomer and one open conformation monomer is lost in the GK^{M271I} dimers. Furthermore, the open conformation exhibited in every GK^{M271I} monomer demonstrates a larger degree of domain motion when compared to the GK^{WT} open conformation, although the domain motion is less than the GK^{235KGG} open conformation. The GK^{M271I} monomers are each held in the open conformation due to the Ile271 mutation in the hinge region that obstructs the normal domain motion between domains I and II. The inflexible nature of the GK^{M271I} monomer conformation could also be responsible for preventing the GK^{M271I} dimers from forming tetramers in the presence of FBP and thus reducing FBP inhibition.

In conclusion, the GK^{D72A}, GK^{235KGG}, and GK^{M271I} crystal structures provide an overview of several mutations that evolved in glycerol kinase as a result of the selection pressure of *E. coli* growth on glycerol. The GK^{D72A} structure revealed novel FBP binding loop conformations supported by altered intramolecular interaction networks. The novel FBP binding loops in GK^{D72A} in turn disrupt the wild-type FBP binding site. The monomers in the GK^{235KGG} structure displayed an increased range of monomer conformations compared to previous structures. Also, the resistance of GK^{235KGG} and GK^{M271I} dimers to tetramer formation in the presence of FBP explains the decreased FBP inhibition compared to wild-type GK. Lastly, a novel quaternary structure consisting exclusively of open conformation monomers was revealed in the GK^{M271I} structure.

Chapter 5

MICROFLUIDIC DIALYSIS DEVICE FOR MEMBRANE PROTEIN CRYSTALLIZATION

Introduction

High-resolution structure determination for integral membrane proteins remains a challenging task for crystallographers owing to the difficulty of producing well-ordered membrane protein crystals. While approximately 30% of the proteins encoded by an organism's genome are integral membrane proteins (*70, 71*), less than 2% of the structures in the RCSB Protein Data Bank are membrane proteins (*72*). Integral membrane proteins are involved in several fundamental biological processes including the active transport of ions and metabolites across membranes, forming junctions between cells, and are responsible for the non-selective permeability of membranes to small molecules. Integral membrane proteins are also of great therapeutic interest for the biotechnology industry and comprise the majority of current drug targets (*73, 74*). The first three-dimensional membrane protein crystals were obtained for bacteriorhodopsin and matrix porin in 1980 (*75, 76*) and laid the foundation for the field of membrane protein crystallography.

The amphiphilic nature of membrane proteins requires the use of amphipathic detergents for the isolation, purification, and crystallization of membrane proteins (*77, 78*). The hydrophobic tails of detergent monomers coalesce around the hydrophobic core of membrane proteins to form a micelle belt, replacing the native lipid bilayer and leaving only the

hydrophilic regions of the membrane proteins exposed to the aqueous solution. Crystallization experiments with protein-detergent micelles can produce either two-dimensional or three-dimensional crystals (Figure 5.1). Two-dimensional crystals involve hydrophobic interactions between the hydrophobic surfaces of membrane proteins to form thin sheet crystals for electron microscopy experiments (*79*). Alternatively, three-dimensional crystals are supported largely through hydrophilic interactions and are used for X-ray diffraction experiments (*80*). Type I three-dimensional crystals consist of stacked two-dimensional crystals held together through hydrophilic contacts between membrane proteins in different sheets. Type II three-dimensional crystals involve hydrophilic interactions between the polar regions of the membrane proteins and detergent micelle interactions. The type II crystals are similar to soluble protein crystals and most membrane protein structures are generated from type II crystals (*81*).

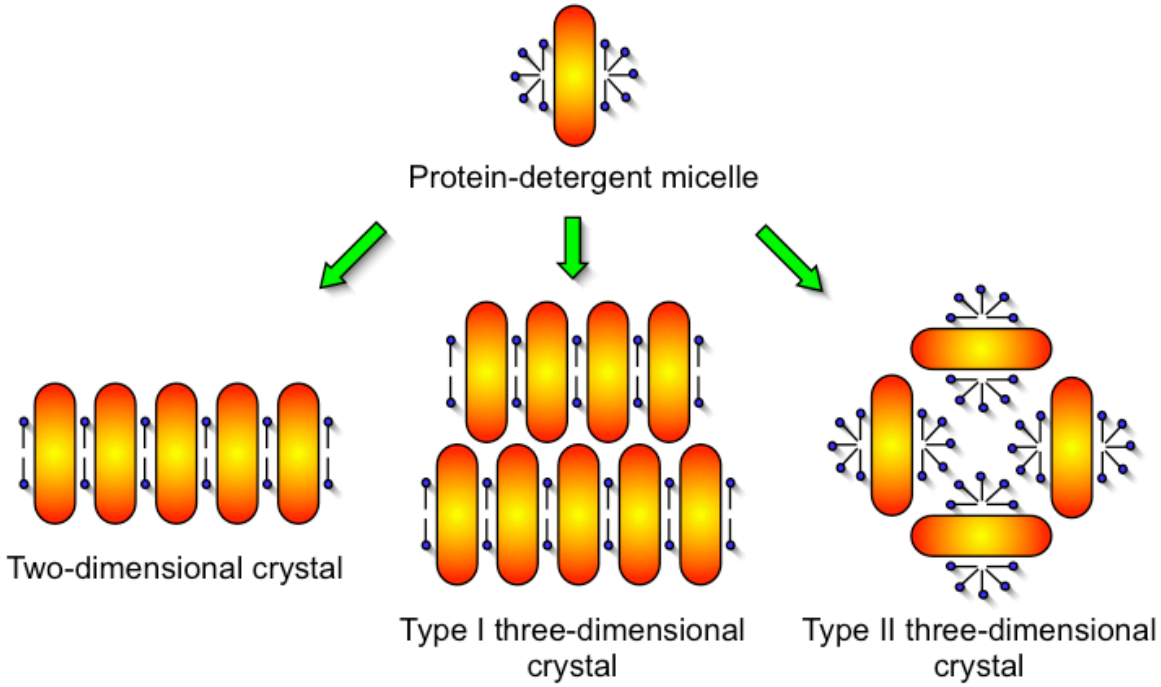

Figure 5.1: Crystallization of protein-detergent micelle solutions. Protein-detergent micelles can form three types of crystals: two-dimensional sheet crystals, type I three-dimensional stacked sheet crystals, and type II three-dimensional crystals. The hydrophobic core of the membrane protein is yellow and the hydrophilic ends are red. The blue detergent monomers interact with the hydrophobic region of the protein. Figure was adapted from (*82*).

Although protein-detergent micelle solutions can be crystallized, the removal of membrane proteins from their native lipid environments may not be the best strategy for membrane crystallization. The lipid bilayer was shown to be critical for maintaining membrane protein structure and activity (*83, 84*), and the physical forces exerted on a protein molecule in a detergent micelle are different than in a phospholipid bilayer. As a result, a number of crystallization methods were developed to crystallize membrane proteins in a lipid environment that more closely resembles the native membrane. The in cubo crystallization method involves embedding membrane proteins in a three-dimensional lipid cubic phase bilayer and adding precipitating agents to promote crystallization (*85*). A second method entails the formation of three-dimensional crystals by driving vesicle fusion of bacteriorhodopsin membranes with small amounts of detergent and precipitating agents (*86*). Lastly, a bicelle crystallization method involves mixing membrane proteins with a lipid-amphiphile mixture and adding precipitants to form three-dimensional bicelle crystals (*81*). While these methods have been used successfully to determine structures for bacterial membrane proteins (*87–105*), the more general utilization of these methods for challenging membrane protein targets has not been realized. Therefore, a crystallization platform enabling the use of a broader range of detergent-solubilized membrane protein samples in

lipid crystallization experiments would have great utility for membrane protein crystallization.

A microfluidic dialysis device for membrane protein crystallization is presented that was designed to perform multiple crystallization experiments in a lipid environment using detergent-solubilized membrane protein samples. The microfluidic device incorporates a dialysis platform for the removal of detergent monomers from protein-detergent-lipid solutions with a free interface diffusion crystallization platform. Dialysis is an ideal technique for the removal of detergents from protein-detergent-lipid solutions since detergent monomers are free to diffuse across the dialysis membrane, whereas phospholipids are trapped in lipid bilayers and are not involved in the dialysis experiment. Dialysis experiments are currently used to remove excess detergent monomers from detergent-solubilized membrane protein samples for two-dimensional crystallization experiments (*79*). The dialysis platform alleviates any restrictions on detergent use for sample preparation, since the detergent monomers will be subsequently removed, and broadens the range of membrane protein targets available for lipid crystallization experiments.

A detergent-solubilized *Streptomyces lividans* KcsA potassium channel is used to demonstrate the utility of the microfluidic dialysis device for membrane protein crystallization. Previous structural and functional analysis of the KcsA potassium channel established phospholipids are required for the correct folding and activity of KcsA (*106*), making KcsA an ideal sample for crystallization experiments in a lipid environment. A modified lipid cubic phase crystallization strategy and a bicelle crystallization strategy were

designed and implemented for the KcsA channel to explore the full capabilities of the microfluidic dialysis device.

Experimental Procedures

Device Fabrication and Experimental Setup. The microfluidic dialysis device for membrane protein crystallization was fabricated using multilayer soft lithography (*7*) and a detailed fabrication protocol is presented in Appendix A. The dialysis membrane used within each device is a single sheet of dry cellulose membrane (Spectra/Por 132680, 12–14 kDa molecular weight cutoff, 20 μm thick) of dimensions 5.22 x 1.90 cm. The fabrication protocol for the control version of the dialysis device without dialysis membrane is also presented in Appendix A.

The experimental setup for the dialysis devices began by filling each of the dialysis reservoirs with 150 μl of dialysis reagent and waiting five minutes to prime the dialysis membrane. Next, the interface control line and the containment control lines were primed with Poly(3,3,3-trifluoropropylmethylsiloxan) (FMS) oil (Hampton Research) and the interface control line was actuated at 20 psi. Once all of the interface valves were closed, gel loading tips with 6 μl of crystallization reagent and 6 μl of protein sample were inserted into opposite sides of the device and pressurized to 5 psi to load the solutions onto the device. When all of the chambers were finished dead-end filling, the containment control lines were actuated at 20 psi. Finally, the pressure on the interface control line was released and each of the free interface diffusion experiments was initiated. Dialysis devices were incubated at

room temperature for up to two weeks and cryoprotectant can be introduced by diffusion through the dialysis reservoirs an hour before crystal harvesting.

Protein Preparation. The *Streptomyces lividans* KcsA detergent-solubilized protein sample was provided by Roderick MacKinnon at Rockefeller University. The KcsA sample was stored at 1.6 mg/ml in storage buffer at 4 °C (150 mM potassium chloride, 20 mM Tris·HCl (pH 7.5), and 10 mM n-decyl-β-D-maltoside (DM)). The KcsA dialysis buffer used in the dialysis devices was the storage buffer without detergent (150 mM potassium chloride, 20 mM Tris·HCl (pH 7.5)). The KcsA sample was used at 1.6 mg/ml for bicelle preparation, vesicle preparation, and for the initial crystallization experiments performed in the absence of lipids. A portion of the sample was concentrated to 8 mg/ml using a microcentrifuge device with a 10 kDa molecular weight cutoff for additional crystallization experiments.

Bicelle Preparation. A 1,2-dimyristoyl-*sn*-glycero-3-phosphocholine/3-[(Cholamidopropyl)dimethylammonio]-1-propane-sulfonate (DMPC/CHAPS) lipid/detergent bicelle solution was prepared as previously reported with minor modifications (*81*). Briefly, a 40% 3:1 (DMPC:CHAPS) molar ratio bicelle mixture was created by combining 30 mg of room temperature DMPC and 10 mg of CHAPS in 100 μl of water and mixing on ice. Next, the bicelle mixture was combined with KcsA at a 4:1 (KcsA:bicelle) volume ratio and mixed on ice to create the protein/bicelle mixture. The final bicelle preparation contained a 1.3 mg/ml KcsA (with 8 mM DM)/8% bicelle mixture. The bicelle preparation was stored at 4 °C to keep the solution in liquid form for crystallization experiments. DMPC powder was purchased from Avanti Polar Lipids and CHAPS powder was purchased from Anatrace.

Vesicle Preparation. DMPC vesicle preparation was modified from a previously reported method (*107*). The DMPC vesicles were prepared by mixing 4 mg of room temperature DMPC in 200 μl of KcsA storage buffer without detergent (150 mM potassium chloride, 20 mM Tris·HCl (pH 7.5)). The lipid solution was sonicated for one hour in 20-minute increments until the solution became clear. Next, the lipid vesicle mixture was combined with KcsA at a 20:1 (KcsA:vesicle) volume ratio and sonicated for an additional 10 minutes. The final vesicle preparation contained a 1.5 mg/ml KcsA (with 9.5 mM DM)/1 mg/ml vesicle mixture. The vesicle preparation was stored at 4 °C for crystallization experiments.

Crystallization Experiments. Initial crystallization experiments were performed using nanoliter volume microfluidic free interface diffusion screening devices as previously described (*4, 12*). The crystallization experiments were designed around the previously reported crystallization conditions for KcsA-Fab complex structures (*108–110*). The initial crystallization screen was implemented with four samples: KcsA at 1.6 mg/ml, KcsA at 8 mg/ml, KcsA bicelle preparation at 1.3 mg/ml, and the KcsA vesicle preparation at 1.5 mg/ml. All crystallization experiments were performed at room temperature for up to two weeks. The optimal crystallization conditions for each sample were transported to microfluidic scale-up diffraction devices for diffraction analysis (*6*). The crystallization conditions were subsequently transported to the microfluidic dialysis device. Crystals grown in the dialysis device can be harvested for in situ diffraction analysis as previously described for a microfluidic scale-up diffraction device (*6*).

Diffraction Analysis. Diffraction data for KcsA was collected at station 8.3.1 of the Advanced Light Source (Lawrence Berkeley National Laboratory), at an incident wavelength of 1.0 Å with a 30 second exposure and 1º oscillation. All diffraction data was collected at room temperature from crystals within scale-up diffraction devices.

Crystallization Results

Design of Microfluidic Dialysis Device. The microfluidic dialysis device for membrane protein crystallization simultaneously performs large-scale free interface diffusion crystallization experiments and dialysis experiments for detergent removal. The free interface diffusion design in the dialysis device was modified from a microfluidic scale-up diffraction device that was successfully used for in situ structure determination of novel proteins (*6, 13*). Each dialysis device performs 25 unique free interface diffusion experiments utilizing one crystallization reagent and one protein sample. The dialysis device contains five individually addressable dialysis reservoirs (labeled A–E) and each dialysis reservoir covers five free interface diffusion experiments (Figure 5.2). The protein:reagent chamber ratios used in the five experiments are 3:1, 3:2, 1:1, 2:3, and 1:3, with a total reaction volume of 180 nl per free interface diffusion experiment. The free interface diffusion path length between the protein and reagent chambers varies in each of the dialysis reservoirs, ranging from 0.7 cm in reservoir A to 0.5 cm in reservoir E. The multiple chamber ratios and path lengths in each dialysis device allow for a systematic investigation of parameters to determine which combination promotes optimal crystal growth for each reagent. Additional versions of the dialysis device were designed utilizing one of the five protein:reagent chamber ratios and multiple free interface diffusion path lengths to allow for

detailed dialysis reagent screening. The development of a successful fabrication procedure for the dialysis device is presented below in the Dialysis Device Fabrication Results section.

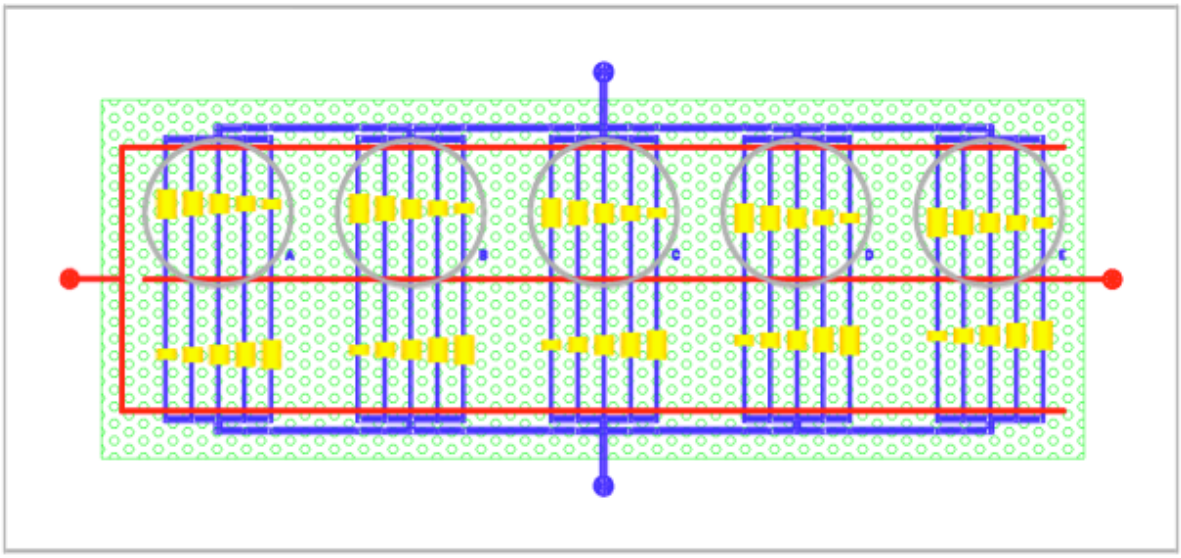

Figure 5.2: Microfluidic dialysis device for membrane protein crystallization. The gold protein and reagent chambers are at the top and bottom of the device, respectively, and are connected by the blue flow channels. The red interface control line is in the center of the device and the red containment control lines are at the top and bottom of the device. The green dialysis membrane is incorporated over the functional features of the device, and the grey circular dialysis reservoirs are centered over the protein chambers. Notice that all of the input connections are outside of the membrane border to prevent membrane tearing when punching the input ports during device assembly.

Initial Crystallization Experiments. A series of positive control crystallization experiments were initially performed in the dialysis device using two crystallization targets previously

crystallized with microfluidic devices (*6, 13*). Since the crystallization targets were soluble samples, no detergent was present in either sample to dialyze out of solution and the sample storage buffers were used for dialysis reagents. A large rhombohedral lysozyme crystal appeared after one day in the dialysis device and crystal growth continued for several days in the presence of the dialysis reagent (Figure 5.3A–B). Additionally, GK^{G230D} cubic crystals formed in the dialysis device after three days (Figure 5.3C). The crystallization reagent used to produce the cubic crystals for GK^{G230D} in the dialysis device was the same reagent that produced a large rhombohedral crystal in the scale-up diffraction device (see Figure 3.4B for comparison). The initial crystallization experiments demonstrate the dialysis devices can be successfully used for protein crystallization in the presence of a dialysis reagent.

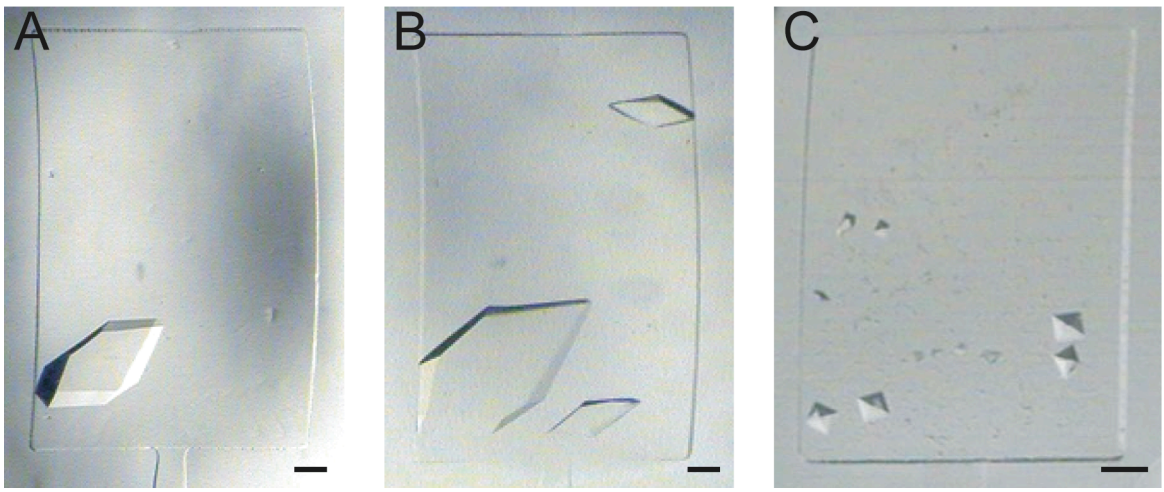

Figure 5.3: Dialysis device validation crystallization experiments. (A) Lysozyme rhombohedral crystal grown in 0.6 M sodium chloride and 100 mM sodium acetate (pH 4.5) after one day of dialysis. The lysozyme was used at 165 mg/ml in storage buffer (100 mM sodium acetate (pH 4.5)) and the dialysis reagent used in the crystallization experiment was

the lysozyme storage buffer. (B) The same lysozyme crystallization experiment after five days of dialysis. (C) GK^{G230D} cubic crystals grown in 300 mM magnesium chloride, 100 mM Tris·HCl (pH 8.5), and 20% PEG 1500. GK^{G230D} was used at 30 mg/ml in standard buffer (20 mM Tris·HCl (pH 7.5), 10 mM glycerol, and 1 mM βME). The dialysis reagent used in the crystallization experiment was the GK^{G230D} standard buffer. The scale bars represent 200 μm.

Crystallization Strategy for KcsA. A crystallization strategy for the detergent-solubilized KcsA potassium channel sample was developed to incorporate the dialysis device for membrane protein crystallization into the existing microfluidics-based crystallization platform. Four distinct KcsA samples were utilized in the crystallization strategy: 1.6 mg/ml detergent-solubilized KcsA in the absence of lipids, 8 mg/ml detergent-solubilized KcsA in the absence of lipids, a KcsA bicelle mixture, and a KcsA vesicle mixture. The detergent-solubilized KcsA samples were used to investigate the combined effects of free interface diffusion crystallization experiments and removal of excess detergent through dialysis on membrane protein crystallization. The KcsA bicelle mixture was used to test the utility of detergent removal from a protein bicelle solution to promote bicelle crystallization. Lastly, the KcsA vesicle mixture was used to investigate whether detergent removal from a protein vesicle solution induces lipid cubic phase crystallization.

To begin, the KcsA samples were screened using microfluidic free interface diffusion screening devices to identify the optimal crystallization reagents for each sample (*4, 12*). The 1.6 mg/ml KcsA sample formed hexagonal crystals with numerous crystallization

reagents in the screening device (Figure 5.4A). Similar crystallization reagents also produced hexagonal crystals from the 8 mg/ml KcsA sample (Figure 5.4B). In general, the hexagonal crystals formed using the 8 mg/ml KcsA sample were larger than the hexagonal crystals grown using the 1.6 mg/ml KcsA sample. The KcsA bicelle mixture formed small crystals in the presence of multiple crystallization reagents (Figure 5.4C), none of which compared to the hexagonal crystals grown in the absence of bicelles. On the other hand, several successful crystallization reagents were identified for the KcsA vesicle mixture. The KcsA vesicle mixture formed large well-defined hexagonal crystals with one crystallization reagent (Figure 5.4D) and cubic crystals with two additional crystallization reagents (Figure 5.4E–F). Overall, crystallization reagents were identified for each of the KcsA samples using the microfluidic screening devices and the best crystal hits were observed for the KcsA vesicle mixture.

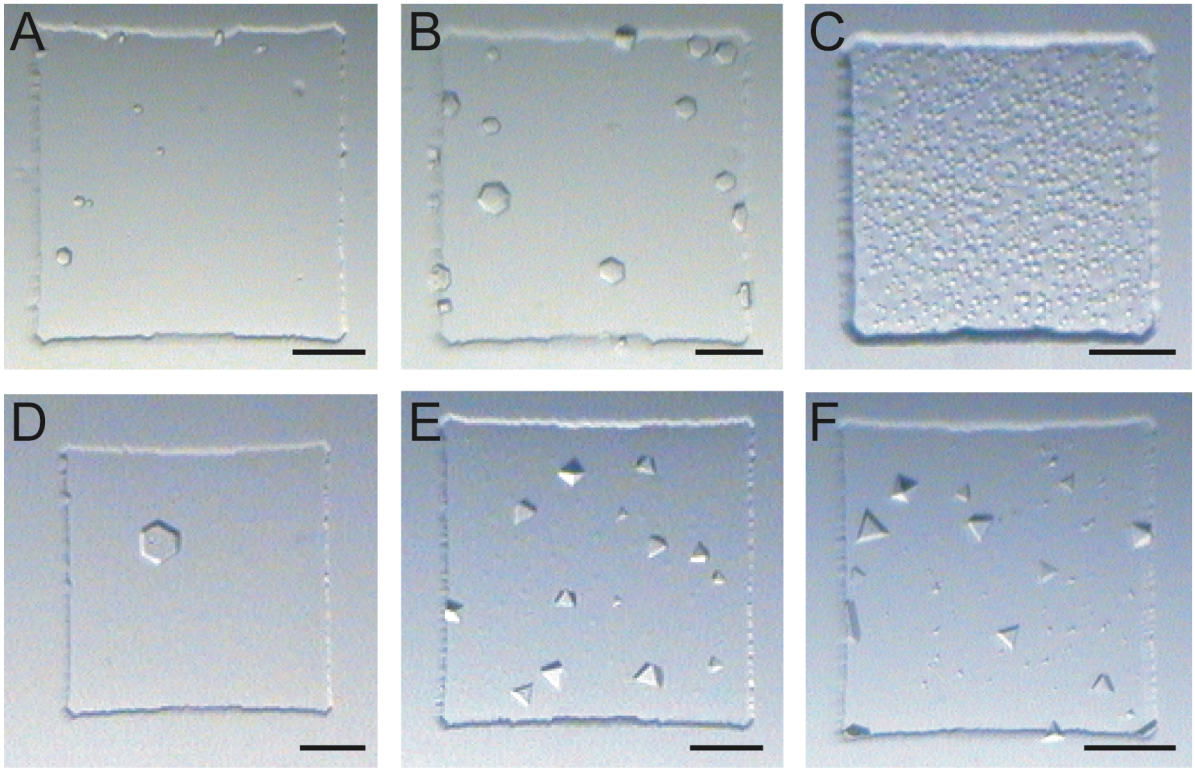

Figure 5.4: KcsA crystals in free interface diffusion screening devices. (A) KcsA hexagonal crystals grown in 150 mM calcium chloride, 100 mM Hepes (pH 7.5), and 52% PEG 400. KcsA was used at 1.6 mg/ml in storage buffer. (B) KcsA hexagonal crystals grown in 200 mM calcium chloride, 100 mM Hepes (pH 7.5), and 50% PEG 400. KcsA was used at 8 mg/ml in storage buffer. (C) KcsA bicelle crystals grown in 50 mM magnesium acetate, 100 mM sodium acetate (pH 5.4), and 21% PEG 400. (D) KcsA vesicle hexagonal crystal grown in 50 mM magnesium acetate, 100 mM sodium acetate (pH 5.2), and 24% PEG 400. (E) KcsA vesicle cubic crystals grown in 50 mM magnesium acetate, 100 mM sodium acetate (pH 5.4), and 18% PEG 400. (F) KcsA vesicle cubic crystals grown in 50 mM magnesium acetate, 100 mM sodium acetate (pH 5.4), and 24% PEG 400. The scale bars represent 100 μm.

The best crystallization reagents for each KcsA sample were transported to two larger format free interface diffusion crystallization devices. The first larger format crystallization device is a control version of the dialysis device where the dialysis membrane is replaced with a solid layer of PDMS elastomer. Crystallization experiments were performed in the control version of the dialysis device to observe the scaled-up free interface diffusion crystallization results in the absence of dialysis and to observe the best mixing ratios for crystal formation. The 1.6 mg/ml KcsA sample formed rhombohedral crystals with two crystallization reagents (Figure 5.5A–B). A combination of hexagonal and cubic crystals also formed with a third crystallization reagent (Figure 5.5C–D). The KcsA vesicle sample formed rhombohedral crystals of various sizes with multiple crystallization conditions (Figure 5.5E–G). The KcsA bicelle sample did not crystallize in the larger format crystallization devices. This was not surprising since a previous crystallization survey demonstrated the translation of crystal hits to larger formats depends upon the crystal quality achieved in the smaller format experiments (*12*).

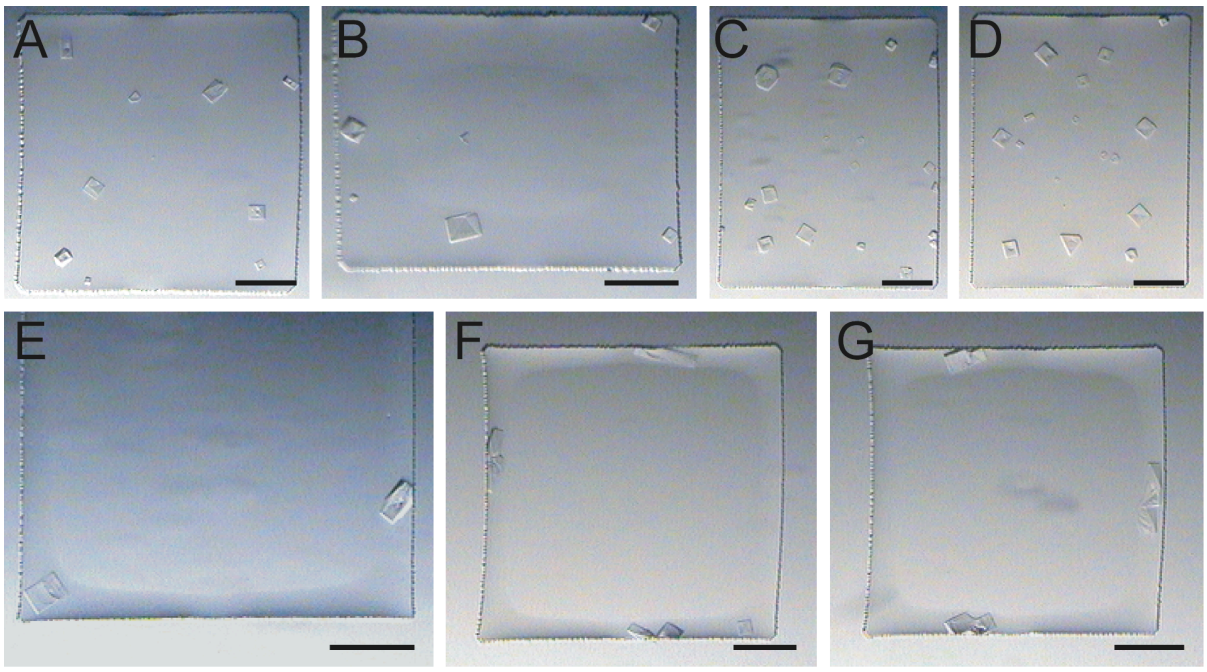

Figure 5.5: Larger format KcsA crystallization experiments. A control version of the dialysis device without dialysis membrane was used for the larger format crystallization experiments. (A) KcsA rhombohedral crystals grown in 250 mM calcium chloride, 100 mM Hepes (pH 7.5), and 44% PEG 400. KcsA was used at 1.6 mg/ml in storage buffer. (B) KcsA rhombohedral crystals grown in 50 mM magnesium acetate, 100 mM sodium acetate (pH 5.6), and 26% PEG 400. KcsA was used at 1.6 mg/ml in storage buffer. (C–D) KcsA hexagonal and cubic crystals grown in 150 mM calcium chloride, 100 mM Hepes (pH 7.5), and 52% PEG 400. KcsA was used at 1.6 mg/ml in storage buffer. (E) KcsA vesicle rhombohedral crystals grown in 50 mM magnesium acetate, 100 mM sodium acetate (pH 5.4), and 22% PEG 400. (F–G) KcsA vesicle rhombohedral crystals grown in 50 mM magnesium acetate, 100 mM sodium acetate (pH 5.2), and 20% PEG 400. The scale bars represent 200 μm.

Diffraction Analysis. The crystallization conditions were also transported to scale-up diffraction devices for diffraction analysis of the crystal hits for different KcsA samples (*6*). The 1.6 mg/ml KcsA sample formed rhombohedral crystals of dimensions 100 μm x 100 μm x 100 μm with multiple reagents. The 8 mg/ml KcsA sample also formed rhombohedral crystals of dimensions 100 μm x 100 μm x 150 μm. Numerous crystals grown from the 1.6 mg/ml and 8 mg/ml KcsA samples were screened and no diffraction patterns were observed for any of the crystals. All diffraction data collection was done at room temperature to avoid altering the diffraction resolution of the crystals by using cryoprotectants. Since the initial KcsA structures were produced using a truncated KcsA sample and a KcsA-Fab complex (*108–110*), the diffraction limit of the full-length KcsA sample alone has not been established. The KcsA vesicle sample formed cubic crystals of dimensions 150 μm x 150 μm x 150 μm that diffracted to 17 Å (Figure 5.6). The appearance of a diffraction pattern for the lipid vesicle sample demonstrates that the lipid cubic phase crystallization technique improves the crystal quality for KcsA compared to crystals grown using detergent-solubilized KcsA in the absence of lipids.

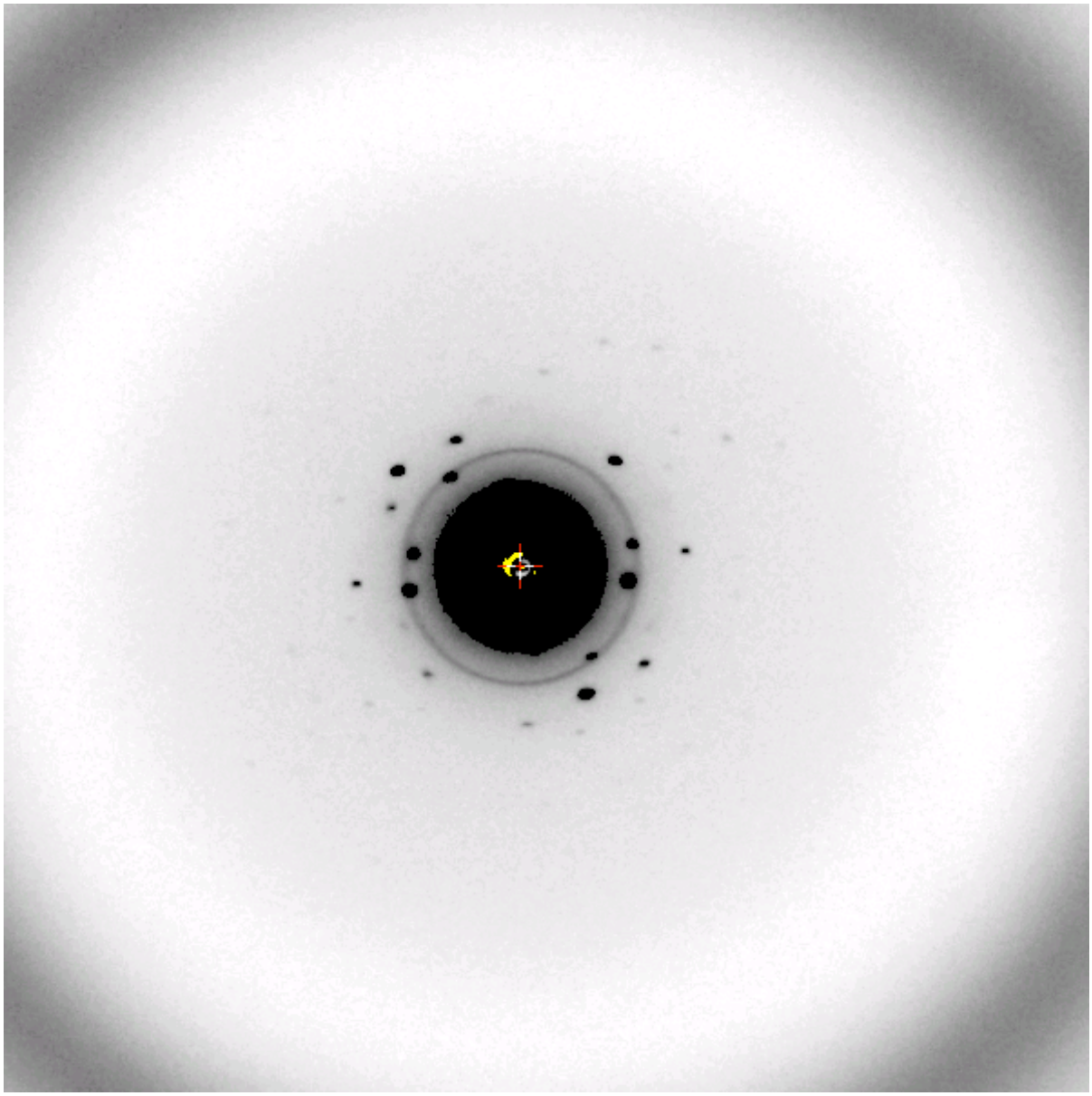

Figure 5.6: In situ diffraction analysis of larger format crystals. The KcsA vesicle crystal was grown in 50 mM magnesium acetate, 100 mM sodium citrate, and 18% PEG 400. A 150 μm x 150 μm x 150 μm cubic crystal diffracted to 17 Å.

Finally, the KcsA samples were transported to the dialysis device for crystallization. The 1.6 mg/ml KcsA sample formed microcrystals when a dialysis reagent composed of a 1:1

mixture of the KcsA dialysis buffer and the crystallization reagent was used for the dialysis experiment (Figure 5.7A). Parallel experiments using only KcsA dialysis buffer for the dialysis reagent did not produce any crystals. Decreasing the concentration of precipitating agent in the crystallization condition eliminated the microcrystals and instead produced a small crystal surrounded by light protein aggregation (Figure 5.7B). Once again, the crystal only formed when a 1:1 mixture of KcsA dialysis buffer and crystallization reagent was used for the dialysis reagent. Alternatively, the 1.6 mg/ml KcsA sample formed a larger crystal with a third crystallization reagent when KcsA dialysis buffer was used for the dialysis reagent (Figure 5.7C). The same crystallization experiment with the 8 mg/ml KcsA sample also produced crystals (Figure 5.7D).

Several dialysis devices were assembled with the KcsA vesicle sample and the KcsA bicelle sample, and crystals were produced using the KcsA vesicle sample. The KcsA vesicle sample formed single crystals with multiple crystallization reagents when the KcsA dialysis buffer was used for the dialysis reagent (Figure 5.7E–G). For reference, the KcsA vesicle crystals shown in Figure 5.7F–G were grown using the same condition as the lipid-free KcsA crystals in Figure 5.7C–D. The inability of the KcsA bicelle sample to crystallize in the dialysis devices was expected since the no crystals formed in the larger format control devices. The crystallization results for the KcsA samples are summarized in Table 5.1.

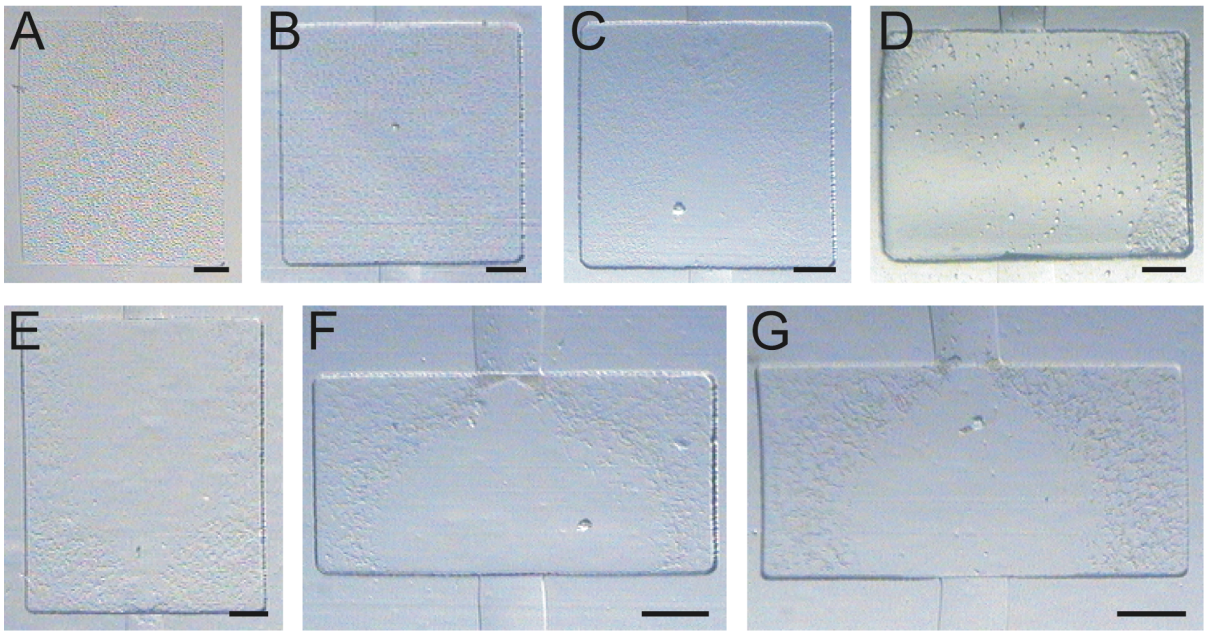

Figure 5.7: KcsA crystals in dialysis devices. (A) KcsA microcrystals grown in 50 mM magnesium acetate, 100 mM sodium acetate (pH 5.6), and 26% PEG 400. KcsA was used at 1.6 mg/ml. (B) KcsA crystal grown in 50 mM magnesium acetate, 100 mM sodium acetate (pH 5.0), and 20% PEG 400. KcsA was used at 1.6 mg/ml. (C) KcsA crystal grown in 250 mM calcium chloride, 100 mM Hepes (pH 7.5), and 44% PEG 400. KcsA was used at 1.6 mg/ml. (D) KcsA crystals grown in the same reagent as in (C) and KcsA was used at 8 mg/ml. (E) KcsA vesicle crystals grown in 50 mM magnesium acetate, 100 mM sodium acetate (pH 5.0), and 23% PEG 400. (F–G) KcsA vesicle crystals grown in the same reagent as in (C) and (D). The dialysis reagent used for (A) and (B) was a 1:1 mixture of the KcsA dialysis buffer (150 mM potassium chloride and 20 mM Tris·HCl (pH 7.5)) and the corresponding crystallization reagent. The dialysis reagent used for (C–G) was the KcsA dialysis. The scale bars represent 200 μm.

Table 5.1: KcsA crystallization results

	Experiment	Sample	Crystals	Diffraction
1.	Screening device	KcsA no lipids—1.6 mg/ml	Hexagonal crystals	Not tested
		KcsA no lipids—8 mg/ml	Hexagonal crystals	Not tested
		KcsA bicelles	Microcrystals	Not tested
		KcsA vesicles	Hexagonal and cubic crystals	Not tested
2.	Scale-up diffraction device	KcsA no lipids—1.6 mg/ml	Rhombohedral crystals	No
		KcsA no lipids—8 mg/ml	Rhombohedral crystals	No
		KcsA bicelles	No	
		KcsA vesicles	Cubic crystals	17 Å
3.	Control dialysis device	KcsA no lipids—1.6 mg/ml	Rhombohedral crystals	Not tested
		KcsA vesicles	Rhombohedral crystals	Not tested
		KcsA bicelles	No	
4.	Dialysis device	KcsA no lipids—1.6 mg/ml	Small crystal	Not tested
		KcsA no lipids—8 mg/ml	Small crystal	Not tested
		KcsA bicelles	Microcrystals	Not tested
		KcsA vesicles	Small crystal	Not tested

Comparison of the crystallization results in the larger format crystallization devices and in the dialysis device demonstrate that crystal quality is affected by the incorporation of the dialysis platform into the free interface diffusion crystallization experiment. When the crystallization reagent diffuses across the free interface diffusion channel into the protein reaction chamber two processes can occur: the reagent can diffuse into the protein solution to initiate crystal nucleation, and the reagent can diffuse across the dialysis membrane into the dialysis reservoir. Since the crystallization reagent is composed of small molecules with radii on the order of 1 Å and the dialysis membrane has a molecular weight cutoff of 12 kDa, the pores in the dialysis membrane are so large that the small molecules are essentially free to immediately diffuse into the dialysis reservoir. The diffusion of the small molecules into the dialysis reservoir is problematic since it occurs at a faster rate than crystal nucleation: by the Stokes-Einstein equation, small molecules with 1 Å radius have a diffusion constant on the

order of 1000 $\mu m^2/s$ in water (*111*), whereas crystal nucleation occurs on the order of minutes to hours. Additionally, the volumetric difference between the dialysis reservoir and the crystallization chamber is problematic; the 150 μm dialysis reservoir is 1600 times as large as the 90 nl crystallization chamber volume. Thus, equilibration of the crystallization reagents across the dialysis membrane causes over a thousandfold dilution of the crystallization reagent and essentially removes the reagent from the free interface diffusion experiment.

The successful crystallization experiments using 50% crystallization reagent in the dialysis reservoir overcame the volumetric difference by reducing the dilution of crystallization reagent during equilibration down to twofold, leaving half of the crystallization reagent in the reaction chamber for crystal nucleation. Therefore, the most straightforward solution to improve crystal growth in the dialysis device would be to increase the amount of crystallization reagent in the dialysis reservoir to completely eliminate the dialysis of the crystallization reagent from the free interface diffusion experiment. Additionally, the dialysis reservoir could be sealed with a layer of FMS oil at the beginning of the free interface diffusion experiment to allow crystal nucleation to initiate before replacing the oil with dialysis reagent for detergent removal.

Overall, the crystallization strategy for KcsA was successfully implemented to produce KcsA crystals in a lipid cubic phase environment. The lipid cubic phase crystallization method was a more successful crystallization method in the dialysis devices than the bicelle crystallization strategy. Future experiments to optimize the dialysis reagent composition

could improve the size and quality of the KcsA lipid cubic crystals grown in the dialysis device.

Dialysis Device Fabrication Results

The procedure for constructing the dialysis device is outlined below. All of the fabrication challenges encountered during device fabrication are discussed in detail.

Membrane Integration in the Dialysis Device. A dialysis membrane forms the interface between the free interface diffusion crystallization chambers and the large dialysis reservoirs in the dialysis device. Incorporation of the dialysis membrane within the device requires complete bonding between the cellulose dialysis membrane and the elastomeric polydimethylsiloxane (PDMS) material of the device. If not, leaking will occur between the two materials when fluids are introduced into the device. Two techniques are currently used for membrane bonding to PDMS: placing a membrane between two oxygen plasma-treated layers of PDMS for irreversible bonding (*112, 113*), and a stamping procedure using a thin layer of uncured PDMS prepolymer to adhesively bond a piece of membrane between two layers of PDMS (*114*).

Initial attempts at membrane incorporation using oxygen plasma-treatment were unsuccessful in the dialysis device due to the 20 μm thickness of the membrane. When a membrane section is placed between two layers of PDMS an air pocket forms around the border of the membrane to accommodate the membrane thickness. Plasma-treatment of the device minimizes but does not eliminate the air pocket around the membrane border. Consequently,

the membrane edges are not completely bonded to the PDMS in plasma treated devices and fluid leaks around the membrane border into the air pocket when the devices are loaded. The previous plasma treatment procedure used 6 μm thick nanoporous membrane (*115*), less than one third as thick as the membrane required for dialysis experiments in the dialysis device. One possible solution for the incomplete bonding would be to incorporate a section of membrane with the same dimensions as the dialysis device to eliminate any membrane border within the device. Unfortunately, this solution was not viable since the punching process to create the input/output (I/O) fluid ports in the completed device caused membrane tearing. Therefore, I/O port punching in the dialysis device requires that the membrane is completely encompassed within the device and plasma-treatment does not appear to be the optimal technique for dialysis membrane integration in the device.

The stamping technique for adhesive membrane bonding was subsequently examined and a modified stamping procedure was developed for the dialysis device. The stamping procedure involves stamping each of the following components in a thin layer of PDMS prepolymer: the dialysis reservoir PDMS layer, the crystallization experiment PDMS layer (crystallization chamber side down), and the four edges of the dialysis membrane (see Figure 2 in (*114*) and Figure 5.9E for details). Once all of the components are covered in a thin film of prepolymer, the membrane is placed on the stamped side of dialysis reservoir layer and the stamped side of the crystallization experiment layer is aligned on top of the membrane, completely encapsulating the dialysis membrane within the device. The prepolymer acts like glue between the PDMS layers and the membrane, and the prepolymer is fully incorporated into the device when the assembled device is cured. The prepolymer also forms a leakage-

free barrier around the membrane edge, thereby eliminating the air pocket around the membrane border that appeared during plasma-treatment membrane incorporation.

The major modification to the stamping procedure for the dialysis device membrane integration was the composition and production of the PDMS prepolymer layers. The original stamping procedure involved diluting uncured PDMS prepolymer with different ratios of toluene solvent and spinning each mixture onto a glass slide at a uniform speed to achieve different prepolymer thicknesses (*114*). While this method was effectively used to produce prepolymer films as thin as 1 μm, toluene is a volatile and hazardous solvent that is difficult to work with and requires all stamping procedures and subsequent device fabrication steps be performed inside a fume hood. Alternatively, pure PDMS prepolymer was used in the dialysis device stamping procedure and a range of prepolymer thicknesses were created by spinning prepolymer onto silicon wafers using different spin speeds. A complete characterization of PDMS thicknesses across a range of spin speeds verified PDMS prepolymer films as thin as 2 μm were attainable using maximal spin speeds (Figure 5.8).

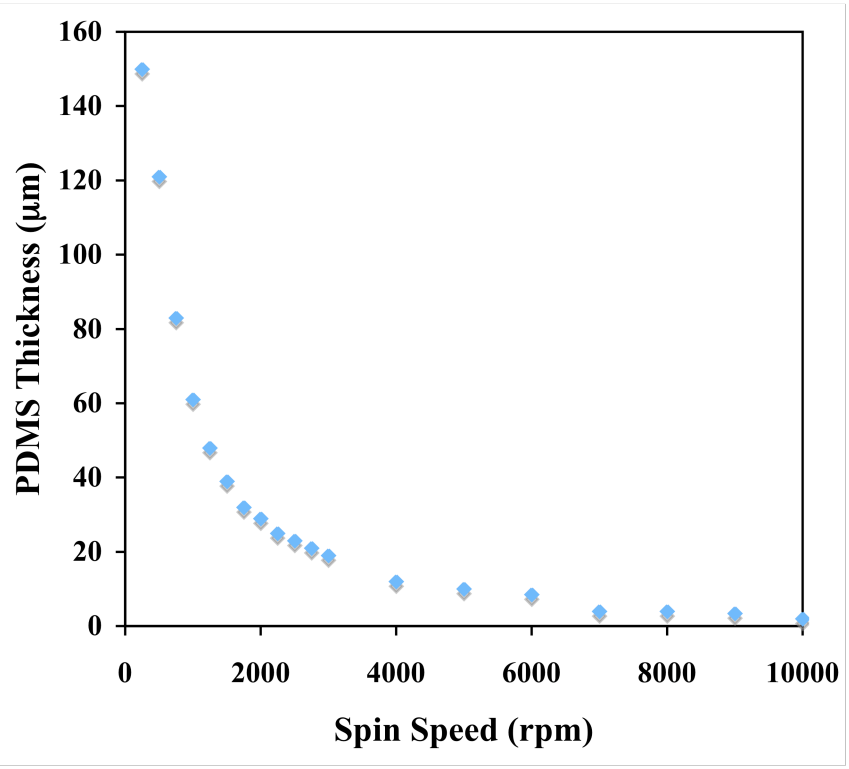

Figure 5.8: Plot of PDMS elastomer thickness versus spin speed. For all spin speeds, PDMS elastomer (General Electrics RTV 615; 10 parts A: 1 part B) was spun onto a blank silicon wafer for 60 seconds and cured at 80 °C for three hours to completely cure the polymer. Film thicknesses were measured using a profilometer after a small section of the cured polymer was removed from each silicon wafer with a scalpel.

It is critical to use the correct prepolymer thickness in the stamping procedure to avoid damaging the free interface diffusion crystallization channel and chamber features. If the prepolymer layer is too thick, the 22 μm high rounded channels and the 95 μm high chambers in the stamped layer are filled with prepolymer and disappear during the stamping procedure. A systematic investigation of stamping procedures with different prepolymer

thicknesses confirmed a 2 μm prepolymer thickness was optimal for complete membrane bonding and maintaining feature integrity between the crystallization experiment layer and the dialysis membrane. Alternatively, the dialysis reservoir layer does not contain any micron-scale features and a 10 μm prepolymer thickness was optimal for complete membrane bonding to the dialysis reservoir layer. The 10 μm prepolymer thickness was also used to stamp the edges of the dialysis membrane. Overall, a total of 12 μm of prepolymer material was integrated around the membrane within the dialysis device for complete membrane bonding.

Functional Valve Incorporation in the Dialysis Device. The incorporation of functional control valves into the dialysis device requires the use of push down valve geometry to allow the free interface diffusion device features to directly contact the dialysis membrane (Figure 5.9A). Push up control valves placed below the dialysis membrane and the flow channels do not actuate due to the stiffness of the membrane material situated in between the control valves and the flow channels. The primary challenge with the push down valve geometry is placing the control valves in close enough proximity to the flow channels given the 95 μm height of the crystallization chambers. When a thin layer of PDMS is spun onto the flow layer, the height of the crystallization chambers creates a gap in between the flow channels and the control valves and prevents bonding between the layers (Figure 5.9B). The gap between the control valves and the flow layer is alleviated if the uncured flow layer is permitted to relax onto the flow mold until the PDMS becomes level with the crystallization chambers (Figure 5.9C). The level flow layer is then bonded to the control layer to create a free interface diffusion device with integrated push down control valves (Figure 5.9D). The

stamping procedure for membrane integration is applied to the free interface diffusion device and the reservoir layer to complete the dialysis device (Figure 5.9E–F).

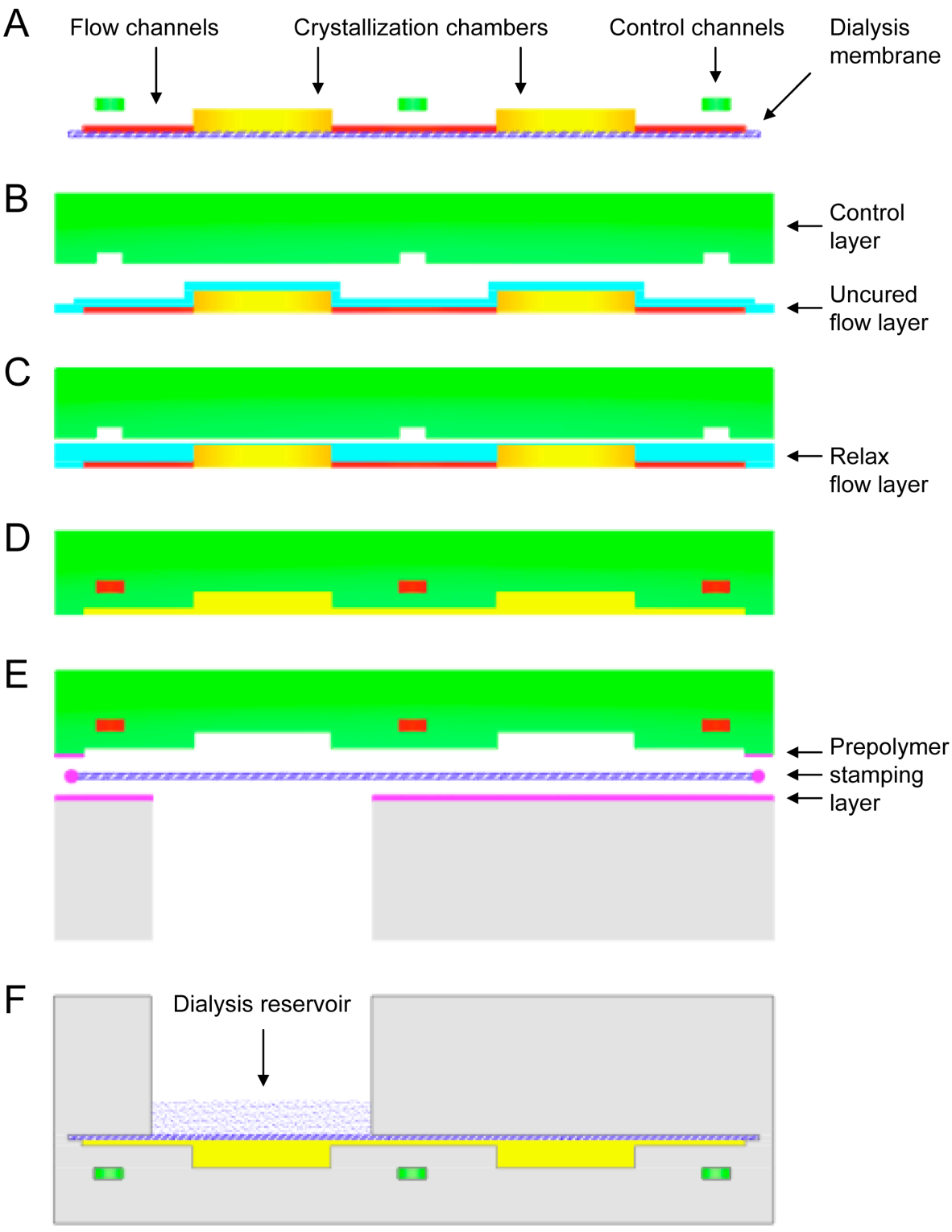
A
Flow channels
Crystallization chambers
Control channels
Dialysis membrane
B
Control layer
Uncured flow layer
C
Relax flow layer
D
E
Prepolymer
stamping
layer
F
Dialysis reservoir

Figure 5.9: Overview of dialysis device assembly. (A) Cross section of the dialysis device features. The green push down control valves are located above the red flow channels and are level with the top of the gold crystallization chambers. The blue dialysis membrane is located below the flow and control features and forms the lower boundary of the flow channels and the crystallization chambers. (B) Problematic push down valve incorporation. Spinning PDMS onto the 95 μm tall crystallization chambers creates a large gap between the flow channels and the control valves. (C) Solution for valve incorporation. The gap between the control valves and the flow channels is minimized by allowing the uncured PDMS to relax on the flow layer until the PDMS is level with the crystallization chambers. (D) Device with functional push down control valves. (E) Stamping method for dialysis membrane integration within the device. The reservoir layer, the flow layer, and the membrane edges are stamped in a thin layer of prepolymer and carefully combined with the membrane in the center. (F) Completed device with integrated dialysis membrane. Note that the completed device is inverted to place the dialysis reservoirs on the top of the device. See Appendix A for the detailed fabrication protocol.

Dialysis Device Validation. The assembly procedure outlined in Figure 5.8 was successfully implemented to construct dialysis devices for membrane protein crystallization (Figure 5.10). All components of the dialysis devices were critically examined before any crystallization experiments were undertaken. First, membrane integrity within the dialysis device was investigated (Figure 5.11A). The dialysis reservoirs were filled with water for two hours to verify the membrane was completely bonded to the device and does not detach from the device during dialysis. The slight membrane distortion over the flow chambers is the normal

result of exposing dialysis membrane to fluid and confirms the flow layer stamping did not affect the integrity of the membrane. As expected, the membrane distortion only occurs in areas of the device where the membrane did not come into contact with the prepolymer adhesion layer during the stamping procedure. Next, sample loading into crystallization chambers primed with a dialysis reagent was explored (Figure 5.11B). The chambers were loaded using dead-end filling and no leaking occurred between the flow layer features and the incorporated dialysis membrane boundary in the chambers.

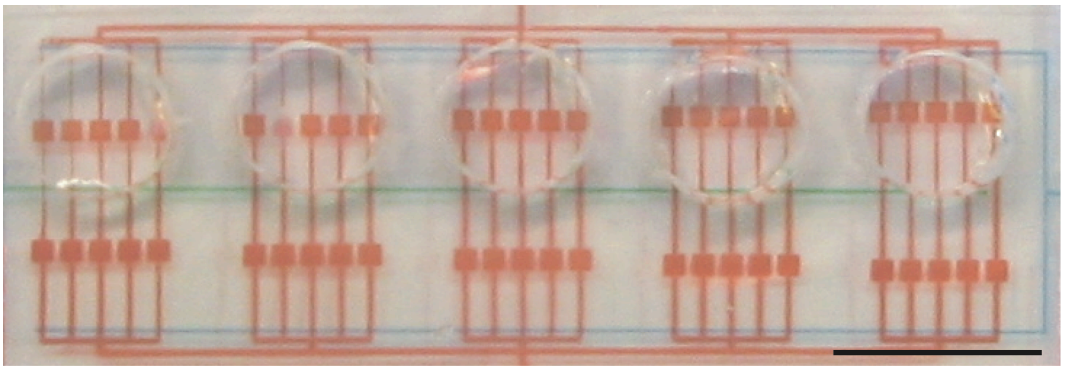

Figure 5.10: Successful membrane integration in the dialysis device. A dialysis device is loaded with red dye in the protein and reagent lines, green dye in the interface control line, and blue dye in the containment lines. The dialysis reservoirs are filled with water. The scale bar represents 1 cm.

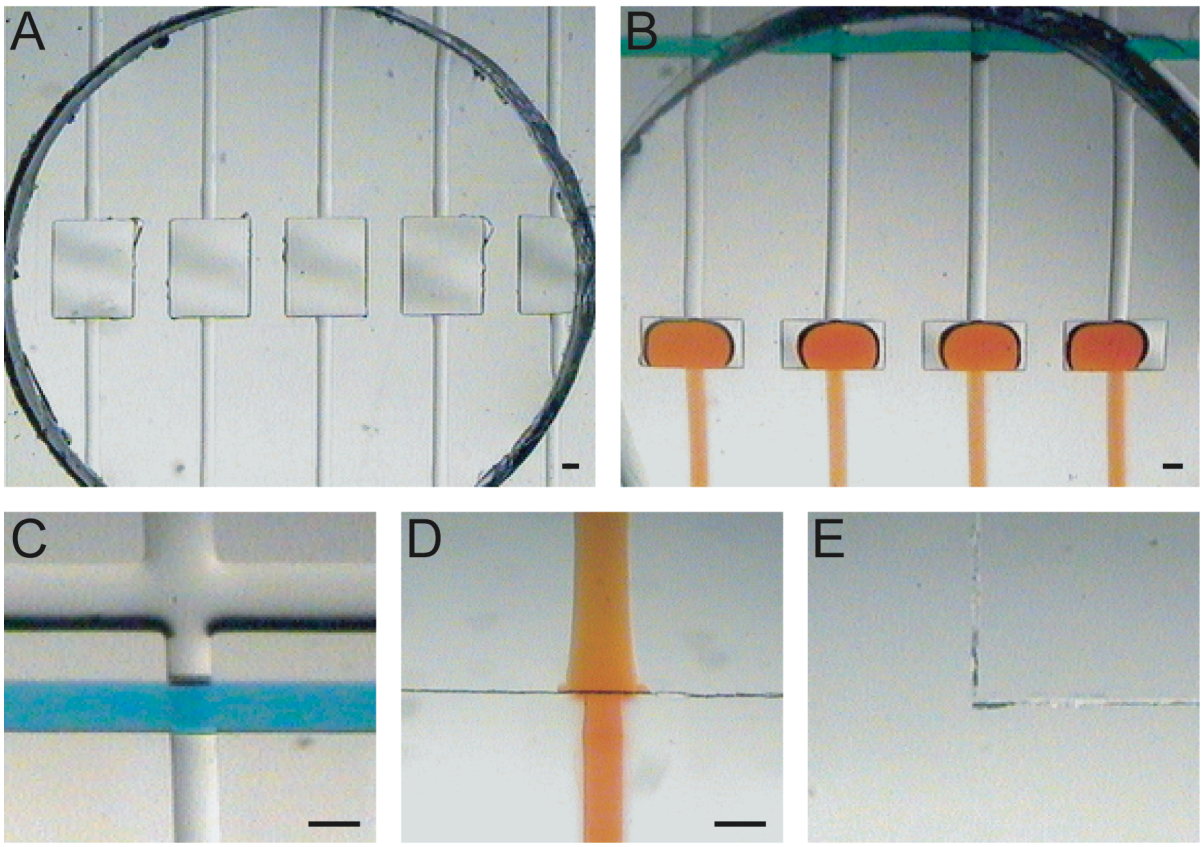

Figure 5.11: Validation of the dialysis device features. (A) Membrane integrity during dialysis. Prolonged exposure to water in the dialysis reservoir does not cause the membrane to detach from the dialysis device. (B) Dead-end filling of crystallization chambers. The dialysis membrane was primed with water for five minutes before loading red dye into the flow channels at 5 psi. (C) Push down valve actuation. The containment line was filled with blue dye and actuated at 20 psi to close the flow channel. (D) Intact flow channels at the membrane border. The flow channels are intact after the stamping procedure and no leakage occurred at the membrane border when the flow channel was loaded with red dye. (E) Seamless integration of the dialysis membrane within the dialysis device. The scale bars represent 200 μm.

Push down valve actuation was also tested to ensure the control valves were functional in the device (Figure 5.11C). Actuation of the containment control line completely sealed off the crystallization reagent inlet from the rest of the device. The use of the dialysis membrane to form one of the walls in the flow channel does not appear to affect valve actuation in the dialysis device. Next, fluid flow across the membrane border during device loading was examined (Figure 5.11D). The protein sample and crystallization reagent inlet ports are located outside of the membrane border, requiring the flow channels to cross the membrane border during loading. Fluid was introduced into the device through the protein sample inlet port and the fluid traveled across the intact flow channel at the membrane border without leaking. Lastly, the membrane integration within the dialysis device was examined at the membrane border and no air pockets were evident (Figure 5.11E). The membrane border was seamlessly integrated into the device as a result of the membrane edge stamping during device assembly. Overall, every component in the device was functional and the dialysis device is ready for crystallization experiments.

In conclusion, a dialysis device for membrane protein crystallization was designed and constructed for the utilization of lipid bilayer environments in membrane protein crystallization experiments. The dialysis device successfully integrated a cellulose membrane into an elastomeric device and is the first demonstration of valve incorporation into a device with an integrated membrane. The dialysis device allows for the exploration of novel membrane protein crystallization techniques to incorporate lipids into detergent-solubilized membrane protein samples during crystallization. The dialysis device was

extensively characterized and validation experiments using KcsA potassium channels and lipid vesicles produced protein crystals in a lipid cubic phase environment.

Appendix A

FABRICATION PROTOCOLS

Dialysis Device Design

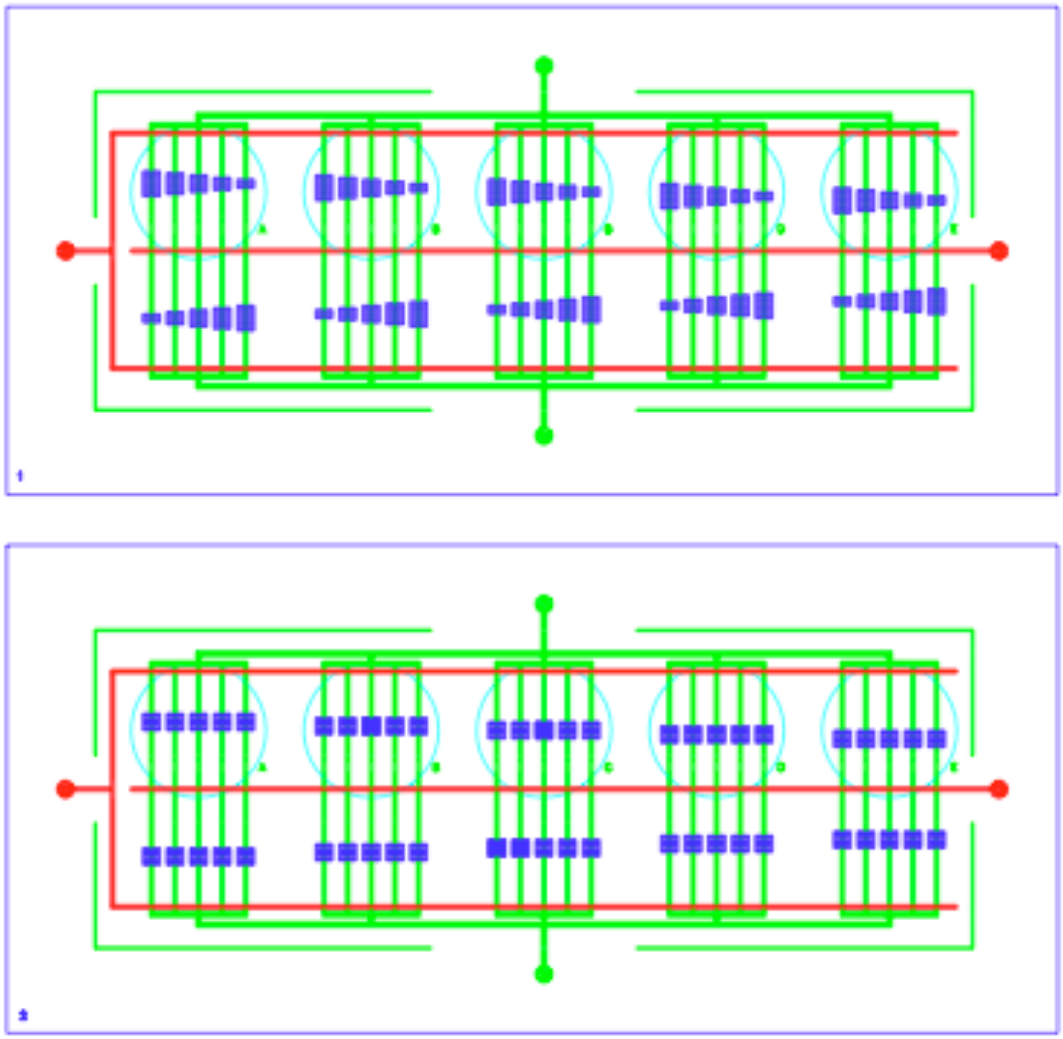

Figure A.1: Assembled dialysis device. Two versions of the dialysis device are shown with different protein:reagent chamber ratios and different free interface diffusion path lengths.

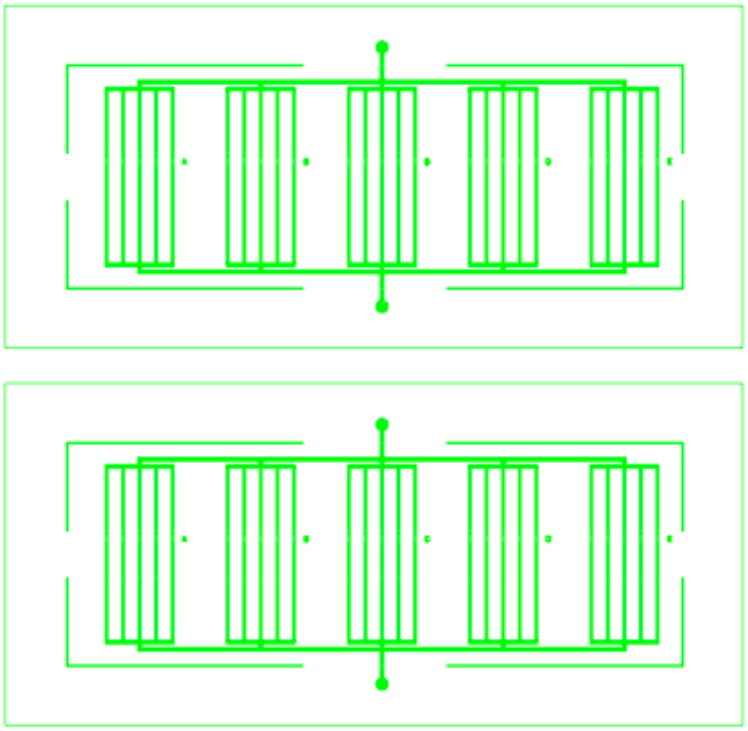

Figure A.2: Dialysis device rounded channel flow layer mask

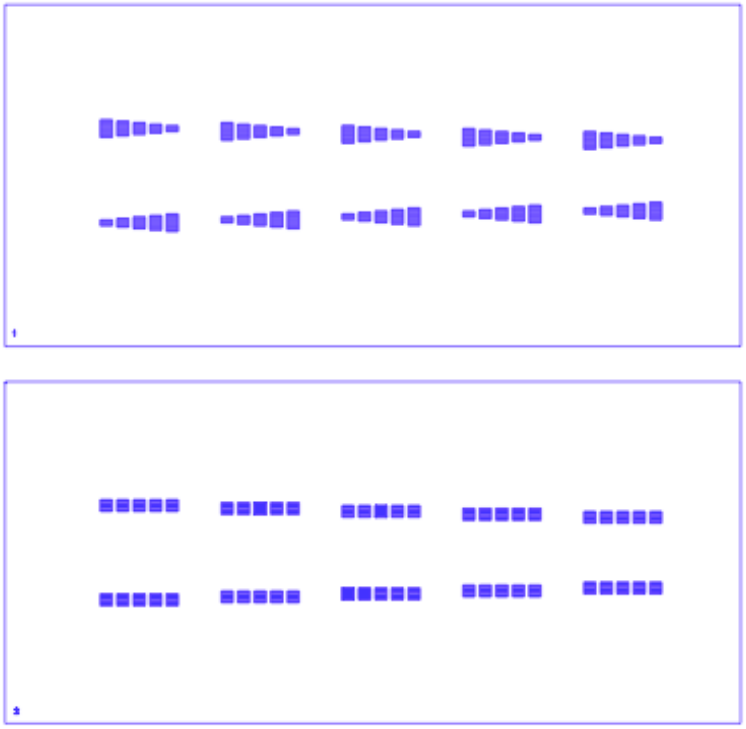

Figure A.3: Dialysis device chamber flow layer mask

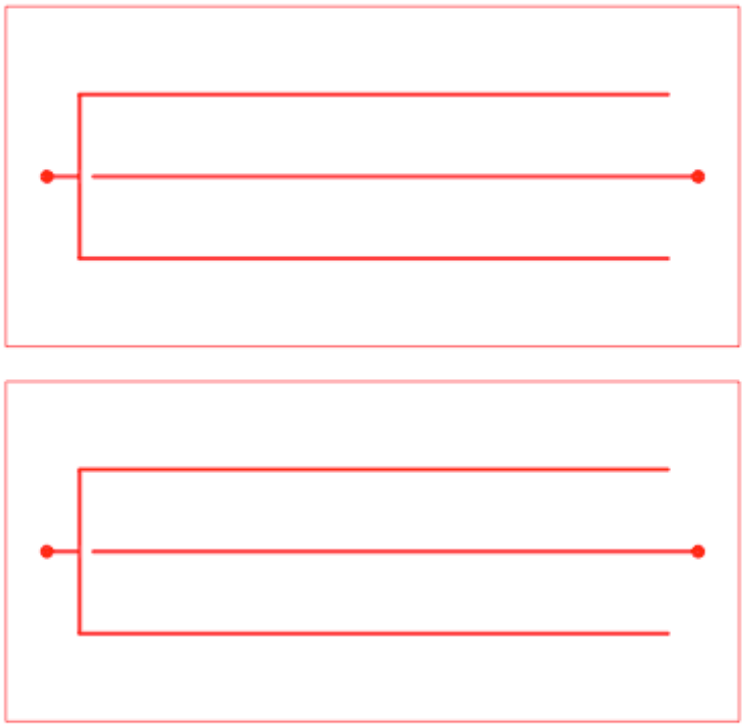

Figure A.4: Dialysis device control layer mask

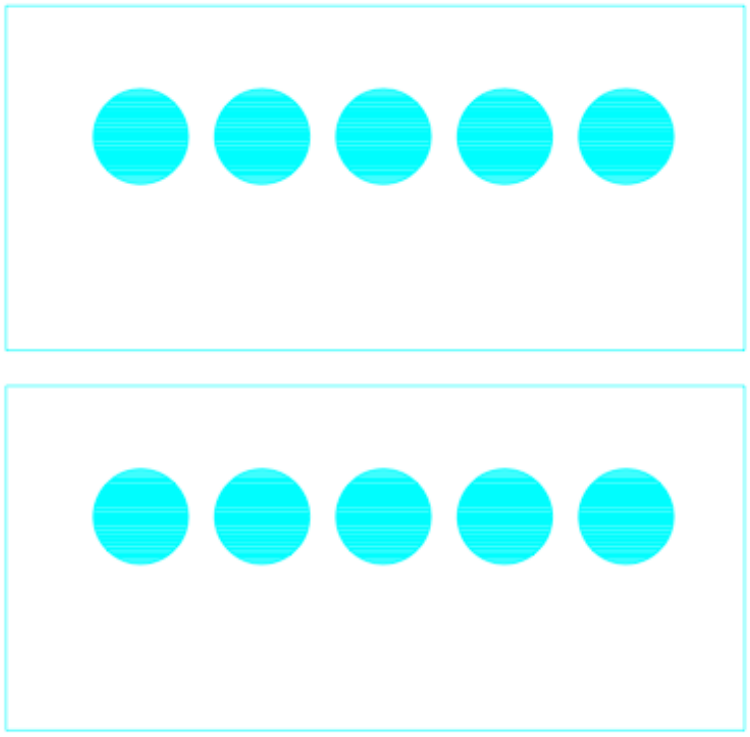

Figure A.5: Dialysis device reservoir layer mask

Dialysis Device: Mold Fabrication
4 inch silicon wafer substrate

I. Flow Mold—Rounded Channels

a. Clean Wafers:	Rinse with acetone, isopropanol, and dry.
b. Prime Wafers:	2 min hexamethyldisilazane (HMDS) vapor treatment
c. Spin SPR 220-7:	500 rpm for 75 sec, 136 rpm/sec ramp Film thickness = 22 μm
d. Pre-Exposure Bake:	2 min 65 °C / 5 min 115 °C / 2 min 65 °C
e. Expose Wafer:	75 sec at 8 mW/cm^2 Karl Suss aligner, soft contact mode, 250 μm gap
f. Develop:	5 min in MF-319 Developer (Microposit) Rinse with H_20 and dry.
g. Hard Bake:	Ramp from 65 °C to 200 °C. Bake for 60 min at 200 °C. Ramp down to 65 °C.

Flow Mold—Chambers

a. Spin SU8-100:	500 rpm for 20 sec, 136 rpm/sec ramp 3000 rpm for 55 sec, 136 rpm/sec ramp Let sit for 10 min. Film thickness = 95 μm
b. Pre-Exposure Bake:	10 min 65 °C / 30 min 95 °C / 2 min 65 °C
c. Expose Wafer:	65 sec at 8 mW/cm^2 Karl Suss aligner, soft contact mode, 250 μm gap
d. Post-Exposure Bake:	5 min 65 °C / 25 min 95 °C / 2 min 65 °C
e. Develop:	2 min in SU-8 Developer (Microchem) Rinse with acetone, isopropanol, and dry.
f. Hard Bake:	Bake for 60 min at 150 °C.

II. Control Mold

a. Clean Wafers:	Rinse with acetone, isopropanol, and dry.
b. Spin SU8-50:	500 rpm for 20 sec, 136 rpm/sec ramp 2500 rpm for 55 sec, 136 rpm/sec ramp Let sit for 5 min. Film thickness = 45 μm
c. Pre-Exposure Bake:	6 min 65 °C / 15 min 95 °C / 2 min 65 °C
d. Expose Wafer:	45 sec at 8 mW/cm^2 Karl Suss aligner, soft contact mode, 250 μm gap
e. Post-Exposure Bake:	5 min 65 °C / 15 min 95 °C / 2 min 65 °C
f. Develop:	2 min in SU-8 Developer Rinse with acetone, isopropanol, and dry.
g. Hard Bake:	Bake for 60 min at 150 °C.

III. Reservoir Mold

a. Clean Wafers:	Rinse with acetone, isopropanol, and dry.
b. Spin SU8-2025:	3000 rpm for 75 sec, 136 rpm/sec ramp Film thickness = 20 μm
c. Pre-Exposure Bake:	2 min 65 °C / 5 min 95 °C / 2 min 65 °C
d. Expose Wafer:	25 sec at 8 mW/cm^2 Karl Suss aligner, soft contact mode, 250 μm gap
e. Post-Exposure Bake:	5 min 65 °C / 10 min 95 °C / 2 min 65 °C
f. Develop:	1 min in SU-8 Developer Rinse with acetone, isopropanol, and dry.
g. Hard Bake:	Bake for 60 min at 150 °C.

Dialysis Device: Device Fabrication
4 inch silicon wafer substrate

1.	TMCS Treat Molds:	Expose flow mold, control mold, reservoir mold, and one blank wafer to trimethylchlorosilane (TMCS) for 2 min.
2.	Prepare Flow Layer:	Combine 20:1 GE 615 RTV (20 g A:1 g B). Mix in hybrid mixer: 3 min mix / 5 min degas. Pour 5 ml 20:1 onto flow mold. Spin at 2500 rpm for 70 sec, 136 rpm/sec ramp. Let PDMS relax for 30 min before curing.
3.	Prepare Control Layer:	Start while flow layer is relaxing. Combine 5:1 GE 615 RTV (20 g A:4 g B). Mix in hybrid mixer: 3 min mix / 5 min degas. Pour 14 g 5:1 onto control mold. Degas for 15 min in bell jar.
4.	Cure Flow Layer:	Bake for 40 min at 80 °C.
5.	Cure Control Layer:	Bake for 20 min at 80 °C.
6.	Control/Flow Bonding:	Remove control layer from mold. Punch control inlets with 20 gauge punch. Cut devices out and clean with tape. Align control devices onto flow layer. Degas aligned device for 5 min. Bake for 120 min at 80 °C.
7.	Prepare Reservoir Layer:	Start during control/flow bonding. Combine 20:1 GE 615 RTV (40 g A:2 g B). Mix in hybrid mixer: 3 min mix / 5 min degas. Pour 40 ml 20:1 onto reservoir mold. Degas for 15 min in bell jar. Bake for 60 min at 80 °C.
8.	Prepare Stamping Layers:	Start while spacer layer is curing. Combine 10:1 GE 615 RTV (10 g A:1 g B). Mix in hybrid mixer: 3 min mix / 5 min degas. Pour 5 ml 10:1 onto flow mold. Spin first blank wafer at 10,000 rpm for 3 min, 136 rpm/sec ramp, Film Thickness = 2 μm. Spin second blank wafer at 5,000 rpm for 2 min, 136 rpm/sec ramp, Film Thickness = 10 μm.

		Cut a single sheet of membrane (Spectra/Por 132680, 12–14 kDa cutoff) to the size of 5.22 x 1.90 cm.
9.	Assemble Device:	Remove bonded device from flow mold. Punch flow inlets with 20 gauge punch. Clean with tape. Remove reservoir layer from mold. Punch reservoir holes with 8 mm punch. Cut reservoir layer down to size and clean with tape. Stamp bonded device in 2 μm stamp for 30 sec. Stamp membrane edges in 10 μm stamp using tweezers. Carefully place membrane onto stamped flow layer. Push all bubbles out using tweezers. Stamp reservoir layer in 10 μm stamp for 30 sec. Carefully place reservoir layer onto membrane/device. Push all bubbles out using tweezers. Place device reservoir side up onto a blank wafer. Cure assembled device at RT overnight. Bake for 120 min at 80 °C.
10.	Prepare Blank Layer:	Combine 20:1 GE 615 RTV (20 g A:1 g B). Mix in hybrid mixer: 3 min mix / 5 min degas. Pour 5 ml 20:1 onto flow mold. Spin at 2000 rpm for 70 sec, 136 rpm/sec ramp. Bake for 30 min at 80 °C.
11.	Complete The Device:	Remove device from blank wafer. Repunch control and flow inlets with 20 gauge punch. Cut devices down to size and clean with tape. Place device reservoir-side-up on blank layer. Bake for 60 min at 80 °C. Remove from blank layer and place on glass slide.

Control Version of Dialysis Device Without Membrane: Device Fabrication
4 inch silicon wafer substrate

1.	TMCS Treat Molds:	Expose flow mold, control mold, and one blank wafer to TMCS for 2 min.
2.	Prepare Flow Layer:	Combine 20:1 GE 615 RTV (20 g A:1 g B). Mix in hybrid mixer: 3 min mix / 5 min degas. Pour 5 ml 20:1 onto flow mold. Spin at 2500 rpm for 70 sec, 136 rpm/sec ramp. Let PDMS relax for 30 min before curing.
3.	Prepare Control Layer:	Start while flow layer is relaxing. Combine 5:1 GE 615 RTV (20 g A:4 g B). Mix in hybrid mixer: 3 min mix / 5 min degas. Pour 14 g 5:1 onto control mold. Degas for 15 min in bell jar.
4.	Cure Flow Layer:	Bake for 40 min at 80 °C.
5.	Cure Control Layer:	Bake for 20 min at 80 °C.
6.	Control/Flow Bonding:	Remove control layer from mold. Punch control inlets with 20 gauge punch. Cut devices out and clean with tape. Align control devices onto flow layer. Degas aligned device for 5 min. Bake for 120 min at 80 °C.
7.	Prepare Blank Layer:	Start during control/flow bonding. Combine 20:1 GE 615 RTV (40 g A:2 g B). Mix in hybrid mixer: 3 min mix / 5 min degas. Pour 40 ml 20:1 onto blank wafer. Degas for 15 min in bell jar. Bake for 60 min at 80 °C.
8.	Assemble Device:	Remove bonded device from flow mold. Punch flow inlets with 20 gauge punch. Cut out device and clean with tape. Place device on blank layer. Bake overnight at 80 °C. Remove from blank layer and cut device down to size. Place on glass slide.

Screening Device Design

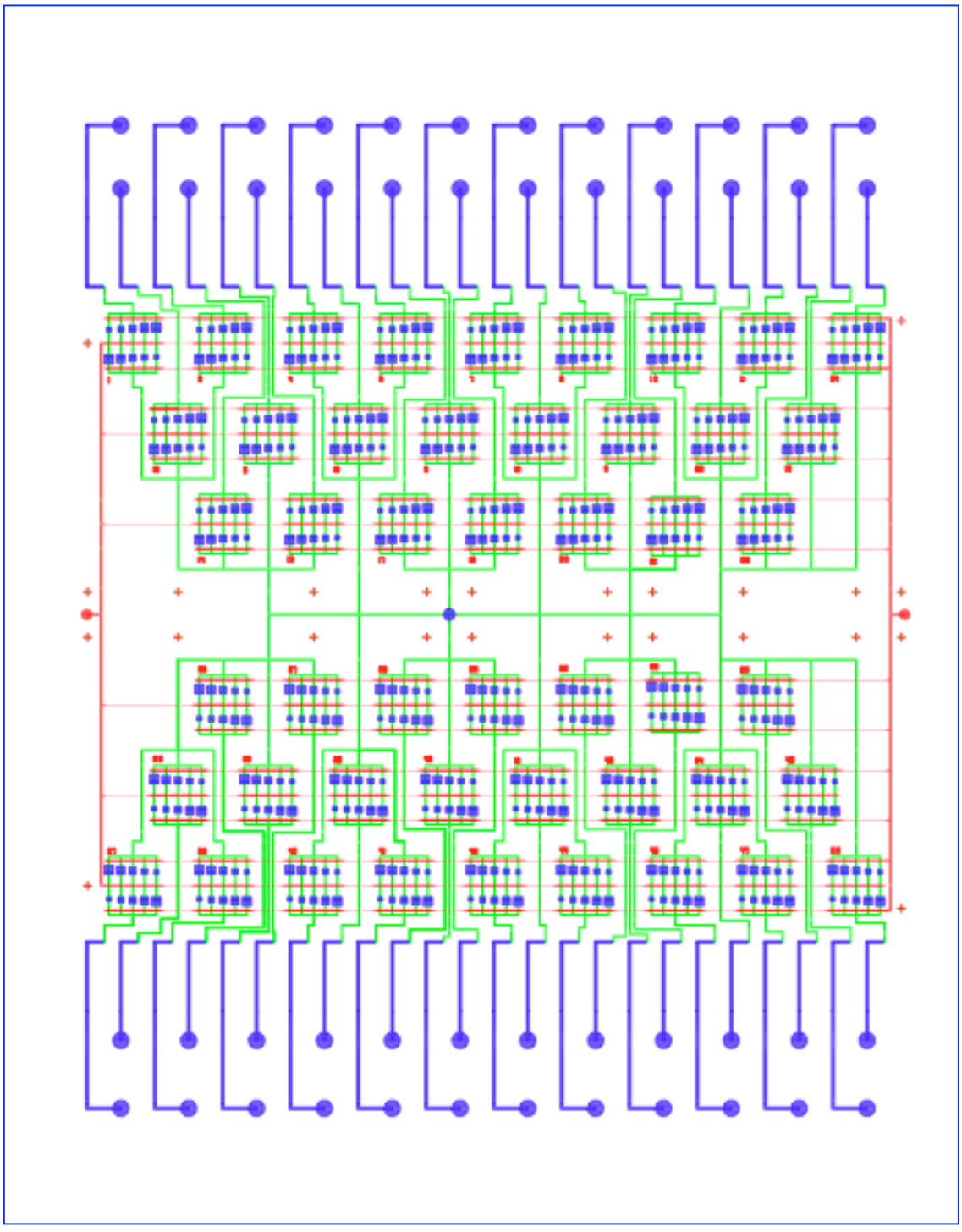

Figure A.6: Assembled screening device

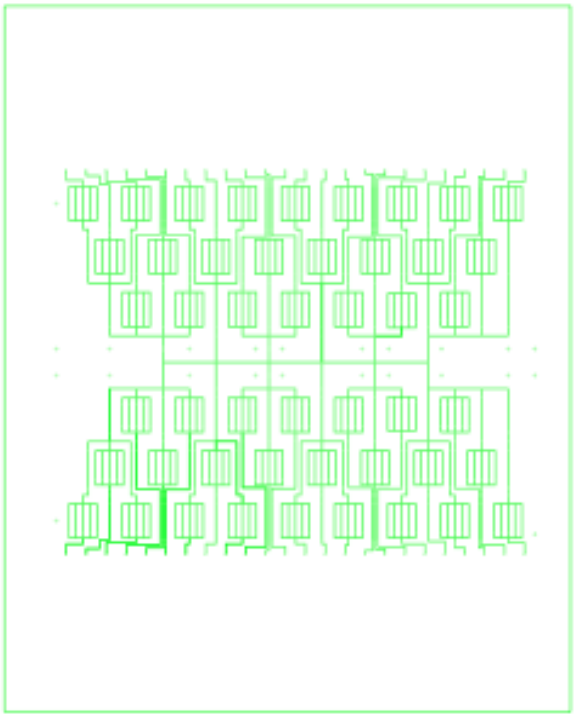

Figure A.7: Screening device rounded channel flow layer mask

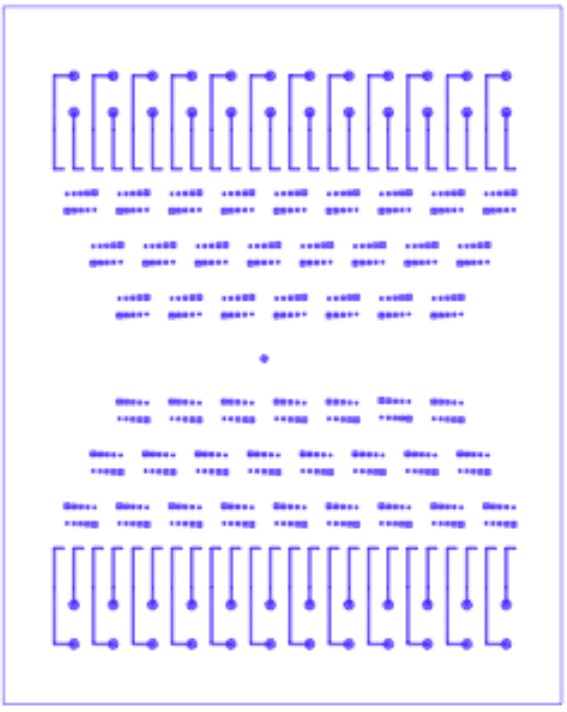

Figure A.8: Screening device chamber flow layer mask

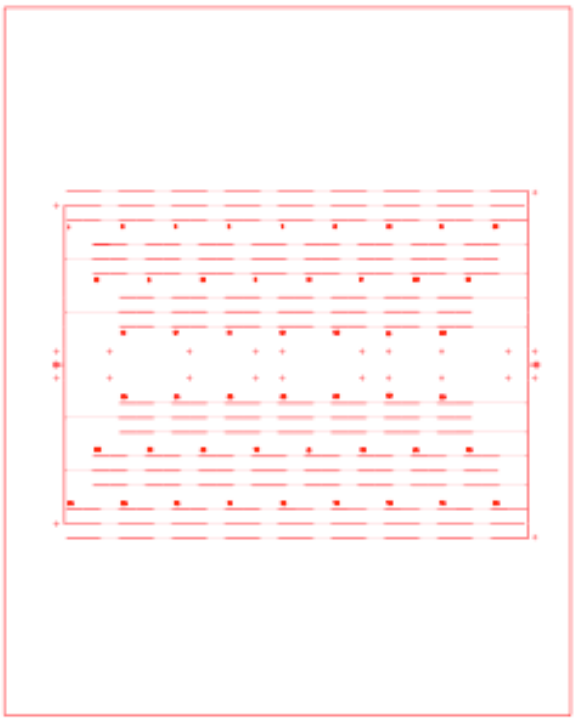

Figure A.9: Screening device control layer mask

Screening Device: Mold Fabrication
3 inch silicon wafer substrate

I. Flow Mold—Rounded Channels

a. Clean Wafers:	Rinse with acetone, isopropanol, and dry.
b. Prime Wafers:	2 min HMDS vapor treatment
c. Spin SPR 220-7:	900 rpm for 75 sec, 136 rpm/sec ramp Film thickness = 12 μm
d. Pre-Exposure Bake:	2 min 65 °C / 5 min 115 °C / 2 min 65 °C
e. Expose Wafer:	45 sec at 8 mW/cm^2 Karl Suss aligner, soft contact mode, 250 μm gap
f. Develop:	1 min in MF-319 Developer Rinse with H_20 and dry.
g. Hard Bake:	Ramp from 65 °C to 200 °C. Bake for 60 min at 200 °C. Ramp down to 65 °C.

Flow Mold—Chambers and I/O Channels

a. Spin SU8-50:	500 rpm for 20 sec, 136 rpm/sec ramp 2500 rpm for 55 sec, 136 rpm/sec ramp Let sit for 10 min. Film thickness = 45 μm
b. Pre-Exposure Bake:	6 min 65 °C / 15 min 95 °C / 2 min 65 °C
c. Expose Wafer:	45 sec at 8 mW/cm^2 Karl Suss aligner, soft contact mode, 250 μm gap
d. Post-Exposure Bake:	5 min 65 °C / 15 min 95 °C / 2 min 65 °C
e. Develop:	2 min in SU-8 Developer Rinse with acetone, isopropanol, and dry.
f. Hard Bake:	Bake for 60 min at 150 °C.

II. Control Mold

a. Clean Wafers:	Rinse with acetone, isopropanol, and dry.
b. Spin SU8-2025:	3000 rpm for 75 sec, 136 rpm/sec ramp Film thickness = 20 μm
c. Pre-Exposure Bake:	2 min 65 °C / 5 min 95 °C / 2 min 65 °C
d. Expose Wafer:	25 sec at 8 mW/cm^2 Karl Suss aligner, soft contact mode, 250 μm gap
e. Post-Exposure Bake:	5 min 65 °C / 10 min 95 °C / 2 min 65 °C
f. Develop:	1 min in SU-8 Developer Rinse with acetone, isopropanol, and dry.
g. Hard Bake:	Bake for 60 min at 150 °C.

Screening Device: Device Fabrication
3 inch silicon wafer substrate

1.	TMCS Treat Molds:	Expose flow mold, control mold, and one blank wafer to TMCS for 2 min.
2.	Prepare Flow Layer:	Combine 5:1 GE 615 RTV (30 g A:6 g B). Mix in hybrid mixer: 3 min mix / 5 min degas. Pour 30 g 5:1 onto flow mold. Degas for 15 min in bell jar.
3.	Prepare Control Layer:	Combine 20:1 GE 615 RTV (20 g A:1 g B). Mix in hybrid mixer: 3 min mix / 5 min degas. Pour 5 ml 20:1 onto flow mold. Spin at 2000 rpm for 70 sec, 136 rpm/sec ramp.
4.	Cure Flow Layer:	Bake for 20 min at 80 °C.
5.	Cure Control Layer:	Bake for 40 min at 80 °C.
6.	Flow/Control Bonding:	Remove flow layer from mold. Punch flow inlets with 14 gauge and 20 gauge punches. Cut device out and clean with tape. Align devices onto control layer. Bake for 80 min at 80 °C.
7.	Prepare Blank Layer:	Start during flow/control bonding. Combine 30:1 GE 615 RTV (30 g A:1 g B). Mix in hybrid mixer: 3 min mix / 5 min degas. Pour 5 ml 20:1 onto flow mold. Spin at 2000 rpm for 70 sec, 136 rpm/sec ramp. Bake for 45 min at 80 °C.
8.	Assemble The Device:	Remove device from control mold. Punch control inlets with 20 gauge punch. Cut device down to size and clean with tape. Place device on blank layer. Bake overnight at 80 °C. Remove from blank layer and place on glass slide.

Formulator Device Design

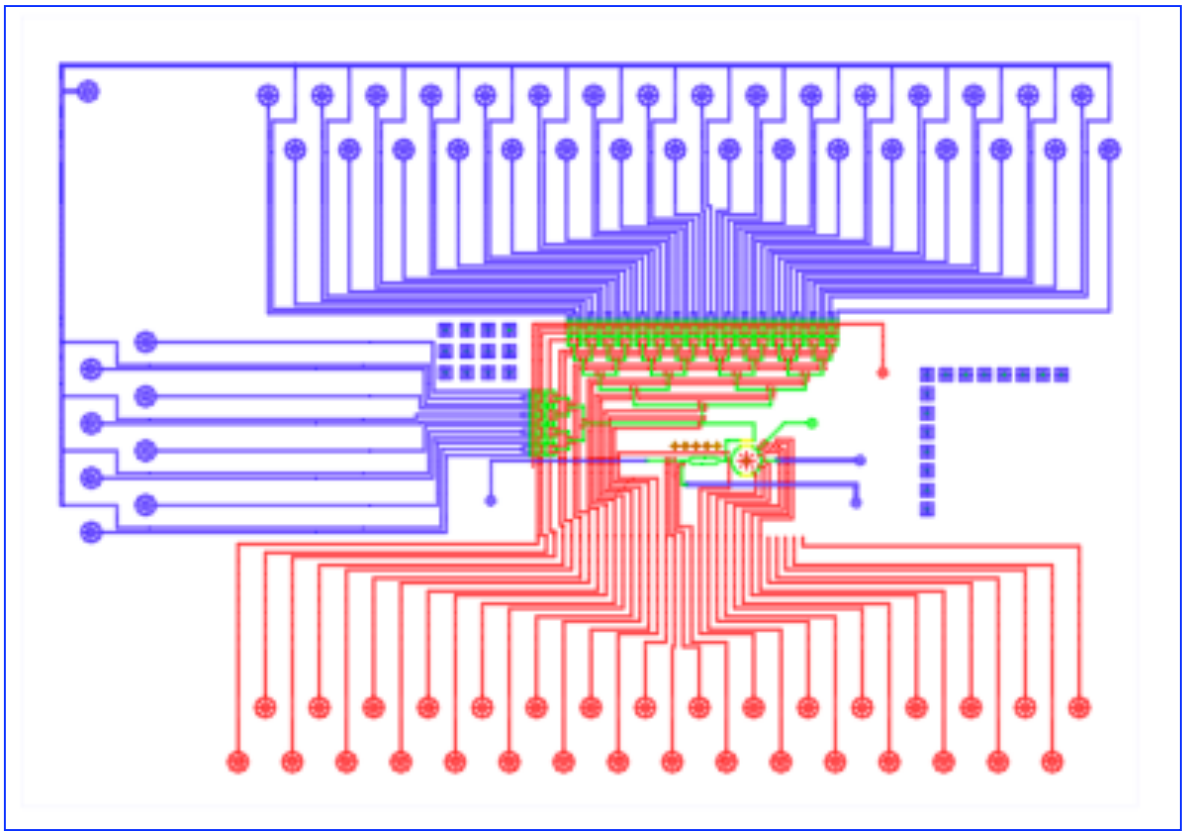

Figure A.10: Assembled formulator device

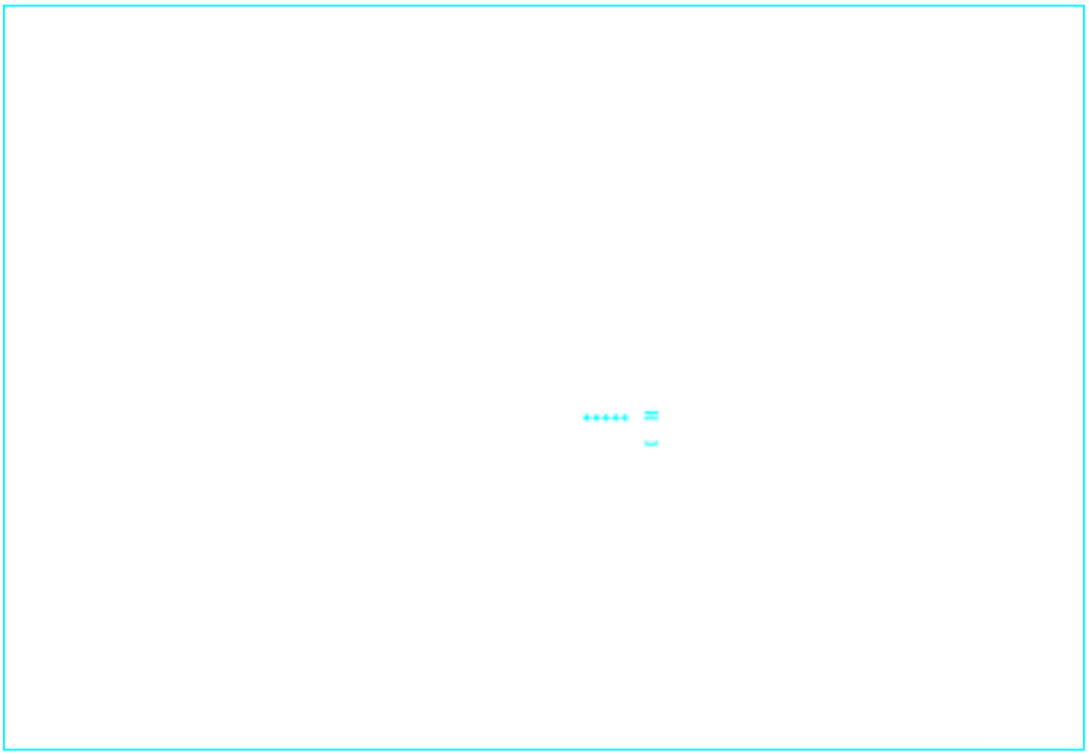

Figure A.11: Formulator device rotary mixer flow layer mask

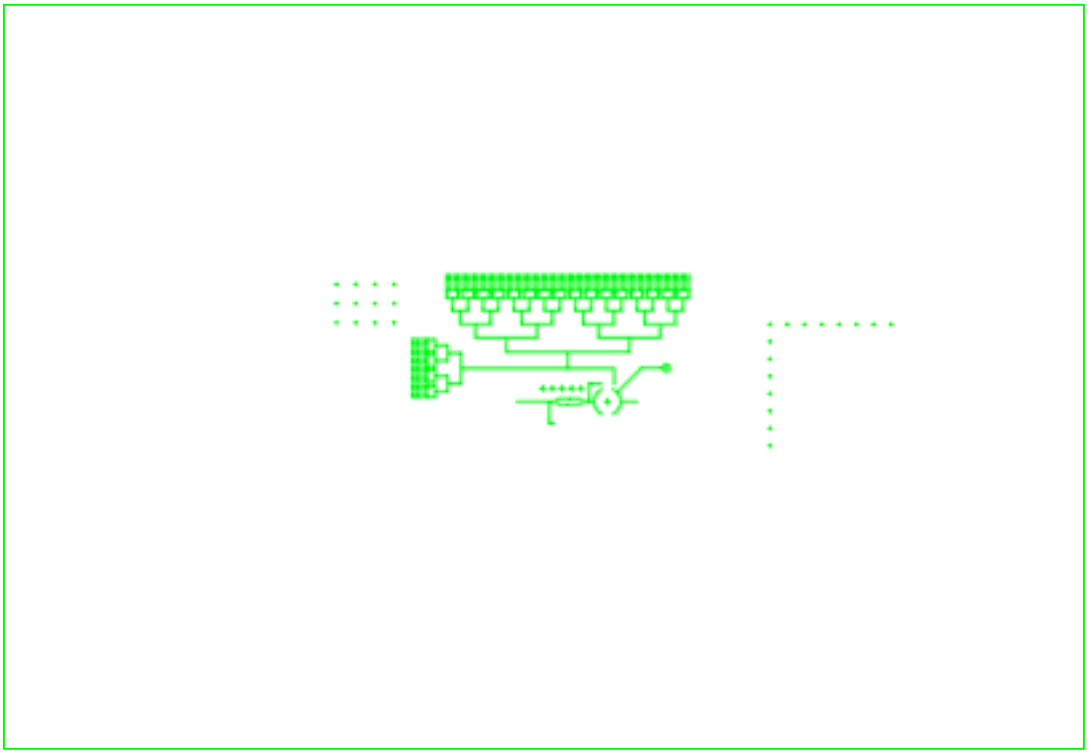

Figure A.12: Formulator device rounded channel flow layer mask

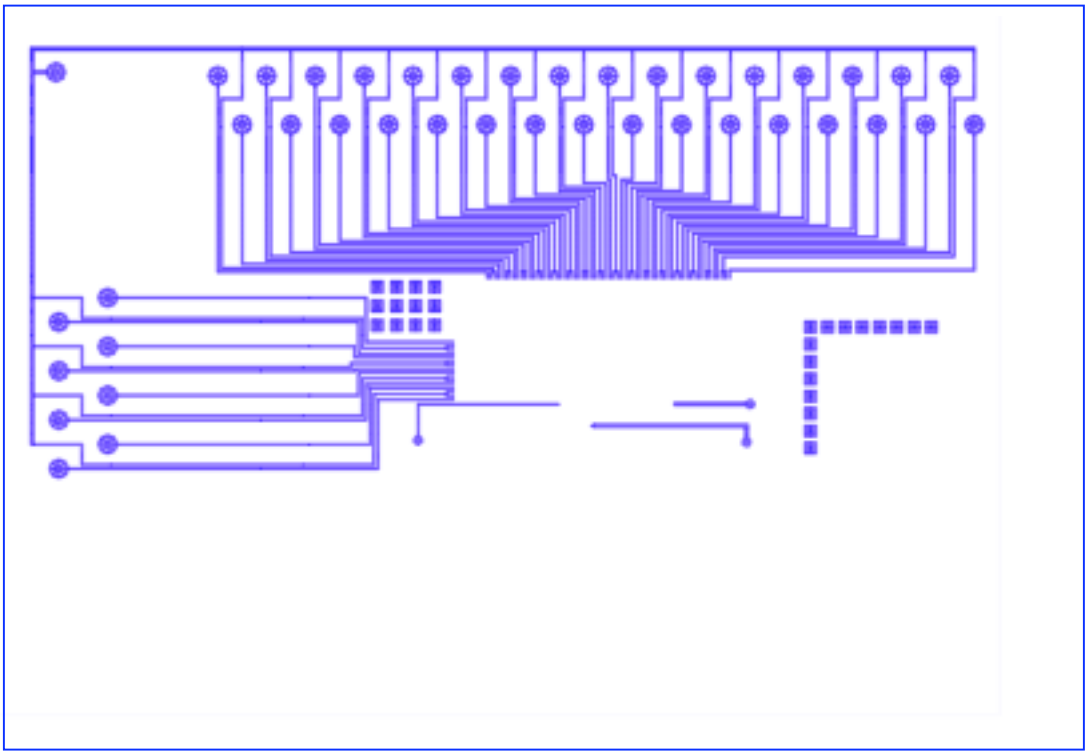

Figure A.13: Formulator device I/O channel flow layer mask

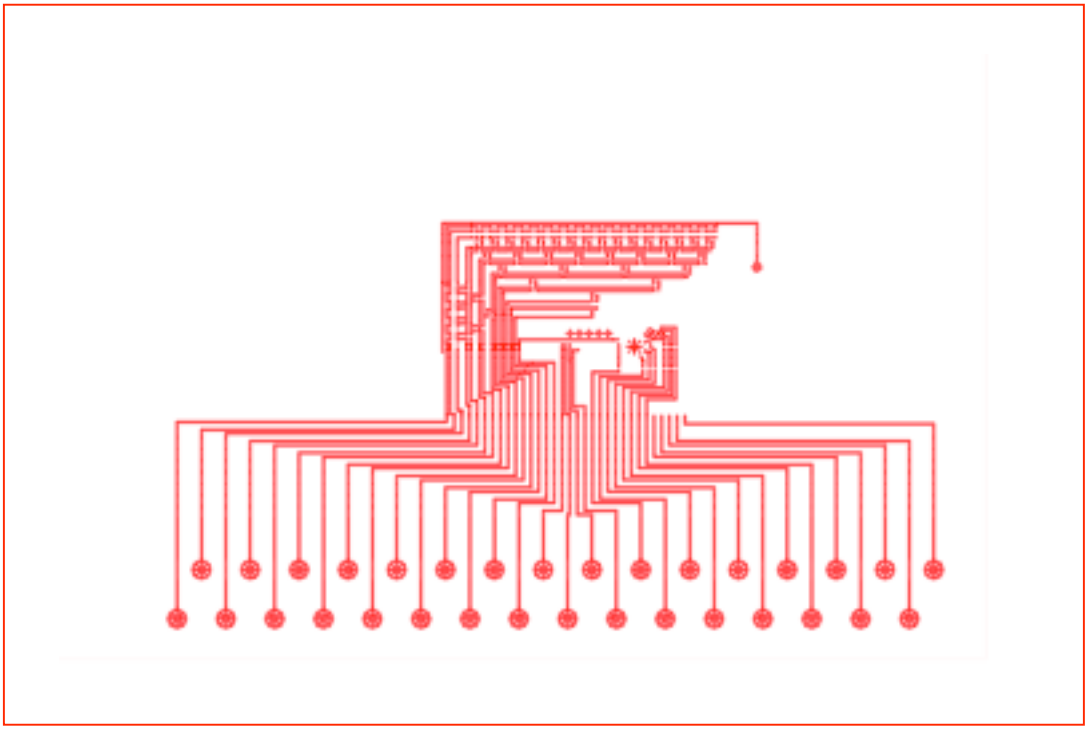

Figure A.14: Formulator device control layer mask

Formulator Device: Mold Fabrication
3 inch silicon wafer substrate

I. Flow Mold—Rotary Mixer

a. Clean Wafers:	Rinse with acetone, isopropanol, and dry.
b. Spin SU8-2015:	3000 rpm for 75 sec, 136 rpm/sec ramp Film thickness = 12 μm
c. Pre-Exposure Bake:	2 min 65 °C / 5 min 95 °C / 2 min 65 °C
d. Expose Wafer:	20 sec at 8 mW/cm^2 Karl Suss aligner, soft contact mode, 250 μm gap
e. Post-Exposure Bake:	5 min 65 °C / 10 min 95 °C / 2 min 65 °C
f. Develop:	1 min in SU-8 Developer Rinse with acetone, isopropanol, and dry.
g. Hard Bake:	Bake for 60 min at 150 °C.

Flow Mold—Rounded Channels

a. Clean Wafers:	Rinse with acetone, isopropanol, and dry.
b. Prime Wafers:	2 min HMDS vapor treatment
c. Spin SPR 220-7:	900 rpm for 75 sec, 136 rpm/sec ramp Film thickness = 12 μm
d. Pre-Exposure Bake:	2 min 65 °C / 5 min 115 °C / 2 min 65 °C
e. Expose Wafer:	45 sec at 8 mW/cm^2 Karl Suss aligner, soft contact mode, 250 μm gap
f. Develop:	1 min in MF-319 Developer Rinse with H_20 and dry.
g. Hard Bake:	Ramp from 65 °C to 200 °C. Bake for 60 min at 200 °C. Ramp down to 65 °C.

Flow Mold—I/O Channels

a. Spin SU8-50:	500 rpm for 20 sec, 136 rpm/sec ramp 2000 rpm for 55 sec, 136 rpm/sec ramp Let sit for 10 min. Film thickness = 50 μm
b. Pre-Exposure Bake:	6 min 65 °C / 15 min 95 °C / 2 min 65 °C
c. Expose Wafer:	45 sec at 8 mW/cm^2 Karl Suss aligner, soft contact mode, 250 μm gap
d. Post-Exposure Bake:	5 min 65 °C / 15 min 95 °C / 2 min 65 °C
e. Develop:	2 min in SU-8 Developer Rinse with acetone, isopropanol, and dry.
f. Hard Bake:	Bake for 60 min at 150 °C.

II. Control Mold

a. Clean Wafers:	Rinse with acetone, isopropanol, and dry.
b. Spin SU8-2025:	3000 rpm for 75 sec, 136 rpm/sec ramp Film thickness = 20 μm
c. Pre-Exposure Bake:	2 min 65 °C / 5 min 95 °C / 2 min 65 °C
d. Expose Wafer:	25 sec at 8 mW/cm^2 Karl Suss aligner, soft contact mode, 250 μm gap
e. Post-Exposure Bake:	5 min 65 °C / 10 min 95 °C / 2 min 65 °C
f. Develop:	1 min in SU-8 Developer Rinse with acetone, isopropanol, and dry.
g. Hard Bake:	Bake for 60 min at 150 °C.

Formulator Device: Device Fabrication
3 inch silicon wafer substrate

1.	TMCS Treat Molds:	Expose flow mold, control mold, and one blank wafer to TMCS for 2 min.
2.	Prepare Flow Layer:	Combine 5:1 GE 615 RTV (30 g A:6 g B). Mix in hybrid mixer: 3 min mix / 5 min degas. Pour 30 g 5:1 onto flow mold. Degas for 15 min in bell jar.
3.	Prepare Control Layer:	Combine 20:1 GE 615 RTV (20 g A:1 g B). Mix in hybrid mixer: 3 min mix / 5 min degas. Pour 5 ml 20:1 onto flow mold. Spin at 2000 rpm for 70 sec, 136 rpm/sec ramp.
4.	Cure Flow Layer:	Bake for 20 min at 80 °C.
5.	Cure Control Layer:	Bake for 40 min at 80 °C.
6.	Flow/Control Bonding:	Remove flow layer from mold. Punch flow inlets with 20 gauge punch. Cut device out and clean with tape. Align devices onto control layer. Bake for 80 min at 80 °C.
7.	Prepare Blank Layer:	Start during flow/control bonding. Combine 30:1 GE 615 RTV (30 g A:1 g B). Mix in hybrid mixer: 3 min mix / 5 min degas. Pour 5 ml 20:1 onto flow mold. Spin at 2000 rpm for 70 sec, 136 rpm/sec ramp. Bake for 45 min at 80 °C.
8.	Assemble The Device:	Remove device from control mold. Punch control inlets with 20 gauge punch. Cut device down to size and clean with tape. Place device on blank layer. Bake overnight at 80 °C. Remove from blank layer and place on glass slide.

Scale-Up Diffraction Device Design

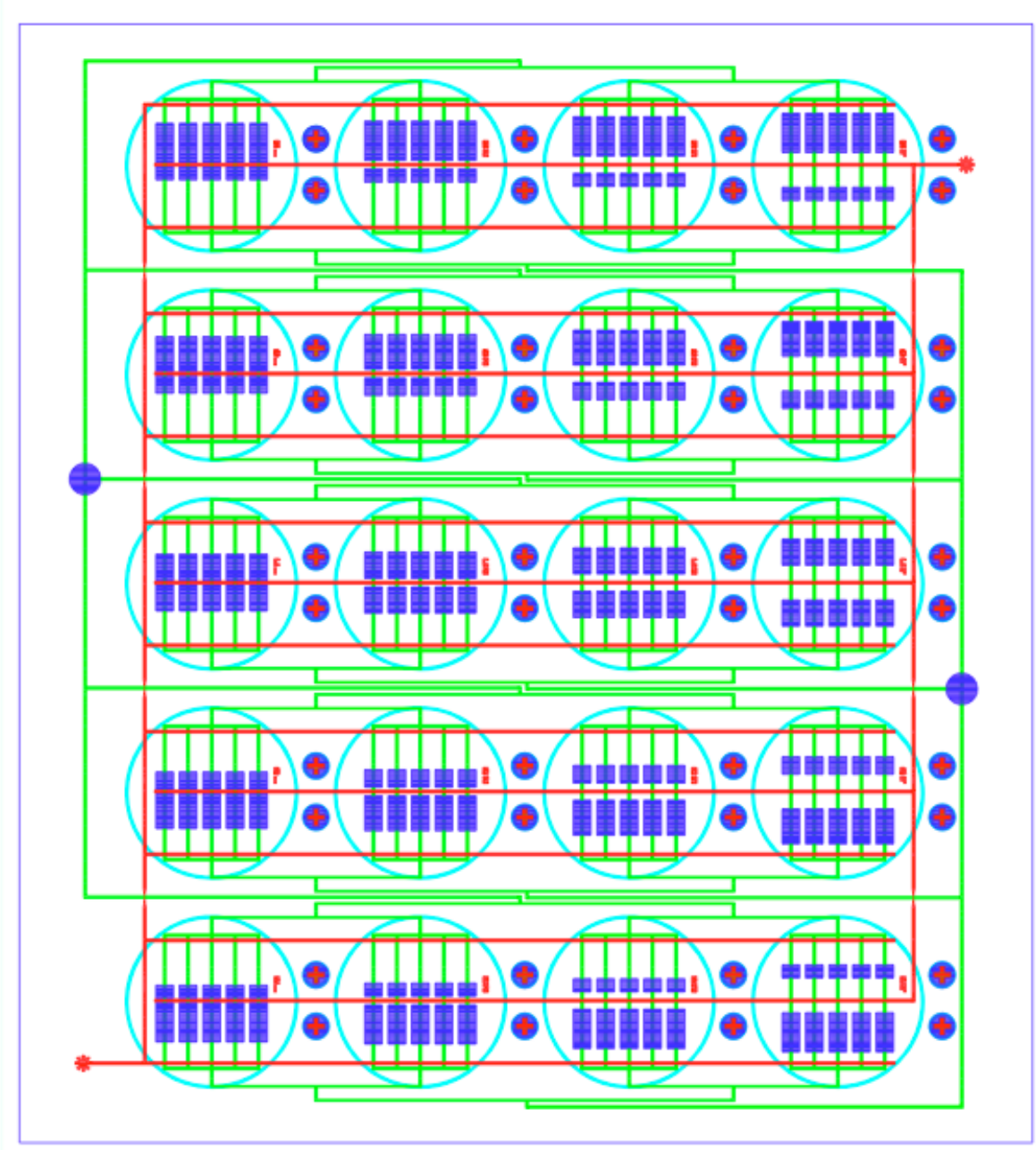

Figure A.15: Assembled scale-up diffraction device

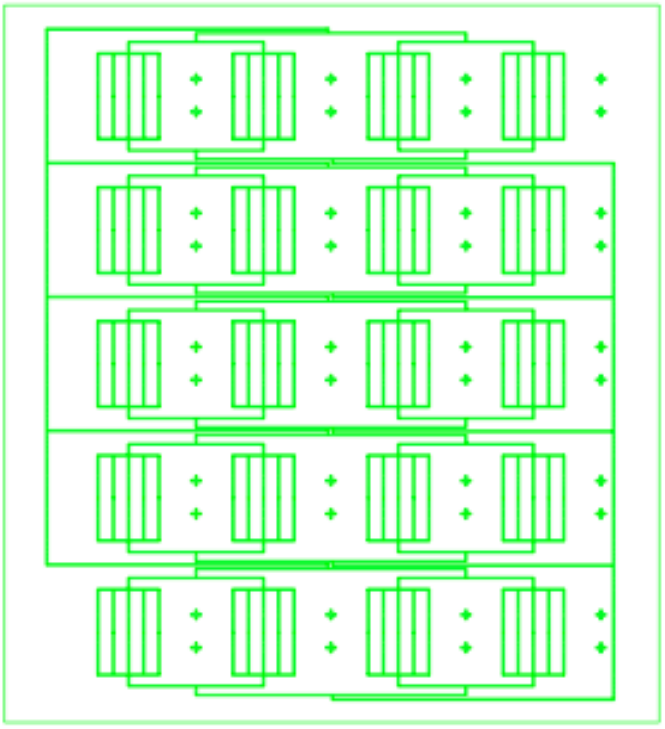

Figure A.16: Scale-up device rounded channel flow layer mask

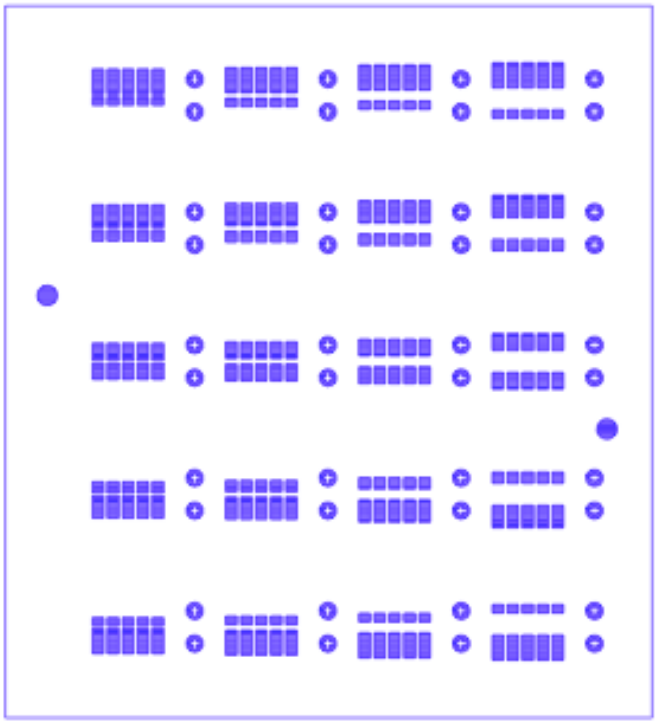

Figure A.17: Scale-up device chamber flow layer mask

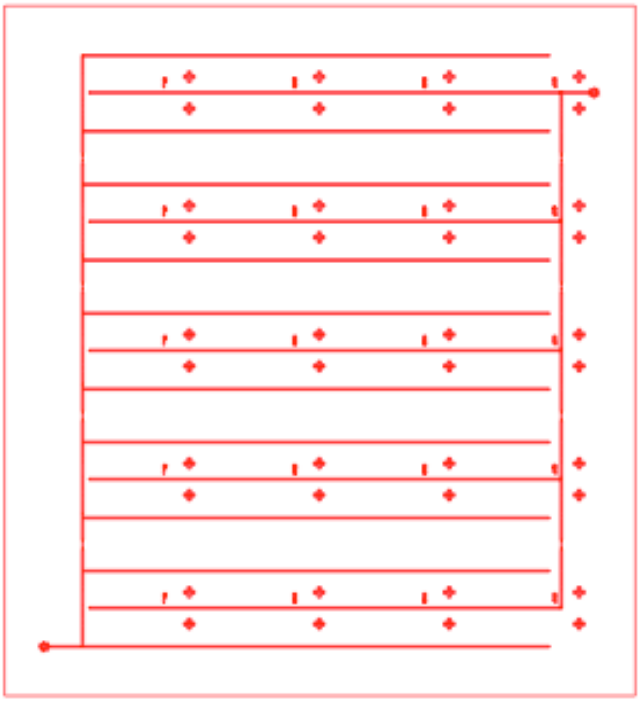

Figure A.18: Scale-up device control layer mask

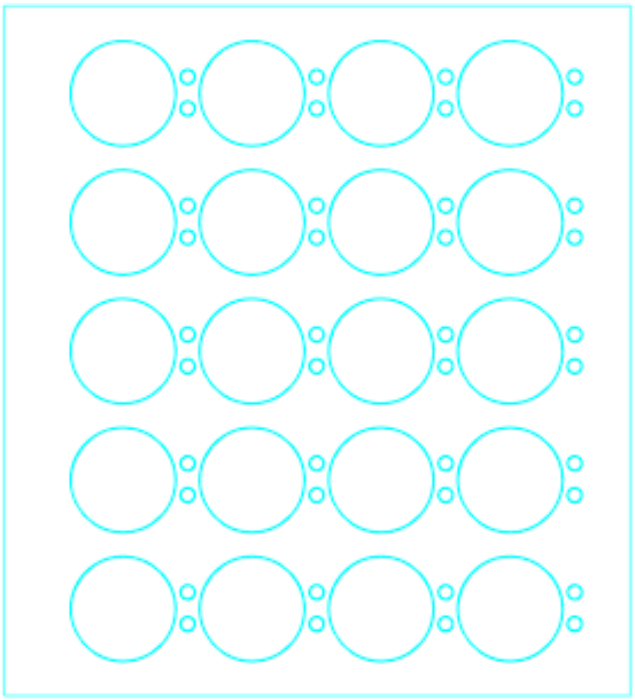

Figure A.19: Scale-up device reservoir layer mask

Scale-up Diffraction Device: Mold Fabrication
3 inch silicon wafer substrate

I. Flow Mold—Rounded Channels

a. Clean Wafers:	Rinse with acetone, isopropanol, and dry.
b. Prime Wafers:	2 min HMDS vapor treatment
c. Spin SPR 220-7:	900 rpm for 75 sec, 136 rpm/sec ramp Film thickness = 12 μm
d. Pre-Exposure Bake:	2 min 65 °C / 5 min 115 °C / 2 min 65 °C
e. Expose Wafer:	45 sec at 8 mW/cm^2 Karl Suss aligner, soft contact mode, 250 μm gap
f. Develop:	1 min in MF-319 Developer Rinse with H_20 and dry.
g. Hard Bake:	Ramp from 65 °C to 200 °C. Bake for 60 min at 200 °C. Ramp down to 65 °C.

Flow Mold—Chambers

a. Spin SU8-100:	500 rpm for 20 sec, 136 rpm/sec ramp 1500 rpm for 55 sec, 136 rpm/sec ramp Let sit for 15 min. Film thickness = 150 μm
b. Pre-Exposure Bake:	10 min 65 °C / 30 min 95 °C / 2 min 65 °C
c. Expose Wafer:	75 sec at 8 mW/cm^2 Karl Suss aligner, soft contact mode, 250 μm gap
d. Post-Exposure Bake:	5 min 65 °C / 25 min 95 °C / 2 min 65 °C
d. Develop:	3 min in SU-8 Developer Rinse with acetone, isopropanol, and dry.
e. Hard Bake:	Bake for 60 min at 150 °C.

II. Control Mold

a. Clean Wafers:	Rinse with acetone, isopropanol, and dry.
b. Spin SU8-2025:	3000 rpm for 75 sec, 136 rpm/sec ramp Film thickness = 20 μm
c. Pre-Exposure Bake:	2 min 65 °C / 5 min 95 °C / 2 min 65 °C
d. Expose Wafer:	25 sec at 8 mW/cm^2 Karl Suss aligner, soft contact mode, 250 μm gap
e. Post-Exposure Bake:	5 min 65 °C / 10 min 95 °C / 2 min 65 °C
f. Develop:	1 min in SU-8 Developer Rinse with acetone, isopropanol, and dry.
g. Hard Bake:	Bake for 60 min at 150 °C.

III. Reservoir Mold

a. Clean Wafers:	Rinse with acetone, isopropanol, and dry.
b. Spin SU8-2025:	3000 rpm for 75 sec, 136 rpm/sec ramp Film thickness = 20 μm
c. Pre-Exposure Bake:	2 min 65 °C / 5 min 95 °C / 2 min 65 °C
d. Expose Wafer:	25 sec at 8 mW/cm^2 Karl Suss aligner, soft contact mode, 250 μm gap
e. Post-Exposure Bake:	5 min 65 °C / 10 min 95 °C / 2 min 65 °C
f. Develop:	1 min in SU-8 Developer Rinse with acetone, isopropanol, and dry.
g. Hard Bake:	Bake for 60 min at 150 °C.

Scale-Up Diffraction Device: Device Fabrication
3 inch silicon wafer substrate

1.	TMCS Treat Molds:	Expose flow mold, control mold, reservoir mold, and one blank wafer to TMCS for 2 min.
2.	Prepare Flow Layer:	Combine 5:1 GE 615 RTV (35 g A:7 g B). Mix in hybrid mixer: 3 min mix / 5 min degas. Pour 6 g 5:1 onto flow mold. Spin at 350 rpm for 70 sec, 136 rpm/sec ramp.
3.	Prepare Reservoir Layer:	Pour 30 g 5:1 onto reservoir mold. Degas for 15 min in bell jar.
4.	Cure Flow Layer:	Bake for 20 min at 80 °C.
5.	Cure Reservoir Layer:	Bake for 40 min at 80 °C.
6.	Prepare Second Flow Layer:	Start while reservoir layer is curing. Combine 20:1 GE 615 RTV (20 g A:1 g B). Mix in hybrid mixer: 3 min mix / 5 min degas. Pour 5 ml 20:1 onto flow mold. Spin at 2000 rpm for 70 sec, 136 rpm/sec ramp.
7.	Cure Second Flow Layer:	Bake for 25 min at 80 °C.
8.	Prepare Control Layer:	Start while second flow layer is curing. Combine 20:1 GE 615 RTV (20 g A:1 g B). Mix in hybrid mixer: 3 min mix / 5 min degas. Pour 5 ml 20:1 onto flow mold. Spin at 1700 rpm for 70 sec, 136 rpm/sec ramp.
9.	Flow/Reservoir Bonding:	Remove reservoir layer from mold. Punch reservoir holes with 8 mm punch. Cut reservoir layer down to size and clean with tape. Align reservoir layer onto flow layer. Bake for 60 min at 80 °C.
10.	Cure Control Layer:	Bake for 60 min at 80 °C.
11.	Flow/Control Bonding:	Remove flow/reservoir devices from mold. Punch control inlets with 20 gauge punch. Cut devices out and clean with tape. Align devices onto control layer. Degas aligned device for 5 min.

		Bake for 60 min at 80 °C.
12.	Prepare Blank Layer:	Start while second flow layer is curing. Combine 30:1 GE 615 RTV (30 g A:1 g B). Mix in hybrid mixer: 3 min mix / 5 min degas. Pour 5 ml 20:1 onto flow mold. Spin at 2000 rpm for 70 sec, 136 rpm/sec ramp. Bake for 45 min at 80 °C.
13.	Assemble The Device:	Remove device from control mold. Punch control inlets with 20 gauge punch. Cut devices down to size and clean with tape. Place device on blank layer. Degas device for 5 min. Bake overnight at 80 °C. Remove from blank layer and place on glass slide.

Appendix B

FORMULATOR RECIPES

I. Crystallization Survey Solubility Screening Conditions

Condition	Salt Solution	Buffer	(% Precipitant / % Protein)
1	0.10 M ammonium acetate	0.1 M sodium acetate pH 4.5	80 / 2.5
2	0.10 M ammonium acetate	0.1 M sodium acetate pH 4.5	67.5 / 15
3	0.10 M ammonium acetate	0.1 M sodium acetate pH 4.5	52.5 / 30
4	0.10 M ammonium acetate	0.1 M sodium acetate pH 4.5	37.5 / 40
5	0.10 M ammonium acetate	0.1 M sodium acetate pH 4.5	22.5 / 60
6	0.10 M ammonium acetate	0.1 M sodium acetate pH 4.5	7.5 / 75
7	0.08 M sodium acetate	0.1 M sodium acetate pH 4.5	80 / 2.5
13	0.13 M ammonium chloride	0.1 M sodium acetate pH 4.5	80 / 2.5
19	0.13 M sodium chloride	0.1 M sodium acetate pH 4.5	80 / 2.5
25	0.05 M potassium sodium chloride	0.1 M sodium acetate pH 4.5	80 / 2.5
31	0.10 M ammonium sulfate	0.1 M sodium acetate pH 4.5	80 / 2.5
37	0.18 M sodium nitrate	0.1 M sodium acetate pH 4.5	80 / 2.5
43	0.05 M magnesium acetate	0.1 M sodium acetate pH 4.5	80 / 2.5
49	0.05 M magnesium chloride	0.1 M sodium acetate pH 4.5	80 / 2.5
55	0.05 M magnesium sulfate	0.1 M sodium acetate pH 4.5	80 / 2.5
61	0.13 M potassium acetate	0.1 M sodium acetate pH 4.5	80 / 2.5
67	0.08 M potassium chloride	0.1 M sodium acetate pH 4.5	80 / 2.5
73	0.05 M potassium phosphate	0.1 M sodium acetate pH 4.5	80 / 2.5
79	0.10 M sodium phosphate	0.1 M sodium acetate pH 4.5	80 / 2.5
85	0.10 M ammonium acetate	0.1 M sodium citrate pH 6.5	80 / 2.5
91	0.08 M sodium acetate	0.1 M sodium citrate pH 6.5	80 / 2.5
97	0.13 M ammonium chloride	0.1 M sodium citrate pH 6.5	80 / 2.5
103	0.13 M sodium chloride	0.1 M sodium citrate pH 6.5	80 / 2.5
109	0.05 M potassium sodium chloride	0.1 M sodium citrate pH 6.5	80 / 2.5
115	0.10 M ammonium sulfate	0.1 M sodium citrate pH 6.5	80 / 2.5
121	0.18 M sodium nitrate	0.1 M sodium citrate pH 6.5	80 / 2.5
127	0.05 M magnesium acetate	0.1 M sodium citrate pH 6.5	80 / 2.5
133	0.05 M magnesium chloride	0.1 M sodium citrate pH 6.5	80 / 2.5
139	0.05 M magnesium sulfate	0.1 M sodium citrate pH 6.5	80 / 2.5
145	0.13 M potassium acetate	0.1 M sodium citrate pH 6.5	80 / 2.5
151	0.08 M potassium chloride	0.1 M sodium citrate pH 6.5	80 / 2.5
157	0.05 M potassium phosphate	0.1 M sodium citrate pH 6.5	80 / 2.5
163	0.10 M sodium phosphate	0.1 M sodium citrate pH 6.5	80 / 2.5
169	0.10 M ammonium acetate	0.1 M Tris·HCl pH 8.5	80 / 2.5
175	0.08 M sodium acetate	0.1 M Tris·HCl pH 8.5	80 / 2.5
181	0.13 M ammonium chloride	0.1 M Tris·HCl pH 8.5	80 / 2.5
187	0.13 M sodium chloride	0.1 M Tris·HCl pH 8.5	80 / 2.5
193	0.05 M potassium sodium chloride	0.1 M Tris·HCl pH 8.5	80 / 2.5
199	0.10 M ammonium sulfate	0.1 M Tris·HCl pH 8.5	80 / 2.5

Condition	Salt Solution	Buffer	(% Precipitant / % Protein)
205	0.18 M sodium nitrate	0.1 M Tris·HCl pH 8.5	80 / 2.5
211	0.05 M magnesium acetate	0.1 M Tris·HCl pH 8.5	80 / 2.5
217	0.05 M magnesium chloride	0.1 M Tris·HCl pH 8.5	80 / 2.5
223	0.05 M magnesium sulfate	0.1 M Tris·HCl pH 8.5	80 / 2.5
229	0.13 M potassium acetate	0.1 M Tris·HCl pH 8.5	80 / 2.5
235	0.08 M potassium chloride	0.1 M Tris·HCl pH 8.5	80 / 2.5
241	0.05 M potassium phosphate	0.1 M Tris·HCl pH 8.5	80 / 2.5
247	0.10 M sodium phosphate	0.1 M Tris·HCl pH 8.5	80 / 2.5
253	0.10 M ammonium acetate	0.1 M CAPS[1] pH 10.5	80 / 2.5
259	0.08 M sodium acetate	0.1 M CAPS pH 10.5	80 / 2.5
265	0.13 M ammonium chloride	0.1 M CAPS pH 10.5	80 / 2.5
271	0.13 M sodium chloride	0.1 M CAPS pH 10.5	80 / 2.5
277	0.05 M potassium sodium chloride	0.1 M CAPS pH 10.5	80 / 2.5
283	0.10 M ammonium sulfate	0.1 M CAPS pH 10.5	80 / 2.5
289	0.18 M sodium nitrate	0.1 M CAPS pH 10.5	80 / 2.5
295	0.05 M magnesium acetate	0.1 M CAPS pH 10.5	80 / 2.5
301	0.05 M magnesium chloride	0.1 M CAPS pH 10.5	80 / 2.5
307	0.05 M magnesium sulfate	0.1 M CAPS pH 10.5	80 / 2.5
313	0.13 M potassium acetate	0.1 M CAPS pH 10.5	80 / 2.5
319	0.08 M potassium chloride	0.1 M CAPS pH 10.5	80 / 2.5
325	0.05 M potassium phosphate	0.1 M CAPS pH 10.5	80 / 2.5
331	0.10 M sodium phosphate	0.1 M CAPS pH 10.5	80 / 2.5
332	0.10 M sodium phosphate	0.1 M CAPS pH 10.5	67.5 / 15
333	0.10 M sodium phosphate	0.1 M CAPS pH 10.5	52.5 / 30
334	0.10 M sodium phosphate	0.1 M CAPS pH 10.5	37.5 / 40
335	0.10 M sodium phosphate	0.1 M CAPS pH 10.5	22.5 / 60
336	0.10 M sodium phosphate	0.1 M CAPS pH 10.5	7.5 / 75

Condition	Precipitant Stock Concentration (% w/w)
1-336	100% PEG 300
337-672	100% PEG 350 MME
673-1008	100% PEG 550 MME
1089-1344	50% PEG 1500
1345-1680	50% PEG 2000 MME
1681-2016	50% PEG 3350
2017-2352	50% PEG 5000 MME
2353-2688	50% PEG 8000

II. GK^{G230D} Solubility Screening Conditions

Condition	Salt Solution	Buffer	(% Precipitant / % Protein)
1	0.4 M ammonium acetate	0.1 M citric acid pH 3.5	70 / 5
2	0.4 M ammonium acetate	0.1 M citric acid pH 3.5	60 / 15
3	0.4 M ammonium acetate	0.1 M citric acid pH 3.5	45 / 30
4	0.4 M ammonium acetate	0.1 M citric acid pH 3.5	30 / 45
5	0.4 M ammonium acetate	0.1 M citric acid pH 3.5	15 / 60
6	0.4 M ammonium acetate	0.1 M citric acid pH 3.5	5 / 70
7	0.3 M sodium acetate	0.1 M citric acid pH 3.5	70 / 5
13	0.5 M ammonium chloride	0.1 M citric acid pH 3.5	70 / 5
19	0.5 M sodium chloride	0.1 M citric acid pH 3.5	70 / 5
25	0.4 M ammonium sulfate	0.1 M citric acid pH 3.5	70 / 5
31	0.7 M sodium nitrate	0.1 M citric acid pH 3.5	70 / 5
37	0.2 M sodium thiosulfate	0.1 M citric acid pH 3.5	70 / 5
43	0.2 M lithium sulfate	0.1 M citric acid pH 3.5	70 / 5
49	0.2 M sodium formate	0.1 M citric acid pH 3.5	70 / 5
55	0.2 M magnesium acetate	0.1 M citric acid pH 3.5	70 / 5
61	0.2 M magnesium chloride	0.1 M citric acid pH 3.5	70 / 5
67	0.2 M magnesium sulfate	0.1 M citric acid pH 3.5	70 / 5
73	0.5 M potassium acetate	0.1 M citric acid pH 3.5	70 / 5
79	0.3 M potassium chloride	0.1 M citric acid pH 3.5	70 / 5
85	0.2 M potassium phosphate	0.1 M citric acid pH 3.5	70 / 5
91	0.4 M sodium phosphate	0.1 M citric acid pH 3.5	70 / 5
97	0.2 M lithium chloride	0.1 M citric acid pH 3.5	70 / 5
103	0.4 M ammonium acetate	0.1 M MES[2] pH 6.5	70 / 5
109	0.3 M sodium acetate	0.1 M MES pH 6.5	70 / 5
115	0.5 M ammonium chloride	0.1 M MES pH 6.5	70 / 5
121	0.5 M sodium chloride	0.1 M MES pH 6.5	70 / 5
127	0.4 M ammonium sulfate	0.1 M MES pH 6.5	70 / 5
133	0.7 M sodium nitrate	0.1 M MES pH 6.5	70 / 5
139	0.2 M sodium thiosulfate	0.1 M MES pH 6.5	70 / 5
145	0.2 M lithium sulfate	0.1 M MES pH 6.5	70 / 5
151	0.2 M sodium formate	0.1 M MES pH 6.5	70 / 5
157	0.2 M magnesium acetate	0.1 M MES pH 6.5	70 / 5
163	0.2 M magnesium chloride	0.1 M MES pH 6.5	70 / 5
169	0.2 M magnesium sulfate	0.1 M MES pH 6.5	70 / 5
175	0.5 M potassium acetate	0.1 M MES pH 6.5	70 / 5
181	0.3 M potassium chloride	0.1 M MES pH 6.5	70 / 5
187	0.2 M potassium phosphate	0.1 M MES pH 6.5	70 / 5
193	0.4 M sodium phosphate	0.1 M MES pH 6.5	70 / 5
199	0.2 M lithium chloride	0.1 M MES pH 6.5	70 / 5
205	0.4 M ammonium acetate	0.1 M Hepes pH 7.5	70 / 5
211	0.3 M sodium acetate	0.1 M Hepes pH 7.5	70 / 5
217	0.5 M ammonium chloride	0.1 M Hepes pH 7.5	70 / 5
223	0.5 M sodium chloride	0.1 M Hepes pH 7.5	70 / 5
229	0.4 M ammonium sulfate	0.1 M Hepes pH 7.5	70 / 5
235	0.7 M sodium nitrate	0.1 M Hepes pH 7.5	70 / 5
241	0.2 M sodium thiosulfate	0.1 M Hepes pH 7.5	70 / 5
247	0.2 M lithium sulfate	0.1 M Hepes pH 7.5	70 / 5

Condition	Salt Solution	Buffer	(% Precipitant / % Protein)
253	0.2 M sodium formate	0.1 M Hepes pH 7.5	70 / 5
259	0.2 M magnesium acetate	0.1 M Hepes pH 7.5	70 / 5
265	0.2 M magnesium chloride	0.1 M Hepes pH 7.5	70 / 5
271	0.2 M magnesium sulfate	0.1 M Hepes pH 7.5	70 / 5
277	0.5 M potassium acetate	0.1 M Hepes pH 7.5	70 / 5
283	0.3 M potassium chloride	0.1 M Hepes pH 7.5	70 / 5
289	0.2 M potassium phosphate	0.1 M Hepes pH 7.5	70 / 5
295	0.4 M sodium phosphate	0.1 M Hepes pH 7.5	70 / 5
301	0.2 M lithium chloride	0.1 M Hepes pH 7.5	70 / 5
307	0.4 M ammonium acetate	0.1 M Tris·HCl pH 8.5	70 / 5
313	0.3 M sodium acetate	0.1 M Tris·HCl pH 8.5	70 / 5
319	0.5 M ammonium chloride	0.1 M Tris·HCl pH 8.5	70 / 5
325	0.5 M sodium chloride	0.1 M Tris·HCl pH 8.5	70 / 5
331	0.4 M ammonium sulfate	0.1 M Tris·HCl pH 8.5	70 / 5
337	0.7 M sodium nitrate	0.1 M Tris·HCl pH 8.5	70 / 5
343	0.2 M sodium thiosulfate	0.1 M Tris·HCl pH 8.5	70 / 5
349	0.2 M lithium sulfate	0.1 M Tris·HCl pH 8.5	70 / 5
355	0.2 M sodium formate	0.1 M Tris·HCl pH 8.5	70 / 5
361	0.2 M magnesium acetate	0.1 M Tris·HCl pH 8.5	70 / 5
367	0.2 M magnesium chloride	0.1 M Tris·HCl pH 8.5	70 / 5
373	0.2 M magnesium sulfate	0.1 M Tris·HCl pH 8.5	70 / 5
379	0.5 M potassium acetate	0.1 M Tris·HCl pH 8.5	70 / 5
385	0.3 M potassium chloride	0.1 M Tris·HCl pH 8.5	70 / 5
391	0.2 M potassium phosphate	0.1 M Tris·HCl pH 8.5	70 / 5
397	0.4 M sodium phosphate	0.1 M Tris·HCl pH 8.5	70 / 5
403	0.2 M lithium chloride	0.1 M Tris·HCl pH 8.5	70 / 5
409	0.4 M ammonium acetate	0.1 M TAPS[3] pH 9.5	70 / 5
415	0.3 M sodium acetate	0.1 M TAPS pH 9.5	70 / 5
421	0.5 M ammonium chloride	0.1 M TAPS pH 9.5	70 / 5
427	0.5 M sodium chloride	0.1 M TAPS pH 9.5	70 / 5
433	0.4 M ammonium sulfate	0.1 M TAPS pH 9.5	70 / 5
439	0.7 M sodium nitrate	0.1 M TAPS pH 9.5	70 / 5
445	0.2 M sodium thiosulfate	0.1 M TAPS pH 9.5	70 / 5
451	0.2 M lithium sulfate	0.1 M TAPS pH 9.5	70 / 5
457	0.2 M sodium formate	0.1 M TAPS pH 9.5	70 / 5
463	0.2 M magnesium acetate	0.1 M TAPS pH 9.5	70 / 5
469	0.2 M magnesium chloride	0.1 M TAPS pH 9.5	70 / 5
475	0.2 M magnesium sulfate	0.1 M TAPS pH 9.5	70 / 5
481	0.5 M potassium acetate	0.1 M TAPS pH 9.5	70 / 5
487	0.3 M potassium chloride	0.1 M TAPS pH 9.5	70 / 5
493	0.2 M potassium phosphate	0.1 M TAPS pH 9.5	70 / 5
499	0.4 M sodium phosphate	0.1 M TAPS pH 9.5	70 / 5
505	0.2 M lithium chloride	0.1 M TAPS pH 9.5	70 / 5
506	0.2 M lithium chloride	0.1 M TAPS pH 9.5	60 / 15
507	0.2 M lithium chloride	0.1 M TAPS pH 9.5	45 / 30
508	0.2 M lithium chloride	0.1 M TAPS pH 9.5	30 / 45
509	0.2 M lithium chloride	0.1 M TAPS pH 9.5	15 / 60
510	0.2 M lithium chloride	0.1 M TAPS pH 9.5	5 / 70

Condition	Precipitant Stock Concentration (% w/w)
1-510	Salt Solutions
511-1020	100% PEG 300
1021-1530	100% PEG 550 MME
1531-2040	50% PEG 1500
2041-2550	50% PEG 3350
2551-3060	50% PEG 5000 MME
3061-3570	50% PEG 8000
3571-4080	30% PEG 20,000

III. GK^{D72A}, GK^{235KGG}, and GK^{M271I} Solubility Screening Conditions

Condition	Salt Solution	Buffer	(% Precipitant / % Protein)
1	0.4 M ammonium acetate	0.1 M citric acid pH 3.5	70 / 5
2	0.4 M ammonium acetate	0.1 M citric acid pH 3.5	60 / 15
3	0.4 M ammonium acetate	0.1 M citric acid pH 3.5	45 / 30
4	0.4 M ammonium acetate	0.1 M citric acid pH 3.5	30 / 45
5	0.4 M ammonium acetate	0.1 M citric acid pH 3.5	15 / 60
6	0.4 M ammonium acetate	0.1 M citric acid pH 3.5	5 / 70
7	0.3 M sodium acetate	0.1 M citric acid pH 3.5	70 / 5
13	0.5 M ammonium chloride	0.1 M citric acid pH 3.5	70 / 5
19	0.5 M sodium chloride	0.1 M citric acid pH 3.5	70 / 5
25	0.4 M ammonium sulfate	0.1 M citric acid pH 3.5	70 / 5
31	0.7 M sodium nitrate	0.1 M citric acid pH 3.5	70 / 5
37	0.2 M sodium thiosulfate	0.1 M citric acid pH 3.5	70 / 5
43	0.2 M lithium sulfate	0.1 M citric acid pH 3.5	70 / 5
49	0.2 M sodium formate	0.1 M citric acid pH 3.5	70 / 5
55	0.2 M magnesium acetate	0.1 M citric acid pH 3.5	70 / 5
61	0.2 M magnesium chloride	0.1 M citric acid pH 3.5	70 / 5
67	0.2 M magnesium sulfate	0.1 M citric acid pH 3.5	70 / 5
73	0.5 M potassium acetate	0.1 M citric acid pH 3.5	70 / 5
79	0.3 M potassium chloride	0.1 M citric acid pH 3.5	70 / 5
85	0.2 M potassium phosphate	0.1 M citric acid pH 3.5	70 / 5
91	0.4 M sodium phosphate	0.1 M citric acid pH 3.5	70 / 5
97	0.2 M lithium chloride	0.1 M citric acid pH 3.5	70 / 5
103	0.4 M ammonium acetate	0.1 M sodium citrate pH 5.5	70 / 5
109	0.3 M sodium acetate	0.1 M sodium citrate pH 5.5	70 / 5
115	0.5 M ammonium chloride	0.1 M sodium citrate pH 5.5	70 / 5
121	0.5 M sodium chloride	0.1 M sodium citrate pH 5.5	70 / 5
127	0.4 M ammonium sulfate	0.1 M sodium citrate pH 5.5	70 / 5
133	0.7 M sodium nitrate	0.1 M sodium citrate pH 5.5	70 / 5
139	0.2 M sodium thiosulfate	0.1 M sodium citrate pH 5.5	70 / 5
145	0.2 M lithium sulfate	0.1 M sodium citrate pH 5.5	70 / 5
151	0.2 M sodium formate	0.1 M sodium citrate pH 5.5	70 / 5
157	0.2 M magnesium acetate	0.1 M sodium citrate pH 5.5	70 / 5
163	0.2 M magnesium chloride	0.1 M sodium citrate pH 5.5	70 / 5
169	0.2 M magnesium sulfate	0.1 M sodium citrate pH 5.5	70 / 5
175	0.5 M potassium acetate	0.1 M sodium citrate pH 5.5	70 / 5
181	0.3 M potassium chloride	0.1 M sodium citrate pH 5.5	70 / 5
187	0.2 M potassium phosphate	0.1 M sodium citrate pH 5.5	70 / 5
193	0.4 M sodium phosphate	0.1 M sodium citrate pH 5.5	70 / 5
199	0.2 M lithium chloride	0.1 M sodium citrate pH 5.5	70 / 5
205	0.4 M ammonium acetate	0.1 M Hepes pH 7.5	70 / 5
211	0.3 M sodium acetate	0.1 M Hepes pH 7.5	70 / 5
217	0.5 M ammonium chloride	0.1 M Hepes pH 7.5	70 / 5
223	0.5 M sodium chloride	0.1 M Hepes pH 7.5	70 / 5
229	0.4 M ammonium sulfate	0.1 M Hepes pH 7.5	70 / 5
235	0.7 M sodium nitrate	0.1 M Hepes pH 7.5	70 / 5
241	0.2 M sodium thiosulfate	0.1 M Hepes pH 7.5	70 / 5
247	0.2 M lithium sulfate	0.1 M Hepes pH 7.5	70 / 5

Condition	Salt Solution	Buffer	(% Precipitant / % Protein)
253	0.2 M sodium formate	0.1 M Hepes pH 7.5	70 / 5
259	0.2 M magnesium acetate	0.1 M Hepes pH 7.5	70 / 5
265	0.2 M magnesium chloride	0.1 M Hepes pH 7.5	70 / 5
271	0.2 M magnesium sulfate	0.1 M Hepes pH 7.5	70 / 5
277	0.5 M potassium acetate	0.1 M Hepes pH 7.5	70 / 5
283	0.3 M potassium chloride	0.1 M Hepes pH 7.5	70 / 5
289	0.2 M potassium phosphate	0.1 M Hepes pH 7.5	70 / 5
295	0.4 M sodium phosphate	0.1 M Hepes pH 7.5	70 / 5
301	0.2 M lithium chloride	0.1 M Hepes pH 7.5	70 / 5
307	0.4 M ammonium acetate	0.1 M Tris·HCl pH 8.5	70 / 5
313	0.3 M sodium acetate	0.1 M Tris·HCl pH 8.5	70 / 5
319	0.5 M ammonium chloride	0.1 M Tris·HCl pH 8.5	70 / 5
325	0.5 M sodium chloride	0.1 M Tris·HCl pH 8.5	70 / 5
331	0.4 M ammonium sulfate	0.1 M Tris·HCl pH 8.5	70 / 5
337	0.7 M sodium nitrate	0.1 M Tris·HCl pH 8.5	70 / 5
343	0.2 M sodium thiosulfate	0.1 M Tris·HCl pH 8.5	70 / 5
349	0.2 M lithium sulfate	0.1 M Tris·HCl pH 8.5	70 / 5
355	0.2 M sodium formate	0.1 M Tris·HCl pH 8.5	70 / 5
361	0.2 M magnesium acetate	0.1 M Tris·HCl pH 8.5	70 / 5
367	0.2 M magnesium chloride	0.1 M Tris·HCl pH 8.5	70 / 5
373	0.2 M magnesium sulfate	0.1 M Tris·HCl pH 8.5	70 / 5
379	0.5 M potassium acetate	0.1 M Tris·HCl pH 8.5	70 / 5
385	0.3 M potassium chloride	0.1 M Tris·HCl pH 8.5	70 / 5
391	0.2 M potassium phosphate	0.1 M Tris·HCl pH 8.5	70 / 5
397	0.4 M sodium phosphate	0.1 M Tris·HCl pH 8.5	70 / 5
403	0.2 M lithium chloride	0.1 M Tris·HCl pH 8.5	70 / 5
409	0.4 M ammonium acetate	0.1 M TAPS pH 9.5	70 / 5
415	0.3 M sodium acetate	0.1 M TAPS pH 9.5	70 / 5
421	0.5 M ammonium chloride	0.1 M TAPS pH 9.5	70 / 5
427	0.5 M sodium chloride	0.1 M TAPS pH 9.5	70 / 5
433	0.4 M ammonium sulfate	0.1 M TAPS pH 9.5	70 / 5
439	0.7 M sodium nitrate	0.1 M TAPS pH 9.5	70 / 5
445	0.2 M sodium thiosulfate	0.1 M TAPS pH 9.5	70 / 5
451	0.2 M lithium sulfate	0.1 M TAPS pH 9.5	70 / 5
457	0.2 M sodium formate	0.1 M TAPS pH 9.5	70 / 5
463	0.2 M magnesium acetate	0.1 M TAPS pH 9.5	70 / 5
469	0.2 M magnesium chloride	0.1 M TAPS pH 9.5	70 / 5
475	0.2 M magnesium sulfate	0.1 M TAPS pH 9.5	70 / 5
481	0.5 M potassium acetate	0.1 M TAPS pH 9.5	70 / 5
487	0.3 M potassium chloride	0.1 M TAPS pH 9.5	70 / 5
493	0.2 M potassium phosphate	0.1 M TAPS pH 9.5	70 / 5
499	0.4 M sodium phosphate	0.1 M TAPS pH 9.5	70 / 5
505	0.2 M lithium chloride	0.1 M TAPS pH 9.5	70 / 5
506	0.2 M lithium chloride	0.1 M TAPS pH 9.5	60 / 15
507	0.2 M lithium chloride	0.1 M TAPS pH 9.5	45 / 30
508	0.2 M lithium chloride	0.1 M TAPS pH 9.5	30 / 45
509	0.2 M lithium chloride	0.1 M TAPS pH 9.5	15 / 60
510	0.2 M lithium chloride	0.1 M TAPS pH 9.5	5 / 70

Condition	Precipitant Stock Concentration (% w/w)
1-510	Salt Solutions
511-1020	100% PEG 300
1021-1530	100% PEG 550 MME
1531-2040	50% PEG 1500
2041-2550	50% PEG 2000 MME
2551-3060	50% PEG 3350
3061-3570	50% PEG 5000 MME
3571-4080	50% PEG 8000
4081-4590	30% PEG 20,000

[1] CAPS, 3-(cyclohexylamino)-1-propanesulfonic acid
[2] MES, 2-(N-morpholino)ethanesulfonic acid

Appendix C

CRYSTALLIZATION SURVEY PHASE DIAGRAMS

1. bR D85S Phase Diagrams:

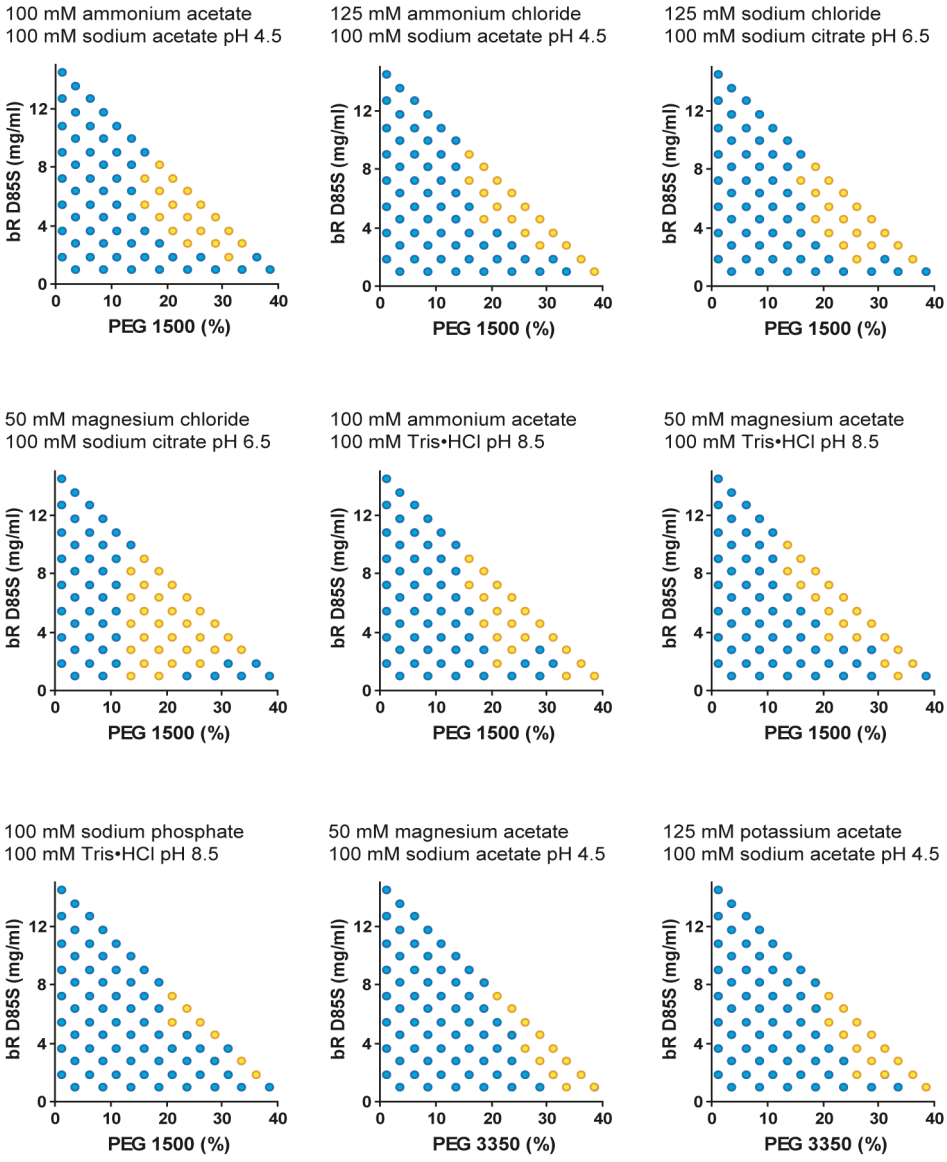

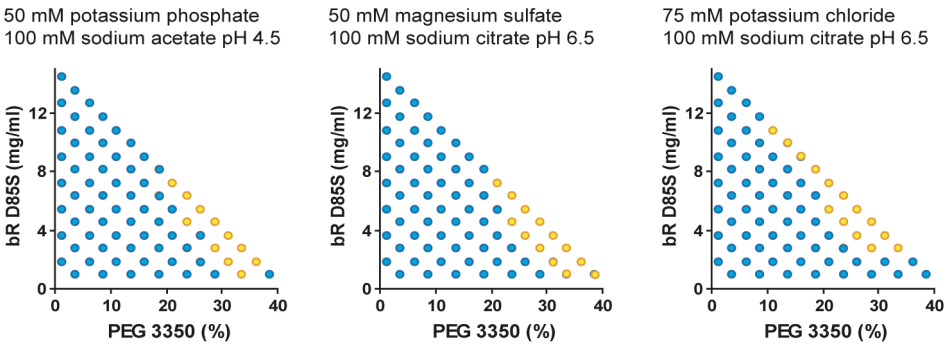

2. bR Phase Diagrams:

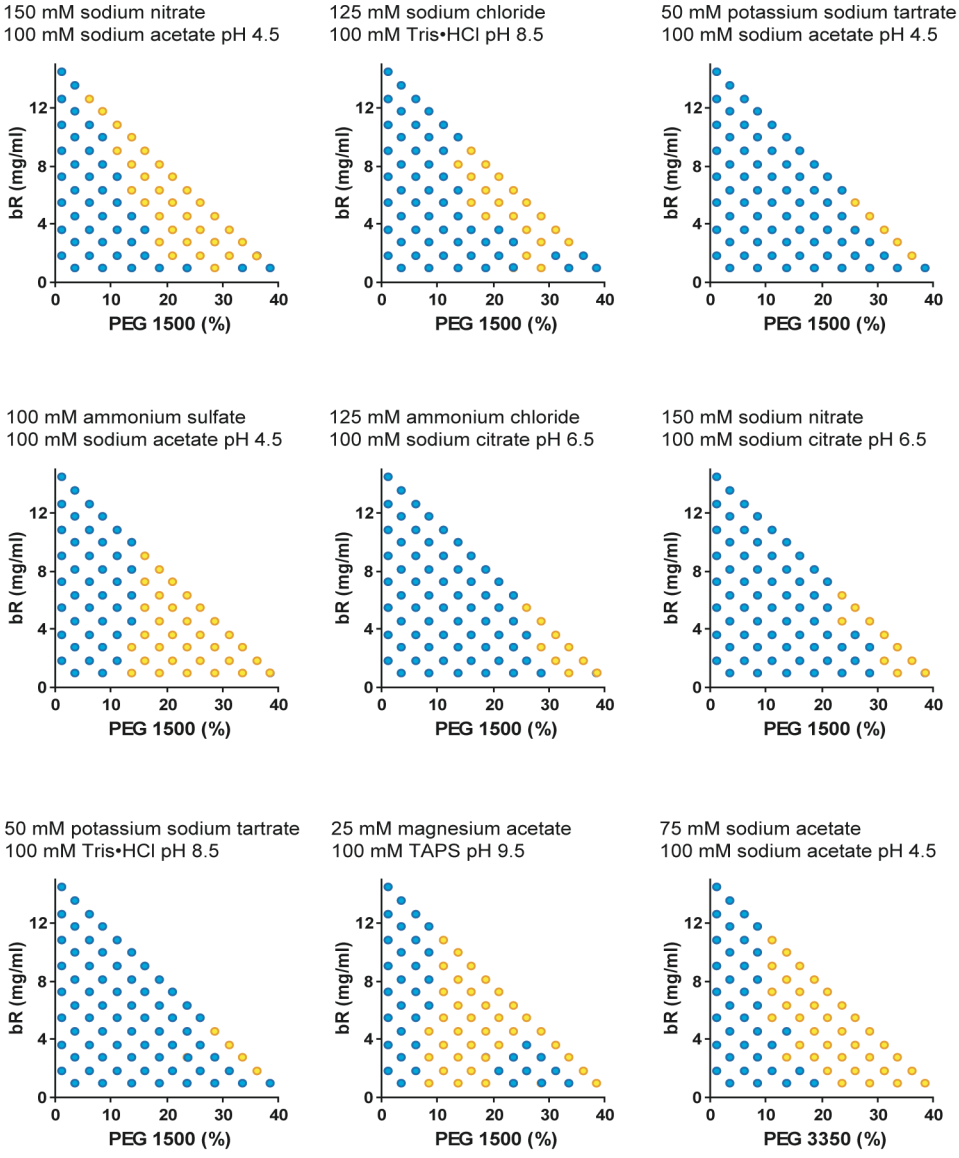

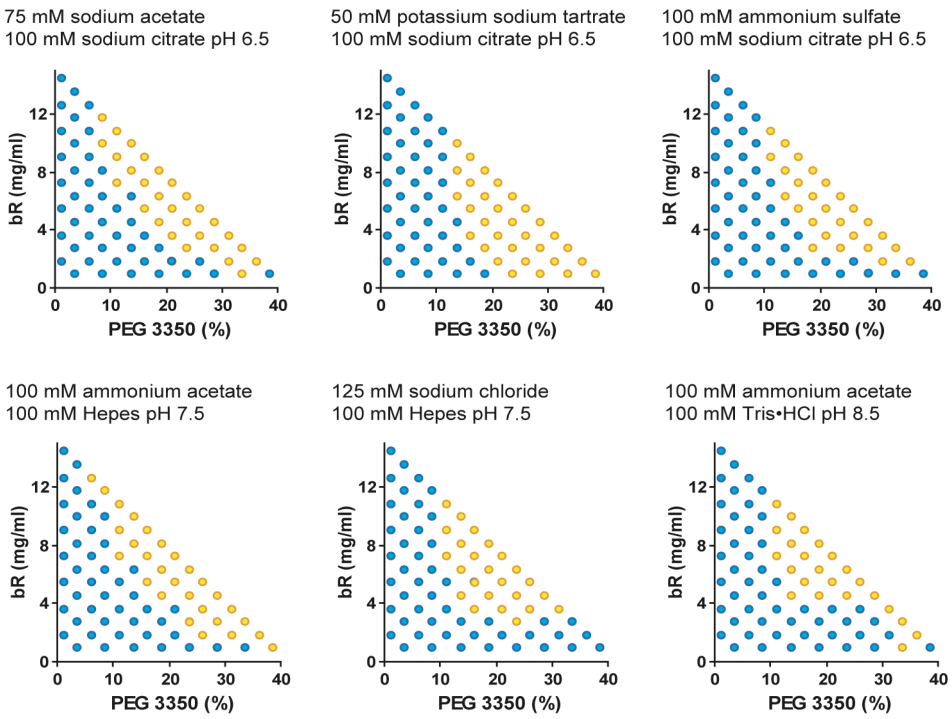

3. Cbb3 Phase Diagrams:

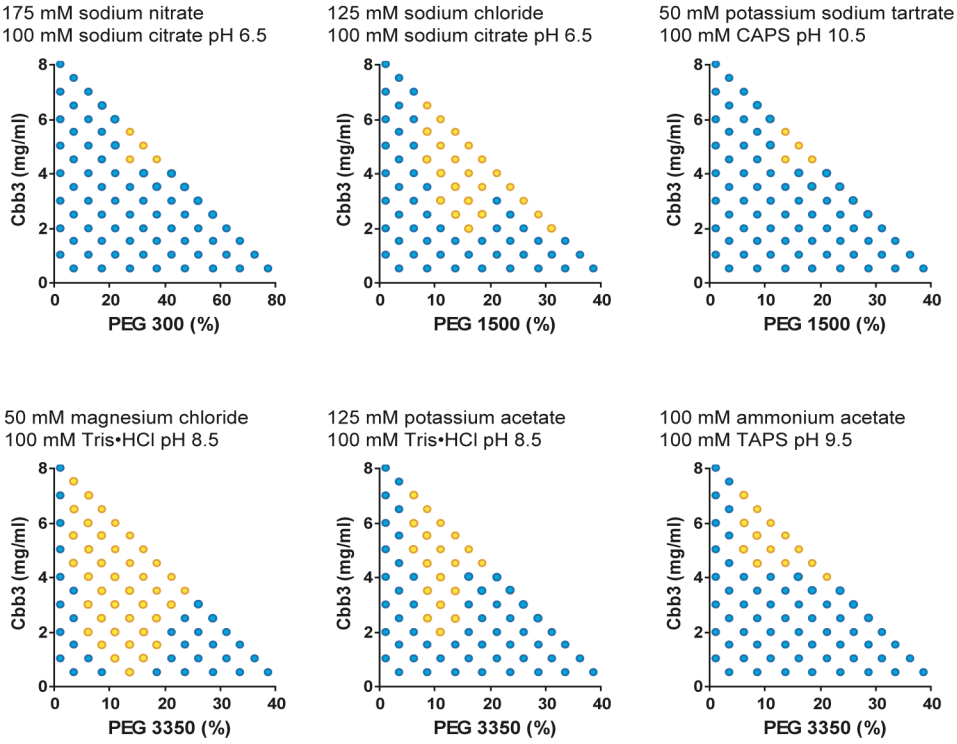

100 mM sodium phosphate
100 mM TAPS pH 9.5

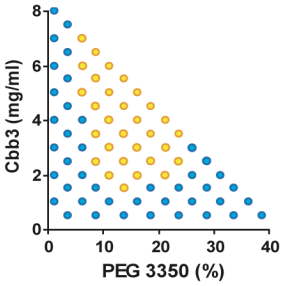

125 mM sodium chloride
100 mM sodium acetate pH 4.5

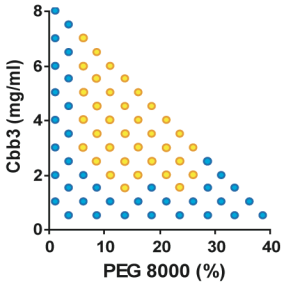

50 mM magnesium sulfate
100 mM sodium acetate pH 4.5

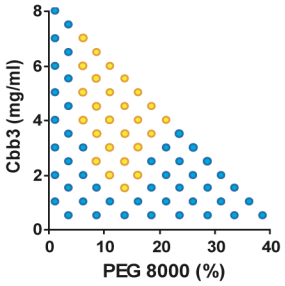

75 mM sodium acetate
100 mM sodium citrate pH 6.5

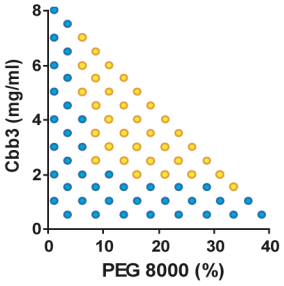

125 mM potassium acetate
100 mM sodium citrate pH 6.5

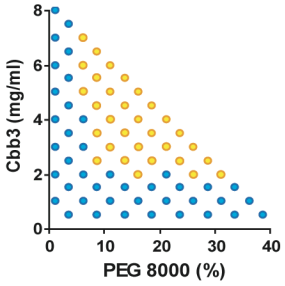

125 mM ammonium chloride
100 mM Tris•HCl pH 8.5

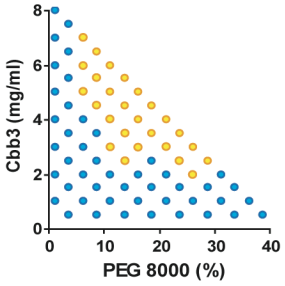

50 mM magnesium acetate
100 mM Tris•HCl pH 8.5

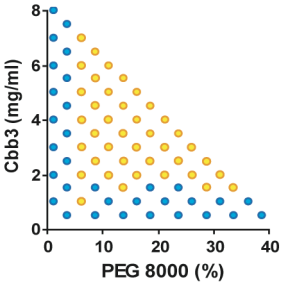

50 mM potassium sodium tartrate
100 mM TAPS pH 9.5

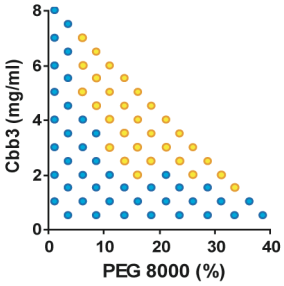

75 mM potassium chloride
100 mM TAPS pH 9.5

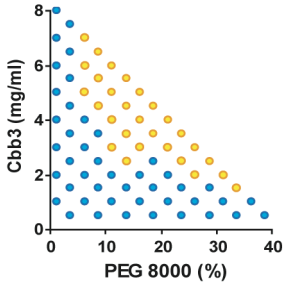

50 mM magnesium chloride
100 mM sodium acetate pH 4.5

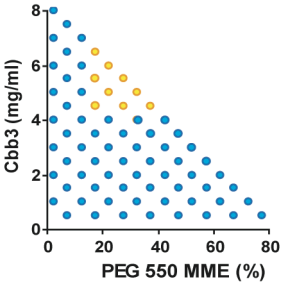

4. AlaRS Phase Diagrams:

200 mM ammonium chloride
100 mM sodium acetate pH 4.5

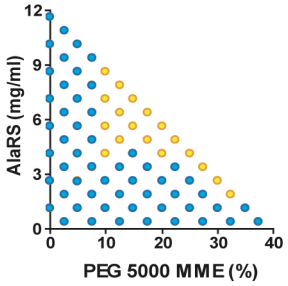

100 mM potassium chloride
100 mM sodium acetate pH 4.5

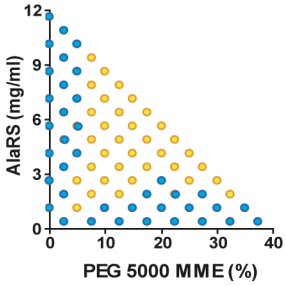

50 mM sodium acetate
100 mM sodium citrate pH 5.5

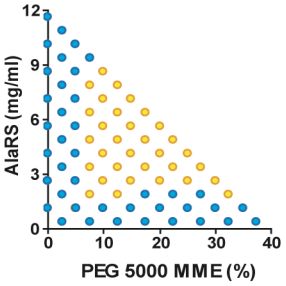

200 mM ammonium acetate
100 mM Hepes pH 6.5

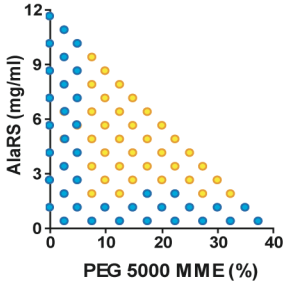

200 mM ammonium chloride
100 mM Imidazole pH 7.5

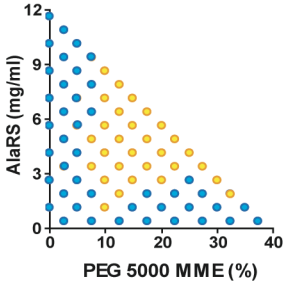

250 mM sodium chloride
100 mM TAPS pH 9.0

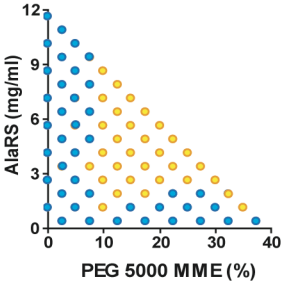

100 mM potassium acetate
100 mM TAPS pH 9.0

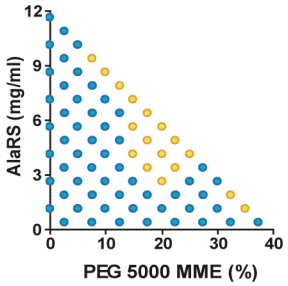

200 mM ammonium chloride
100 mM CAPS pH 10.5

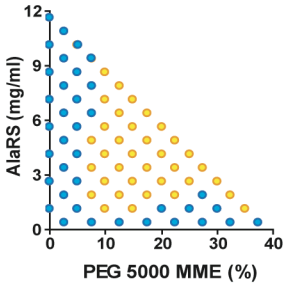

200 mM ammonium acetate
100 mM sodium acetate pH 4.5

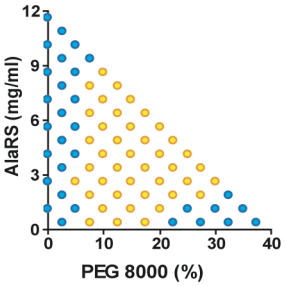

50 mM potassium sodium tartrate
100 mM sodium acetate pH 4.5

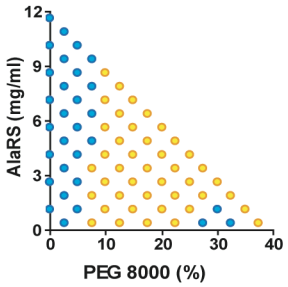

250 mM sodium chloride
100 mM Hepes pH 6.5

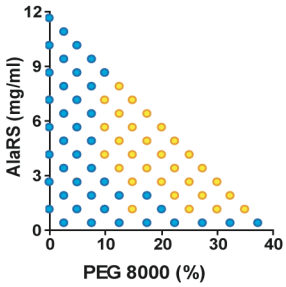

100 mM magnesium sulfate
100 mM Hepes pH 6.5

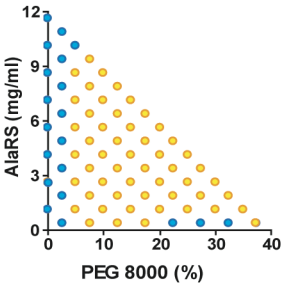

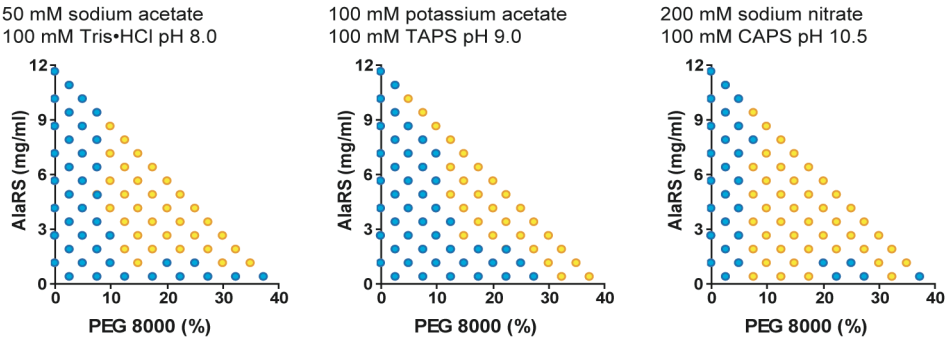
50 mM sodium acetate
100 mM Tris•HCl pH 8.0
100 mM potassium acetate
100 mM TAPS pH 9.0
200 mM sodium nitrate
100 mM CAPS pH 10.5
AlaRS (mg/ml)
PEG 8000 (%)

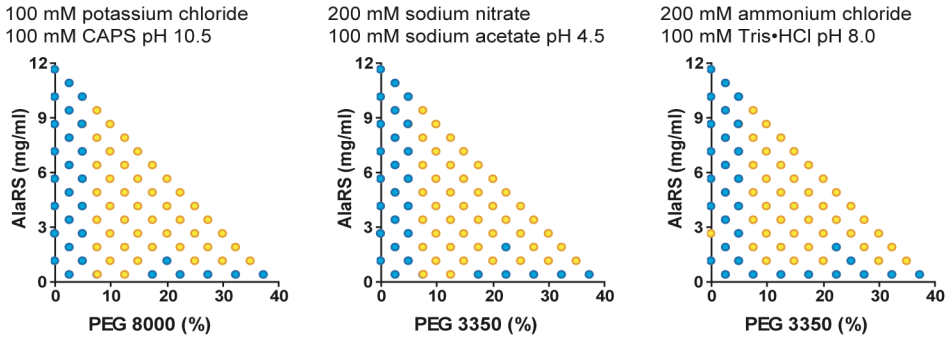
100 mM potassium chloride
100 mM CAPS pH 10.5
200 mM sodium nitrate
100 mM sodium acetate pH 4.5
200 mM ammonium chloride
100 mM Tris•HCl pH 8.0
AlaRS (mg/ml)
PEG 8000 (%)
PEG 3350 (%)

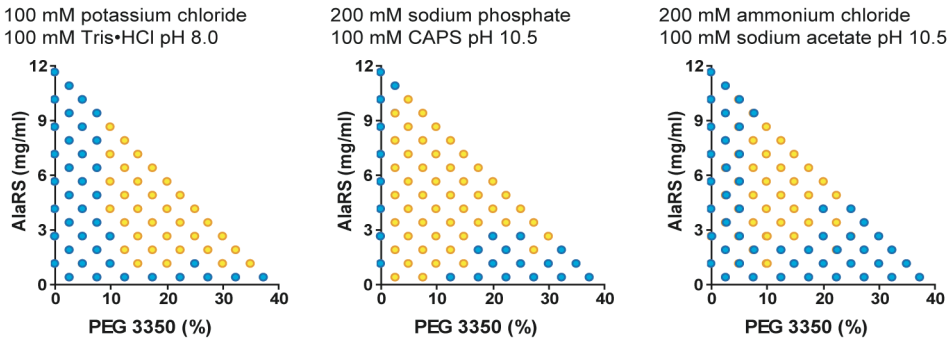
100 mM potassium chloride
100 mM Tris•HCl pH 8.0
200 mM sodium phosphate
100 mM CAPS pH 10.5
200 mM ammonium chloride
100 mM sodium acetate pH 10.5
AlaRS (mg/ml)
PEG 3350 (%)

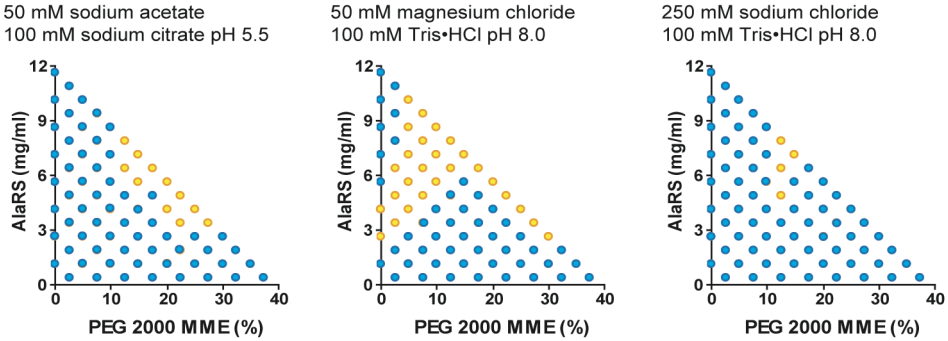
50 mM sodium acetate
100 mM sodium citrate pH 5.5
50 mM magnesium chloride
100 mM Tris•HCl pH 8.0
250 mM sodium chloride
100 mM Tris•HCl pH 8.0
AlaRS (mg/ml)
PEG 2000 MME (%)

5. Fis1 Phase Diagrams:

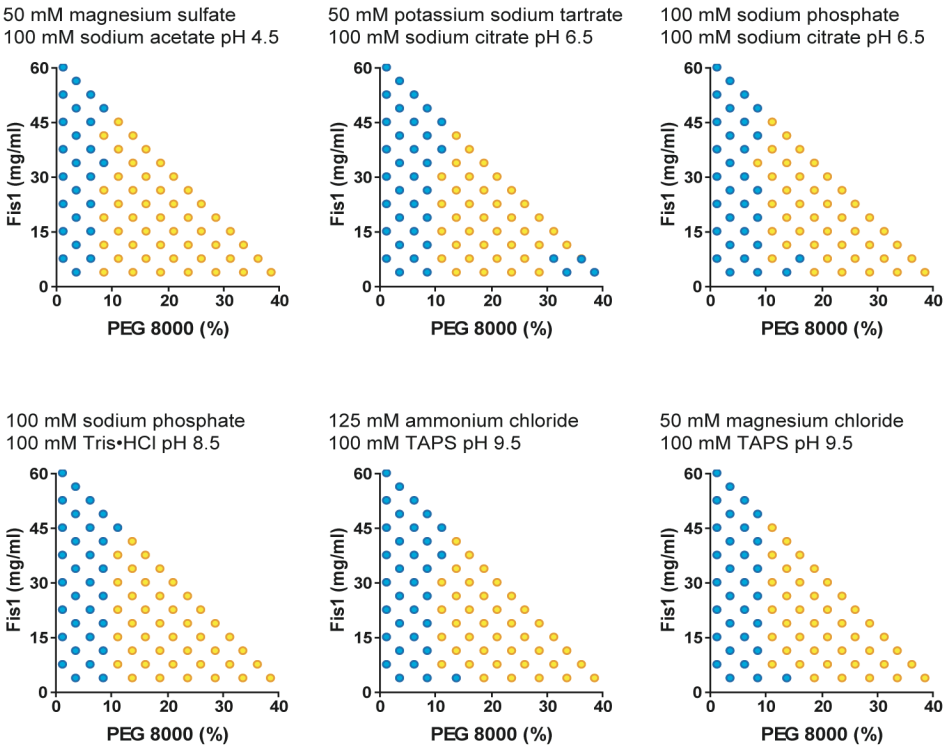

6. P450 1-12G Phase Diagrams:

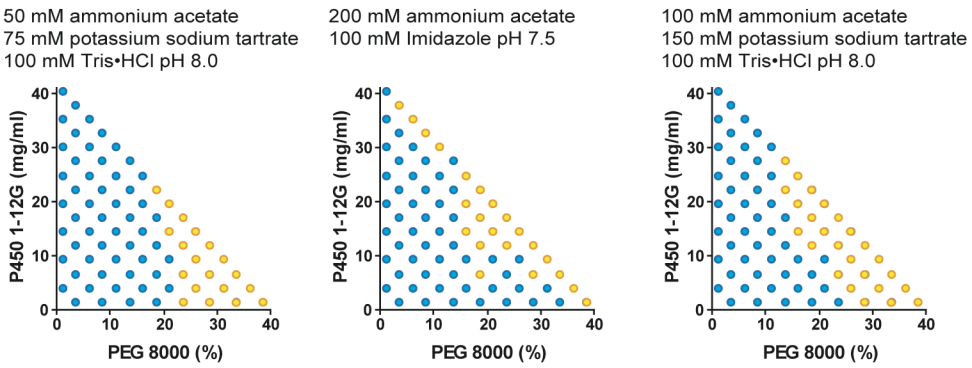

100 mM ammonium sulfate
150 mM potassium sodium tartrate
100 mM Tris•HCl pH 8.0

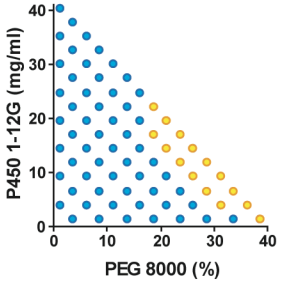

25 mM ammonium chloride
150 mM potassium sodium tartrate
100 mM Tris•HCl pH 8.0

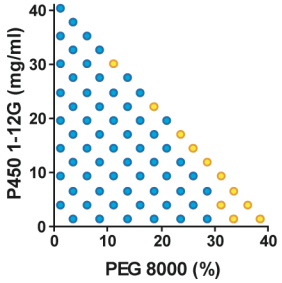

100 mM ammonium acetate
150 mM potassium sodium tartrate
100 mM Tris•HCl pH 8.0

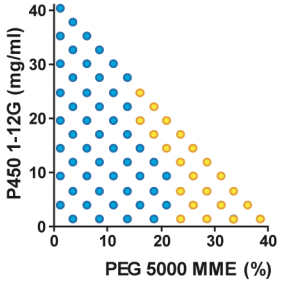

100 mM ammonium acetate
150 mM potassium sodium tartrate
100 mM Imidazole pH 7.5

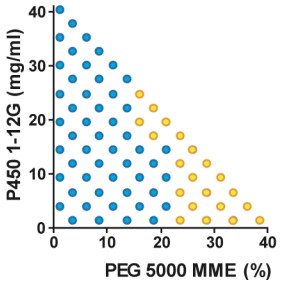

7. SMC/ScpA Phase Diagrams:

200 mM ammonium chloride
100 mM sodium acetate pH 4.5

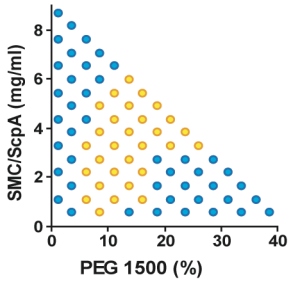

100 mM magnesium sulfate
100 mM sodium acetate pH 4.5

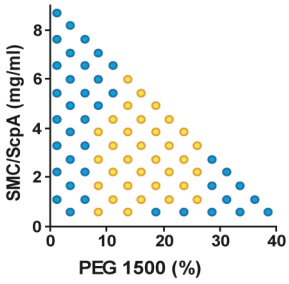

200 mM potassium phosphate
100 mM sodium acetate pH 4.5

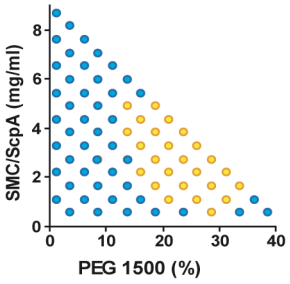

50 mM magnesium acetate
100 mM Tris•HCl pH 8.0

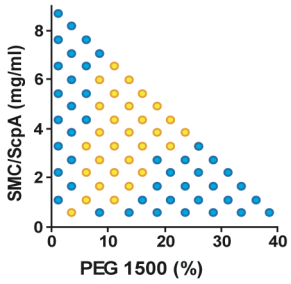

100 mM potassium acetate
100 mM Tris•HCl pH 8.0

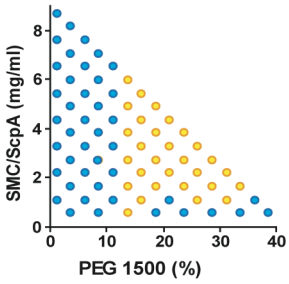

100 mM potassium chloride
100 mM Tris•HCl pH 8.0

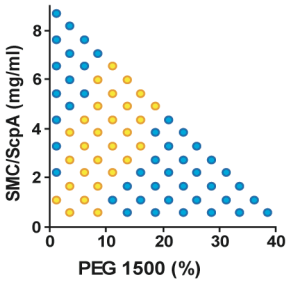

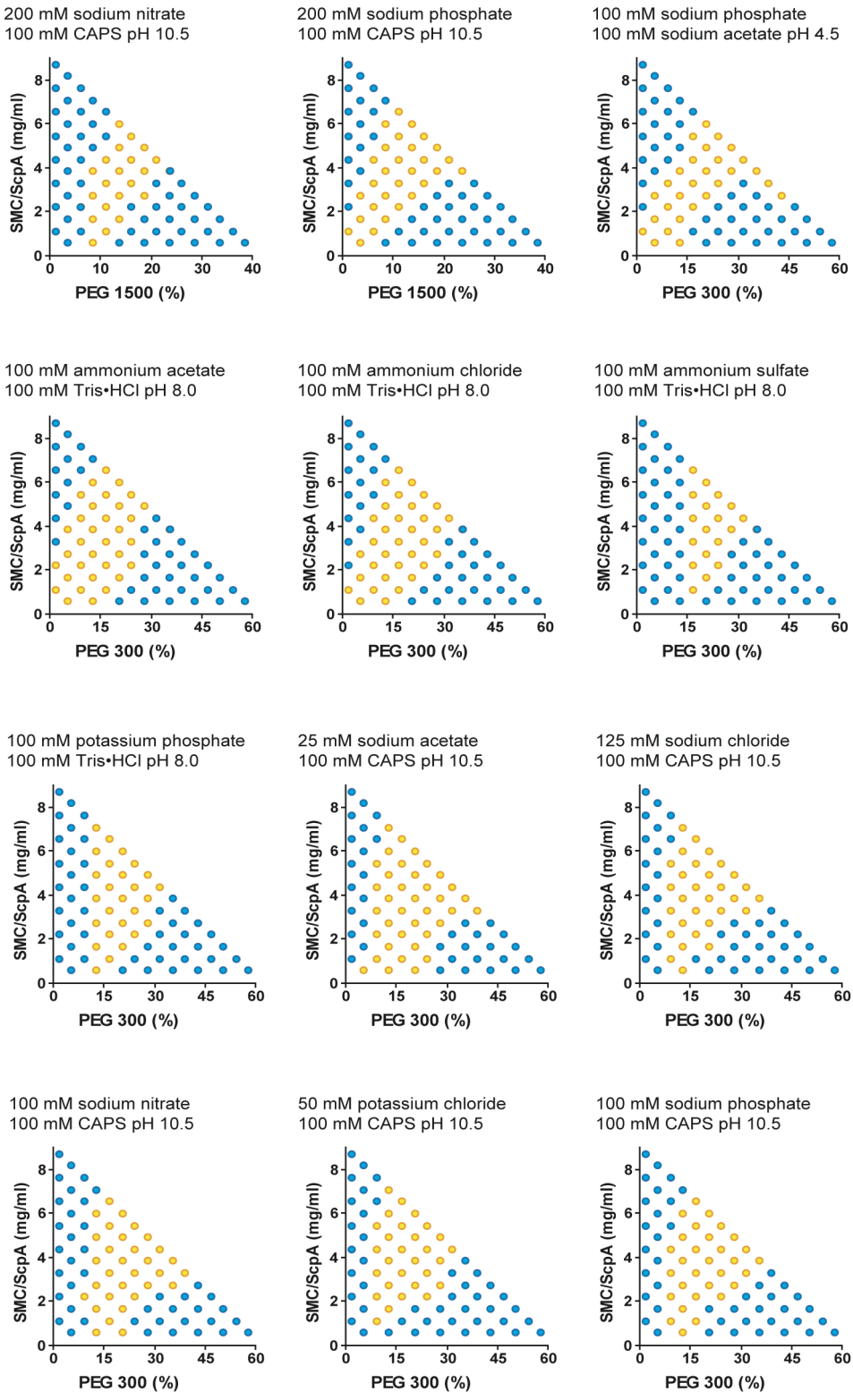
200 mM sodium nitrate
100 mM CAPS pH 10.5
200 mM sodium phosphate
100 mM CAPS pH 10.5
100 mM sodium phosphate
100 mM sodium acetate pH 4.5
100 mM ammonium acetate
100 mM Tris•HCl pH 8.0
100 mM ammonium chloride
100 mM Tris•HCl pH 8.0
100 mM ammonium sulfate
100 mM Tris•HCl pH 8.0
100 mM potassium phosphate
100 mM Tris•HCl pH 8.0
25 mM sodium acetate
100 mM CAPS pH 10.5
125 mM sodium chloride
100 mM CAPS pH 10.5
100 mM sodium nitrate
100 mM CAPS pH 10.5
50 mM potassium chloride
100 mM CAPS pH 10.5
100 mM sodium phosphate
100 mM CAPS pH 10.5
SMC/ScpA (mg/ml)
PEG 1500 (%)
PEG 300 (%)

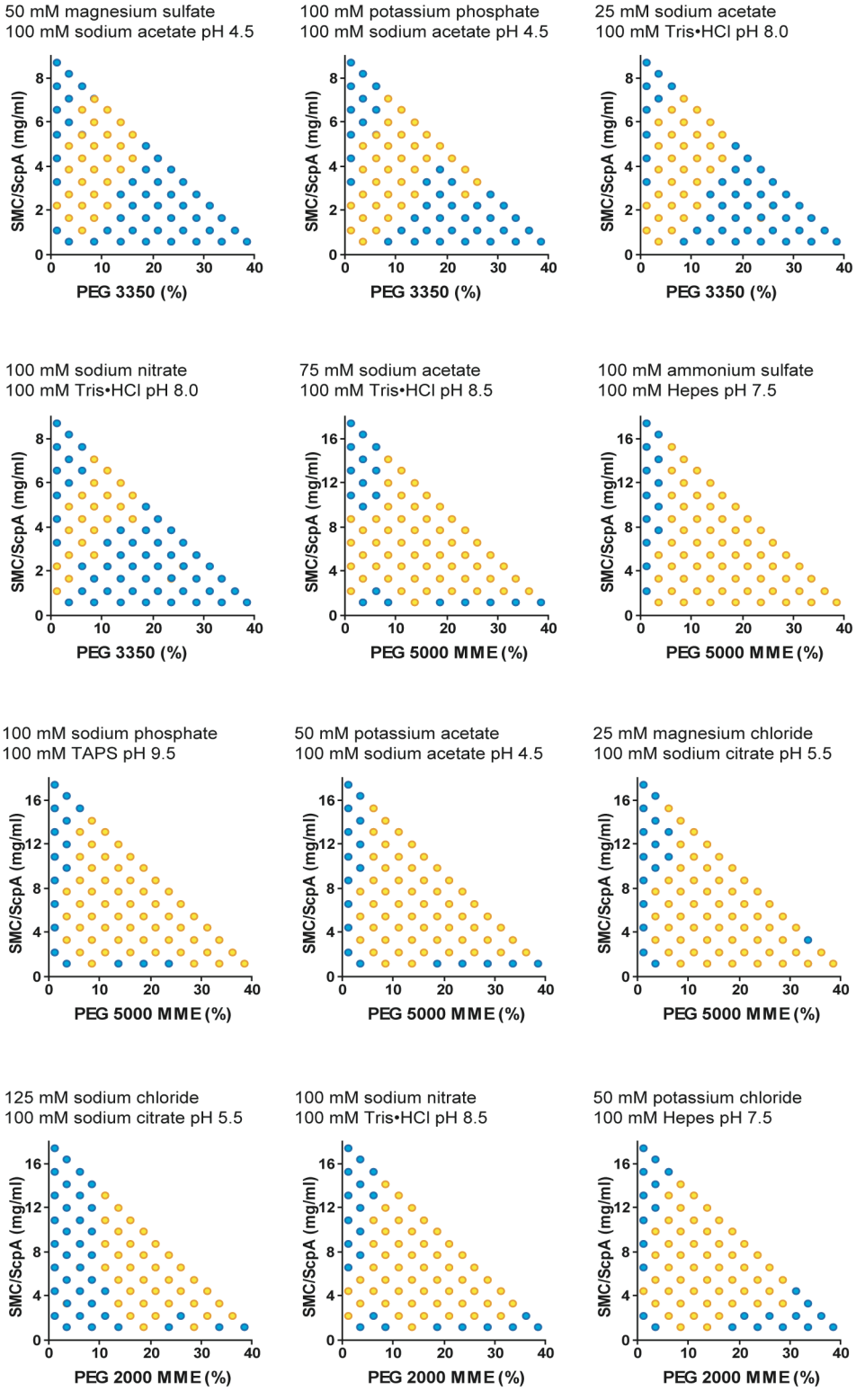
50 mM magnesium sulfate
100 mM sodium acetate pH 4.5
100 mM potassium phosphate
100 mM sodium acetate pH 4.5
25 mM sodium acetate
100 mM Tris•HCl pH 8.0
100 mM sodium nitrate
100 mM Tris•HCl pH 8.0
75 mM sodium acetate
100 mM Tris•HCl pH 8.5
100 mM ammonium sulfate
100 mM Hepes pH 7.5
100 mM sodium phosphate
100 mM TAPS pH 9.5
50 mM potassium acetate
100 mM sodium acetate pH 4.5
25 mM magnesium chloride
100 mM sodium citrate pH 5.5
125 mM sodium chloride
100 mM sodium citrate pH 5.5
100 mM sodium nitrate
100 mM Tris•HCl pH 8.5
50 mM potassium chloride
100 mM Hepes pH 7.5
SMC/ScpA (mg/ml)
PEG 3350 (%)
PEG 5000 MME (%)
PEG 2000 MME (%)

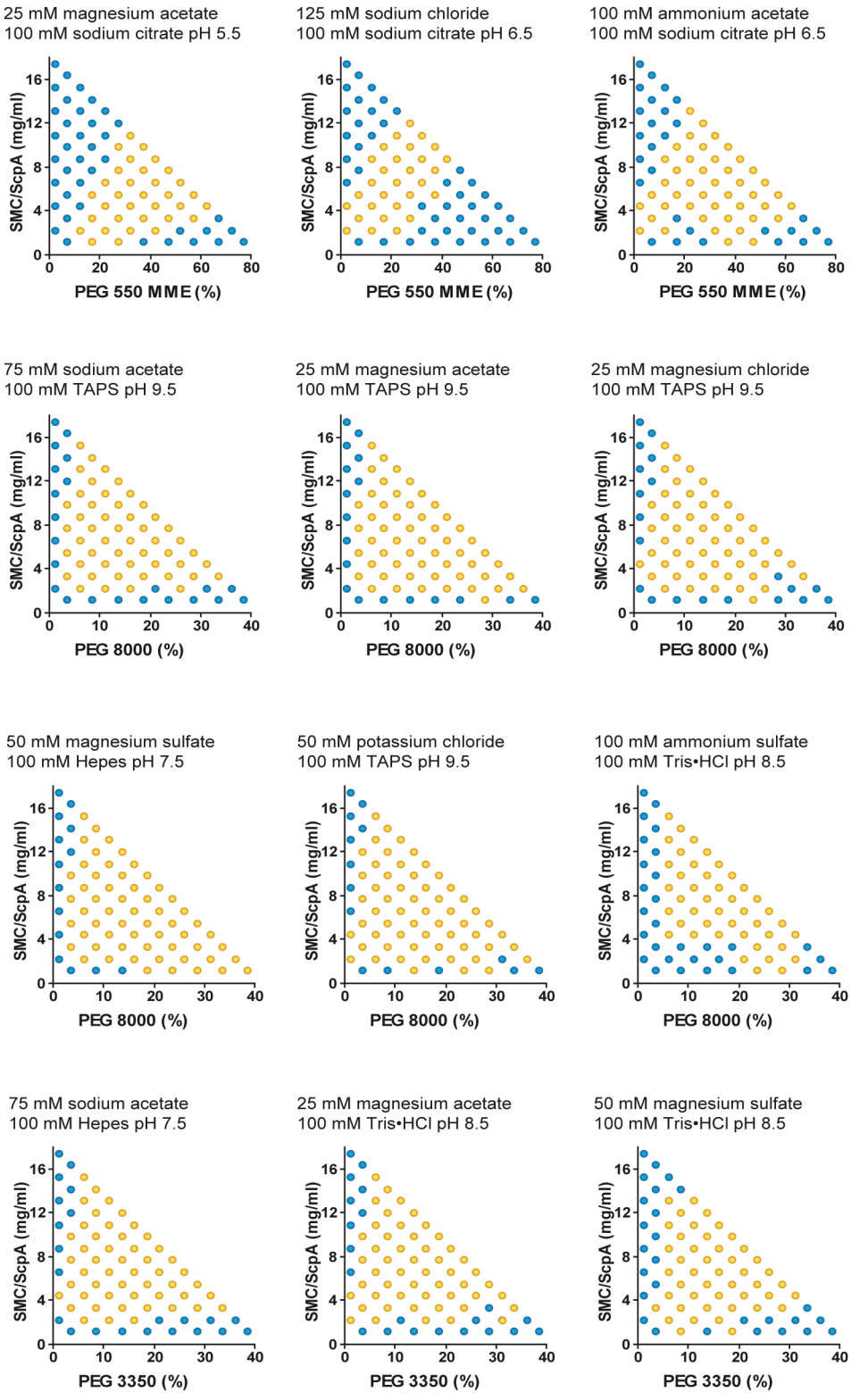
25 mM magnesium acetate
100 mM sodium citrate pH 5.5
125 mM sodium chloride
100 mM sodium citrate pH 6.5
100 mM ammonium acetate
100 mM sodium citrate pH 6.5
75 mM sodium acetate
100 mM TAPS pH 9.5
25 mM magnesium acetate
100 mM TAPS pH 9.5
25 mM magnesium chloride
100 mM TAPS pH 9.5
50 mM magnesium sulfate
100 mM Hepes pH 7.5
50 mM potassium chloride
100 mM TAPS pH 9.5
100 mM ammonium sulfate
100 mM Tris•HCl pH 8.5
75 mM sodium acetate
100 mM Hepes pH 7.5
25 mM magnesium acetate
100 mM Tris•HCl pH 8.5
50 mM magnesium sulfate
100 mM Tris•HCl pH 8.5
SMC/ScpA (mg/ml)
PEG 550 MME (%)
PEG 8000 (%)
PEG 3350 (%)

50 mM potassium acetate
100 mM TAPS pH 9.5

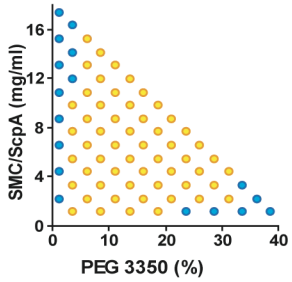

100 mM ammonium acetate
100 mM sodium citrate pH 6.5

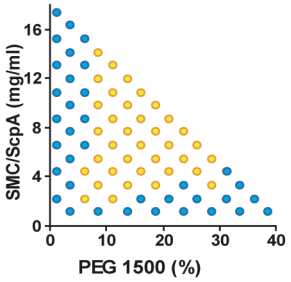

125 mM sodium chloride
100 mM TAPS pH 9.5

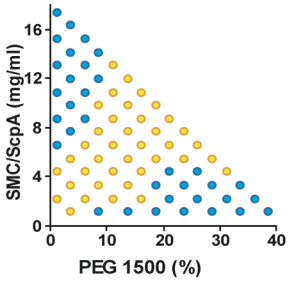

100 mM sodium phosphate
100 mM sodium citrate pH 5.5

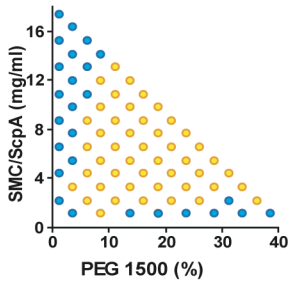

8. P2X Phase Diagrams:

600 mM sodium chloride
100 mM TAPS pH 9.5

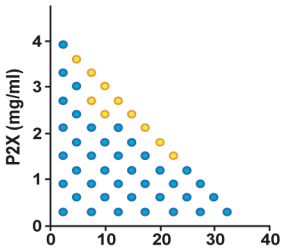

300 mM lithium chloride
100 mM CHES pH 10.5

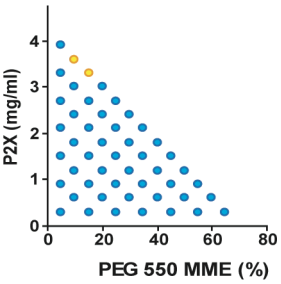

200 mM magnesium acetate
100 mM sodium citrate pH 5.5

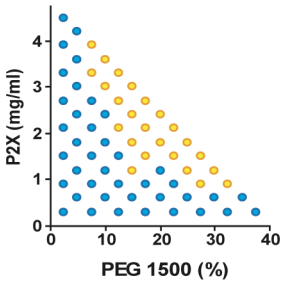

200 mM magnesium sulfate
100 mM Hepes pH 7.5

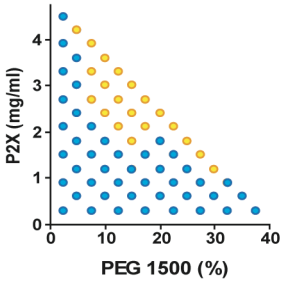

200 mM magnesium chloride
100 mM Citric Acid pH 3.5

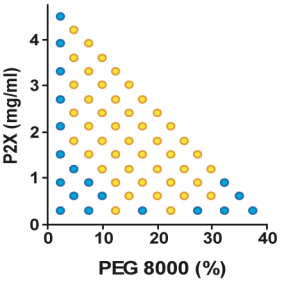

500 mM potassium acetate
100 mM sodium citrate pH 5.5

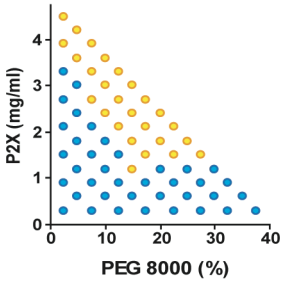

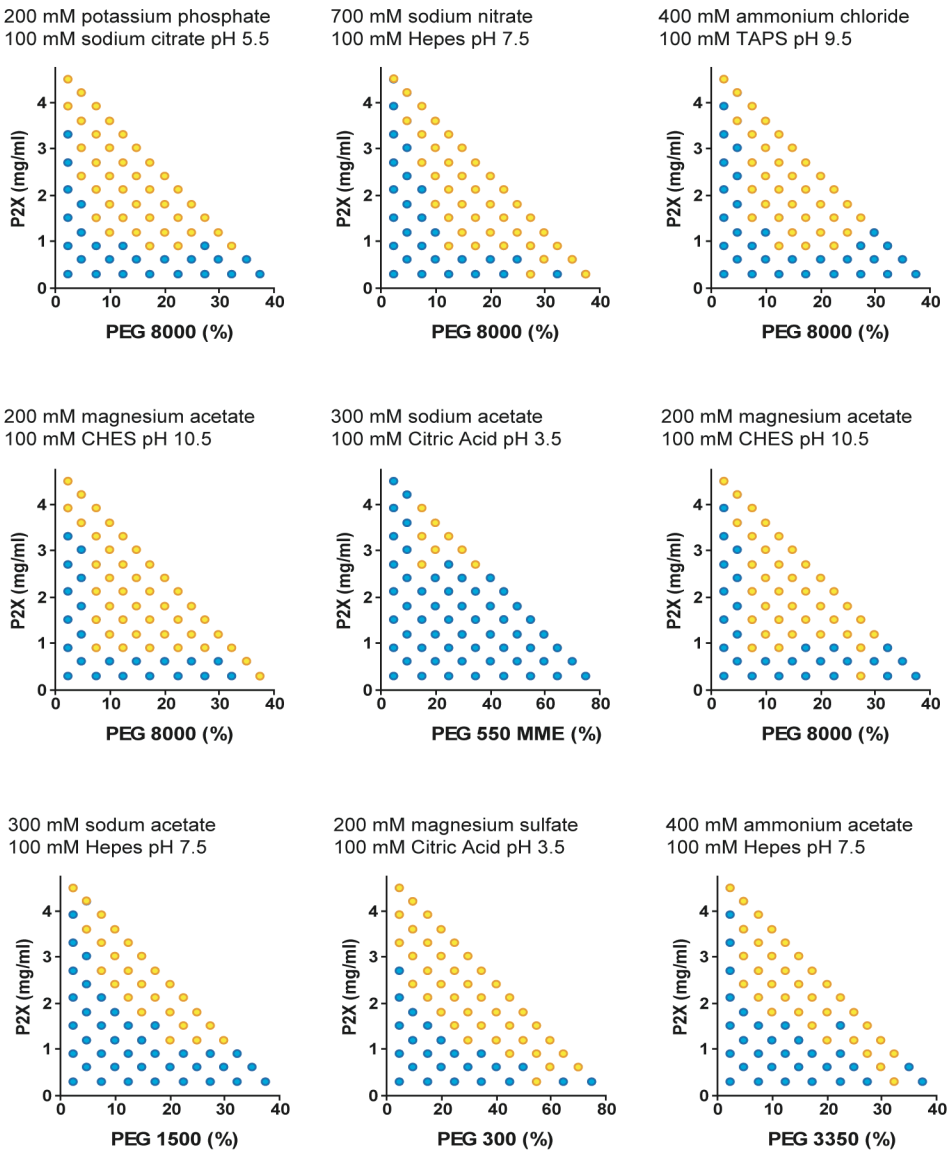

9. AMG Phase Diagrams:

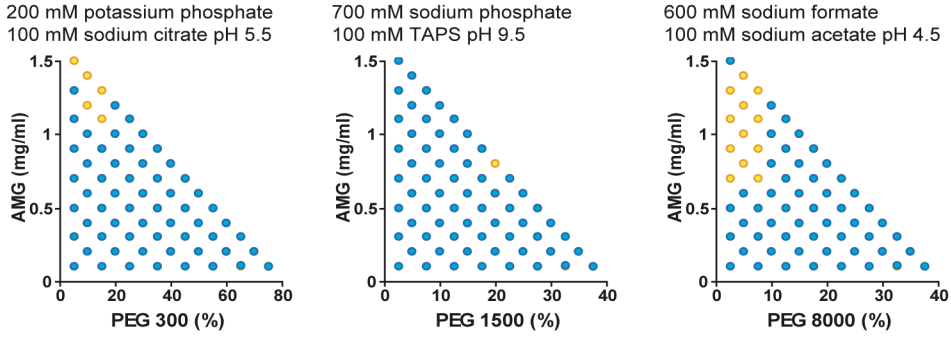

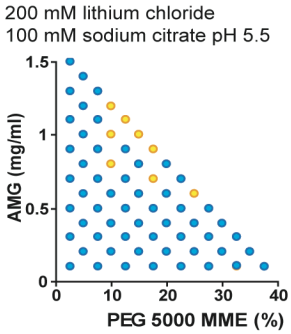

10. VCP/Vimp Phase Diagrams:

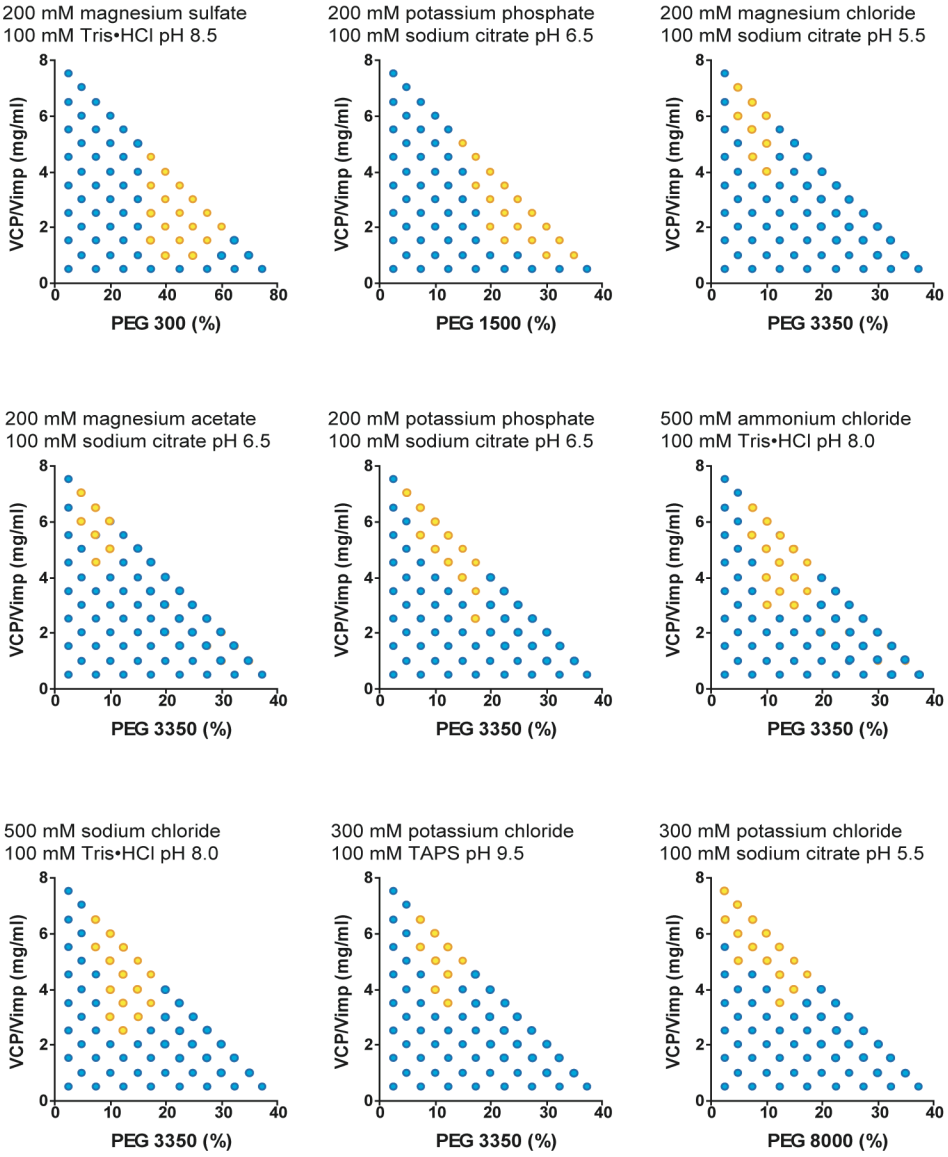

11. Tf/TfR Phase Diagrams:

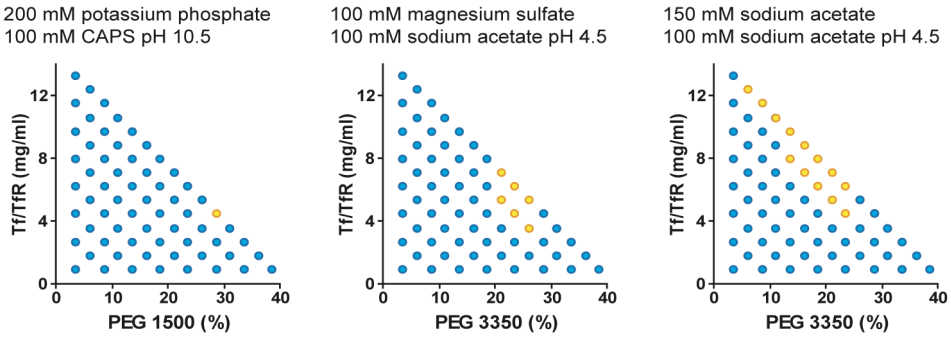

Appendix D

GLYCEROL KINASE EXPRESSION AND PURIFICATION PROTOCOLS

I. Protein Expression

GK^{G230D} and GK^{M271I} are in pETBlue2 vectors (Novagen) and have non-cleavable C-terminal HSV and His_6-tags. GK^{D72A} and GK^{235KGG} are in pETBlue1 vectors (Novagen) and have cleavable N-terminal His_6-tags.

1. Transfect the clones into BL21(DE3) chemically competent cells (Invitrogen).
    - Thaw cells on ice for 10 min.
    - Add 1 μl of the clones to the cells and incubate on ice for 30 min.
    - Heat shock the cells for 30 sec in a 42 °C water bath and return to ice.
    - Add 250 μl of SOC medium to cells and place in shaker for one hour at 37 °C, 250 rpm.
    - Plate 50 μl of cells onto an LB ampicillin (AMP) plate (50 μg/ml AMP) and incubate overnight at 37 °C.
2. Prepare starter culture and begin protein expression.
    - Pick one colony from the LB AMP plate and place in 100 ml of 37 °C LB AMP (50 μg/ml AMP).
    - Shake starter culture overnight at 37 °C, 250 rpm.
    - Prepare 2 L of LB AMP (50 μg/ml AMP) in a 4 L flask and store at 37 °C.
    - The next morning, add the starter culture to the 2 L of LB AMP and shake at 37 °C, 250 rpm until flask reaches an OD600 of 0.75 (approximately 2 hours).

- Inoculate cells with 1 mM isopropyl β-D-1-thiogalactopyranoside (IPTG) and shake for 4 hours.
- Spin down culture for 30 min at 4 °C, 4000 rpm.
- Remove supernatant, divide into 4 pellets, and store at -80 °C until purification.

II. Protein Purification for GK^{G230D} and GK^{M271I}

1. Sonicate cells.

- Thaw one pellet on ice for 20 min.
- Resuspend pellet on ice with 45 ml of:

  200 mM sodium chloride
  10 mM Tris·HCl pH 7.4
  1 mM PMSF protease inhibitor

- Sonicate solution on ice to lyse cells using the following recipe:

  a. Sonicate for 10 sec.
  b. Pause for 10 sec.
  c. Repeat 20 sec pattern for 2 min.

- Spin down sonicated solution for 30 min at 4 °C, 5000 rpm.
- Move supernatant to a clean tube for nickel-nitrilotriacetic acid (Ni-NTA) purification.

2. Ni-NTA purification of supernatant

- Add 1 ml of Ni-NTA resin (Qiagen) to the supernatant and incubate for 1 hour at 4 °C.
- Load the supernatant/resin mixture into a 10 ml disposable chromatography column (BioRad).
- Wash the column with 20 ml of wash buffer:

200 mM sodium chloride
10 mM Tris·HCl pH pH 7.4

- Elute the protein with an Imidazole gradient:

    1. 2 ml of wash buffer with 20 mM Imidazole
    2. 2 ml of wash buffer with 50 mM Imidazole
    3. 5 ml of wash buffer with 200 mM Imidazole

- Analyze with a PAGE gel to find the protein (usually in the 50 mM fraction).

- Dialyze the protein overnight at 4 °C for anion exchange into:

    100 mM potassium chloride
    20 mM Tris·HCl pH 8.0
    10 mM glycerol
    1mM βME

3. Anion exchange of Ni-NTA purified sample

- Concentrate dialyzed protein at 4 °C to 1 ml for anion exchange.

- Prepare two solutions for anion exchange:

    Solution A: 20 mM Tris·HCl pH 8.0
    10 mM glycerol
    1 mM βME

    Solution B: 1M potassium chloride
    20 mM Tris·HCl pH 8.0
    10 mM glycerol
    1 mM βME

- Prepare the Mono Q 5/50 GL column (GE Life Sciences) in the FPLC:

    a. Place line A1 in Solution A.
    b. Place line A2 into H_2O.
    c. Place line B1 in Solution B.
    d. Pump-Wash-Purify lines A1, A2, and B1.
    e. Flow line A2 at 0.5 ml/min and connect the column.
    f. Flush one cv (1 ml) of line A2 at 1 ml/min.
    g. Flush one cv of line A1 at 1 ml/min.
    h. Put the column into starting buffer for the sample (90% line A1, 10% line B1).
    i. Load 1 ml of protein into the injection loop and start purification:

1. Run 0.25 cv of 90% line A1, 10% line B1.
2. Pump inject sample.
   a. Set at gradient to 100% line B1 over the course of 15 cv.
   b. Collect 0.5 ml fractions once gradient begins.

- Analyze with a PAGE gel to find the protein (usually around 30–40% B1).
- Dialyze the protein overnight at 4 °C for gel filtration into:

  20 mM Tris·HCl pH 7.5
  10 mM glycerol
  1mM βME

4. Gel filtration of anion-exchange purified sample

- Concentrate dialyzed protein at 4 °C to 200 μl for gel filtration.
- Prepare one solution for gel filtration:

  Solution A: 20 mM Tris·HCl pH 7.5
  10 mM glycerol
  1 mM βME

- Prepare the Superdex 200 10/30 GL column (GE Life Sciences) in the Fast Protein Liquid Chromatography (FPLC) system:

  a. Place line A1 in Solution A.
  b. Place line B1 in H_2O.
  c. Pump-Wash-Purify lines A1 and B1.
  d. Flow line B1 at 0.5 ml/min and connect the column.
  e. Flush one column volume (cv) (24 ml) of line B1 at 0.5 ml/min.
  f. Flush one cv of line A1 at 0.5 ml/min.
  g. Load 200 μl of protein into the injection loop and start purification:

     1. Run 0.25 cv of line A1.
     2. Pump inject sample.
     3. Run 1.25 cv of line A1 and collect 0.5 ml fractions.

- Analyze with a polyacrylamide gel electrophoresis (PAGE) gel to find the protein (usually around 12 ml).
- Collect the fractions with protein, and if the protein is pure enough (at least 95%), concentrate to 30 mg/ml, flash freeze, and store at -80 °C.

- If protein is less than 95% pure, concentrate fractions to 200 μl and run a second gel filtration column.

III. Protein Purification for GK^{D72A} and GK^{235KGG}

1. Sonicate cells.

- Thaw one pellet on ice for 20 min.
- Resuspend pellet on ice with 45 ml of:

  200 mM sodium chloride
  10 mM Tris·HCl pH 7.4
  1 mM PMSF protease inhibitor

- Sonicate solution on ice to lyse cells using the following recipe:

  a. Sonicate for 10 sec.
  b. Pause for 10 sec.
  c. Repeat 20 sec pattern for 2 min.

- Spin down sonicated solution for 30 min at 4 °C, 5000 rpm.
- Move supernatant to a clean tube for Ni-NTA purification.

2. Ni-NTA purification of supernatant

- Add 1 ml of Ni-NTA resin to the supernatant and incubate for 1 hour at 4 °C.
- Load the supernatant/resin mixture into a 10 ml disposable chromatography column.
- Wash the column with 20 ml of wash buffer:

  200 mM sodium chloride
  10 mM Tris·HCl pH 7.4

- Elute the protein with an Imidazole gradient:

  a. 2 ml of wash buffer with 20 mM Imidazole
  b. 2 ml of wash buffer with 50 mM Imidazole
  c. 5 ml of wash buffer with 200 mM Imidazole

- Analyze with a PAGE gel to find the protein (usually in the 50 mM fraction).
- Dialyze the protein overnight at 4 °C for His_6-tag cleavage into:

    20 mM Tris·HCl pH 7.5
    10 mM glycerol
    1mM βME

3. Removal of N-terminal His_6-tag

- Prepare His_6-tag cleavage reaction using Tobacco Etch Virus (TEV) Protease (Invitrogen):

    150 µl 0.1 M dithiothreitol (DTT)
    750 µl 20X TEV Buffer
    1000 U TEV Protease

- Add dialyzed protein to the cleavage reaction and incubate for 3 hours at 21 °C.
- Upon completion of cleavage, perform Ni-NTA purification to remove AcTEV Protease and the cleaved N-terminal His_6-tags.
- Add 1 ml of Ni-NTA resin to the reaction and incubate for 1 hour at 4 °C.
- Load the protein/resin mixture into a 10 ml disposable chromatography column.
- Collect the flow through and wash the column with 20 ml of wash buffer:

    20 mM Tris·HCl pH 7.5
    10 mM glycerol
    1mM βME

- Analyze with a PAGE gel to find the protein (usually in the flow-through).
- Dialyze the protein overnight at 4 °C for gel filtration into:

    20 mM Tris·HCl pH 7.5
    10 mM glycerol
    1mM βME

4. Gel filtration of Ni-NTA purified sample

- Concentrate dialyzed protein at 4 °C to 200 μl for gel filtration.
- Prepare one solution for gel filtration:

  Solution A: 20 mM Tris·HCl pH 7.5
  10 mM glycerol
  1 mM βME

- Prepare the Superdex 200 10/30 GL column in the FPLC system:

  a. Place line A1 in Solution A.
  b. Place line B1 in H_2O.
  c. Pump-Wash-Purify lines A1 and B1.
  4. Flow line B1 at 0.5 ml/min and connect the column.
  5. Flush one cv (24 ml) of line B1 at 0.5 ml/min.
  6. Flush one cv of line A1 at 0.5 ml/min.
  7. Load 200 μl of protein into the injection loop and start purification:

     1. Run 0.25 cv of line A1.
     2. Pump inject sample.
     3. Run 1.25 cv of line A1 and collect 0.5 ml fractions.

- Analyze with a PAGE gel to find the protein (usually around 12 ml).
- Collect the fractions with protein, and if the protein is pure enough (at least 95%), concentrate to 30 mg/ml, flash freeze, and store at -80 °C.
- If protein is less than 95% pure, concentrate fractions to 200 μl and run a second gel filtration column.

Appendix E

CRYSTALLIZATION EXPERIMENTAL TALLY

Crystallization Target	Solubility Screening	Phase Diagrams	Screening Devices	Diffraction Devices	Dialysis Devices	Total
19S Lid	3906	1	14	4		7738
AlaRS	4826	39	15			11234
AMG	6019	24	4			8707
bR	3529	17	8	4		7073
bR D85S	3705	19	7	2		6953
Cbb3	3459	29	9	8		8507
Fis1	4840	18	7			7816
P450 1-12G	3816	9	27	14		12344
VCP/VimpC	6307	18	10	9		10903
P2X	6374	45	16			13454
SMC/ScpA	2767	55	16			10567
Tf/TfR	8005	17	4			10189
GK^{G230D}	18095	37	21	19	2	27749
GK^{235KGG}	8257	0	24	52		19217
GK^{D72A}	9114	0	10	13		12814
GK^{M271I}	6698	0	26	54		18338
GK^{Q37P}	4141	0	9	14		7701
GK^{W53G}	0	0	16	5		4340
KcsA Channel	0	0	13	9	50	5270
Actomyosin	3926	32	5			7430
B1DGH	10938	65	14	23		21278
GPCR	2652	0				2652
hALR2 T113A	3122	0	8	4		5442
hALR2 F115Y	0	0	8	4		2320
Hop2/Mnd1	2693	21	24	10		10965
Mfn1	1347	0				1347
MukBEF	4008	0				4008
MukEF	4676	17	4			6860
Full P450 1-12G	0	0	16	2		4040
Tf/DNA	2806	0	1			3046
Tf/DNA Sample 2	8075	6	10			10907
VimpC	0	25	5			3000
YxiN RNA-P	3865	52	5			8809
Total Experiments	*151966*	*39312*	*85440*	*25000*	*1300*	*303018*

Bibliography

1. Scapin, G. (2006) Structural biology and drug design. *Curr. Pharm. Des. 12*, 2087–2097.
2. Dickerson, R. E., Kendrew, J. C., and Standberg, B. E. (1961) The crystal structure of myoglobin: phase determination to a resolution of 2 Å by the method of isomorphous replacement. *Acta Crystallogr. 14*, 1188–1195.
3. Chayen, N. E., and Saridakis, E. (2008) Protein crystallization: from purified protein to diffraction-quality crystal. *Nat. Methods 5*, 147–153.
4. Hansen, C. L., Skordalakes, E., Berger, J., and Quake, S. R. (2002) A robust and scalable microfluidic metering method that allows protein crystal growth by free interface diffusion. *Proc. Natl. Acad. Sci. U. S. A. 99*, 16531–16536.
5. Zheng, B., Roach, L. S., and Ismagilov, R. F. (2003) Screening of protein crystallization conditions on a microfluidic chip using nanoliter-size droplets. *J. Am. Chem. Soc. 125*, 11170–11171.
6. Hansen, C. L., Classen, S., Berger, J. M., and Quake, S. R. (2006) A microfluidic device for kinetic optimization of protein crystallization and in situ structure determination. *J. Am. Chem. Soc. 128*, 3142–3143.
7. Unger, M. A., Chou, H., Thorsen, T., Scherer, A., and Quake, S. R. (2000) Monolithic microfabricated valves and pumps with multilayer soft lithography. *Science 288*, 113–116.
8. Chou, H. P., Unger, M. A., and Quake, S. R. (2001) A microfabricated rotary pump. *Biomed. Microdevices 3*, 323–330.

9. Thorsen, T., Maerkl, S. J., and Quake, S. R. (2002) Microfluidic large-scale integration. *Science 298*, 580–584.

10. Hansen, C. L., Sommer, M. O., and Quake, S. R. (2004) Systematic investigation of protein phase behavior with a microfluidic formulator. *Proc. Natl. Acad. Sci. U. S. A. 101*, 14431–14436.

11. Squires, T. M., and Quake, S. R. (2004) Microfluidics: fluid physics at the nanoliter scale. *Rev. Mod. Phys. 7*, 977–1026.

12. Anderson, M. J., Hansen, C. L., and Quake, S. R. (2006) Phase knowledge enables rational screens for protein crystallization. *Proc. Nat. Acad. Sci. U. S. A. 103*, 16746–16751.

13. Anderson, M. J., DeLaBarre, B., Raghunathan, A., Palsson, B. O., Brunger, A. T., and Quake, S. R. (2007) Crystal structure of a hyperactive *Escherichia coli* glycerol kinase mutant Gly230 → Asp obtained using microfluidic crystallization devices. *Biochemistry 46*, 5722–5731.

14. Carter, C. W., Jr., and Carter, C. W. (1979) Protein crystallization using incomplete factorial experiments. *J. Biol. Chem. 254*, 12219–12223.

15. Jancarik, J., and Kim, S.-H. (1991) Sparse matrix sampling: a screening method for crystallization of proteins. *J. Appl. Crystallogr. 24*, 409–411.

16. Carbonnaux, C., Ries-Kautt, M., and Ducruix, A. (1995) Relative effectiveness of various anions on the solubility of acidic *Hypoderma lineatum* collagenase at pH 7.2. *Protein Sci. 4*, 2123–2128.

17. Ewing, F., Forsythe, E., and Pusey, M. (1994) Orthorhombic lysozyme solubility. *Acta Crystallogr. D40*, 424–428.

18. Forsythe, E. L., Judge, R. A., and Pusey, M. L. (1999) Tetragonal chicken egg white lysozyme solubility in sodium chloride solutions. *J. Chem. Eng. Data 44*, 637–640.

19. Gaucher, J.-F., Ries-Kautt, M., Reiss-Husson, F., and Ducruix, A. (1997) Solubility diagram of the *Rhodobacter sphaeroides* reaction center as a function of PEG concentration. *FEBS Lett. 401*, 113–116.

20. Odahara, T., Ataka, M., and Katsura, T. (1994) Phase diagram determination to elucidate the crystal growth of the photoreaction center from *Rhodobacter sphaeroides*. *Acta Crystallogr. D30*, 639–642.

21. Ries-Kautt, M. M., and Ducruix, A. F. (1989) Relative effectiveness of various ions on the solubility and crystal growth of lysozyme. *J. Biol. Chem. 264*, 745–748.

22. Saridakis, E., and Chayen, N. E. (2003) Systematic improvement of protein crystals by determining the supersolubility curves of phase diagrams. *Biophys. J. 84*, 1218–1222.

23. Saridakis, E. E. G., Shaw Stewart, P. D., Lloyd, L. F., and Blow, D. M. (1994) Phase diagram and dilution experiments in the crystallization of carboxypeptidase G2. *Acta Crystallogr. D50*, 293–297.

24. Sauter, C., Lorber, B., Kern, D., Cavarelli, J., Moras, D., and Giege, R. (1999) Crystallogenesis studies on yeast aspartyl-tRNA synthetase: use of phase diagram to improve crystal quality. *Acta Crystallogr. D55*, 149–156.

25. Yoshizaki, I., Nakamura, H., Fukuyama, S., Komatsu, H., and Yoda, S. (2004) Scientific approach to the optimization of protein crystallization conditions for microgravity experiments. *Ann. N.Y. Acad. Sci. 1027*, 28–47.

26. Sommer, M. O. A., and Larsen, S. (2005) Crystallizing proteins on the basis of their precipitation diagram determined using a microfluidic formulator. *J. Synchrotron Rad. 12*, 779–785.

27. Hofmeister, F. (1888) *Arch. Exp. Pathol. Pharmakol. 24*, 247–260.

28. Ibarra, R. U., Edwards, J. S., and Palsson, B. O. (2002) *Escherichia coli* K-12 undergoes adaptive evolution to achieve in silico predicted optimal growth. *Nature 420*, 186–189.

29. Honisch, C., Raghunathan, A., Cantor, C. R., Palsson, B. O., and van den Boom, D. (2004) High-throughput mutation detection underlying adaptive evolution of *Escherichia coli*-K12. *Genome Res. 14*, 2495–2502.

30. Herring, C. D., Raghunathan, A., Honisch, C., Patel, T., Applebee, M. K., Joyce, A. R., Albert, T. J., Blattner, F. R., van den Boom, D., Cantor, C. R., and Palsson, B. O. (2006) Comparative genome sequencing of *Escherichia coli* allows observation of bacterial evolution on a laboratory timescale. *Nat. Genet. 38*, 1406–1412.

31. Zwaig, N., Kistler, W. S., and Lin, E. C. C. (1970) Glycerol kinase, the pacemaker for the dissimilation of glycerol in *Escherichia coli*. *J. Bacteriol. 102*, 753–759.

32. Lin, E. C. C., Koch, J. P., Chused, T. M., and Jorgensen, S. E. (1962) Utilization of L-α-glycerophosphate by *Escherichia coli* without hydrolysis. *Proc. Nat. Acad. Sci. USA 48*, 2145–2150.

33. de Riel, J. K., and Paulus, H. (1978a) Subunit dissociation in the allosteric regulation of glycerol kinase from *Escherichia coli.* 1. Kinetic evidence. *Biochemistry 17*, 5134–5140.

34. de Riel, J. K., and Paulus, H. (1978b) Subunit dissociation in the allosteric regulation of glycerol kinase from *Escherichia coli*. 2. Physical evidence. *Biochemistry 17*, 5141–5145.

35. de Riel, J. K., and Paulus, H. (1978c) Subunit dissociation in the allosteric regulation of glycerol kinase from *Escherichia coli.* 3. Role in desensitization. *Biochemistry 17*, 5146–5150.

36. Pettigrew, D. W., Yu, G.-J., and Liu, Y. (1990) Nucleotide regulation of *Escherichia coli* glycerol kinase: initial-velocity and substrate binding studies. *Biochemistry 29*, 8620–8627.

37. Hurley, J. H. (1996) The sugar kinase/heat shock protein 70/actin superfamily: implications of conserved structure for mechanism. *Annu. Rev. Biophys. Biomol. Struct. 25*, 137–162.

38. Bystrom, C. E., Pettigrew, D. W., Branchaud, B. P., O'Brien, P., and Remington, S. J. (1999) Crystal structure of Escherichia coli glycerol kinase variant S58→W in complex with nonhydrolyzable ATP analogues reveal a putative active conformation of the enzyme as a result of domain motion. *Biochemistry 38*, 3508–3518.

39. Thorner, J. W., and Paulus, H. (1973) Catalytic and allosteric properties of glycerol kinase from Escherichia coli. *J. Biol. Chem. 248*, 3922–3932.

40. Bennett, W. S., Jr., and Steitz, T. A. (1978) Glucose-induced conformational change in yeast hexokinase. *Proc. Natl. Acad. Sci. U. S. A. 75*, 4848–4852.

41. Chik, J. K., Lindberg, U., and Schutt, C. E. (1996) The structure of an open state of β-actin at 2.65 Å resolution. *J. Mol. Biol. 263*, 607–623.

42. Postma, P. W., Epstein, W., Schuitema, A. R. J., and Nelson, S. O. (1984) Interaction between III^{Glc} of the phosphoenolpyruvate:sugar phosphotransferase system and glycerol kinase of *Salmonella typhimurium*. *J. Bacteriol. 158*, 351–353.

43. Novotny, M. J., Frederickson, W. L., Waygood, E. B., and Saier, M. H., Jr. (1985) Allosteric regulation of glycerol kinase by enzyme III^{Glc} of the phosphotransferase system in *Escherichia coli* and *Salmonella typhimurium*. *J. Bacteriol. 162*, 810–816.

44. Zwaig, N., and Lin, E. C. C. (1966) Feedback inhibition of glycerol kinase, a catabolic enzyme in *Escherichia coli*. *Science 153*, 755–757.

45. Hurley, J., Faber, H., Worthylake, D., Meadow, N., Roseman, S., Pettigrew, D., and Remington, S. (1993) Structure of the regulatory complex of *Escherichia coli* III^{Glc} with glycerol kinase. *Science 259*, 673–677.

46. Feese, M. D., Faber, H. R., Bystrom, C. E., Pettigrew, D. W., and Remington, S. J. (1998) Glycerol kinase from Escherichia coli and an Ala65→Thr mutant: the crystal structures reveal conformational changes with implications for allosteric regulation. *Structure 6*, 1407–1418.

47. Ormo, M. O., Bystrom, C. E., and Remington, S. J. (1998) Crystal structure of a complex of *Escherichia coli* glycerol kinase and an allosteric effector fructose 1,6-bisphosphate. *Biochemistry 37*, 16565–16572.

48. Pettigrew, D. W., Ma, D. P., Conrad, C. A., and Johnson, J. R. (1988) *Escherichia coli* glycerol kinase. Cloning and sequencing of the glpK gene and the primary structure of the enzyme. *J. Biol. Chem. 263*, 135–139.

49. Pettigrew, D., Liu, W., Holmes, C., Meadow, N., and Roseman, S. (1996) A single amino acid change in *Escherichia coli* glycerol kinase abolishes glucose control of glycerol utilization *in vivo*. *J. Bacteriol. 178*, 2846–2852.

50. Liu, W., Faber, H. R., Feese, M. D., Remington, S. J., and Pettigrew, D. W. (1994) *Escherichia coli* glycerol kinase: role of a tetramer interface in regulation by fructose 1,6-bisphosphate and phosphotransferase system regulatory protein III^{Glc}. *Biochemistry 33*, 10120–10126.

51. Faber, H. R., Pettigrew, D. W., and Remington, S. J. (1989) Crystallization and preliminary X-ray studies of *Escherichia coli* glycerol kinase. *J. Mol. Biol. 207*, 637–639.

52. Hames, C., Halbedel, S., Schilling, O., and Stulke, J. (2005) Multiple-mutation reaction: a method for simultaneous introduction of multiple mutations into the *glpK* gene of *Mycoplasma pneumoniae*. *Appl. Environ. Microbiol. 71*, 4097–4100.

53. Honisch, C., Raghunathan, A., Cantor, C. R., Palsson, B. O., and van den Boom, D. (2004) High-throughput mutation detection underlying adaptive evolution of *Escherichia coli*-K12. *Genome Res. 14*, 2495–2502.

54. Wyatt, P. J. (1993) Light scattering and the absolute characterization of macromolecules. *Analytica Chimica Acta 272*, 1–40.

55. Zhu, H., Ownby, D. W., Riggs, C. K., Nolasco, N. J., Stoops, J. K., and Riggs, A. F. (1996) Assembly of the gigantic hemoglobin of the earthworm *Lumbricus terrestris*. *J. Biol. Chem. 271*, 30007–30021.

56. Otwinowski, Z., and Minor, W. (1997) Processing X-ray diffraction data collection in oscillation mode. *Methods Enzymol. 276*, 307–326.

57. Brunger, A. T., Adams, P. D., Clore, G. M., DeLano, W. L., Gros, P., Grosse-Kunstleve, R. W., Jiang, J.-S., Kuszewski, J., Nilges, M., Pannu, N. S., Read, R. J., Rice, L. M., Simonson, T., and Warren, G. L. (1993) Crystallography & NMR system: a new software suite for macromolecular structure determination. *Acta Crystallogr. D Biol. Crystallogr. 54*, 905–921.

58. Jones, T. A., Zou, J.-Y., Cowan, S. W., and Kjeldgaard, M. (1991) Improved methods for building protein models in electron density maps and the location of errors in these models. *Acta Crystallogr. A 47*, 110–119.

59. Lovell, S. C., Davis, I. W., Arendall, W. B., III, de Bakker, P. I., Word, J. M., Prisant, M. G., Richardson, J. S., and Richardson, D. C. (2003) Structure validation by Calpha geometry: phi, psi and Cbeta deviation. *Proteins 50*, 437–450.

60. Winn, M. D., Isupov, M. N., and Murshudov, G. N. (2001) Use of TLS parameters to model anisotropic displacements in macromolecular refinement. *Acta Crystallogr. D Biol. Crystallogr, 57*, 122–133.

61. Wriggers, W., and Schulten, K. (1997) Protein domain movements: detection of rigid domains and visualization of hinges in comparisons of atomic coordinates. *Proteins: Struct., Funct., and Genet. 29*, 1–14.

62. Brunger, A. (1993) Assessment of phase accuracy by cross validation: the free R value. *Acta Crystallogr. D49*, 24–36.

63. DeLano, W. L. (2002) The PyMOL Molecular Graphics System. DeLano Scientific, San Carlos, CA.

64. Strong, M., Sawaya, M. R., Wang, S., Phillips, M., Cascio, D., and Eisenberg, D. (2006) Toward the structural genomics of complexes: crystal structure of a PE/PPE

protein complex from *Mycobacterium tuberculosis*. *Proc. Natl. Acad. Sci. U. S. A. 103*, 8060–8065.

65. Collaborative Computation Project, and Number 4. (1994) The CCP4 suite: programs for protein crystallography. *Acta Crystallogr. D50*, 760–763.

66. Emsley, P., and Cowtan, K. (2004) Coot: model-building tools for molecular graphics. *Acta Crystallogr. D60*, 2126–2132.

67. Murshudov, G. N., Vagin, A. A., and Dodson, E. J. (1997) Refinement of macromolecular structures by the Maximum-Likelihood Method. *Acta Crystallogr. D53*, 240–255.

68. van den Bedem, H., Lotan, I., Latombe, J.-C., and Deacon, A. (2005) Real-space protein-model completion: an inverse-kinematics approach. *Acta Crystallogr. D61*, 2–13.

69. Adams, P. D., Grosse-Kunstleve, R. W., Hung, L.-W., Ioerger, T. R., McCoy, A. J., Moriarty, W., Read, R. J., Sacchettini, J. C., Sauter, N. K., and Terwilliger, T. C. (2002) PHENIX: building new software for automate crystallographic structure determination. *Acta Crystallogr. D58*, 1948–1954.

70. Wallin, E., and von Heijne, G. (1998) Genome-wide analysis of integral membrane proteins from eubacterial, archaean, and eukaryotic organisms. *Protein Sci. 7*, 1029–1038.

71. Stevens, T. J., and Arkin, I. T. (2000) Do more complex organisms have a greater proportion of membrane proteins in their genomes? *Proteins 39*, 417–420.

72. Tusnady, G., Dosztanyi, Z., and Simon, I. (2004) Transmembrane proteins in the Protein Data Bank: identification and classification. *Bioinformatics 20*, 2964–2972.

73. Drews, J. (2000) Drug discovery: a historical perspective. *Science 287*, 1960–1964.

74. Imming, P., Sinning, C., and Meyer, A. (2006) Drugs, their targets and the nature and number of drug targets. *Nat. Rev. Drug Discov. 5*, 821–834.

75. Michel, H., and Oesterhelt, D. (1980) Three-dimensional crystals of membrane proteins: bacteriorhodopsin. *Proc. Nat. Acad. Sci. U. S. A. 77*, 1283–1285.

76. Garavito, R. M., and Rosenbusch, J. P. (1980) Three-dimensional crystals of an integral membrane protein. *J. Cell Biol. 86*, 327–329.

77. Helenius, A., and Simons, K. (1975) Solubilization of membranes by detergents. *Biochim. Biophys. Acta 415*, 29–79.

78. le Maire, M., Champeil, P., and Moller, J. V. (2000) Interaction of membrane proteins and lipids with solubilizing detergents. *Biophys. Acta 1508*, 86–111.

79. Kuhlbrandt, W. (1992) Two-dimensional crystallization of membrane proteins. *Q. Rev. Biophys. 25*, 1–49.

80. Michel, H. (1983) Crystallization of membrane proteins. *Trends Biochem. Sci. 8*, 56–59.

81. Faham, S., and Bowie, J. (2002) Bicelle crystallization: a new method for crystallizing membrane proteins yields a monomeric bacteriorhodopsin structure. *J. Mol. Biol. 316*, 1–6.

82. Sutton, B. J., and Sohi, M. K. (1994) Crystallization of membrane proteins for X-ray analysis. *Methods Mol. Bio. 27*, 1–18.

83. Lee, A. G. (1998) How lipids interact with an intrinsic membrane protein: the case of the calcium pump. *Biochim. Biophys. Acta 1376*, 381–390.

84. le Courte, J., and Kaback, H. R. (2000) Structure-function relationships of integral membrane proteins: membrane transporters versus channels. *Biopolymers 55*, 297–307.

85. Landau, E. M., and Rosenbusch, J. P. (1996) Lipidic cubic phases: a novel concept for the crystallization of membrane proteins. *Proc. Natl. Acad. Sci. U. S. A. 93*, 14532–14535.

86. Takeda, K., Sato, H., Hino, T., Kono, M., Fukada, K., Sakurai, I., Okada, T., and Kouyama, T. (1998) A novel three-dimensional crystal of bacteriorhodopsin obtained by successive fusion of the vesicular assemblies. *J. Mol. Biol. 283*, 463–474.

87. Pebay-Peyroula, E., Rummel, G., Rosenbusch, J. P., and Landau, E. M. (1997) X-ray structure of bacteriorhodopsin at 2.5 angstroms from microcrystals grown in lipidic cubic phases. *Science 277*, 1676–1681.

88. Luecke, H., Richter, H. T., and Lanyi, J. K. (1998) Proton transfer pathways in bacteriorhodopsin at 2.3 angstrom resolution. *Science 280*, 1934–1937.

89. Edman, K., Nollert, P., Royant, A., Belrhali, H., Pebay-Peyroula, E., Hajdu, J., Neutze, R., and Landau, E. M. (1999) High-resolution X-ray structure of an early intermediate in the bacteriorhodopsin photocycle. *Nature 401*, 822–826.

90. Luecke, H., Schobert, B., Richter, H. T., Cartailler, J. P., and Lanyi, J. K. (1999a) Structural changes in bacteriorhodopsin during ion transport at 2 angstrom resolution. *Science 286*, 255–260.

91. Luecke, H., Schobert, B., Richter, H. T., Cartailler, J. P., and Lanyi, J. K. (1999b) Structure of bacteriorhodopsin at 1.55 Å resolution. *J. Mol. Biol. 291*, 899–911.

92. Chiu, M. L., Nollert, P., Loewen, M. C., Belrhali, H., Pebay-Peyroula, E., Rosenbusch, J. P., and Landau, E. M. (2000) Crystallization in cubo: general applicability to membrane proteins. *Acta Crystallogr. D56*, 781–784.

93. Royant, A., Edman, K., Ursby, E., Pebay-Peyroula, E., Landau, E. M., and Neutze, R. (2000) Helix deformation is coupled to vectorial proton transport in the photocycle of bacteriorhodopsin. *Nature 406*, 645–648.

94. Royant, A., Nollert, P., Edman, K., Neutze, R., Landau, E. M., Pebay-Peyroula, E., and Navarro, J. (2001) X-ray structure of sensory rhodopsin II at 2.1 Å resolution. *Proc. Nat. Acad. Sci. U. S. A. 98*, 10131–10136.

95. Rouhani, S., Cartailler, J. P., Facciotti, M. T., Walian, P., Needleman, R., Lanyi, J. K., Glaeser, R. M., and Luecke, H. (2001) Crystal structure of the D85S mutant of bacteriorhodopsin: model of an O-like photocycle intermediate. *J. Mol. Biol. 313*, 615–628.

96. Luecke, H., Schovert, B., Lanyi, J. K., Spudich, E. N., and Spudich, J. L. (2001) Crystal structure of a sensory rhodopsin II at 2.4 angstroms: insights into color tuning and transducer interaction. *Science 293*, 1499–1503.

97. Gordeliy, V. I., Labahn, J., Moukhametzianov, R., Efremov, R., Granzin, J., Schlesinger, R., Buldt, G., Savopol, T., and Engelhard, M. (2002) Molecular basis of transmembrane signaling by sensory rhodopsin II- transducer complex. *Nature 419*, 484–487.

98. Matsui, Y., Sakai, K., Murakami, M., Shiro, Y., Adachi, S., Okumura, H., and Kouyama, T. (2002) Specific damage induced by X-ray radiation and structural

changes in the primary photoreaction of bacteriorhodopsin. *J. Mol. Biol. 324*, 469–481.

99. Kouyama, T., Nishikawa, T., Tokuhisa, T., and Okumura, H. (2004) Crystal structure of the L intermediate of bacteriorhodopsin: evidence for vertical translocation of a water molecular during the proton pumping cycle. *J. Mol. Biol. 335*, 531–546.

100. Takeda, K., Matsui, Y., Kamiya, N., Adachi, S., Okumura, H., and Tsutomu, K. (2004) Crystal structure of the M intermediate of bacteriorhodopsin: allosteric structural changes mediated by sliding movement of a transmembrane helix. *J. Mol. Biol. 341*, 1023–1037.

101. Faham, S., Yang, D., Bare, E., Yohannan, S., Whitelegge, J. P., and Bowie, J. U. (2004) Side-chain contributions to membrane protein structure and activity. *J. Mol. Biol. 335*, 297–305.

102. Faham, S., Boulting, G. L., Massey, E. A., Yohannan, S., Yang, D., and Bowie, J. (2005) Crystallization of bacteriorhodopsin from bicelle formulations at room temperature. *Protein Sci. 14*, 836–840.

103. Nishikawa, T., Murakami, M., and Kouyama, T. (2005) Crystal structure of the 13-*cis* isomer of bacteriorhodopsin in the dark-adapted state. *J. Mol. Biol. 352*, 319–328.

104. Cherezov, V., Yamashita, E., Liu, W., Zhalnina, M., Cramer, W. A., and Caffrey, M. (2006) In meso structure of the cobalamin transporter, BtuB, at 1.95 Å resolution. *J. Mol. Biol. 364*, 716–734.

105. Yoshimura, K., and Kouyama, T. (2008) Structural role of bacterioruberin in the trimeric structure of archaerhodopsin-2. *J. Mol. Biol. 2008*, 1267–1281.

106. Valiyaveetil, F. I., Zhou, Y., and MacKinnon, R. (2002) Lipids in the structure, folding, and function of the KcsA K+ channel. *Biochemistry 41*, 10771–10777.

107. Schmidt-Krey, I. (2007) Electron crystallography of membrane proteins: two-dimensional crystallization and screening by electron microscopy. *Methods 41*, 417–426.

108. Doyle, D. A., Cabral, J. M., Pfuetzner, R. A., Kuo, A., Gulbis, J. M., Cohen, S. L., Chait, B. T., and MacKinnon, R. (1998) The structure of the potassium channel: molecular basis of K+ conduction and selectivity. *Science 280*, 69–77.

109. Zhou, Y., Morais-Cabral, J. H., Kaufman, A., and MacKinnon, R. (2001) Chemistry of ion coordination and hydration revealed by a K+ channel-Fab complex at 2.0 Å resolution. *Nature 414*, 43–48.

110. Zhou, M., and MacKinnon, R. (2004) A mutant KcsA K+ channel with altered conduction properties and selectivity filter ion distribution. *J. Mol. Biol. 338*, 839–846.

111. Middleman, S. (1998) *An introduction to mass and heat transfer.* John Wiley & Sons Inc., New York.

112. Cannon, D. M., Jr., Kuo, T.-C., Bohn, P. W., and Sweedler, J. V. (2003) Nanocapillary array interconnects for gated analyte injections and electrophoretic separations in multilayer microfluidic architectures. *Anal. Chem. 75*, 2224–2230.

113. Kuo, T.-C., Cannon, D. M., Jr., Shannon, M. A., Bohn, P. W., and Sweedler, J. V. (2003) Hybrid three-dimensional nanofluidic/microfluidic devices using molecular gates. *Sens. Actuators 102*, 223–233.

114. Chueh, B.-H., Huh, D., Krytsos, C. R., Houssin, T., and Nobuyuki, F. (2007) Leakage-free bonding of porous membranes into layered microfluidic array systems. *Anal. Chem. 79*, 3504–3508.

115. Long, Z., Liu, D., Ye, N., Qin, J., and Lin, B. (2006) Integration of nanoporous membranes for sample filtration/preconcentration in microchip electrophoresis. *Electrophoresis 27*, 4927–4934.